Aus der Kinderklinik und Kinderpoliklinik im Dr. von Haunerschen Kinderspital

Ludwig-Maximilians-Universität München

Direktor: Prof. Dr. med. Dr. sci. nat. Christoph Klein

Kumulative Habilitationsschrift

zur Erlangung der Venia Legendi

im Fach Kinder- und Jugendmedizin

Analyse molekularer Grundlagen benigner und maligner hämatologischer Erkrankungen zur Entwicklung neuer und zielgerichteter Therapien

vorgelegt von

Dr. med. Vera Binder-Blaser

2025

FACHMENTORAT

Prof. Dr. med. Dr. sci. nat. Christoph Klein

Prof. Dr. med. Irmela Jeremias

Prof. Dr. med. Nicole Angela Terpolilli

INHALT

1. EINFÜHRUNG

1.1 MOLEKULARE GRUNDLAGEN DER GESUNDEN HÄMATOPOESE UND DER KRANKHEITSENTSTEHUNG

Ein vertieftes Verständnis der molekularen Grundlagen der gesunden Hämatopoese ist essenziell, um die Mechanismen der Krankheitsentstehung zu ergründen und dadurch Prognose und Therapieoptionen – insbesondere im Kontext individualisierter Behandlungsansätze – zu optimieren. Die vorliegende Arbeit widmet sich der molekularen Charakterisierung hämatopoetischer Erkrankungen, die im Knochenmark entstehen. Neben der Untersuchung von Immundefekten und „bone marrow failure"-Syndromen, bei denen Panzytopenien und ein komplettes Versagen der hämatopoetischen Funktion zugrunde liegen, liegt der Schwerpunkt auf Leukämien, der häufigsten malignen Erkrankungsgruppe im Kindesalter.

Bei der Diagnosestellung von Leukämien, insbesondere von B-Vorläuferleukämien – der in der pädiatrischen Onkologie vorherrschenden Form – erfolgt die Risikoeinschätzung anhand von Kriterien wie der initialen Leukozytenzahl im peripheren Blut, dem Alter, dem Immunphänotyp sowie zytogenetischen und molekulargenetischen Befunden (Campbell et al, 2023; Smith et al, 1996; Testi et al, 2019). Während die initiale Therapie auf diesen Parametern basiert, wird im weiteren Verlauf vor allem das Ansprechen auf die Behandlung (evaluierbar durch den Minimal Residual Disease [MRD]-Verlauf) herangezogen, um das Therapieschema gegebenenfalls anzupassen (Campbell et al, 2023; Smith et al, 1996; Stutterheim et al, 2022; Testi et al, 2019). Trotz dieser etablierten prognostischen Faktoren und verbesserter Therapieansätze kommt es bei einem signifikanten Anteil von Patienten zu Rückfällen, deren Behandlung nach wie vor eine große Herausforderung darstellt (Eckert et al, 2021; Nguyen et al, 2008). Die frühzeitige Identifikation von Patienten mit erhöhtem Rezidivrisiko ist daher unabdingbar, um therapeutische Anpassungen bereits zum Zeitpunkt der Diagnosestellung in Betracht zu ziehen.

1.2 MOLEKULARE MARKER (SOMATISCH UND KEIMBAHN) FÜR RISIKOSTRATIFIZIERUNG UND THERAPIEENTSCHEIDUNG

Die molekulare Heterogenität kindlicher Leukämien übersteigt die bisher durch konventionelle Risikostratifizierung erfassten Faktoren. Am Beispiel der akuten lymphoblastischen Leukämie (ALL) zeigt sich, wie die detaillierte Analyse somatischer sowie Keimbahnmutationen zur Verbesserung der Therapie beigetragen hat. Bestimmte somatische Veränderungen, etwa Hyperdiploidie (>50 Chromosomen oder DNA-Index ≥1,16) und die t(12;21)-Translokation, die zur Bildung des ETV6-RUNX1-Fusionsgens führt, sind mit einer günstigen Prognose verbunden und treten vornehmlich bei jungen Kindern mit relativ niedrigen Leukozytenzahlen auf. Im Gegensatz dazu korrelieren Hypodiploidie (<44

Chromosomen), Ph-positive oder Ph-like ALLs, sowie Translokationen von KMT2A, MEF2D, BCL2/MYC und TCF3-HLF mit einem ungünstigen Outcome, wobei diese genetischen Veränderungen vermehrt bei Jugendlichen oder jungen Erwachsenen, mit hohen initialen Leukozytenzahlen und/oder ZNS-Beteiligung, beobachtet werden. Säuglingsleukämien sind zudem stark mit KMT2A-Translokationen assoziiert.

Genomweite Analysen haben ein enges Zusammenspiel zwischen vererbten und somatischen Mutationen in der ALL aufgezeigt. Konstitutionelle Syndrome wie Down-Syndrom und Ataxia-telangiectatica erhöhen das Risiko für B-Zell-Leukämien (häufig mit CRLF2-Rearrangement) sowie T-Zell-ALL, während familiäre Krebssyndrome wie das Li-Fraumeni-Syndrom, die konstitutionelle Mismatch Repair Deficiency sowie andere DNA-Reparaturstörungen (z. B. Nijmegen-Breakage-Syndrom) generell mit einer erhöhten Malignitätsinzidenz assoziiert sind. Obwohl eine familiäre Leukämieprädisposition selten ist, haben Untersuchungen sporadischer Varianten zur Identifizierung prädisponierender Mutationen geführt, wie zum Beispiel TP53-Keimbahnmutationen bei niedrig hypodiploiden B-ALLs, ETV6-Varianten bei hyperdiploiden ALLs und PAX5-Mutationen bei B-ALLs. Diese Suszeptibilitätsgene sind häufig auch Ziele somatischer Mutationen, wie beispielsweise ETV6 und PAX5 bei B-ALL oder TP53 bei hypodiploider ALL. In genomweiten Assoziationsstudien (GWAS) konnten nicht kodierende Varianten in mindestens 13 Loci identifiziert werden, die, wenn auch einzeln mit einem moderaten Risiko (1,5- bis 2-fach), kumulativ das Leukämierisiko erheblich steigern können (Inaba & Mullighan, 2020).

Die detaillierte genetische Charakterisierung der ALL differenziert dabei zwischen verschiedenen Subtypen. So umfasst die B-ALL über 20 genetische Subtypen, die sich durch chromosomale Aneuploidien, rearrangementbedingte Deregulierung von Onkogenen oder die Bildung chimärer Transkriptionsfaktoren sowie Punktmutationen auszeichnen. Während beispielsweise High-Hyperdiploidie (>50 Chromosomen) mit Mutationen im Ras-Signalweg und Chromatinmodulatoren wie CREBBP ein gutes Outcome indiziert, ist Low-Hypodiploidie – häufig verbunden mit IKZF2-Deletion und TP53-Mutationen (teilweise vererbt) – mit einer schlechten Prognose verknüpft. Translokationsgetriebene Subtypen wie t(12;21) (ETV6-RUNX1) sind prognostisch günstig, während t(9;22) (BCR-ABL1), t(4;11) (KMT2A/AFF1) sowie iAMP21 mit ungünstigen Verläufen assoziiert sind. Neben transcription factor-getriebenen Veränderungen existieren auch kinaseaktivierte Subtypen, wie Ph+ und Ph-like ALL, deren molekulare Komplexität und therapeutische Zielbarkeit – beispielsweise durch Tyrosinkinaseinhibitoren – intensiv untersucht werden bzw. bereits im klinischen Einsatz sind (Inaba & Mullighan, 2020).

Bei T-Zell-Leukämien dominieren neben Veränderungen in T-Linien-spezifischen Transkriptionsfaktoren insbesondere Aberrationen im NOTCH1/MYC-Signalweg sowie in der Zellzykluskontrolle. Über 90 % der T-ALLs lassen sich anhand charakteristischer Genexpressionsprofile in Subgruppen einteilen, wobei NOTCH1-Aktivierung (durch

Mutationen oder FBXW7-Inaktivierung) und häufige Deletionen von Tumorsuppressorgenen wie CDKN2A/CDKN2B wesentliche Treiber dieser Erkrankung darstellen (Inaba & Mullighan, 2020).

Die Analyse der Genetik des Rückfalls hat gezeigt, dass die subklonale Komplexität und klonalen Dynamiken unter Therapie von zentraler Bedeutung sind. Leukämie-initiierende Fusionen bleiben oft klonal bestehen, während zusätzliche, teilweise subklonale Mutationen (z. B. in FLT3, NRAS, KRAS, CREBBP, SETD2, NR3C1/NR3C2) im Verlauf der Behandlung entstehen können und zur Chemoresistenz beitragen. Das Monitoring der Mutationsdynamik während der Induktion ermöglicht somit eine frühzeitige Identifikation von Patienten, die von einer Modifikation der Therapie profitieren könnten (Inaba & Mullighan, 2020).

Die daraus abgeleiteten zielgerichteten Therapiestrategien zielen darauf ab, die standardmäßige Chemotherapie durch den Einsatz von molekular spezifischen Inhibitoren zu ergänzen oder zu ersetzen. Beispiele hierfür sind ABL1-Tyrosinkinaseinhibitoren wie Imatinib, Dasatinib und Ponatinib in der Behandlung von Ph+ ALL, sowie der Einsatz von JAK-Inhibitoren (z. B. Ruxolitinib) bei ALL mit JAK/STAT-Aktivierung. Darüber hinaus zeigen zielgerichtete Ansätze mit Venetoclax (BCL-2-Inhibitor), Proteasom- und mTOR-Inhibitoren sowie epigenetischen Modulatoren vielversprechende Ergebnisse in präklinischen Studien, insbesondere bei Hochrisiko-Subtypen (Inaba & Mullighan, 2020).

1.3 ZEBRAFISCH ALS MODELLORGANISMUS

Der Zebrafisch hat sich als exzellentes Modell zur Untersuchung des hämatologischen Systems etabliert (de Jong & Zon, 2005). Mit der Expression von Orthologen für mehr als 82 % der humanen, krankheitsassoziierten Gene bietet er ein erhebliches Potential, humane Erkrankungen wie Krebs zu modellieren (Howe et al, 2013). Darüber hinaus ist das hämatopoetische System des Zebrafisches, insbesondere in Bezug auf Wachstumsfaktoren, Chemo- und Zytokine sowie Transkriptionsfaktoren, evolutionär stark konserviert (Jing & Zon, 2011). Bereits 2–6 Tage nach der Fertilisation lokalisiert sich die hämatopoetische Nische im posterioren Bereich des Fisches, im sogenannten caudal hematopoietic tissue (CHT), welches mikroskopisch hervorragend zugänglich ist.

Die natürliche Transparenz der Zebrafischlarven sowie die Möglichkeit, spezifische Nischenzellen wie Endothelzellen und Makrophagen mittels Fluoreszenzmarkierung in vivo zu visualisieren, erlauben eine detaillierte Einzelzellanalyse der Interaktionen zwischen Leukämiezellen und ihren umgebenden Nischenzellen. Da embryonale Zebrafische in den ersten Wochen kein adaptiertes Immunsystem besitzen (Lam et al, 2004), sind sie ideale Empfänger humaner Zellen. So konnten Pruvot et al. (Pruvot et al, 2011) nachweisen, dass transplantierte humane Leukämiezellen in Zebrafischlarven bis zu sechs Tage überleben und proliferieren. Zudem zeigte Sacco et al. (Sacco et al, 2016), dass Krebsarten, die typischerweise

Knochenmarksmetastasen bilden, bevorzugt im CHT anwachsen, während andere Tumorarten dieses Verhalten nicht aufweisen.

Ein weiterer Vorteil des Zebrafischmodells ist die Möglichkeit, fluoreszenzmarkierte hämatopoetische Zellen *in vivo* nachzuverfolgen – nicht nur in Larven, sondern auch in genetisch modifizierten, transparenten Casper-Fischen (White et al, 2008). Dieses einzigartige Merkmal ermöglicht kompetitive Transplantationsassays in Echtzeit und mit Einzelzellauflösung, eine Methode, die in keinem anderen Tiermodell in vergleichbarer Form realisierbar ist (Binder & Zon, 2012).

Im Rahmen des Habilitationsprojekts wurden zur Beantwortung spezifischer Forschungsfragen sowohl *in vitro* Versuche, als auch *in vivo* kompetitive Transplantationsassays im Zebrafisch- und Mausmodell durchgeführt. Ergänzend kamen Xenotransplantationsassays im Zebrafisch zum Einsatz, bei denen humane Leukämiezellen transplantiert wurden, um weitere Einblicke in die Pathogenese hämatopoetischer Erkrankungen zu gewinnen.

2. MOTIVATION UND ZIELE DES HABILITATIONSPROJEKTS

2.1. MOTIVATION FÜR DIE ARBEITEN

Das vorliegende Habilitationsprojekt „Analyse molekularer Grundlagen benigner und maligner hämatologischer Erkrankungen zur Entwicklung neuer und zielgerichteter Therapien“ hat zum Ziel, durch die detaillierte Aufdeckung molekularer Mechanismen hämatopoetischer Erkrankungen – insbesondere von Leukämien – neuartige Therapiestrategien zu entwickeln. Dabei werden genetische Veränderungen auf unterschiedlichen Ebenen untersucht: Zum einen erfolgt die Analyse von Mutationen im kodierenden Anteil des Genoms mittels Verfahren wie „targeted sequence capture“ und Whole Exome Sequenzierung, zum anderen werden auch nicht für Proteine kodierende Bereiche, sogenannte mikroRNAs (miRNAs), untersucht. Diese kleinen regulatorischen RNAs steuern weitreichend Proteinnetzwerke und modulieren komplette Signalkaskaden.

Ergänzend kommen Einzelzellsequenzierungen (Whole Genome und Whole Transcriptome) zum Einsatz, um genetische Veränderungen in auch sehr kleinen Anteilen spezifischer Zellpopulationen zu identifizieren und deren funktionelle Relevanz zu untersuchen. Ein vertieftes Verständnis der molekularen Grundlagen der gesunden Hämatopoese, der Mechanismen der Krankheitsentstehung sowie der Genotyp-Phänotyp-Korrelation hämatopoetischer Erkrankungen verbessert die Prognoseeinschätzung und ermöglicht die Identifikation neuer Zielstrukturen, die den Weg zu individualisierten Therapieoptionen ebnen.

Zukünftige Herausforderungen liegen sowohl in der vollständigen Heilung aller leukämieerkrankten Kinder als auch in der Minimierung von Therapie-Nebenwirkungen und Spätfolgen. Die molekular basierte, individualisierte Präzisionsmedizin stellt hierbei einen der größten Hoffnungsträger für innovative Behandlungskonzepte dar.

2.2 DIE ZIELE DIESES HABILITATIONSPROJEKTS:

(i) Die Weiterentwicklung und Optimierung von Methoden zur präzisen Analyse der molekularen Grundlagen benigner und maligner hämatopoetischer Erkrankungen,
(ii) die funktionelle Evaluation molekularer Veränderungen,
(iii) die Identifikation von Krankheitsursachen, die neben stamm- oder leukämiezellintrinsischen auch nischenvermittelte Aspekte berücksichtigen, sowie
(iv) die Entwicklung neuer pharmakologischer Ansatzpunkte für personalisierte Therapiekonzepte.

3. WISSENSCHAFTLICHE ERKENNTNISSE DES HABILITATIONSPROJEKTS

3.1 EIGENE FORSCHUNGSARBEITEN UND DEREN BEDEUTUNG FÜR DAS FACHGEBIET

3.1.1 THE GENOTYPE OF THE ORIGINAL WISKOTT PHENOTYPE

Binder V, Albert MH, Kabus M, Bertone M, Meindl A, Belohradsky BH

The genotype of the original Wiskott phenotype

N Engl J Med. **2006** Oct 26:355(17): 1790-3

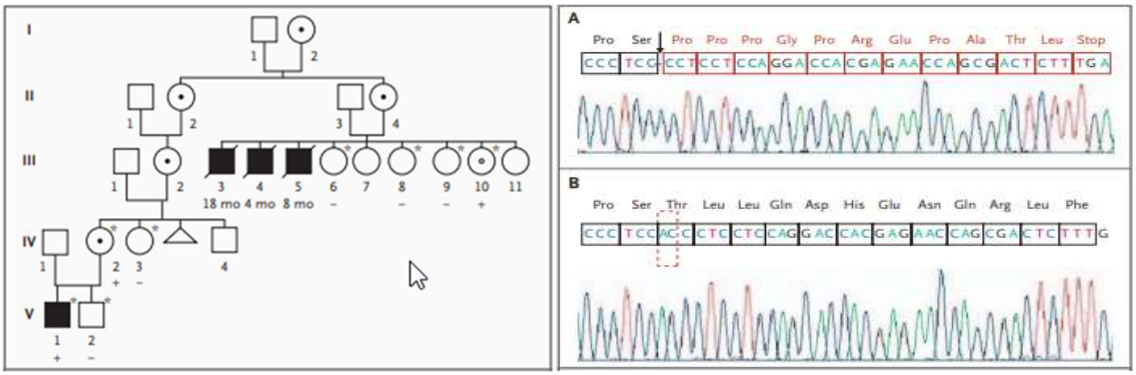

Das Wiskott–Aldrich-Syndrom (WAS) stellt einen X-chromosomal vererbten, kombinierten Immundefekt dar, der sich klinisch durch Thrombozytopenie, das Vorliegen von kleinen Thrombozyten, Ekzeme sowie eine erhöhte Prädisposition für Autoimmunerkrankungen und Krebserkrankungen manifestiert. Die Erkrankung wird durch Mutationen im WAS-Gen verursacht, das auf Xp11.22–p11.23 lokalisiert ist und bereits 1994 kloniert wurde. Mutationen im WAS-Gen führen in der Regel zu einer Verkürzung oder zum vollständigen Fehlen des WAS-Proteins (WASP) in den betroffenen Zellen, was sich in einer breiten phänotypischen Variabilität äußert – von der schweren Form des Syndroms bis hin zu milderen Manifestationen wie der X-chromosomal bedingten Thrombozytopenie oder Neutropenie. Da WASP in nahezu allen Zellen des hämatopoetischen Systems exprimiert wird, ist eine Korrektur in mehreren Zelllinien erforderlich. Dies bildet auch die Grundlage für therapeutische Ansätze wie die hämatopoetische Stammzelltransplantation (HSCT) oder Gentherapien.

Im Rahmen unserer Untersuchungen an Familienmitgliedern der ursprünglich 1937 von Wiskott klinisch beschriebenen Patienten konnten wir eine neue Frameshift-Mutation in Exon 1 des WAS-Gens identifizieren. Diese Mutation entspricht vermutlich dem hypothetisierten Genotyp, der die schwere Form des Wiskott–Aldrich-Syndroms bei den von Wiskott beschriebenen drei Brüdern verursacht hat.

Die Aufklärung des zugrunde liegenden Gendefekts ist von zentraler Bedeutung für die Analyse der Genotyp-Phänotyp-Korrelation bei WAS. Insbesondere stellt sich die Frage, inwieweit der identifizierte Gendefekt spezifische Zelltypen des Immunsystems beeinflusst und welche zellulären Mechanismen zur klinischen Heterogenität beitragen. Unsere Ergebnisse zeigen, dass eine strikte Genotyp-Phänotyp-Korrelation nicht vorliegt: Identische Mutationen können in unterschiedlichen Familienmitgliedern zu einer breiten Variabilität phänotypischer Ausprägungen und somit zu sehr unterschiedlichen klinischen Verläufen führen. Diese Beobachtungen unterstreichen, dass neben dem primären Gendefekt weitere modulierende Faktoren – etwa epigenetische Modifikationen oder Umwelteinflüsse – entscheidend zur Expression des Krankheitsbildes beitragen.

Die Identifizierung der ursächlichen Mutation bei den ursprünglich klinisch beschriebenen WAS-Patienten stellt einen wesentlichen Fortschritt in der genetischen Charakterisierung dieser Erkrankung dar. Sie liefert einen wichtigen Baustein für das Verständnis der Genotyp-Phänotyp-Korrelation und ermöglicht eine präzisere Einschätzung des Schweregrades bei genetischer Diagnosestellung. Dies ist insbesondere relevant für die klinische Beratung und Therapieentscheidung, da die Kenntnis des zugrunde liegenden Gendefekts unter anderem die frühzeitige Indikation einer Knochenmarktransplantation oder Gentherapie erleichtert.

Insgesamt trägt die vorliegende Arbeit dazu bei, das komplexe Zusammenspiel genetischer und modulierender Faktoren bei WAS besser zu verstehen und bildet die Grundlage für eine individualisierte therapeutische Entscheidungsfindung im Rahmen der Behandlung dieses schwerwiegenden Immundefekts. Zusammengefasst aus (Binder et al, 2006).

3.1.2 A NOVEL MTDNA LARGE-SCALE MUTATION CLINICALLY EXCLUSIVELY PRESENTING WITH REFRACTORY ANEMIA: IS THERE A CHANCE TO PREDICT DISEASE PROGRESSION?

Binder V, Steenpass L, Laws HJ, Ruebo J, Borkhardt A

A novel mtDNA large-scale mutation clinically exclusively presenting with refractory anemia: is there a chance to predict disease progression?

J Pediatr Hematol Oncol. **2012** May;34(4):283-92.

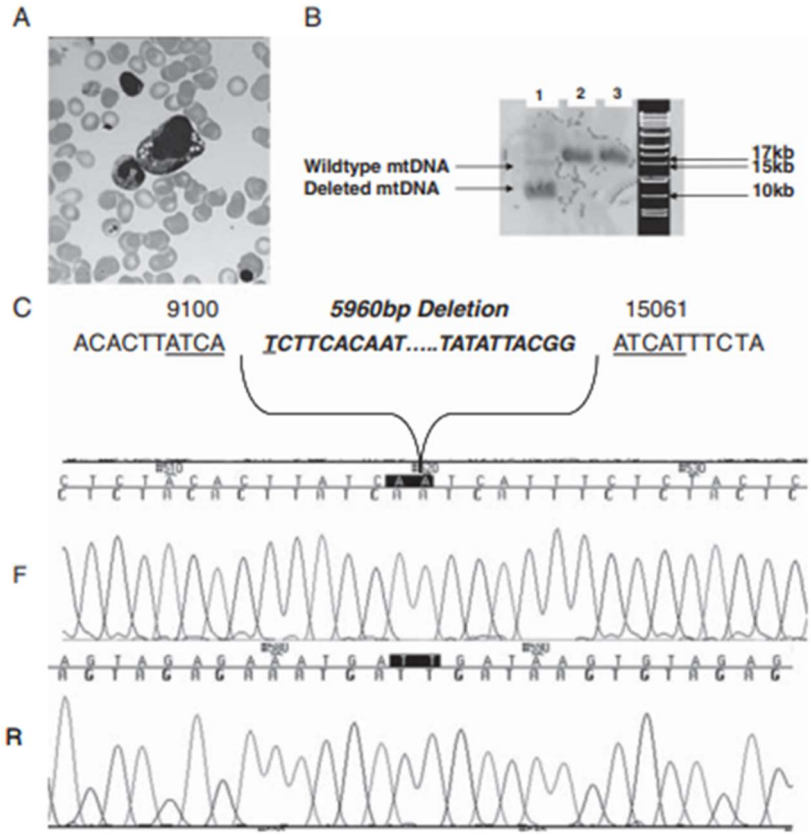

Mitochondriale Erkrankungen gehören zu den komplexesten genetischen Störungen, da sie durch Mutationen in der mitochondrialen DNA (mtDNA) oder der nukleären DNA verursacht werden können. Die humane mtDNA ist ein zirkuläres Minichromosom mit einer Länge von 16,5 kb, das maternal vererbt wird und mehrere tausend Kopien pro Zelle enthalten kann. Mutationen in der mtDNA können entweder homoplasmisch (alle Kopien sind identisch) oder heteroplasmisch (Koexistenz von mutierter und Wildtyp-mtDNA) vorliegen, wobei der Heteroplasmiegrad durch mitotische Segregation variieren kann.

Ein zentrales Problem in der Erforschung mitochondrialer Erkrankungen ist die geringe Genotyp-Phänotyp-Korrelation. Das bedeutet, dass identische mtDNA-Deletionen bei verschiedenen Individuen zu sehr unterschiedlichen klinischen Manifestationen führen können. Während einige Patienten nur eine isolierte Organbeteiligung zeigen, entwickeln andere Multisystemerkrankungen, die mehrere Organe betreffen, darunter das zentrale Nervensystem, die Muskulatur, das Herz-Kreislauf-System und das hämatopoetische System.

Große Deletionen der mtDNA werden vermutlich durch Fehlpaarungen zwischen kurzen repetitiven Sequenzen (4–13 bp) während der mtDNA-Replikation in der Oogenese verursacht. Diese Deletionen können zu einer erheblichen Einschränkung der oxidativen Phosphorylierung führen, was insbesondere in energieintensiven Geweben wie dem Gehirn, den Muskeln und dem Knochenmark zu schweren Funktionsstörungen führt.

Die Diagnosestellung mitochondrialer Erkrankungen erfordert eine umfassende molekulargenetische Analyse. Da mitochondriale Defekte zu einer Vielzahl klinischer Symptome führen können, bleibt die Früherkennung schwierig, insbesondere wenn initial nur ein einzelnes Organsystem betroffen ist. Zu den mitochondrialen Syndromen mit hämatologischer Manifestation gehören das Pearson-Syndrom (PS) und das Kearns-Sayre-Syndrom (KSS), die beide durch große mtDNA-Deletionen verursacht werden.

In unserer Studie beschrieben wir einen acht Monate alten Jungen, der sich klinisch ausschließlich mit einer therapierefraktären makrozytären Anämie präsentierte. Die genetische Analyse ergab eine bislang unbekannte Deletion in der mtDNA, die essenzielle Gene der oxidativen Phosphorylierung betraf. Diese Mutation zeigte Ähnlichkeiten zu Deletionen, die mit dem Pearson-Syndrom oder dem Kearns-Sayre-Syndrom assoziiert sind.

Unsere systematische Analyse aller auf MitoMap veröffentlichten Fälle zeigte jedoch, dass es keine eindeutige Genotyp-Phänotyp-Korrelation gibt. Das bedeutet, dass Patienten mit der gleichen mtDNA-Mutation sehr unterschiedliche klinische Verläufe zeigen können. Während einige Betroffene ausschließlich eine hämatologische Auffälligkeit entwickeln, manifestiert sich bei anderen eine Multisystemerkrankung mit neurodegenerativen und metabolischen Symptomen.

Diese Erkenntnisse verdeutlichen die fehlende Vorhersagbarkeit des Krankheitsverlaufs bei mtDNA-Deletionen und unterstreichen die Notwendigkeit einer langfristigen klinischen Überwachung. Insbesondere bei Patienten, die sich initial mit einer isolierten hämatologischen Symptomatik präsentieren, müssen potenzielle spätere multisystemische Manifestationen berücksichtigt werden.

Unsere Studie liefert einen wichtigen Beitrag zum Verständnis der molekularen Grundlagen mitochondrialer Erkrankungen mit hämatologischer Beteiligung. Sie zeigt, dass die klinische Variabilität selbst innerhalb derselben genetischen Mutation enorm ist, was eine standardisierte Therapieplanung erschwert.

Zukünftige Studien sollten sich darauf konzentrieren, weitere molekulare Mechanismen der mtDNA-Deletionskrankheiten zu entschlüsseln, um potenzielle biomarkerbasierte Prognosemodelle zu entwickeln. Gleichzeitig sind Fortschritte in der gentherapeutischen Korrektur mitochondrialer Defekte erforderlich, um gezielte Behandlungsstrategien für betroffene Patienten zu ermöglichen.

Unsere Ergebnisse verdeutlichen zudem die Bedeutung einer frühzeitigen genetischen Diagnostik und einer interdisziplinären Betreuung von Patienten mit mtDNA-Deletionen, um eine bestmögliche klinische Versorgung sicherzustellen. Zusammengefasst aus (Binder et al, 2012)

3.1.3 A NEW WORKFLOW FOR WHOLE GENOME SEQUENCING OF SINGLE HUMAN CELLS

Binder V*, Bartenhagen C*, Okpanyi V, Gombert M, Moehlendick B, Behrens B, Klein HU, Rieder H, Krell PFI, Dugas M, Stoecklein NH and Borkhardt A.

**** Both authors contributed equally to this work***

A new workflow for whole genome sequencing of single human cells.

Hum Mutat. 2014 Oct;35(10):1260-70.

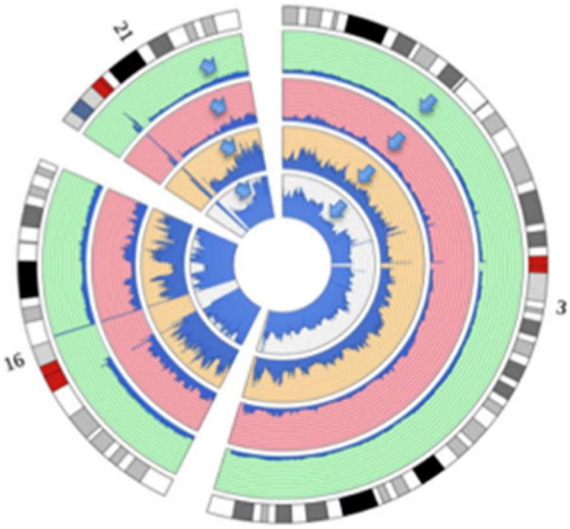

Die unvoreingenommene Amplifikation des Gesamtgenoms (Whole-Genome Amplification, WGA) einzelner Zellen stellt eine zentrale Methode zur Untersuchung der genetischen Heterogenität und klonalen Evolution maligner Erkrankungen dar. Insbesondere in der Krebsforschung ist die Analyse individueller Zellen entscheidend, um die genetische Vielfalt innerhalb eines Tumors oder einer Leukämie zu charakterisieren und die für die Krankheitsprogression verantwortlichen Zellklone zu identifizieren. Aufgrund der enormen Komplexität des menschlichen Genoms sind jedoch bisherige WGA-Methoden häufig durch unvollständige und ungleichmäßige Amplifikationen oder hohe Raten von Allelverlust (allele dropout) limitiert.

In dieser Studie wurde ein neuer experimenteller Workflow etabliert, der eine auf Adapter-Linker-PCR basierende WGA-Strategie mit einer Sequenzierung der zweiten Generation kombiniert. Diese Methodenkombination ermöglicht die hochauflösende Analyse einzelner Zellgenome bis auf die Basenpaarebene und stellt einen bedeutenden Fortschritt in der Einzelzellgenomik dar. Durch die Optimierung des WGA-Protokolls konnte eine

bemerkenswert hohe Abdeckung von bis zu 74 % des gesamten menschlichen Genoms erreicht werden. Die Detektion von Kopienzahlvariationen (copy number variations, CNVs) und Verlusten der Heterozygotie (loss of heterozygosity, LOH) in Einzelzellgenomen zeigte eine beeindruckende Übereinstimmung von bis zu 99 % mit Ergebnissen aus gepoolter genomischer DNA.

Ein entscheidender Vorteil der entwickelten Methode liegt in der außergewöhnlich niedrigen Allelverlust-Rate von nur 2 %, was eine präzise Bestimmung von Allelfrequenzen ermöglicht und Unregelmäßigkeiten im Amplifikationsprozess minimiert. Zudem erlaubt die Sequenzierung mit gepaarten Leseenden (paired-end sequencing) eine umfassende genomweite Analyse struktureller Varianten, die bei der Untersuchung genetischer Instabilität von besonderer Bedeutung sind. Der direkte Vergleich mit etablierten WGA-Methoden zeigt, dass dieser Ansatz eine besonders hohe Genauigkeit und Reproduzierbarkeit bietet und somit neue Möglichkeiten für die Einzelzellanalytik eröffnet.

In der Krebsforschung ist mittlerweile anerkannt, dass maligne Erkrankungen, einschließlich Leukämien, nicht monoklonale Entitäten sind, sondern aus einem heterogenen Zellgemisch bestehen, innerhalb dessen einige Zellklone Stammzellpotenzial besitzen. Die Charakterisierung dieser zellulären Heterogenität auf molekularer Ebene ist essenziell für die Entwicklung personalisierter Therapiekonzepte, da nur durch ein tiefgehendes Verständnis der klonalen Zusammensetzung eines Tumors gezielt jene Zellen identifiziert und therapiert werden können, die für die Tumorprogression und Therapieresistenz verantwortlich sind.

Die hier präsentierte Methodik leistet einen entscheidenden Beitrag zur hochauflösenden Analyse des Gesamtgenoms auf Einzelzellebene und stellt eine leistungsfähige Plattform zur Untersuchung der genetischen Architektur von Tumoren und Leukämien dar. Durch die Kombination einer optimierten PCR-basierten WGA mit Next-Generation-Sequenzierung (NGS) wird eine hochpräzise Erfassung genomischer Veränderungen in einzelnen Zellen ermöglicht. Diese technologische Weiterentwicklung trägt maßgeblich zur Erforschung der genetischen Diversität innerhalb maligner Erkrankungen bei und könnte zukünftig eine Schlüsselrolle in der individualisierten Onkologie spielen. Zusammengefasst aus (Binder et al, 2014)

3.1.4 VARIANT RS1801157 IN THE 3'UTR OF SDF-1B AND HEALTHY-DONOR G-CSF RESPONSIVENESS

Schulz M*, Karpova D*, Spohn G, Damert A, Seifried E, ***Binder V,**** and Bonig H*.

**** These authors contributed equally to this work***

Variant rs1801157 in the 3'UTR of SDF-1ß and healthy-donor G-CSF responsiveness

Plos One. **2015** Mar 24;10(3):e0121859.

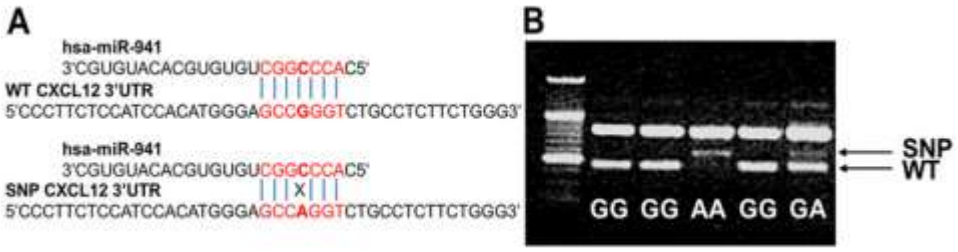

MicroRNAs (miRNAs) sind kurze, etwa 20 Nukleotide lange, nicht-kodierende RNA-Moleküle, die eine zentrale Rolle in der posttranskriptionellen Genregulation spielen. Ihre Funktion beruht auf der spezifischen Bindung der „Seed"-Region an komplementäre Sequenzen in der 3'-untranslatierten Region (3'UTR) ihrer Ziel-mRNAs, wodurch sie die Translation hemmen oder den Abbau der Ziel-mRNA fördern. Auf diese Weise regulieren miRNAs essenzielle zelluläre Prozesse wie Überleben, Apoptose, Proliferation und Differenzierung. Sie sind in hochkomplexen regulatorischen Netzwerken organisiert, die aus fein abgestimmten Mechanismen der Regulation und Gegenregulation bestehen. Diese Netzwerke machen es äußerst anspruchsvoll, die funktionelle Relevanz genetischer Variationen in miRNA-kodierenden Genen oder in deren Zielsequenzen innerhalb der 3'UTRs zu charakterisieren (Schulz et al., 2015).

Ein Beispiel für einen potenziellen miRNA-vermittelten Regulationsmechanismus wurde im Zusammenhang mit der G-CSF-Responsivität untersucht, einer individuellen Variabilität in der Mobilisierung hämatopoetischer Stammzellen nach G-CSF-Gabe. Ein Einzelnukleotid-Polymorphismus (SNP), rs1801157, in der 3'UTR des Chemokins CXCL12 wurde ursprünglich mit einer erhöhten Anfälligkeit für X4-trope HIV-Infektionen in Verbindung gebracht. Spätere Studien mit kleinen Patientenkohorten deuteten darauf hin, dass dieser SNP möglicherweise die Mobilisierungsantwort auf G-CSF beeinflussen könnte. Bioinformatische Analysen legten nahe, dass der SNP die Bindungsaffinität von microRNA-941 (miR-941) an die 3'UTR von

CXCL12 verändern könnte und somit eine regulatorische Rolle bei der Stammzellmobilisierung spielen könnte.

Um diesen Zusammenhang zu überprüfen, wurde eine umfangreiche Kohorte von 515 gesunden Stammzellspendern analysiert. Dabei wurde die Assoziation zwischen dem CXCL12-3'UTR-SNP und der G-CSF-Responsivität untersucht sowie die potenzielle Rolle von miR-941 in diesem Kontext analysiert. Die Allelverteilung des SNPs entsprach den erwarteten Häufigkeiten in der untersuchten Population. Die Mobilisierungseffizienz von $CD34^+$-Zellen zeigte jedoch keine signifikanten Unterschiede zwischen Trägern des Wildtyp-Allels, heterozygoten oder homozygoten SNP-Trägern, auch nicht unter Berücksichtigung geschlechtsspezifischer Unterschiede. Zudem konnte die Expression von miR-941 in nicht-hämatopoetischen Knochenmarkszellen nicht nachgewiesen werden, und funktionelle Analysen ergaben keine Interaktion zwischen miR-941 und der CXCL12-3'UTR.

Diese Ergebnisse widerlegen die Hypothese, dass der SNP rs1801157 über eine veränderte miR-941-Bindung die G-CSF-Responsivität beeinflusst. Während frühere, kleinere Studien auf eine mögliche Assoziation hingedeutet hatten, konnte dieser Effekt in einer größeren und methodisch umfassenderen Kohorte nicht bestätigt werden. Dies unterstreicht die Bedeutung groß angelegter Replikationsstudien, insbesondere bei komplexen regulatorischen Mechanismen, die durch miRNAs vermittelt werden. Zusammengefasst aus (Schulz et al, 2015)

3.1.5 HSA-MIR-125B-2 IS HIGHLY EXPRESSED IN CHILDHOOD ETV6/RUNX1 (TEL/AML1) LEUKEMIAS AND CONFERS SURVIVAL ADVANTAGE TO GROWTH INHIBITORY SIGNALS INDEPENDENT OF P53.

Gefen N,[*] ***Binder V,**** Zakiova M, Morrow M, Novosel A, Hertzberg L, Williams O, Trka J, Borkhardt A, Izraeli S.

**** Both authors contributed equally to this work***

Hsa-mir-125b-2 is highly expressed in childhood ETV6/RUNX1 (TEL/AML1) leukemias and confers survival advantage to growth inhibitory signals independent of p53.

Leukemia. **2010** Jan;24(1):89-96.

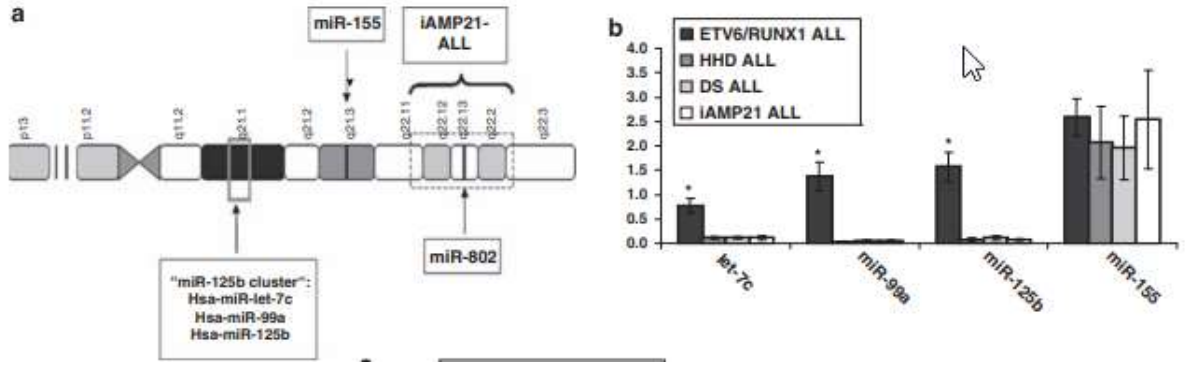

MicroRNAs (miRNAs) sind regulatorische RNA-Moleküle, die die Expression zahlreicher Proteine in einer dosisabhängigen Weise steuern. Aufgrund der Tatsache, dass Trisomie 21 mit einem erhöhten Risiko für die Entwicklung von Leukämien assoziiert ist, wurde die Hypothese aufgestellt, dass eine verstärkte Expression von auf Chromosom 21 kodierten miRNAs zur leukämogenen Wirkung dieser Chromosomenaberration beiträgt. Um diese Annahme zu überprüfen, wurde die Expression von Chromosom-21-miRNAs mittels quantitativer RT-PCR in verschiedenen Subtypen der akuten lymphoblastischen Leukämie (ALL) im Kindesalter analysiert. Dabei wurden sowohl numerische Veränderungen (Trisomie oder Tetrasomie von Chromosom 21) als auch strukturelle Aberrationen, insbesondere die ETV6/RUNX1-Translokation, berücksichtigt.

Überraschenderweise zeigte sich, dass nicht die Trisomie 21, sondern die ETV6/RUNX1-Translokation mit einer verstärkten Expression des hsa-mir-125b-2-Clusters assoziiert war. Dieses Cluster umfasst drei miRNAs und ist für die Regulation zahlreicher zellulärer Prozesse von Bedeutung. Funktionelle Studien zeigten, dass die erhöhte Expression von hsa-mir-125b-2 unabhängig von der Anwesenheit des ETV6/RUNX1-Fusionsproteins stattfand. Dies wurde

sowohl durch experimentelle Modulation der ETV6/RUNX1-Expression als auch durch Chromatin-Immunpräzipitationsanalysen bestätigt.

In funktionellen Zellmodellen vermittelte die Überexpression von hsa-mir-125b-2 einen deutlichen Überlebensvorteil in Ba/F3-Zellen, indem sie die Apoptose nach IL-3-Entzug sowie nach Exposition gegenüber einem breiten Spektrum apoptoseinduzierender Stimuli verhinderte. Mechanistisch geschah dies durch eine Hemmung der Caspase-3-Aktivierung. Umgekehrt führte eine gezielte Herunterregulation von endogenem miR-125b in der ETV6/RUNX1-positiven Leukämiezelllinie REH zu einer erhöhten Apoptoserate nach Behandlung mit Doxorubicin oder Staurosporin. Interessanterweise blieb der p53-Proteinspiegel in diesen Experimenten unverändert, was darauf hindeutet, dass der antiapoptotische Effekt von hsa-mir-125b-2 unabhängig von p53 vermittelt wird.

Diese Ergebnisse zeigen, dass die erhöhte Expression von hsa-mir-125b-2 in ETV6/RUNX1-positiven ALL-Zellen eine zentrale Rolle bei der Resistenz gegenüber wachstumshemmenden Signalen spielt. Die Erkenntnisse liefern zudem Hinweise darauf, dass eine gezielte Inhibition von miR-125b ein potenzieller therapeutischer Ansatz zur Sensibilisierung von Leukämiezellen für apoptotische Signale sein könnte. Dies wird durch unabhängige Studien bestätigt, die die onkogene Funktion von miR-125b ebenfalls nachweisen konnten. Zusammengefasst aus (Gefen et al, 2010; Shaham et al, 2012).

3.1.6 EPOXYEICOSATRIENOIC ACIDS ENHANCE HAEMATOPOIETIC STEM AND PROGENITOR CELL SPECIFICATION AND ENGRAFTMENT

Li P*, Lahvic JL*, ***Binder V****, Pugach E, Riley EB, Tamplin OJ, Panigrahy D, Bowman T, Heffner GC, McKinney-Freeman S, Schlaeger TM, Daley GQ, Zeldin DC, and Zon LI

**** These authors contributed equally to this work***

Epoxyeicosatrienoic Acids Enhance Haematopoietic Stem and Progenitor Cell Specification and Engraftment

Nature. 2015 Jul 23;523(7561):468-71.

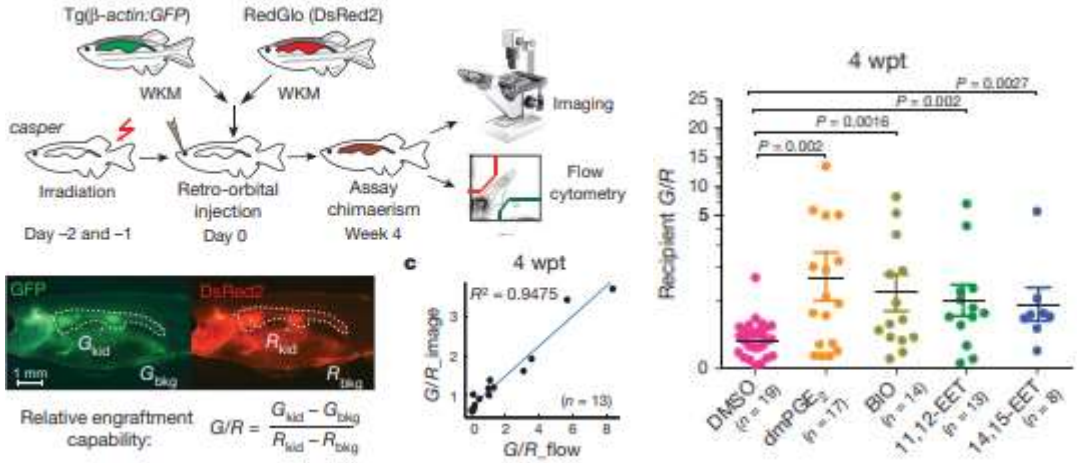

Die hämatopoetische Stamm- und Progenitorzelltransplantation (HSPC-Transplantation) stellt eine etablierte Therapie für zahlreiche lebensbedrohliche hämatologische Erkrankungen, insbesondere für Leukämien, dar. Der Erfolg dieser Therapie hängt maßgeblich von der Effizienz des Engraftments ab, also von der Einwanderung, Ansiedlung und langfristigen Funktionalität der transplantierten HSPCs in der Knochenmarksnische des Empfängers. Trotz der klinischen Bedeutung sind die molekularen und zellulären Mechanismen, die diesen Prozess steuern, bislang nicht vollständig verstanden.

Ein besseres Verständnis dieser Mechanismen könnte dazu beitragen, die Erfolgsrate von HSPC-Transplantationen zu verbessern, insbesondere durch die gezielte pharmakologische Beeinflussung des Engraftment-Prozesses. In dieser Studie wurde daher ein experimentelles System entwickelt, um die Regulationsmechanismen des HSPC-Engraftments systematisch zu untersuchen und potenzielle therapeutische Ansätze zu identifizieren.

Als Modellsystem wurde der Zebrafisch (Danio rerio) genutzt, dessen Hämatopoese evolutionär hoch konserviert ist und sich in vielen Aspekten mit der des Menschen ähnelt. Zudem ermöglicht der Zebrafisch durch seine Transparenz in frühen Entwicklungsstadien eine

hochauflösende *in vivo*-Bildgebung, wodurch das Engraftment von HSPCs nicht-invasiv über längere Zeiträume verfolgt werden kann.

In dieser Studie wurde ein kompetitiver HSPC-Transplantationsassay im adulten Zebrafischmodell etabliert. Dabei wurde die *in-vivo*-Mikroskopie als nicht-invasiver Readout genutzt, um die Dynamik des Engraftments in Echtzeit zu untersuchen. Dieses System wurde für ein chemisches Screening eingesetzt, um Substanzen mit potenziell engraftment-fördernden Eigenschaften zu identifizieren.

Das chemische Screening ergab, dass Epoxyeicosatrienoic Acids (EETs), eine Klasse von bioaktiven Lipiden, das Engraftment hämatopoetischer Stammzellen signifikant verbessern. Dies stellt einen neuartigen molekularen Mechanismus dar, der zuvor nicht mit hämatopoetischen Prozessen in Verbindung gebracht wurde.

Um die funktionelle Relevanz dieser Lipide weiter zu charakterisieren, wurde das Modell des Zebrafischembryos genutzt, in dem sich der hämatopoetische Stammzellpool in einer frühen Entwicklungsphase bildet. Hier zeigte sich, dass insbesondere 11,12-EET die Spezifikation von HSPCs fördert, indem es die Aktivierung eines einzigartigen AP-1- und RUNX1-Transkriptionsprogramms in hämogenen Endothelzellen (den Vorläuferzellen der hämatopoetischen Stammzellen) induziert.

Die beobachteten pro-hämatopoetischen Effekte von EETs werden durch die Aktivierung des Phosphatidylinositol-3-OH-Kinase (PI3K)-Signalwegs, insbesondere von PI(3)Kγ, vermittelt. Dieser Signalweg spielt eine zentrale Rolle in der Regulation hämatopoetischer Entwicklungsprozesse und konnte nun erstmals mit der Steuerung des Engraftments hämatopoetischer Stammzellen in Verbindung gebracht werden.

In adulten HSPCs bewirkte 11,12-EET ebenfalls eine Aktivierung hämatopoetischer Transkriptionsprogramme, insbesondere durch die Aktivierung von AP-1, einem Transkriptionsfaktor, der an der Regulation von zellulären Migrationsprozessen beteiligt ist. Durch diese Mechanismen wird die Migrationsfähigkeit der HSPCs erhöht, was wiederum zu einem verbesserten Engraftment in der Empfängernische führt.

Ein entscheidender Befund dieser Studie ist die evolutionäre Konservierung der EET-vermittelten Effekte. Die gleichen Mechanismen, die in Zebrafischen beobachtet wurden, konnten auch in Säugetiermodellen bestätigt werden. Dies legt nahe, dass EETs eine fundamentale Rolle in der Regulation hämatopoetischer Entwicklungs- und Regenerationsprozesse spielen und nicht nur auf das Zebrafischmodell beschränkt sind.

Diese Studie liefert neue, grundlegende Erkenntnisse zur molekularen Steuerung des HSPC-Engraftments und stellt eine innovative experimentelle Methode zur Untersuchung dieses

Prozesses vor. Durch die Identifikation von EETs als pro-hämatopoetische Lipide wurde ein bislang unbekannter, evolutionär konservierter Signalweg entdeckt, der die hämatopoetische Entwicklung und Regeneration reguliert.

Langfristig könnte die Nutzung von EETs oder verwandten Molekülen dazu beitragen, die Erfolgsraten hämatopoetischer Stammzelltransplantationen zu verbessern und somit die Überlebenschancen von Patienten mit schweren hämatologischen Erkrankungen zu erhöhen. Zusammengefasst aus (Li et al, 2015).

3.1.7. MICROENVIRONMENTAL CONTROL OF HEMATOPOIETIC STEM CELL FATE VIA CXCL8 AND PROTEIN KINASE C

Binder V*, Li W*, Faisal M, Oyman K, Calkins DL, Shaffer J, Teets EM, Sher S, Magnotte A, Belardo A, Deruelle W, Gregory TC, Orwick S, Hagedorn EJ, Perlin JR, Avagyan S, Lichtig A, Barrett F, Ammerman M, Yang S, Zhou Y, Carson WE, Shive HR, Blachly JS, Lapalombella R, Zon LI, Blaser BW.

**** These authors contributed equally to this work***

Microenvironmental control of hematopoietic stem cell fate via CXCL8 and protein kinase C.

Cell Rep. 2023 May 30;42(5):112528

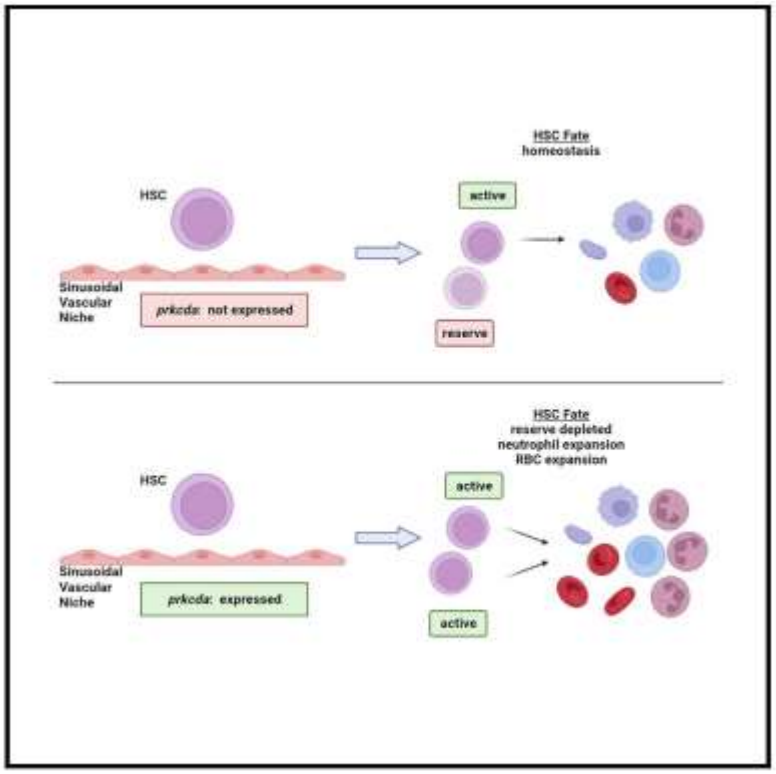

Die Regulation der hämatopoetischen Stammzellen (HSCs) durch ihre Mikroumgebung ist ein zentrales Thema der Stammzellbiologie. Veränderungen in der HSC-Differenzierung und -Selbsterneuerung können zu primären hämatopoetischen Erkrankungen führen. Trotz der bekannten Bedeutung der vaskulären Nische für die HSC-Homöostase sind die molekularen Mechanismen, durch die diese Mikroumgebung das Schicksal der HSCs beeinflusst, noch unzureichend verstanden.

In dieser Studie wurde ein innovativer genetischer Ansatz verwendet, um die Interaktion zwischen HSCs und ihrer sinusoidalen vaskulären Nische systematisch zu untersuchen. Das Ziel war es, Faktoren zu identifizieren, die die phylogenetische Verteilung des HSC-Pools

regulieren, also die klonale Zusammensetzung und Expansion bestimmter HSC-Populationen unter nativen Bedingungen.

Zur Analyse der HSC-Dynamik wurde das genetisch codierte Barcoding-System GESTALT (genome editing of synthetic target arrays for lineage tracing) im Zebrafischmodell genutzt. Diese Technologie erlaubt eine präzise Stammbaumrekonstruktion und Verfolgung individueller HSC-Klone über die Zeit.

Mit dieser Methode wurde untersucht, welche Faktoren in der sinusoidalen vaskulären Nische exprimiert werden und das HSC-Schicksal unter physiologischen Bedingungen beeinflussen. Dabei wurde insbesondere der Einfluss von Protein Kinase C delta auf die Klonalität und Differenzierung von HSCs analysiert.

Die dysregulierte Expression von PKC-δ führte zu einer signifikanten Erhöhung der Anzahl von HSC-Klonen um bis zu 80%. Dies resultierte in einer Expansion polymorpher Populationen unreifer Neutrophilen- und erythroider Vorläuferzellen.

Darüber hinaus konnte gezeigt werden, dass PKC-Agonisten wie CXCL8 die Wettbewerbsdynamik um die Nischenbesetzung verstärken und somit die Komposition der HSC-Populationen verändern. Dies deutet darauf hin, dass die sinusoidale Nische eine bislang unerkannte Reservekapazität aufweist, die durch PKC-δ und CXCL8 reguliert wird.

Die Analyse menschlicher Endothelzellen ergab, dass CXCL8 die Assoziation von PKC-δ mit dem fokalen Adhäsionskomplex induziert. Dies führt zur Aktivierung des extrazellulär-signalregulierten Kinase (ERK)-Signalwegs, was wiederum die Expression spezifischer Nischenfaktoren fördert.

Auf zellulärer Ebene wurde mittels Einzelzell-Tracking nachgewiesen, dass eine verstärkte CXCL8/CXCR1-Signalübertragung zu einer verlängerten Interaktion (cuddling) zwischen HSCs und Endothelzellen, einer längeren Verweildauer in der Nische sowie einer erhöhten Proliferationsrate der HSCs führt. Zusätzlich war die Aktivierung der CXCL8/CXCR1-Achse mit einer Volumenzunahme der hämatopoetischen Nische (caudal hematopoietic tissue, CHT) und einer gesteigerten Expression von CXCL12a assoziiert – einem bekannten Regulator der HSC-Homöostase.

Ein entscheidender Befund dieser Studie ist, dass CXCR1 nicht HSC-autonom wirkt, sondern über eine gezielte Modulation der hämatopoetischen Nische die Effizienz des HSC-Engraftments steuert.

Diese Studie liefert fundamentale neue Erkenntnisse zur Regulation der HSC-Nische und zeigt, dass CXCL8 und PKC-δ zentrale Regulatoren der klonalen Expansion und Differenzierung von HSCs sind. Diese Erkenntnisse haben potenzielle klinische Implikationen, insbesondere für die

Verbesserung von Stammzelltransplantationen. Die gezielte pharmakologische Aktivierung der CXCL8/CXCR1-Signalachse könnte eine vielversprechende Strategie sein, um das Engraftment von HSCs in der Empfängernische zu optimieren und somit die Erfolgsrate von Knochenmark- oder Nabelschnurbluttransplantationen zu erhöhen. Zusammengefasst aus (Binder et al, 2023).

3.1.8 IN VIVO MONITORING OF LEUKEMIA-NICHE INTERACTIONS IN A ZEBRAFISH XENOGRAFT MODEL.

Arner A, Ettinger A, Bradley, Blaser BW, Schmid B, Jeremias I, Rostam N, ***Binder-Blaser V.***

In vivo monitoring of leukemia-niche interactions in a zebrafish xenograft model.

Plos One 19(8): e0309415 (2024)

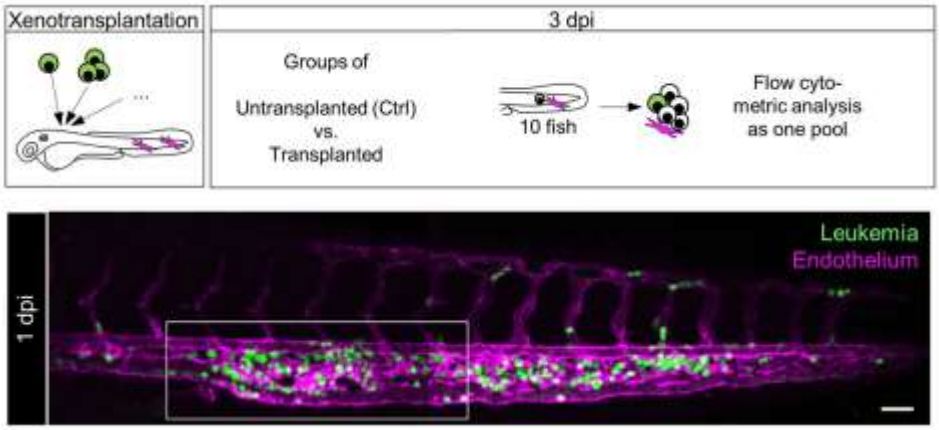

Die akute lymphatische Leukämie (ALL) ist die häufigste maligne Erkrankung im Kindesalter. Während moderne Therapieansätze die Prognose für die meisten Patienten nach der Erstdiagnose erheblich verbessert haben, bleibt die Behandlung von Rezidiven eine große Herausforderung. Die Überlebensrate nach einem Rückfall ist deutlich reduziert, was auf komplexe Mechanismen der Krankheitspersistenz und -progression hinweist. Ein zunehmend anerkanntes Konzept in diesem Zusammenhang ist die Rolle der Tumormikroumgebung, insbesondere der hämatopoetischen Nische, bei der Entstehung, Erhaltung und Wiederkehr der Leukämie. Allerdings sind die zellulären und molekularen Interaktionen innerhalb dieser Nische schwer zu untersuchen, da klassische experimentelle Modelle die komplexen Wechselwirkungen zwischen Leukämiezellen und ihrer Umgebung nur unzureichend abbilden können.

Um diese Limitationen zu überwinden, wurde in der vorliegenden Studie ein innovatives Zebrafisch-Xenotransplantationsmodell entwickelt. Dieses ermöglicht die detaillierte Analyse leukämischer Patientenzellen innerhalb einer orthotopen hämatopoetischen Nische in vivo. Durch den Einsatz konfokaler Mikroskopie und Durchflusszytometrie konnten die Bewegungsmuster, das Engraftment und die Proliferation der transplantierten Leukämiezellen in Echtzeit untersucht werden. Dabei zeigte sich, dass die Zellen gezielt in das caudal hematopoietic tissue (CHT) des Zebrafisches migrierten – eine Nische, die funktionell der fetalen Leber bei Säugetieren entspricht. Nach dem Engraftment proliferierten die

Leukämiezellen und verteilten sich innerhalb des CHT in einem charakteristischen Muster. Im Verlauf der Zeit extravasierte ein Teil der Zellen aus den Blutgefäßen und bildete Zellcluster entlang der dorsalen Aorta, einer Region, die für die hämatopoetische Stammzellbildung eine zentrale Rolle spielt.

Neben der Untersuchung der Leukämiezellen selbst ermöglichte das Modell auch eine detaillierte Charakterisierung ihrer Interaktionen mit Zellen der Mikroumgebung. Dabei konnte gezeigt werden, dass Leukämiezellen in engem Kontakt mit Makrophagen und Endothelzellen stehen. Diese Interaktionen könnten eine entscheidende Rolle für die Etablierung und Persistenz der Leukämie spielen, indem sie beispielsweise Mechanismen der Immunmodulation oder der Unterstützung der Leukämiezellen innerhalb der Nische aktivieren. Die quantitativen Analysen dieser Zell-zu-Zell-Interaktionen bieten eine wertvolle Grundlage, um die komplexen Signalwege und Wechselwirkungen zu entschlüsseln, die zur Leukämieerhaltung und -progression beitragen.

Insgesamt stellt das hier entwickelte Zebrafisch-Xenotransplantationsmodell eine leistungsfähige experimentelle Plattform dar, um Mechanismen der nischenvermittelten Leukämogenese besser zu verstehen. Da das Modell eine hochauflösende Visualisierung von Leukämiezellen innerhalb einer funktionellen und komplexen Mikroumgebung ermöglicht, bietet es weitreichende Anwendungsmöglichkeiten für zukünftige Forschungsarbeiten. Insbesondere könnte es genutzt werden, um neue therapeutische Strategien zu identifizieren, die gezielt auf die Wechselwirkungen zwischen Leukämiezellen und ihrer Nische abzielen. Durch das gezielte Screening von Wirkstoffen, die das Engraftment oder die Persistenz leukämischer Zellen beeinflussen, könnten neue Ansätze zur Verhinderung von Rezidiven entwickelt werden. Die Erkenntnisse dieser Studie liefern somit wichtige Impulse für die Weiterentwicklung der Leukämietherapie und könnten langfristig dazu beitragen, die Prognose für ALL-Patienten mit Rezidiven zu verbessern. Zusammengefasst aus (Arner et al, 2024).

3.2 ÜBERBLICK ZU KOOPERATIVEN FORSCHUNGSBEITRÄGEN IM RAHMEN DES HABILITATIONSTHEMAS

Im Zentrum meines wissenschaftlichen Interesses steht die Entwicklung personalisierter molekularer Ansätze, um die Pathogenese hämatopoetischer Erkrankungen besser zu verstehen und therapeutische Möglichkeiten zu verbessern. Im Rahmen zahlreicher Kooperationsarbeiten wurden mit modernsten molekularen Methoden die genetischen Ursachen und Mechanismen verschiedener Erkrankungen des hämatopoetischen Systems untersucht. Das Spektrum der Analysen umfasst folgende Bereiche:

3.2.1 PRIMÄRE IMMUNDEFEKTE UND „BONE MARROW FAILURE"-SYNDROME

- DIAGNOSTIK ANGEBORENER IMMUNDEFEKTE:
  Mithilfe eines eigens entwickelten 385K-Microarrays, der die Exone von 395 Genen erfasst – welche mit primären Immundefekten und der Immunregulation assoziiert sind – konnte durch „Array-based Sequence Capture" in Kombination mit Next-Generation-Sequenzierung (NGS) bei klinisch verdächtigen Patienten die Diagnostik und Frühdetektion angeborener Immundefekte ressourcen- und zeiteffizient vertieft werden (Ghosh et al, 2012a; Ghosh et al, 2012b).
- SCHWERE APLASTISCHE ANÄMIE (SAA):
  Die SAA ist durch ein hypoplastisches Knochenmark gekennzeichnet, in dem autoreaktive T-Zellen den Abbau von $CD34^+$ Zellen forcieren. Durch den Einsatz einer ungerichteten RNA-Amplifikation konnte eine patientenspezifische Genexpressionsanalyse von $CD34^+$ Zellen bei frisch diagnostizierten Patienten mit SAA (n = 13), refraktärer Anämie (n = 8) und gesunden Kontrollen (n = 10) durchgeführt werden. Hierbei wurden interferonstimulierte Gene, wie das apoptosis-induzierende TRAIL, als prognostisch relevante Marker identifiziert und signifikante Herunterregulationen von Integrinmolekülen sowie das Vorhandensein autoreaktiver anti-Integrin-Antikörper nachgewiesen (Fischer et al, 2012; Schuster et al, 2011).

3.2.2 MALIGNE ERKRANKUNGEN DES HÄMATOPOETISCHEN SYSTEMS (LEUKÄMIEN)

- LEUKÄMIE BEI TRISOMIE 21:
  Bei Kindern mit Trisomie 21 wurde in einer Subgruppe spezifisch eine Mutation in der JAK2-Pseudokinase-Domäne (insbesondere R683) identifiziert, die eine Aktivierung des JAK/STAT-Signalwegs bewirkt und zur Zellimmortalisation beiträgt. Diese Genotyp-Phänotyp-Korrelation, die ausschließlich bei Patienten mit Trisomie 21 auftritt, eröffnet potenzielle therapeutische Ansatzpunkte durch den Einsatz von JAK2-Inhibitoren (Bercovich et al, 2008).
- PÄDIATRISCHE AML – MLL- VS. HLXB9-TRANSLOKATIONEN:
  In der pädiatrischen akuten myeloischen Leukämie (AML) wurden unterschiedliche molekulare Signaturen identifiziert. Im Vergleich zu AMLs mit MLL-Translokationen,

zeigen HLXB9/TEL-positive Leukämien eine signifikante Hochregulation von Genen, die für Zell-Zell-Interaktionen und Zelladhäsion (z. B. EDIL3, CNTNAP5, ANGPT1, DSG2, ITGA9, ITGAV, KDR, SIGLEC6) relevant sind. Diese Daten deuten darauf hin, dass HLXB9 die Interaktion mit der hämatopoetischen Nische verändert und möglicherweise einen Schutzmechanismus gegen Chemotherapie darstellt (Wildenhain et al, 2010).

- KOMPLEXE TRANSLOKATIONEN IN AML:
  Etwa 15 % der pädiatrischen AML-Fälle weisen komplexe Translokationen auf, bei denen das MLL-Gen (11q23) mit MLLT10 (10p) fusioniert. Mithilfe von paired-end DNA-NGS konnten neben der klassischen t(10;11)-Translokation auch zusätzliche strukturelle Varianten, wie die reziproke Fusion des „ring-type zinc finger" Gens RNF214 an das 3'-Ende von MLL, aufgedeckt werden. Dieser Befund deutet auf eine mögliche Beteiligung des Ubiquitinierungssystems an der Leukämieentstehung hin (Ghosh et al, 2013).
- CHROMOSOMALE ABERRATIONEN IN ALL UND RÜCKFALLBIOLOGIE:
  Bei pädiatrischen ALLs ist „near haploidy" (23–29 Chromosomen) mit einer sehr schlechten Prognose verbunden, wohingegen high-hyperdiploide ALLs (51–67 Chromosomen) ein günstigeres Outcome aufweisen. Mittels NGS konnten durch die Analyse uniparentaler Disomien differenzierende Muster identifiziert werden. In der Zelllinie MHH-CALL-2 wurden zahlreiche Mutationen und strukturelle Veränderungen nachgewiesen, die typische onkogene Prozesse – wie den Verlust der Zellzykluskontrolle, gesteigerte Proliferation, defekte DNA-Reparatur, verminderten Zelltod und gestörte epigenetische Regulation – induzieren (Chen et al, 2013). Zudem zeigte die molekulare Analyse von Rückfällen bei high-hyperdiploiden ALLs, dass spezifische Mutationen im RAS-Signalweg sowie in epigenetischen Regulatoren und DNA-Reparaturgenen ausschließlich in der Rückfallgruppe auftreten, was die Heterogenität der Rückfallbiologie unterstreicht (Chen et al, 2015a).

3.2.3 IMMUNOLOGISCHE WECHSELWIRKUNGEN, NISCHENINTERAKTIONEN UND TRANSLATIONALE ANSÄTZE (PRECISION ONCOLOGY)

- INTERAKTION VON LEUKÄMIEZELLEN MIT DER IMMUNOLOGISCHEN NISCHE:
  Es hat sich gezeigt, dass leukämische Zellen über die CD200/TIM-3-Achse die Funktion von T-Zellen im Knochenmark modulieren können. Erhöhte Anteile von TIM-3^{+}CD4^{+} bmT-Zellen in ALL-Fällen mit CD200-Überexpression führen zu einer dysfunktionalen antileukämischen T-Zellantwort, was als signifikanter Risikofaktor für Rückfälle identifiziert wurde (Blaeschke et al, 2020).
- OPTIMIERUNG IMMUNTHERAPEUTISCHER ANSÄTZE:
  Darüber hinaus gewinnt die Rolle des Immunsystems in der Tumorprädisposition und im „Immune Escape" von malignen Erkrankungen, insbesondere Leukämien und Lymphomen, zunehmend an Bedeutung. In diesem Kontext wurden durch Arbeiten

von Willier et al. (Willier et al, 2020) wichtige Erkenntnisse zur immunologischen Tumorprädisposition gewonnen. Ergänzend dazu wurde ein entscheidender Beitrag zur Optimierung der CAR-T-Zelltherapie geleistet, was neue Perspektiven für die zielgerichtete immuntherapeutische Behandlung eröffnet (Willier et al, 2021).

- HSPC-KOLONISATION IM ZEBRAFISCHMODELL:
  Fortschritte in der Fluoreszenzmarkierung von hämatopoetischen Stamm- und Vorläuferzellen (HSPCs) im caudal hämatopoetischen Gewebe (CHT) des Zebrafisches haben gezeigt, dass das Chemokin cxcl8 und sein Rezeptor cxcr1 von zebrafischen Endothelzellen exprimiert werden. Die cxcl8/cxcr1-Signalkaskade fungiert als positiver Regulator der HSPC-Kolonisation, was sich in vermehrten HSPC-Endothelzell-Interaktionen („cuddling“), einer verlängerten Verweildauer der HSPCs im CHT und einer erhöhten Mitosefrequenz äußert. Zudem korreliert diese Signalisierung mit einer Volumenzunahme des CHT und der Induktion von cxcl12a. Parabiotische Zebrafische zeigten, dass cxcr1 HSPCs nicht-zellautonom wirkt und die Transplantationseffizienz von Spender-HSPCs verbessert – ein Mechanismus, der die Umgestaltung des hämatopoetischen Nischenmilieus zur Förderung des HSPC-Engraftments beschreibt und cxcl8/cxcr1 als potenzielles therapeutisches Ziel positioniert (Blaser et al, 2017).
- TRANSLATIONALE ANSÄTZE IN DER PRECISION ONCOLOGY:
  Die detaillierte molekulare Charakterisierung hämatopoetischer Erkrankungen hat die Entwicklung und Adaption neuer Therapieansätze im Rahmen der Precision Oncology ermöglicht. Reverse genetische Ansätze in Maus- und Zebrafischmodellen haben potenziell therapierbare Tumorvulnerabilitäten identifiziert, die den Weg für individualisierte, zielgerichtete Therapien ebnen (Bercovich et al, 2008; Carlet et al, 2021; Raedler et al, 2020).

3.3 ZUSAMMENFASSUNG EIGENER UND KOOPERATIVER FORSCHUNGSARBEITEN UND DEREN BEDEUTUNG FÜR DAS FACHGEBIET

Im Rahmen des Habilitationsprojekts wurden verschiedene Ansätze verfolgt, die das Verständnis hämatopoetischer Erkrankungen vertiefen und den Weg zu individualisierten Therapieoptionen ebnen. So wurde zunächst der Genotyp des ursprünglichen Wiskott–Aldrich-Syndroms untersucht, um die Genotyp-Phänotyp-Korrelation bei dieser seltenen, X-chromosomal vererbten Erkrankung besser zu verstehen. Parallel dazu analysierten wir eine neu entdeckte großskalige mtDNA-Mutation, die klinisch ausschließlich mit refraktärer Anämie auftritt, um Potenziale zur Vorhersage des Krankheitsverlaufs zu evaluieren.

Ein weiterer Schwerpunkt lag auf der Entwicklung eines neuartigen Workflows für die Whole Genome Sequenzierung einzelner menschlicher Zellen, wodurch die detaillierte Untersuchung genetischer Heterogenität und der zugrunde liegenden Krankheitsmechanismen ermöglicht wird. Ergänzend wurde der Einfluss genetischer Varianten, insbesondere der rs1801157-

Variante im 3’-UTR von SDF-1β, auf die Mobilisierung hämatopoetischer Stammzellen bei gesunden Spendern untersucht.

Im Bereich der kindlichen Leukämien wurde gezeigt, dass die hohe Expression von hsa-mir-125b-2 in ETV6/RUNX1-Leukämien einen Überlebensvorteil gegenüber wachstumshemmenden Signalen vermittelt, unabhängig vom p53-Status, und somit onkogene Mechanismen begünstigt. Darüber hinaus identifizierten wir, dass Epoxyeicosatrienoic Acids die Spezifikation und das Engraftment von Stamm- und Vorläuferzellen verbessern können, was potenziell therapeutisch nutzbar ist.

Neben den zellintrinsischen Faktoren wurde auch die mikroenvironmentale Kontrolle des Schicksals hämatopoetischer Stammzellen untersucht. Dabei spielten CXCL8 und Protein Kinase C eine zentrale Rolle bei der Regulierung von Nischeninteraktionen. Abschließend wurde ein präklinisches Zebrafisch-Xenograftmodell entwickelt, das die In-vivo-Überwachung der Interaktion zwischen Leukämiezellen und ihrer Nische ermöglicht und so neue Einblicke in die Mechanismen der Leukämieprogression sowie in potenzielle therapeutische Zielstrukturen liefert.

Die vorgelegten Ergebnisse demonstrieren, dass funktionell-genomische Methoden eine systematische Entdeckung von Krankheitsursachen ermöglichen und translational die Entwicklung personalisierter Therapieansätze vorantreiben. Die gewonnenen Erkenntnisse tragen wesentlich zur Verbesserung der Diagnostik und Therapie hämatopoetischer Erkrankungen bei und liefern wichtige Impulse für zukünftige innovative Behandlungsstrategien. Diese Arbeiten bilden somit die Basis für zukünftige Ansätze in der Precision Oncology, bei denen sowohl intrinsische als auch extrinsische, nischenvermittelte Parameter in die Risikostratifizierung und Therapieentscheidung einfließen.

4. AKTUELLE WISSENSCHAFTLICHE ARBEITEN UND AUSBLICK

In den letzten Jahren hat sich gezeigt, dass nicht nur zellintrinsische Prozesse der hämatopoetischen Stamm- oder Leukämiezellen, sondern vor allem auch ihre Interaktionen mit den umgebenden Nischenzellen – etwa Endothelzellen und Makrophagen – eine zentrale Rolle in der Tumorbiologie und der Therapieantwort spielen. Derzeit basieren Risikoabschätzungen überwiegend auf leukämiezell-intrinsischen Merkmalen. Zunehmende Daten deuten jedoch darauf hin, dass rückfallinduzierende Leukämiezellen ihre Nische effizienter nutzen, um sich vor den Wirkungen der Chemotherapie zu schützen. Für eine Verbesserung der Risikobewertung ist es daher essenziell, das Verhalten der Leukämiezellen in ihrer Mikroumgebung sowie deren Interaktionsmuster mit benachbarten Zellen systematisch zu untersuchen und diese extrinsischen Merkmale in die Risikostratifizierung einzubeziehen.

Relevante Nischenzellen in diesem Kontext sind vor allem Endothelzellen und Makrophagen. Frühere Arbeiten zeigten, dass das Knochenmark von ALL-Patienten eine erhöhte Gefäßdichte aufweist, verglichen mit gesunden Probanden (Perez-Atayde et al, 1997). Zudem korreliert bei unbehandelten Patienten mit akuter myeloischer Leukämie ein erhöhter VEGF-Plasmaspiegel mit einer verringerten Überlebenswahrscheinlichkeit und niedrigeren Remissionsraten (Aguayo et al, 2002). Leukämiezellen können an Endothelzellen haften, in einen ruhenden Zustand übergehen und so den Wirkmechanismen von Chemotherapeutika entgehen – ein Prozess, der nach Therapiebeendigung zur erneuten Proliferation und damit zur Rezidiventstehung beiträgt (Pezeshkian et al, 2013). Parallel dazu fördern tumorassoziierte Makrophagen, die in M2-ähnlicher Form vorliegen, häufig Immunsuppression, Gefäßneubildung, Invasivität und Metastasierung, was mit einem schlechten Ansprechen auf Chemotherapie einhergeht (Komohara et al, 2013; Qian & Pollard, 2010). In einem Mausmodell der T-ALL wurde darüber hinaus gezeigt, dass Makrophagen die Proliferation der Leukämiezellen stimulieren (Chen et al, 2015b).

Ziel unserer aktuellen Arbeiten ist es, die komplexen Interaktionsprozesse zwischen Leukämiezellen und Nischenzellen zu identifizieren und ein objektives Bewertungssystem zu entwickeln, das künftig extrinsische Parameter in die Risikostratifizierung einbezieht. Hierzu wurden kryokonservierte primäre Leukämiezellen vom Zeitpunkt der Erstdiagnose in Zebrafischlarven transplantiert und mittels konfokaler Mikroskopie in Einzelzellauflösung analysiert (Arner et al, 2024).

Im Ausblick erwarten wir, dass Leukämiezellen von Patienten, die ein frühes Rezidiv entwickeln, ihre mikroenvironmentale Nische effizienter nutzen, um sich vor chemotherapeutischen Effekten zu schützen, als Zellen von Patienten ohne Rezidiv. Durch den Einsatz softwarebasierter, standardisierter und automatisierter Analysen sollen diese Beobachtungen in ein numerisches Bewertungssystem (Score) überführt werden. Im nächsten

Schritt werden wir die Genexpressionsprofile von Nischen- und Leukämiezellen nach deren Kontakt mittels Hochdurchsatzsequenzierung analysieren, um die molekularen Signalwege zu identifizieren, die den protektiven Nischeninteraktionen zugrunde liegen. Diese Signalwege sollen zusammen mit dem entwickelten Score als integrale Bestandteile der initialen Risikostratifizierung etabliert werden, um erstmals nischenvermittelte Effekte und deren Einfluss auf das Rezidivrisiko systematisch zu berücksichtigen. Darüber hinaus bieten sie attraktive therapeutische Zielstrukturen, die zukünftig in personalisierten Behandlungsansätzen Anwendung finden könnten.

5. REFERENZEN

Aguayo, A., Kantarjian, H. M., Estey, E. H., Giles, F. J., Verstovsek, S., Manshouri, T., Gidel, C., O'Brien, S., Keating, M. J. & Albitar, M. (2002) Plasma vascular endothelial growth factor levels have prognostic significance in patients with acute myeloid leukemia but not in patients with myelodysplastic syndromes. *Cancer*, 95(9), 1923-30.

Arner, A., Ettinger, A., Blaser, B. W., Schmid, B., Jeremias, I., Rostam, N. & Binder-Blaser, V. (2024) In vivo monitoring of leukemia-niche interactions in a zebrafish xenograft model. *PLoS One*, 19(8), e0309415.

Bercovich, D., Ganmore, I., Scott, L. M., Wainreb, G., Birger, Y., Elimelech, A., Shochat, C., Cazzaniga, G., Biondi, A., Basso, G., Cario, G., Schrappe, M., Stanulla, M., Strehl, S., Haas, O. A., Mann, G., Binder, V., Borkhardt, A., Kempski, H., Trka, J., Bielorei, B., Avigad, S., Stark, B., Smith, O., Dastugue, N., Bourquin, J. P., Tal, N. B., Green, A. R. & Izraeli, S. (2008) Mutations of JAK2 in acute lymphoblastic leukaemias associated with Down's syndrome. *Lancet*, 372(9648), 1484-92.

Binder, V., Albert, M. H., Kabus, M., Bertone, M., Meindl, A. & Belohradsky, B. H. (2006) The genotype of the original Wiskott phenotype. *N Engl J Med*, 355(17), 1790-3.

Binder, V., Bartenhagen, C., Okpanyi, V., Gombert, M., Moehlendick, B., Behrens, B., Klein, H. U., Rieder, H., Ida Krell, P. F., Dugas, M., Stoecklein, N. H. & Borkhardt, A. (2014) A new workflow for whole-genome sequencing of single human cells. *Hum Mutat*, 35(10), 1260-70.

Binder, V., Li, W., Faisal, M., Oyman, K., Calkins, D. L., Shaffer, J., Teets, E. M., Sher, S., Magnotte, A., Belardo, A., Deruelle, W., Gregory, T. C., Orwick, S., Hagedorn, E. J., Perlin, J. R., Avagyan, S., Lichtig, A., Barrett, F., Ammerman, M., Yang, S., Zhou, Y., Carson, W. E., Shive, H. R., Blachly, J. S., Lapalombella, R., Zon, L. I. & Blaser, B. W. (2023) Microenvironmental control of hematopoietic stem cell fate via CXCL8 and protein kinase C. *Cell Rep*, 42(5), 112528.

Binder, V., Steenpass, L., Laws, H. J., Ruebo, J. & Borkhardt, A. (2012) A novel mtDNA large-scale mutation clinically exclusively presenting with refractory anemia: is there a chance to predict disease progression? *J Pediatr Hematol Oncol*, 34(4), 283-92.

Binder, V. & Zon, L. I. (2012) High throughput in vivo phenotyping: The zebrafish as tool for drug discovery for hematopoietic stem cells and cancer *Drug Discovery Today: Disease Models*.

Blaeschke, F., Willier, S., Stenger, D., Lepenies, M., Horstmann, M. A., Escherich, G., Zimmermann, M., Rojas Ringeling, F., Canzar, S., Kaeuferle, T., Rohlfs, M., Binder, V., Klein, C. & Feuchtinger, T. (2020) Leukemia-induced dysfunctional TIM-3(+)CD4(+) bone marrow T cells increase risk of relapse in pediatric B-precursor ALL patients. *Leukemia*, 34(10), 2607-2620.

Blaser, B. W., Moore, J. L., Hagedorn, E. J., Li, B., Riquelme, R., Lichtig, A., Yang, S., Zhou, Y., Tamplin, O. J., Binder, V. & Zon, L. I. (2017) CXCR1 remodels the vascular niche to promote hematopoietic stem and progenitor cell engraftment. *J Exp Med*, 214(4), 1011-1027.

Campbell, M., Kiss, C., Zimmermann, M., Riccheri, C., Kowalczyk, J., Felice, M. S., Kuzmanovic, M., Kovacs, G., Kosmidis, H., Gonzalez, A., Bilic, E., Castillo, L., Kolenova, A., Jazbec, J., Popa, A., Konstantinov, D., Kappelmayer, J., Szczepanski, T., Dworzak, M., Buldini, B., Gaipa, G., Marinov, N., Rossi, J., Nagy, A., Gaspar, I., Stary, J. & Schrappe, M. (2023) Childhood Acute Lymphoblastic Leukemia: Results of the Randomized Acute Lymphoblastic Leukemia Intercontinental-Berlin-Frankfurt-Munster 2009 Trial. *J Clin Oncol*, 41(19), 3499-3511.

Carlet, M., Volse, K., Vergalli, J., Becker, M., Herold, T., Arner, A., Senft, D., Jurinovic, V., Liu, W. H., Gao, Y., Dill, V., Fehse, B., Baldus, C. D., Bastian, L., Lenk, L., Schewe, D. M., Bagnoli, J. W., Vick, B., Schmid, J. P., Wilhelm, A., Marschalek, R., Jost, P. J., Miething, C., Riecken, K., Schmidt-Supprian, M., Binder, V. & Jeremias, I. (2021) In vivo inducible reverse genetics in patients' tumors to identify individual therapeutic targets. *Nat Commun*, 12(1), 5655.

Chen, C., Bartenhagen, C., Gombert, M., Okpanyi, V., Binder, V., Rottgers, S., Bradtke, J., Teigler-Schlegel, A., Harbott, J., Ginzel, S., Thiele, R., Fischer, U., Dugas, M., Hu, J. & Borkhardt, A. (2013) Next-generation-sequencing-based risk stratification and identification of new genes involved in structural and sequence variations in near haploid lymphoblastic leukemia. *Genes Chromosomes Cancer*, 52(6), 564-79.

Chen, C., Bartenhagen, C., Gombert, M., Okpanyi, V., Binder, V., Rottgers, S., Bradtke, J., Teigler-Schlegel, A., Harbott, J., Ginzel, S., Thiele, R., Husemann, P., Krell, P. F., Borkhardt, A., Dugas, M., Hu, J. & Fischer, U. (2015a) Next-generation-sequencing of recurrent childhood high hyperdiploid acute lymphoblastic leukemia reveals mutations typically associated with high risk patients. *Leuk Res*, 39(9), 990-1001.

Chen, S. Y., Yang, X., Feng, W. L., Liao, J. F., Wang, L. N., Feng, L., Lin, Y. M., Ren, Q. & Zheng, G. G. (2015b) Organ-specific microenvironment modifies diverse functional and phenotypic characteristics of leukemia-associated macrophages in mouse T cell acute lymphoblastic leukemia. *J Immunol*, 194(6), 2919-29.

de Jong, J. L. & Zon, L. I. (2005) Use of the zebrafish system to study primitive and definitive hematopoiesis. *Annu Rev Genet*, 39, 481-501.

Eckert, C., Parker, C., Moorman, A. V., Irving, J. A., Kirschner-Schwabe, R., Groeneveld-Krentz, S., Revesz, T., Hoogerbrugge, P., Hancock, J., Sutton, R., Henze, G., Chen-Santel, C., Attarbaschi, A., Bourquin, J. P., Sramkova, L., Zimmermann, M., Krishnan, S., von Stackelberg, A. & Saha, V. (2021) Risk factors and outcomes in children with high-risk B-cell precursor and T-cell relapsed acute lymphoblastic leukaemia: combined analysis of ALLR3 and ALL-REZ BFM 2002 clinical trials. *Eur J Cancer*, 151, 175-189.

Fischer, U., Ruckert, C., Hubner, B., Eckermann, O., Binder, V., Bakchoul, T., Schuster, F. R., Merk, S., Klein, H. U., Fuhrer, M., Dugas, M. & Borkhardt, A. (2012) CD34+ gene expression profiling of individual children with very severe aplastic anemia indicates a pathogenic role of integrin receptors and the proapoptotic death ligand TRAIL. *Haematologica*, 97(9), 1304-11.

Gefen, N., Binder, V., Zaliova, M., Linka, Y., Morrow, M., Novosel, A., Edry, L., Hertzberg, L., Shomron, N., Williams, O., Trka, J., Borkhardt, A. & Izraeli, S. (2010) Hsa-mir-125b-2 is highly expressed in childhood ETV6/RUNX1 (TEL/AML1) leukemias and confers survival advantage to growth inhibitory signals independent of p53. *Leukemia*, 24(1), 89-96.

Ghosh, S., Bartenhagen, C., Okpanyi, V., Gombert, M., Binder, V., Teigler-Schlegel, A., Bradtke, J., Rottgers, S., Dugas, M. & Borkhardt, A. (2013) Recurrent involvement of ring-type zinc finger genes in complex molecular rearrangements in childhood acute myelogeneous leukemia with translocation t(10;11)(p12;q23). *Leukemia*, 27(8), 1745-8.

Ghosh, S., Krux, F., Binder, V., Gombert, M., Niehues, T., Feyen, O., Laws, H. J., Borkhardt, A. & Diseases, P.-N. G. N. o. P. I. (2012a) Array-based sequence capture and next-generation sequencing for the identification of primary immunodeficiencies. *Scand J Immunol*, 75(3), 350-4.

Ghosh, S., Schuster, F. R., Binder, V., Niehues, T., Baldus, S. E., Seiffert, P., Laws, H. J., Borkhardt, A. & Meisel, R. (2012b) Fatal outcome despite full lympho-hematopoietic reconstitution after allogeneic stem cell transplantation in atypical ataxia telangiectasia. *J Clin Immunol*, 32(3), 438-40.

Howe, K., Clark, M. D., Torroja, C. F., Torrance, J., Berthelot, C., Muffato, M., Collins, J. E., Humphray, S., McLaren, K., Matthews, L., McLaren, S., Sealy, I., Caccamo, M., Churcher, C., Scott, C., Barrett, J. C., Koch, R., Rauch, G. J., White, S., Chow, W., Kilian, B., Quintais, L. T., Guerra-Assuncao, J. A., Zhou, Y., Gu, Y., Yen, J., Vogel, J. H., Eyre, T., Redmond, S., Banerjee, R., Chi, J., Fu, B., Langley, E., Maguire, S. F., Laird, G. K., Lloyd, D., Kenyon, E., Donaldson, S., Sehra, H., Almeida-King, J., Loveland, J., Trevanion, S., Jones, M., Quail, M., Willey, D., Hunt, A., Burton, J., Sims, S., McLay, K., Plumb, B., Davis, J., Clee, C., Oliver, K., Clark, R., Riddle, C., Elliot, D., Threadgold, G., Harden, G., Ware, D., Begum, S., Mortimore, B., Kerry, G., Heath, P., Phillimore, B., Tracey, A., Corby, N., Dunn, M., Johnson, C., Wood, J., Clark, S., Pelan, S., Griffiths, G., Smith, M., Glithero, R., Howden, P., Barker, N., Lloyd, C., Stevens, C., Harley, J., Holt, K., Panagiotidis, G., Lovell, J., Beasley, H., Henderson, C., Gordon, D., Auger, K., Wright, D., Collins, J., Raisen, C., Dyer, L., Leung, K., Robertson, L., Ambridge, K., Leongamornlert, D., McGuire, S., Gilderthorp, R., Griffiths, C., Manthravadi, D., Nichol, S., Barker, G., et al (2013) The zebrafish reference genome sequence and its relationship to the human genome. *Nature*, 496(7446), 498-503.

Inaba, H. & Mullighan, C. G. (2020) Pediatric acute lymphoblastic leukemia. *Haematologica*, 105(11), 2524-2539.

Jing, L. & Zon, L. I. (2011) Zebrafish as a model for normal and malignant hematopoiesis. *Dis Model Mech*, 4(4), 433-8.

Komohara, Y., Niino, D., Saito, Y., Ohnishi, K., Horlad, H., Ohshima, K. & Takeya, M. (2013) Clinical significance of CD163(+) tumor-associated macrophages in patients with adult T-cell leukemia/lymphoma. *Cancer Sci*, 104(7), 945-51.

Lam, S. H., Chua, H. L., Gong, Z., Lam, T. J. & Sin, Y. M. (2004) Development and maturation of the immune system in zebrafish, Danio rerio: a gene expression profiling, in situ hybridization and immunological study. *Dev Comp Immunol*, 28(1), 9-28.

Li, P., Lahvic, J. L., Binder, V., Pugach, E. K., Riley, E. B., Tamplin, O. J., Panigrahy, D., Bowman, T. V., Barrett, F. G., Heffner, G. C., McKinney-Freeman, S., Schlaeger, T. M., Daley, G. Q., Zeldin, D. C. & Zon, L. I. (2015) Epoxyeicosatrienoic acids enhance embryonic haematopoiesis and adult marrow engraftment. *Nature*, 523(7561), 468-71.

Nguyen, K., Devidas, M., Cheng, S. C., La, M., Raetz, E. A., Carroll, W. L., Winick, N. J., Hunger, S. P., Gaynon, P. S., Loh, M. L. & Children's Oncology, G. (2008) Factors influencing survival after relapse from acute lymphoblastic leukemia: a Children's Oncology Group study. *Leukemia*, 22(12), 2142-50.

Perez-Atayde, A. R., Sallan, S. E., Tedrow, U., Connors, S., Allred, E. & Folkman, J. (1997) Spectrum of tumor angiogenesis in the bone marrow of children with acute lymphoblastic leukemia. *Am J Pathol*, 150(3), 815-21.

Pezeshkian, B., Donnelly, C., Tamburo, K., Geddes, T. & Madlambayan, G. J. (2013) Leukemia Mediated Endothelial Cell Activation Modulates Leukemia Cell Susceptibility to Chemotherapy through a Positive Feedback Loop Mechanism. *PLoS One*, 8(4), e60823.

Pruvot, B., Jacquel, A., Droin, N., Auberger, P., Bouscary, D., Tamburini, J., Muller, M., Fontenay, M., Chluba, J. & Solary, E. (2011) Leukemic cell xenograft in zebrafish embryo for investigating drug efficacy. *Haematologica*, 96(4), 612-6.

Qian, B. Z. & Pollard, J. W. (2010) Macrophage diversity enhances tumor progression and metastasis. *Cell*, 141(1), 39-51.

Raedler, J., Heyde, S., Kolokythas, M., Eichinger, A., Binder, V., Schmid, I., Klein, C., Feuchtinger, T. & Albert, M. H. (2020) Venetoclax and decitabine for relapsed paediatric myelodysplastic syndrome-related acute myeloid leukaemia with complex aberrant karyotype after second stem cell transplantation. *Br J Haematol*, 189(6), e251-e254.

Sacco, A., Roccaro, A. M., Ma, D., Shi, J., Mishima, Y., Moschetta, M., Chiarini, M., Munshi, N., Handin, R. I. & Ghobrial, I. M. (2016) Cancer Cell Dissemination and Homing to the Bone Marrow in a Zebrafish Model. *Cancer Res*, 76(2), 463-71.

Schulz, M., Karpova, D., Spohn, G., Damert, A., Seifried, E., Binder, V. & Bonig, H. (2015) Variant rs1801157 in the 3'UTR of SDF-1ss does not explain variability of healthy-donor G-CSF responsiveness. *PLoS One*, 10(3), e0121859.

Schuster, F. R., Hubner, B., Fuhrer, M., Eckermann, O., Gombert, M., Dornmair, K., Binder, V., Reuther, S., Krell, P., Keller, T. & Borkhardt, A. (2011) Highly skewed T-cell receptor V-beta chain repertoire in the bone marrow is associated with response to immunosuppressive drug therapy in children with very severe aplastic anemia. *Blood Cancer J*, 1(3), e8.

Shaham, L., Binder, V., Gefen, N., Borkhardt, A. & Izraeli, S. (2012) MiR-125 in normal and malignant hematopoiesis. *Leukemia*, 26(9), 2011-8.

Smith, M., Arthur, D., Camitta, B., Carroll, A. J., Crist, W., Gaynon, P., Gelber, R., Heerema, N., Korn, E. L., Link, M., Murphy, S., Pui, C. H., Pullen, J., Reamon, G., Sallan, S. E., Sather, H., Shuster, J., Simon, R., Trigg, M., Tubergen, D., Uckun, F. & Ungerleider, R. (1996) Uniform approach to risk classification and treatment assignment for children with acute lymphoblastic leukemia. *J Clin Oncol*, 14(1), 18-24.

Stutterheim, J., de Lorenzo, P., van der Sluis, I. M., Alten, J., Ancliffe, P., Attarbaschi, A., Aversa, L., Boer, J. M., Biondi, A., Brethon, B., Diaz, P., Cazzaniga, G., Escherich, G., Ferster, A., Kotecha, R. S., Lausen, B., Leung, A. W., Locatelli, F., Silverman, L., Stary, J., Szczepanski, T., van der Velden, V. H. J., Vora, A., Zuna, J., Schrappe, M., Valsecchi, M. G. & Pieters, R. (2022) Minimal residual disease and outcome characteristics in infant KMT2A-germline acute lymphoblastic leukaemia treated on the Interfant-06 protocol. *Eur J Cancer*, 160, 72-79.

Testi, A. M., Attarbaschi, A., Valsecchi, M. G., Moricke, A., Cario, G., Niggli, F., Silvestri, D., Bader, P., Kuhlen, M., Parasole, R., Putti, M. C., Lang, P., Flotho, C., Mann, G., Rizzari, C., Barisone, E., Locatelli, F., Linderkamp, C., Lauten, M., Suttorp, M., Zimmermann, M., Basso, G., Biondi, A., Conter, V., Schrappe, M. & Group, A.-B. S. (2019) Outcome of adolescent patients with acute lymphoblastic leukaemia aged 10-14 years as compared with those aged 15-17 years: Long-term results of 1094 patients of the AIEOP-BFM ALL 2000 study. *Eur J Cancer*, 122, 61-71.

White, R. M., Sessa, A., Burke, C., Bowman, T., LeBlanc, J., Ceol, C., Bourque, C., Dovey, M., Goessling, W., Burns, C. E. & Zon, L. I. (2008) Transparent adult zebrafish as a tool for in vivo transplantation analysis. *Cell Stem Cell*, 2(2), 183-9.

Wildenhain, S., Ruckert, C., Rottgers, S., Harbott, J., Ludwig, W. D., Schuster, F. R., Beldjord, K., Binder, V., Slany, R., Hauer, J. & Borkhardt, A. (2010) Expression of cell-cell interacting genes distinguishes HLXB9/TEL from MLL-positive childhood acute myeloid leukemia. *Leukemia*, 24(9), 1657-60.

Willier, S., Raedler, J., Blaeschke, F., Stenger, D., Pazos Escudero, M., Jurgeleit, F., Grunewald, T. G. P., Binder, V., Schmid, I., Albert, M. H., Wolf, A. & Feuchtinger, T. (2020) Leukemia escape in immune desert: intraocular relapse of pediatric pro-B-ALL during systemic control by CD19-CAR T cells. *J Immunother Cancer*, 8(2).

Willier, S., Rothamel, P., Hastreiter, M., Wilhelm, J., Stenger, D., Blaeschke, F., Rohlfs, M., Kaeuferle, T., Schmid, I., Albert, M. H., Binder, V., Subklewe, M., Klein, C. & Feuchtinger, T. (2021) CLEC12A and CD33 coexpression as a preferential target for pediatric AML combinatorial immunotherapy. *Blood*, 137(8), 1037-1049.

6. ABKÜRZUNGSVERZEICHNIS

3'UTR	3' untranslated region
ABL1	Abelson Tyrosine-Protein Kinase 1
AFF1	AF4 (ALL1-fused gene from chromosome 4)/FMR2 (FRAXE (fragiles XE-Syndrom)-associated mental retardation protein) family
ALL	Akute Lymphatische Leukämie
AML	Acute myeloid leukemia
ANGPT1	Angiopoietin 1
AP1	Jun Activation Domain Binding Protein 1
B-ALL	B-Lymphozyten Akute Lymphatische Leukämie
BCL2	B-cell chronic lymphatic leukemia/Lymphoma 2, Apoptosis Regulator
BCR	Breakpoint Cluster Region Protein
Bm	bone marrow
bzw	beziehungsweise
CAR	Chimeric Antigen Receptor
CD	Cluster of Differentiaqtion
CDKN2A	Cyclin Dependent Kinase Inhibitor 2A
CDKN2B	Cyclin Dependent Kinase Inhibitor 2B
CHT	Caudal hematopoietic tissue
CNTNAP5	Contactin Associated Protein Family Member 5
CNV	copy number variation
CREBBP	cAMP response element-binding -binding protein
CRLF2	Cytokine Receptor Like Factor 2
CXCL8	Chemokine (C-X-C Motif) Ligand 8
CXCR1	Chemokine (C-X-C Motif) Receptor 1
DNA	Deoxyribonucleic acid
DSG2	Desmoglein 2
EDIL3	EGF (Epidermal Growth Factor) Like Repeats And Discoidin Domains 3
EET	Epoyxeicosatrienoic Acid
ERK	extracellular-signal regulated kinases
ETV6=TEL	Ets Variant Gene 6 (TEL=translocation-Ets-Leukemia Oncogene)
FBXW7	F-Box And WD Repeat Domain Containing 7, E3 Ubiquitin Protein Ligase
FLT3	Fms Related Receptor Tyrosine Kinase 3
G-CSF	Granulocyte colony-stimulating factor
GESTALT	genome editing of synthetic target arrays for lineage tracing
GWAS	Genomweite Assoziationsstudien
HLF	Hepatic Leukemia Factor
HLXB9	Homeobox Protein HB9
HSC	Hematopoietic stem cell
HSCT	Hematopoietic Stem Cell Transplantation
HSPC	Hematopoietic stem and progenitor cells
iAMP21	intrachromosomal amplification on Chromosome 21
IKZF2	Ikaros Family Zinc Finger Protein 2
IL-3	Interleukin 3
ITGA9	Integrin Subunit Alpha 9
ITGAV	Integrin Subunit Alpha V
JAK	Janus Kinase
kb	kilobase
KDR	Kinase Insert Domain Receptor
KMT2A=MLL1	Lysine Methyltransferase 2A=MLL Mixed Lineage Leukemia 1
KRAS	Kirsten Rat Sarcoma Viral Oncogene Homolog

KSS	Kearns-Sayre Syndrom
LOH	loss of heterozygosity
M2	Tumorsupportive Makrophagen
MEF2D	Myocyte Enhancer Factor 2C
miRNA	micro RNA (Ribonucleic acid)
MLLT10	Myeloid/Lymphoid Or Mixed-Lineage Leukemia; Translocated To, 10
MRD	Minimal Residual Disease
mRNA	messenger RNA
mtDNA	mitochondrial DNA
mTOR	Mammalian Target Of Rapamycin
MYC	Myelocytomatosis
NGS	next generation sequencing
NOTCH1	Neurogenic Locus Notch Homolog Protein 1
NR3C1	Nuclear Receptor Subfamily 3 Group C Member 1
NR3C2	Nuclear Receptor Subfamily 3 Group C Member 2
NRAS	Neuroblastoma RAS Viral (V-Ras) Oncogene Homolog
PAX5	Paired Box 5
Ph-positive	Philadelphia Chromosom positiv
PI3K	Phosphatidylinositol 3-Kinase
PKC Delta	Protein Kinase C Delta
PS	Pearson syndrome
RAS	Rat Sarcoma Virus
RNA	Ribonucleic acid
RNF214	Ring Finger Protein 214
RT-PCR	realtime oder reverse transcriptase polymerase chain reaction
RUNX1	Runt-Related Transcription Factor 1
SAA	severe aplastic anemia
SDF-1B=CXCL12	Stromal Cell derived factor 1B= Chemokine (C-X-C Motif) Ligand 12
SETD2	SET domain containing 2
SIGLEC6	Sialic Acid Binding Ig Like Lectin 6
SNP	Single nucleotide Polymorphism
STAT	Signal Transducer And Activator Of Transcription
T-ALL	T-Lymphozyten Akute Lymphatische Leukämie
TCF3	Transcription Factor 3
TIM3	T-Cell Immunoglobulin Mucin Receptor 3
TP53	Tumor Protein P53
TRAIL	TNF (tumor necrosis factor)-related apoptosis-inducing ligand
VEGF	Vascular Endothelial Growth Factor
WAS	Wiskott Aldrich syndrome
WASP	Wiskott Aldrich syndrome Protein
WGA	Whole Genome Amplification

7. LISTE ALLER PUBLIKATIONEN DER KUMULATIVEN HABILITATIONSSCHRIFT

* equal contribution, # corresponding author

Arner, A., Ettinger, A., Blaser, B. W., Schmid, B., Jeremias, I., Rostam, N. & **Binder-Blaser, V#**. (2024) In vivo monitoring of leukemia-niche interactions in a zebrafish xenograft model. PLoS One, 19(8), e0309415.

IF (2024): 2,9

Bercovich, D., Ganmore, I., Scott, L. M., Wainreb, G., Birger, Y., Elimelech, A., Shochat, C., Cazzaniga, G., Biondi, A., Basso, G., Cario, G., Schrappe, M., Stanulla, M., Strehl, S., Haas, O. A., Mann, G., **Binder, V.**, Borkhardt, A., Kempski, H., Trka, J., Bielorei, B., Avigad, S., Stark, B., Smith, O., Dastugue, N., Bourquin, J. P., Tal, N. B., Green, A. R. & Izraeli, S. (2008) Mutations of JAK2 in acute lymphoblastic leukaemias associated with Down's syndrome. Lancet, 372(9648), 1484-92.

IF (2008): 28,4

Binder, V., Albert, M. H., Kabus, M., Bertone, M., Meindl, A. & Belohradsky, B. H. (2006) The genotype of the original Wiskott phenotype. N Engl J Med, 355(17), 1790-3.

IF (2006): 44

Binder, V.*#, Bartenhagen*, C., Okpanyi, V., Gombert, M., Moehlendick, B., Behrens, B., Klein, H. U., Rieder, H., Ida Krell, P. F., Dugas, M., Stoecklein, N. H.# & Borkhardt, A. (2014) A new workflow for whole-genome sequencing of single human cells. Hum Mutat, 35(10), 1260-70.

IF (2014): 5,1

Binder, V.*, Li, W.*, Faisal, M., Oyman, K., Calkins, D. L., Shaffer, J., Teets, E. M., Sher, S., Magnotte, A., Belardo, A., Deruelle, W., Gregory, T. C., Orwick, S., Hagedorn, E. J., Perlin, J. R., Avagyan, S., Lichtig, A., Barrett, F., Ammerman, M., Yang, S., Zhou, Y., Carson, W. E., Shive, H. R., Blachly, J. S., Lapalombella, R., Zon, L. I. & Blaser, B. W. (2023) Microenvironmental control of hematopoietic stem cell fate via CXCL8 and protein kinase C. Cell Rep, 42(5), 112528.

IF (2023): 9,99

Binder, V.#, Steenpass, L., Laws, H. J., Ruebo, J. & Borkhardt, A. (2012) A novel mtDNA large-scale mutation clinically exclusively presenting with refractory anemia: is there a chance to predict disease progression? J Pediatr Hematol Oncol, 34(4), 283-92.

IF (2012): 1,1

Binder, V. & Zon, L. I. (2013) High throughput in vivo phenotyping: The zebrafish as tool for drug discovery for hematopoietic stem cells and cancer. Drug Discovery Today: Disease Models. Volume 10, Issue 1, Spring 2013, Pages e17-e22

Invited Review

Blaeschke, F., Willier, S., Stenger, D., Lepenies, M., Horstmann, M. A., Escherich, G., Zimmermann, M., Rojas Ringeling, F., Canzar, S., Kaeuferle, T., Rohlfs, M., **Binder, V.,** Klein, C. & Feuchtinger, T. (2020) Leukemia-induced dysfunctional TIM-3(+)CD4(+) bone marrow T cells increase risk of relapse in pediatric B-precursor ALL patients. Leukemia, 34(10), 2607-2620.

IF (2020): 9,4

Blaser, B. W., Moore, J. L., Hagedorn, E. J., Li, B., Riquelme, R., Lichtig, A., Yang, S., Zhou, Y., Tamplin, O. J., **Binder, V.** & Zon, L. I. (2017) CXCR1 remodels the vascular niche to promote hematopoietic stem and progenitor cell engraftment. J Exp Med, 214(4), 1011-1027.

IF (2017): 11,9

Carlet, M., Volse, K., Vergalli, J., Becker, M., Herold, T., Arner, A., Senft, D., Jurinovic, V., Liu, W. H., Gao, Y., Dill, V., Fehse, B., Baldus, C. D., Bastian, L., Lenk, L., Schewe, D. M., Bagnoli, J. W., Vick, B., Schmid, J. P., Wilhelm, A., Marschalek, R., Jost, P. J., Miething, C., Riecken, K., Schmidt-Supprian, M., **Binder, V.** & Jeremias, I. (2021) In vivo inducible reverse genetics in patients' tumors to identify individual therapeutic targets. Nat Commun, 12(1), 5655.

IF (2021): 17,7

Chen, C., Bartenhagen, C., Gombert, M., Okpanyi, V., **Binder, V.,** Rottgers, S., Bradtke, J., Teigler-Schlegel, A., Harbott, J., Ginzel, S., Thiele, R., Fischer, U., Dugas, M., Hu, J. & Borkhardt, A. (2013) Next-generation-sequencing-based risk stratification and identification of new genes involved in structural and sequence variations in near haploid lymphoblastic leukemia. Genes Chromosomes Cancer, 52(6), 564-79.

IF (2013): 3,8

Chen, C., Bartenhagen, C., Gombert, M., Okpanyi, V., **Binder, V.,** Rottgers, S., Bradtke, J., Teigler-Schlegel, A., Harbott, J., Ginzel, S., Thiele, R., Husemann, P., Krell, P. F., Borkhardt, A., Dugas, M., Hu, J. & Fischer, U. (2015a) Next-generation-sequencing of recurrent childhood high hyperdiploid acute lymphoblastic leukemia reveals mutations typically associated with high risk patients. Leuk Res, 39(9), 990-1001.

IF (2015): 2,6

Fischer, U., Ruckert, C., Hubner, B., Eckermann, O., **Binder, V.,** Bakchoul, T., Schuster, F. R., Merk, S., Klein, H. U., Fuhrer, M., Dugas, M. & Borkhardt, A. (2012) CD34+ gene expression profiling of individual children with very severe aplastic anemia indicates a pathogenic role of integrin receptors and the proapoptotic death ligand TRAIL. Haematologica, 97(9), 1304-11.

IF (2012): 5,9

Gefen, N.*, **Binder, V.*,** Zaliova, M., Linka, Y., Morrow, M., Novosel, A., Edry, L., Hertzberg, L., Shomron, N., Williams, O., Trka, J., Borkhardt, A. & Izraeli, S. (2010) Hsa-mir-125b-2 is highly expressed in childhood ETV6/RUNX1 (TEL/AML1) leukemias and confers survival advantage to growth inhibitory signals independent of p53. Leukemia, 24(1), 89-96.

IF (2010): 8,9

Ghosh, S., Bartenhagen, C., Okpanyi, V., Gombert, M., **Binder, V.,** Teigler-Schlegel, A., Bradtke, J., Rottgers, S., Dugas, M. & Borkhardt, A. (2013) Recurrent involvement of ring-type zinc finger genes in complex molecular rearrangements in childhood acute myelogeneous leukemia with translocation t(10;11)(p12;q23). Leukemia, 27(8), 1745-8.

IF (2013): 9,4

Ghosh, S., Krux, F., **Binder, V.,** Gombert, M., Niehues, T., Feyen, O., Laws, H. J., Borkhardt, A. & Diseases, P.-N. G. N. o. P. I. (2012a) Array-based sequence capture and next-generation sequencing for the identification of primary immunodeficiencies. Scand J Immunol, 75(3), 350-4.

IF (2012): 2,2

Ghosh, S., Schuster, F. R., **Binder, V.,** Niehues, T., Baldus, S. E., Seiffert, P., Laws, H. J., Borkhardt, A. & Meisel, R. (2012b) Fatal outcome despite full lympho-hematopoietic reconstitution after allogeneic stem cell transplantation in atypical ataxia telangiectasia. J Clin Immunol, 32(3), 438-40.

IF (2012): 3,4

Li, P.*, Lahvic, J. L.*, **Binder, V.*,** Pugach, E. K., Riley, E. B., Tamplin, O. J., Panigrahy, D., Bowman, T. V., Barrett, F. G., Heffner, G. C., McKinney-Freeman, S., Schlaeger, T. M., Daley, G. Q., Zeldin, D. C. & Zon, L. I. (2015) Epoxyeicosatrienoic acids enhance embryonic haematopoiesis and adult marrow engraftment. Nature, 523(7561), 468-71.

IF (2015): 38,1

Raedler, J., Heyde, S., Kolokythas, M., Eichinger, A., **Binder, V.,** Schmid, I., Klein, C., Feuchtinger, T. & Albert, M. H. (2020) Venetoclax and decitabine for relapsed paediatric myelodysplastic syndrome-related acute myeloid leukaemia with complex aberrant karyotype after second stem cell transplantation. Br J Haematol, 189(6), e251-e254.

IF (2020): 5,5

Schulz, M., Karpova, D., Spohn, G., Damert, A., Seifried, E., **Binder, V.** & Bonig, H. (2015) Variant rs1801157 in the 3'UTR of SDF-1ss does not explain variability of healthy-donor G-CSF responsiveness. PLoS One, 10(3), e0121859.

IF (2015): 4,4

Schuster, F. R., Hubner, B., Fuhrer, M., Eckermann, O., Gombert, M., Dornmair, K., **Binder, V.,** Reuther, S., Krell, P., Keller, T. & Borkhardt, A. (2011) Highly skewed T-cell receptor V-beta chain repertoire in the bone marrow is associated with response to immunosuppressive drug therapy in children with very severe aplastic anemia. Blood Cancer J, 1(3), e8.

IF (2011): 12,9

Shaham, L., **Binder, V.,** Gefen, N., Borkhardt, A. & Izraeli, S. (2012) MiR-125 in normal and malignant hematopoiesis. Leukemia, 26(9), 2011-8.

Invited Review

Wildenhain, S., Ruckert, C., Rottgers, S., Harbott, J., Ludwig, W. D., Schuster, F. R., Beldjord, K., **Binder, V.,** Slany, R., Hauer, J. & Borkhardt, A. (2010) Expression of cell-cell interacting genes distinguishes HLXB9/TEL from MLL-positive childhood acute myeloid leukemia. Leukemia, 24(9), 1657-60.

IF (2010): 8,9

Willier, S., Raedler, J., Blaeschke, F., Stenger, D., Pazos Escudero, M., Jurgeleit, F., Grunewald, T. G. P., **Binder, V.,** Schmid, I., Albert, M. H., Wolf, A. & Feuchtinger, T. (2020) Leukemia escape in immune desert: intraocular relapse of pediatric pro-B-ALL during systemic control by CD19-CAR T cells. J Immunother Cancer, 8(2).

IF (2020): 10,3

Willier, S., Rothamel, P., Hastreiter, M., Wilhelm, J., Stenger, D., Blaeschke, F., Rohlfs, M., Kaeuferle, T., Schmid, I., Albert, M. H., **Binder, V.,** Subklewe, M., Klein, C. & Feuchtinger, T. (2021) CLEC12A and CD33 coexpression as a preferential target for pediatric AML combinatorial immunotherapy. Blood, 137(8), 1037-1049

IF (2021): 17,5

8. DANKSAGUNG

Es ist mir ein großes Anliegen, die Gelegenheit zu nutzen, zahlreichen Personen für ihre wertvolle Unterstützung auf meinem wissenschaftlichen und klinischen Werdegang zu danken.

Mein aufrichtiger Dank richtet sich natürlich an meine wissenschaftlichen Mentoren, meinem Doktorvater Prof. Dr. med. B.H. Belohradsky (München) und meinen Betreuern während meiner Postdoktorandenzeit, Prof. Dr. med. A. Borkhardt (München, Düsseldorf), Prof. Dr. med. Shai Izraeli (Tel Aviv) und Prof. Len Zon (Boston). Jeder von ihnen hat auf einzigartige Weise zu meiner Entwicklung und meinem Fortschritt beigetragen.

Schließlich danke ich Prof. Dr. med. C. Klein, dessen Unterstützung und Engagement in den letzten Jahren entscheidend für meine klinische und wissenschaftliche Entwicklung waren. Seine Begeisterung für die molekularen Grundlagen und die klinische Anwendung hat mich stets motiviert, mein Bestes zu geben.

Darüber hinaus danke ich meinen weiteren Fachmentoren und Kollegen, die mich während des Habilitationsprozesses begleitet haben. Ein besonderes Dankeschön gilt Frau Prof. Irmela Jeremias, die mich als äußerst erfolgreiche Wissenschaftlerin sehr inspiriert und die mich vor allem nach meiner Rückkehr aus den USA sehr unterstützt hat. Ein herzlicher Dank geht auch an Frau Dr. rer. nat. Bettina Schmid für Ihre stets unkomplizierte Unterstützung und Hingabe rund um den Zebrafisch.

Ebenso möchte ich meinen oberärztlichen Kollegen in der Klinik, Prof. Dr. Irene Schmid und Prof. Dr. med. Michael Albert, herzlich danken, von denen ich sehr viel lernen durfte und die mir stets mit Rat und Tat zur Seite standen. Ein besonderer Dank gebührt auch meinem geschätzten Kollegen, Freund und Tandempartner Dr. Christian Braun, dessen Einsatz mir geholfen hat, wieder Zeit für die Wissenschaft zu gewinnen.

Ein herzliches Dankeschön geht auch an meine Familie, insbesondere an meine Eltern, die mir meine gesamte Ausbildung ermöglicht und immer an mich geglaubt haben. Ein ganz besonderer Dank gilt meinem Mann Brad, mit dem ich meine Leidenschaft für die Forschung nun schon seit mehr als 10 Jahren teilen darf. Außerdem danke ich meinen lieben Freunden, die mir in all den Jahren unterstützend zur Seite gestanden haben.

9. ABDRUCKE DER DIESER HABILITATIONSSCHRIFT ZUGRUNDE LIEGENDEN EIGENEN ORIGINALARBEITEN

BRIEF REPORT

The Genotype of the Original Wiskott Phenotype

Vera Binder, M.D., Michael H. Albert, M.D., Maria Kabus, M.D., Marko Bertone, Alfons Meindl, Ph.D., and Bernd H. Belohradsky, M.D.

SUMMARY

The Wiskott–Aldrich syndrome is an X-linked hereditary disorder associated with combined immunodeficiency, thrombocytopenia, small platelets, eczema, and increased susceptibility to autoimmune disorders and cancers. It is caused by mutations in the gene (*WAS*) for the Wiskott–Aldrich syndrome protein (WASP). We investigated family members of the patients originally described by Wiskott in 1937 and identified a new frame shift mutation in exon 1 of *WAS*. This mutation is likely to be the hypothesized genotype that caused the severe form of the Wiskott–Aldrich syndrome in the three brothers described by Wiskott.

From the Departments of Hematology and Oncology (V.B., M.H.A.) and Immunology and Infectious Diseases (B.H.B.), Dr. von Haunersches Children's Hospital, Ludwig Maximilians University; and the Department of Obstetrics and Gynecology, Klinikum rechts der Isar, Technical University Munich (M.B., A.M.) — both in Munich; and the Department of Pediatrics, Municipal Hospital Dresden–Neustadt, Academic Section of the Technical University Dresden, Dresden, Germany (M.K.). Address reprint requests to Dr. Meindl, Department of Obstetrics and Gynecology, Klinikum rechts der Isar, Technical University Munich, Ismaninger Straße 22, D-81675 Munich, Germany, or at alfons.meindl@lrz.tu-muenchen.de.

N Engl J Med 2006;355:1790-3.

In 1937, Alfred Wiskott, a German pediatrician, described three brothers who presented shortly after birth with thrombocytopenia, bloody diarrhea, eczema, and recurrent ear infections; all three died early in life from intestinal bleeding and sepsis. Wiskott commented that "the origin of the hemorrhagic diathesis is a dysfunction in the line of the platelets."[1] The observation that all three brothers were affected, whereas their sisters showed no symptoms, led Wiskott to propose that the syndrome is due to a "hereditary thrombopathia."[1] In 1954, Aldrich et al. traced six generations of a family and found that 16 of 40 males, but no females, died of the syndrome first described by Wiskott, thus clearly showing an X-linked mode of inheritance.[2]

The Wiskott–Aldrich syndrome is now known as an X-linked hereditary disorder associated with combined immunodeficiency, thrombocytopenia, small platelets, eczema, and an increased risk of autoimmune disorders and cancers. It has a broad range of phenotypes (Online Mendelian Inheritance in Man no. 301000).[3-6]

The severe form of the Wiskott–Aldrich syndrome and its milder manifestations — X-linked thrombocytopenia and X-linked neutropenia — are caused by mutations in the gene for the Wiskott–Aldrich syndrome protein (*WAS*), located at Xp11.22–p11.23 and cloned in 1994.[7-10] WAS and several related proteins are involved in the reorganization of the actin cytoskeleton by activating the actin-related protein 2/3 complex that mediates actin polymerization in all cells of the hematopoietic system.[3,11-15] Mutations in the *WAS* gene result in truncated or absent WASP in these cells, but there is no strict correlation between the mutant genotype and the expression of WASP or the phenotype of the syndrome.[11,15-18] The disorder can be cured through hematopoietic stem-cell transplantation.[19]

We recruited members of the family described by Wiskott in 1937 in order to identify the hypothesized mutation in *WAS* that caused the severe phenotype of the Wiskott–Aldrich syndrome in the three brothers. Genetic testing for the mutation was carried out in three generations of the kindred.

METHODS

After obtaining written informed consent, we performed mutation analyses in Subjects III-6, III-8, III-9, III-10, IV-2, IV-3, V-1, and V-2 (Fig. 1). Genomic DNA was extracted from peripheral white cells. After amplification, *WAS* exons 1 through 12 were analyzed with the single-strand conformation polymorphism method and the aberrant fragment of exon 1 was investigated by means of double-strand sequencing. All other *WAS* exons from Subjects III-10 and V-1 were reanalyzed through direct sequencing (with the use of a kit from Applied Biosystems). The primer sequences used for amplification and the methods used for the screening of mutations have been described previously.[18] A *WAS* mutation was ruled out in 400 controls (200 men and 200 women) by means of denaturing high-performance liquid chromatography with the Wave system (Transgenomics); the aberrant fragment was observed in DNA from a female carrier, analyzed with the use of buffer B (on a gradient of 53 to 61%) at a running temperature of 64°C.[20,21] To study the expression of the mutant allele, RNA was isolated from an obligate female carrier and transcribed into complementary DNA (cDNA) with the use of a first-strand cDNA synthesis kit (Amersham Biosciences). The cDNA was sequenced with the use of a pair of primers: one located in the 5′ untranslated region (1cF: 5′TCGCCAGAGAAGACAAGGGC3′) and one in exon 3 (3cR: 5′CATCTCCAGCGAAGGTGTGG3′).

RESULTS

Genetic testing for the mutation revealed a deletion of two nucleotides at positions 73 and 74 in *WAS* exon 1 (coding sequence, 73–74delAC[22,23]; the first nucleotide is the A of the ATG translation-initiation codon). This mutation is not listed in WASPbase,[24] an Internet-based database of *WAS* mutations. The deletion results in a frame shift that starts with amino acid 25; the shifted reading frame is open for another 11 amino acids before it results in a stop codon (protein sequence, Thr25ProfsX12[22,23]) (Fig. 2).

To further characterize the 73–74delAC mutation in the coding sequence, we first sought it in 400 normal subjects (200 men and 200 women) serving as controls; none carried the mutation. This result makes it improbable that the mutation is a polymorphic variant in the normal popula-

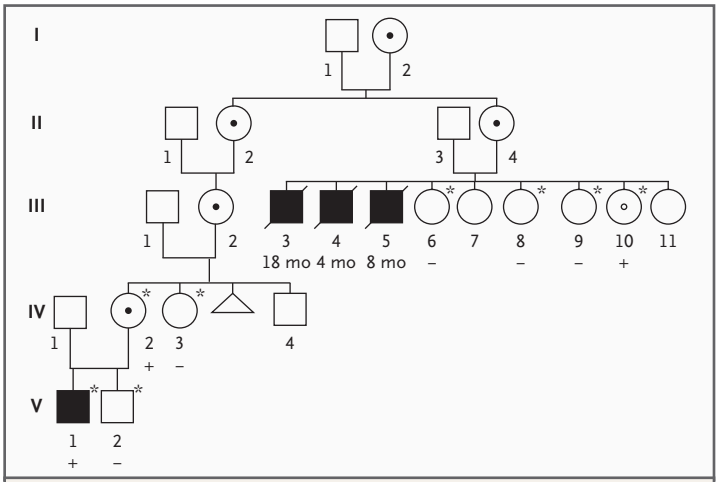

Figure 1. Pedigree of the Three Brothers (Subjects III-3, III-4, and III-5) Described by Wiskott in 1937.

Open symbols represent unaffected family members, solid squares affected men, circles with solid dots obligate female carriers, the circle with an open dot a female carrier identified by gene sequencing, the triangle an aborted fetus, symbols with a slash deceased affected family members, asterisks family members who were genetically tested, a minus sign family members with a negative result on genetic testing for the mutation, and a plus sign family members with a positive result. A positive result indicated that the subject was a carrier of the 73–74delAC mutation in the coding sequence. The age at death is indicated under the symbols representing the three brothers who were originally described by Wiskott.

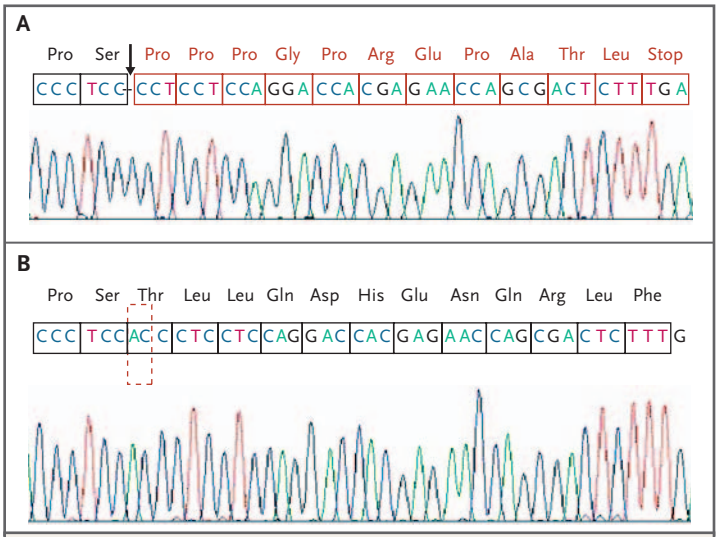

Figure 2. Chromatograms Showing the Mutation in Subject V-1 (Panel A) and the Wild-Type Sequence in the Same Subject after Stem-Cell Transplantation (Panel B).

In Panel A, the black boxes delineate nucleotide triplets upstream of the mutation; the arrow and dashed black line indicate the two nucleotides (AC) in positions 73 and 74 that are deleted in affected persons, causing a frame shift; and the red boxes delineate the nucleotide triplets in the new open reading frame. Panel B shows the position of the nucleotides in the wild type (outlined by dashed box).

tion. Next, we performed RNA analysis in a female carrier (Subject IV-2). She was heterozygous for the aberrant variant in exon 1. However, after the sequencing of exons 1 through 3 of the generated cDNA, we observed monoallelic expression, which indicates the decay of nonsense-mediated messenger RNA (mRNA) (the destruction of mRNA with a premature stop codon) (Fig. 3). This observation is a sign that the 73–74delAC mutation in the coding sequence is likely to result in the complete absence of WASP in affected men.[25]

We identified this mutation in three generations of the pedigree: Subjects III-10, IV-2, and V-1. Subject V-1 had presented with symptoms compatible with the severe form of the Wiskott–Aldrich syndrome: bloody diarrhea, severe infections, eczema, and thrombocytopenia with small platelets. He is alive and well after receiving a hematopoietic stem-cell transplant from an HLA-matched unrelated donor (Fig. 2B). Subject III-10, a sister of the three affected brothers described by Wiskott (Subjects III-3, III-4, and III-5), was identified as a carrier of the mutation, but three of her sisters do not carry the mutation. As expected, Subject IV-2, the mother of Subject V-1, also carries the X-linked mutation (Fig. 1).

DISCUSSION

Our analysis indicates that Subjects II-2 and II-4 were obligate carriers of the 73–74delAC mutation in the coding sequence after they inherited either a germ-line *WAS* mutation from one of their parents (Subjects I-1 and I-2) or the mutation from their mother (Subject I-2, the grandmother of Wiskott's patients), who could have been a silent carrier of an ancestral mutation. Since Subjects III-10 and IV-2 are carriers of the mutation, Subject III-2 must be an obligate female carrier.

Our findings indicate the improbability of a spontaneous mutation in Subject V-1 and provide strong evidence that the three affected brothers (Subjects III-3, III-4, and III-5) also had the 73–74delAC mutation in the coding sequence of *WAS*. Almost 70 years after Wiskott's initial clinical description of the Wiskott–Aldrich syndrome in

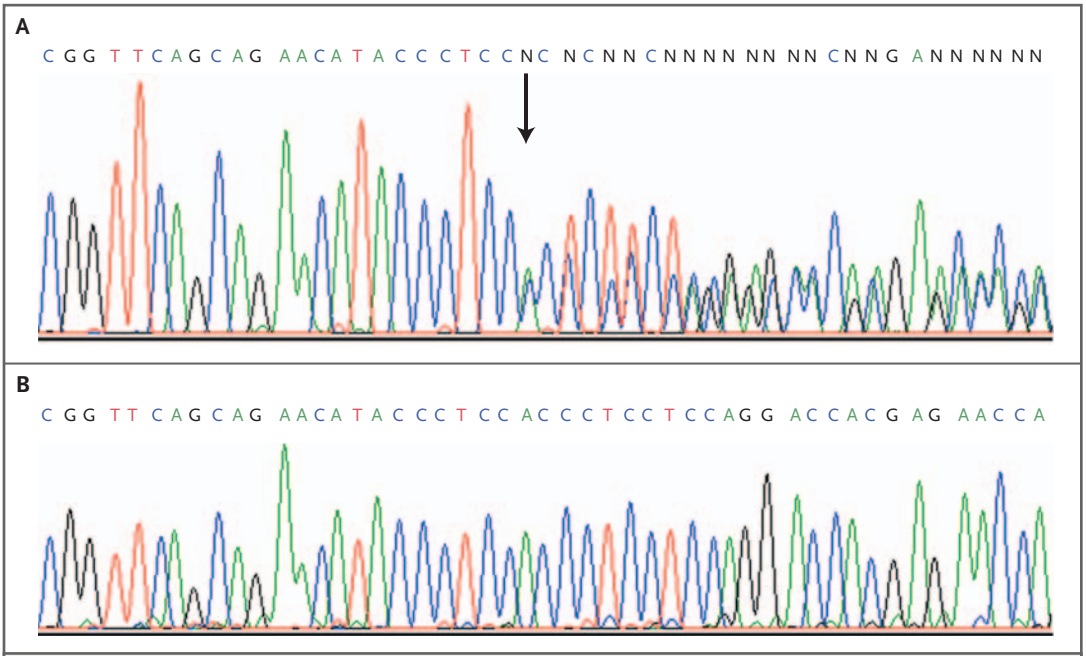

Figure 3. Nonsense-Mediated Decay of Mutant mRNA, as Shown in Genomic DNA (Panel A) and cDNA (Panel B) in a Female Carrier (Subject IV-2).

Panel A shows a chromatogram of genomic DNA in exon 1, revealing a heterozygous frame-shift deletion. The arrow indicates the site of the deletion. Panel B shows a chromatogram of the cDNA, revealing that *WAS* mRNA is expressed from only one allele.

three brothers, we found that a mutation in the X-linked *WAS* gene caused the severe phenotype.

Supported by Deutsche Krebshilfe.

No potential conflict of interest relevant to this article was reported.

We are indebted to Drs. W. Friedrich and K. Schwarz, Department of Pediatrics, University Hospital Ulm, Ulm, Germany, for providing information about the molecular analysis and stem-cell transplantation performed in Subject V-1, as well as for providing blood samples for additional analysis.

REFERENCES

1. Wiskott A. Familiärer, angeborener Morbus Werlhofii? Monatsschr Kinderheilkd 1937;68:212-6.
2. Aldrich RA, Steinberg AG, Campbell DC. Pedigree demonstrating a sex-linked recessive condition characterized by draining ears, eczematoid dermatitis and bloody diarrhea. Pediatrics 1954;13:133-9.
3. Ochs HD, Rosen FS. The Wiskott-Aldrich syndrome. In: Ochs HD, Smith CIE, Puck JM, eds. Primary immunodeficiency diseases: a molecular and genetic approach. New York: Oxford University Press, 1999:292-305.
4. Thrasher AJ, Kinnon C. The Wiskott-Aldrich syndrome. Clin Exp Immunol 2000;120:2-9.
5. Sullivan KE, Mullen CA, Blaese RM, Winkelstein JA. A multiinstitutional survey of the Wiskott-Aldrich syndrome. J Pediatr 1994;125:876-85.
6. Belohradsky BH, Griscelli C, Fundenberg HH, Marget W. The Wiskott-Aldrich syndrome. Ergeb Inn Med Kinderheilkd 1978;41:85-184. (In German.)
7. Derry JM, Ochs HD, Francke U. Isolation of a novel gene mutated in Wiskott-Aldrich syndrome. Cell 1994;78:635-44.
8. Derry JM, Kerns JA, Weinberg KI, et al. WASP gene mutations in Wiskott-Aldrich syndrome and X-linked thrombocytopenia. Hum Mol Genet 1995;4:1127-35.
9. Devriendt K, Kim AS, Mathijs G, et al. Constitutively activating mutation in WASP causes X-linked severe congenital neutropenia. Nat Genet 2001;27:313-7.
10. Ancliff PJBM, Gale RE. Activating mutations in the Wiskott-Aldrich syndrome protein may define a sub-group of severe congenital neutropenia (SCN) with specific and unusual laboratory features. Blood 2001;98:439. abstract.
11. Ochs HD, Notarangelo LD. Structure and function of the Wiskott-Aldrich syndrome protein. Curr Opin Hematol 2005; 12:284-91.
12. Burns S, Cory GO, Vainchenker W, Thrasher AJ. Mechanisms of WASp-mediated hematologic and immunologic disease. Blood 2004;104:3454-62.
13. Notarangelo LD, Ochs HD. Wiskott-Aldrich Syndrome: a model for defective actin reorganization, cell trafficking and synapse formation. Curr Opin Immunol 2003;15:585-91.
14. Thrasher AJ. WASp in immune-system organization and function. Nat Rev Immunol 2002;2:635-46.
15. Imai K, Nonoyama S, Ochs HD. WASP (Wiskott-Aldrich syndrome protein) gene mutations and phenotype. Curr Opin Allergy Clin Immunol 2003;3:427-36.
16. Imai K, Morio T, Zhu Y, et al. Clinical course of patients with WASP gene mutations. Blood 2004;103:456-64.
17. Jin Y, Mazza C, Christie JR, et al. Mutations of the Wiskott-Aldrich syndrome protein (WASP): hotspots, effect on transcription, and translation and phenotype/genotype correlation. Blood 2004;104: 4010-9.
18. Schindelhauer D, Weiss M, Hellebrand H, et al. Wiskott-Aldrich syndrome: no strict genotype-phenotype correlations but clustering of missense mutations in the amino-terminal part of the WASP gene product. Hum Genet 1996;98:68-76.
19. Filipovich AH, Stone JV, Tomany SC, et al. Impact of donor type on outcome of bone marrow transplantation for Wiskott-Aldrich syndrome: collaborative study of the International Bone Marrow Transplant Registry and the National Marrow Donor Program. Blood 2001;97:1598-603.
20. Underhill PA, Jin L, Lin AA, et al. Detection of numerous Y chromosome biallelic polymorphisms by denaturing high-performance liquid chromatography. Genome Res 1997;7:996-1005.
21. Ramser J, Abidi FE, Burckle CA, et al. A unique exonic splice enhancer mutation in a family with X-linked mental retardation and epilepsy points to a novel role of the renin receptor. Hum Mol Genet 2005; 14:1019-27.
22. den Dunnen JT, Antonarakis SE. Mutation nomenclature extensions and suggestions to describe complex mutations: a discussion. Hum Mutat 2000;15:7-12.
23. Human Genome Variation Society. Recommendations for the description of sequence variants. (Accessed September 29, 2006, at http://www.hgvs.org/mutnomen/recs.html.)
24. Imai K. WASPbase: database of published *WAS* gene mutations, updated 29 April 2004. (Accessed September 29, 2006, at http://homepage.mac.com/kohsukeimai/wasp/WASPbase.html.)
25. Maquat LE. Nonsense-mediated mRNA decay: splicing, translation and mRNP dynamics. Nat Rev Mol Cell Biol 2004;5:89-99.

Leukemia (2010) 24, 89–96

www.nature.com/leu

ORIGINAL ARTICLE

Hsa-mir-125b-2 is highly expressed in childhood *ETV6/RUNX1* (TEL/AML1) leukemias and confers survival advantage to growth inhibitory signals independent of p53

N Gefen[1,2,8], V Binder[1,3,8], M Zaliova[4], Y Linka[3], M Morrow[6], A Novosel[3], L Edry[5], L Hertzberg[1,2,7], N Shomron[5], O Williams[6], J Trka[4], A Borkhardt[3] and S Izraeli[1,2]

[1]*Section of Functional Genomics and Leukemia Research, Department of Pediatric Hemato-Oncology, Sheba Medical Center, Tel-Hashomer, Israel;* [2]*Department of Human Molecular Genetics and Biochemistry, Sackler Faculty of Medicine, Tel Aviv University, Tel Aviv, Israel;* [3]*Department of Pediatric Hematology, Oncology and Immunology, Heinrich Heine University, Duesseldorf, Germany;* [4]*Department of Pediatric Hematology and Oncology, Second Faculty of Medicine, Charles University and University Hospital Motol, Childhood Leukemia Investigation Prague, Prague, Czech Republic;* [5]*Department of Cell and Developmental Biology, Sackler Faculty of Medicine, Tel Aviv University, Tel Aviv, Israel;* [6]*Institute of Child Health, University College London, London, UK and* [7]*Department of Physics of Complex Systems, Weizmann Institute of Science, Rehovot, Israel*

MicroRNAs (miRNAs) regulate the expression of multiple proteins in a dose-dependent manner. We hypothesized that increased expression of miRNAs encoded on chromosome 21 (chr 21) contribute to the leukemogenic function of trisomy 21. The levels of chr 21 miRNAs were quantified by qRT–PCR in four types of childhood acute lymphoblastic leukemia (ALL) characterized by either numerical (trisomy or tetrasomy) or structural abnormalities of chr 21. Suprisingly, high expression of the *hsa-mir-125b-2* cluster, consisting of three miRNAs, was identified in leukemias with the structural *ETV6/RUNX1* abnormality and not in ALLs with trisomy 21. Manipulation of *ETV6/RUNX1* expression and chromatin immunoprecipitation studies showed that the high expression of the miRNA cluster is an event independent of the *ETV6/RUNX1* fusion protein. Overexpression of *hsa-mir-125b-2* conferred a survival advantage to Ba/F3 cells after IL-3 withdrawal or a broad spectrum of apoptotic stimuli through inhibition of caspase 3 activation. Conversely, knockdown of the *endogenous* miR-125b in the *ETV6/RUNX1* leukemia cell line REH increased apoptosis after Doxorubicin and Staurosporine treatments. P53 protein levels were not altered by miR-125b. Together, these results suggest that the expression of *hsa-mir-125b-2* in *ETV6/RUNX1* ALL provides survival advantage to growth inhibitory signals in a p53-independent manner.
Leukemia (2010) **24,** 89–96; doi:10.1038/leu.2009.208; published online 5 November 2009
Keywords: acute lymphoblastic leukemia (ALL); *ETV6/RUNX1*; TEL/AML1; microRNA

Introduction

Aberrations in chromosome 21 (chr 21) are commonly found in childhood acute lymphoblastic leukemia (ALL). The high-hyperdiploid ALL (HHD ALL),[1,2] the most common type of childhood ALL with *numerical* chromosomal aberrations, is characterized by 3–4 copies of chr 21 and a variable presence of other specific chromosomal trisomies. The markedly increased incidence of ALL in children with Down's syndrome (DS)[3] strongly suggests that trisomy 21 is leukemogenic, but the chr 21 genes involved in these leukemias are presently unknown. A newly discovered rare subtype of childhood ALL is characterized by an intrachromosomal amplification of a small region within the long arm of chr 21 (iAMP21) around the RUNX1 locus.[4] In contrast to *ETV6/RUNX1* and HHD ALL, it is associated with poor prognosis. The most common *structural* chromosomal aberration in childhood ALL occurring in approximately 25% of pediatric B-cell precursor ALL fuses the RUNX1 (AML1) gene on chr 21 with the ETV6 (TEL) gene on chr 12.[5,6] Although *ETV6/RUNX1* causes a prenatal preleukemic clonal expansion, additional genetic events are required for evolution of leukemia.[7,8]

MicroRNAs (miRNAs) are 20–25 nucleotide long non-coding RNAs that have a vital function in the regulation of protein expression.[9] Currently, there are six validated mature miRNAs encoded on human chr 21 (http://microrna.sanger.ac.uk Figure 1a). *Hsa-mir-99a, hsa-let-7c* and *hsa-mir-125b-2* are clustered together in the same intron of the *C21ORF34* gene on 21q.21.1 (NC_000021.7) (*hsa-mir-125b-2* cluster). *Hsa-mir-125b-1*, the homolog of *Caenorhabditis elegans* lin-4, has been shown to be expressed in solid tumors and associated with enhanced cell proliferation and survival.[10–12] An insertion of *hsa-mir-125b-1* into the IGH locus was described in a patient with B-cell precursor ALL suggesting its involvement in the leukemic process.[13] It has been shown to be expressed in myeloid malignancies and to block myeloid differentiation.[14] Recently, it was also reported to protect from apoptosis through negative regulation of p53 in zebrafish, human neuroblastoma cells and lung fibroblasts, but not in mouse cells.[15] *Hsa-mir-155* has been linked to B-cell development. Others and we have shown its increased expression in lymphomas.[16–19] Strikingly, transgenic expression of miR-155 induced pre-B-cell leukemias and lymphomas in mice,[20] thus miR-155 seems to be a potent oncogene.

The mechanisms of miRNA function suggest that their activity should be *correlated with their dosage* and that each miRNA may regulate multiple targets.[21] Thus, we hypothesized that miRNAs contribute to the oncogenic effects of chromosomal trisomies, a situation in which a small change ($\times 1.5$) in genomic dosage results in profound effects. This hypothesis is strengthened by our recent observations showing a general increase in expression of multiple genes from the trisomic chromosomes.[22] Thus, we expected that miRNAs from chr 21 would be overexpressed in HHD and DS ALL (3–4 copies of chr 21) relative to *ETV6/RUNX1* and iAMP21 leukemias.

Here, we report the surprising observations that unlike most of the genes encoded on chr 21, the expression of the *hsa-mir-125b-2* cluster does not correlate with gene copy number, but

Correspondence: Professor S Izraeli, Section of Functional Genomics and Leukemia Research, Department of Pediatric Hemato-Oncology, Sheba Medical Center, Tel Hashomer, Ramat Gan 52621, Israel.
E-mail: sizraeli@sheba.health.gov.il
[8]These two authors contributed equally to this work.
Received 2 February 2009; revised 17 August 2009; accepted 4 September 2009; published online 5 November 2009

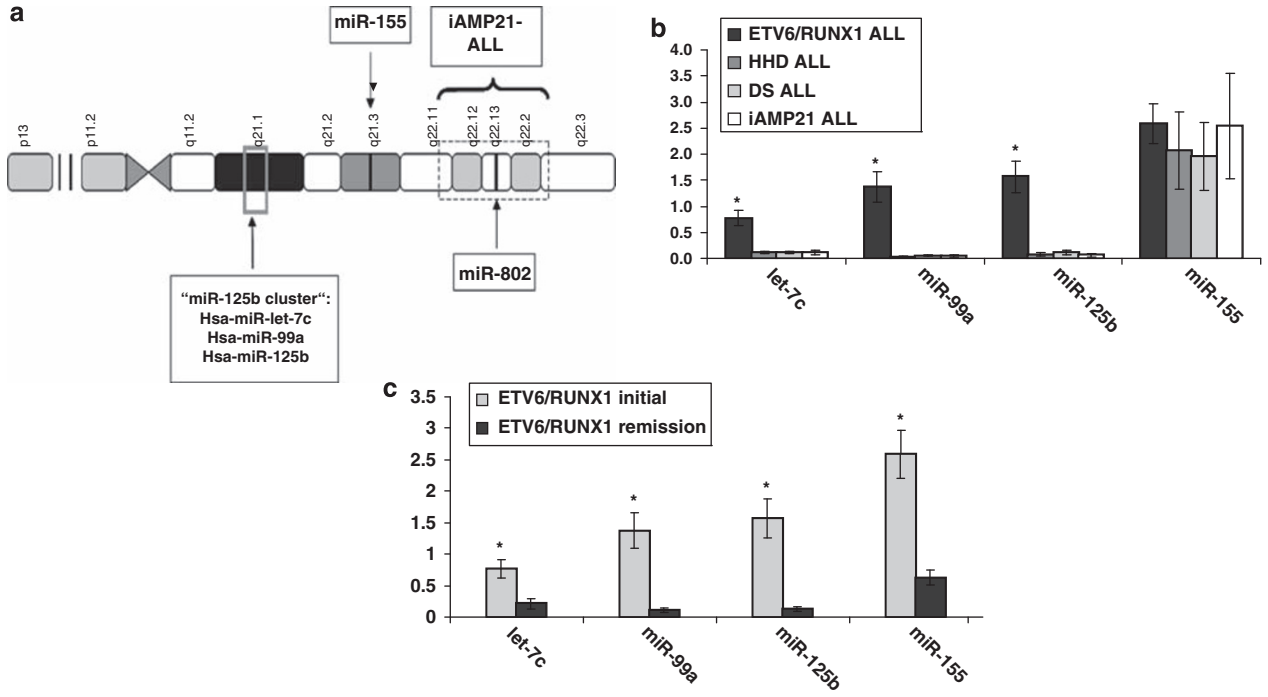

Figure 1 Expression of miRNAs encoded on chr 21 in different leukemia samples. (**a**) Schematic representation of the location of miRNAs encoded on chr 21. The level of the mature *hsa-miR-802* could not be measured because of the lack of an appropriate qRT–PCR-based assay. (**b**, **c**) MiRNA expression was determined by qRT–PCR using the TaqMan *MicroRNA Assays* from *Applied Biosystems.* The numbers on the *y* axis represent relative expression levels of mature miRNA normalized to an internal control (RNU43). Standard errors are indicated. Asterisk marks significance. (**b**) Expression of the chr 21 miRNAs in diagnostic bone marrow samples of different ALL subtypes: *ETV6/RUNX1* (24 patients), DS (10 patients), high hyperdiploid (10 patients), iAMP21 (7 patients) $P<0.05$ (ANOVA). (**c**) Comparison of miRNA expression between diagnosis and remission samples of *ETV6/RUNX1* leukemias $P<0.005$ (*T*-test).

rather is highly expressed in *ETV6/RUNX1* ALL. Additional research suggests that the expression of the *hsa-miR-125b-2* cluster is an independent event in *ETV6/RUNX1* ALL, conferring survival advantage under growth inhibitory and apoptotic conditions in a p53-independent manner.

Materials and methods

Patients

RNA was derived from diagnostic or remission bone marrow samples of childhood ALL patients obtained with informed consent. Diagnostic bone marrow samples contained at least 80% lymphoblasts. The samples were anonymized before shipping except for the information on the genetic subgroup. The study was approved by the IRB of the Israeli Health Ministry and Sheba Medical Center.

The rest of the material and methods are detailed in a supplementary file.

Results

Hsa-mir-125b-2 cluster is highly expressed in ETV6/RUNX1 leukemias

We measured the expression of the mature forms of four miRNAs encoded on chr 21 *(hsa-mir-99a*; *hsa-let-7c*; *hsa-mir-125b-2* and *hsa-mir-155)* by qRT–PCR in RNA derived from diagnostic bone marrow samples of four diverse subtypes of ALL with structural or numerical aberrations of chr 21: *ETV6/RUNX1* ALL ($n=24$), HHD ALL ($n=10$), DS ALL ($n=10$) and iAMP21 ALL ($n=7$). Surprisingly, extra copies of chr 21 did not contribute to the expression level of these miRNAs (Figure 1b). Although *hsa-mir-155* is similarly expressed between the different ALLs, the other miRNAs *hsa-mir-99a*, *hsa-let-7c* and *hsa-mir-125b-2* are up-regulated in the *ETV6/RUNX1* ALL, the subtype of leukemia with a *structural* aberration of chr 21. The expression was derived from the leukemic blasts, as it was not observed in remission samples (Figure 1c). To ensure that the observed results were not because of the normalization to a single internal control (RNU 43), we have extended the miRNA profiling using TaqMan Low Density miRNA arrays (TLDA, ABI) normalizing to two additional internal controls (RNU6 and RNU48). As can be seen in Supplementary Figure 1, the TLDA results are similar to the results obtained with the singleplex miRNA expression profiling.

Hsa-mir-125b-2 cluster is not a target of the ETV6/RUNX1 fusion protein

To test whether *mir-125b-2* is a target of ETV6/RUNX1, we performed overexpression experiments in two mouse hematopoietic progenitor cell systems: Ba/F3 cells and primary mouse embryonic fetal liver progenitors. It has been earlier shown that ectopic expression of *ETV6/RUNX1* in these progenitors induces proliferation of B-cell progenitors, similar to the preleukemia observed in human beings[23] (Supplementary Figure 2). In neither of these cells, the expression level of the *mmu-mir-125b-2* cluster was affected by the fusion protein (Supplementary Figure 3). As overexpression in mouse cells may not represent the relevant model, we have knocked down *ETV6/RUNX1* in the human REH ALL cell line with siRNA

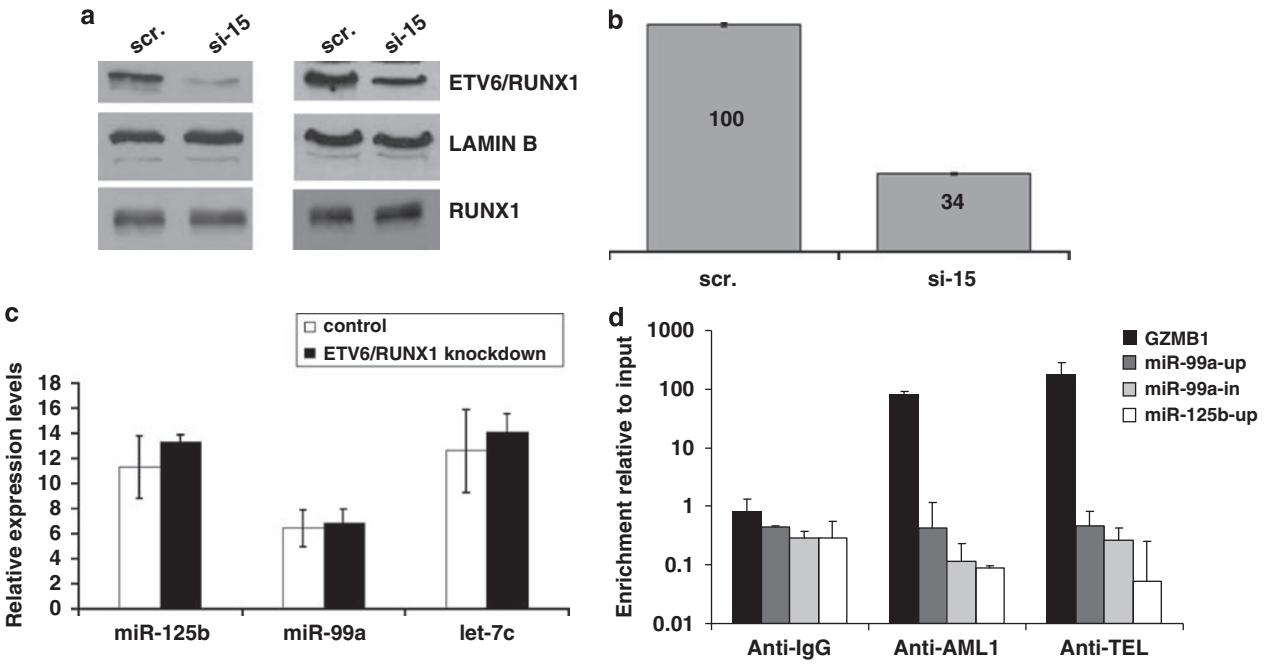

Figure 2 The *hsa-mir-125b-2* cluster is not a target of the *ETV6/RUNX1* fusion protein shown by knockdown of *ETV6/RUNX1* in REH cells. REH cells were transfected with siRNA directed against the fusion part of the ETV6 and RUNX1 genes (see Materials and methods). (**a**) Western blot analysis of *ETV6/RUNX1* knockdown in REH cells: Scr, scramble siRNA; si-15, mixture of siRNAs 1 and 5. Two independent experiments are shown. (**b**) A histogram showing quantification of the average *ETV6/RUNX1* protein level as detected by two independent western blots, determined by the ImageJ software. (**c**) No significant change in expression levels of the *hsa-mir-125b-2* cluster could be observed in REH cells after knockdown of *ETV6/RUNX1* as determined by qRT–PCR. An average of three independent experiments is shown. Expression levels are normalized to an internal control (RNU43). (**d**) qRT–PCR of chromatin immunoprecipitation analysis with anti-ETV6, anti-RUNX1, anti-IgG (served as negative control) or anti-TBP (served as positive control—see Materials and methods). Granzyme B (GZMB1) was used as positive control for the binding of RUNX1. The *y* axis indicates the enrichment normalized to GAPDH from sample and input. Three independent experiments were performed. Standard errors are indicated.

oligonucleotides (oligos) directed against the fusion part of this translocation (Supplementary Figure 4). Two-third silencing efficiency of *ETV6/RUNX1*, but not RUNX1, was observed by qRT–PCR and by western blots 5 days after the first round of transfection (Supplementary Figure 5; Figure 2a and b, respectively). Figure 2c shows that the expression of the *hsa-mir-125b-2* cluster was not influenced by the knockdown of the *ETV6/RUNX1* fusion protein. To further examine whether *ETV6/RUNX1* protein binds to RUNX1 sites on the vicinity of the *hsa-mir-125b-2* cluster, we performed chromatin immunoprecipitation analysis. There are three potential RUNX1 binding sites in the *hsa-mir-125b-2* cluster, one upstream of each miRNA (Supplementary Figure 6). As a positive control, we examined the promoter of granzyme B (GZMB), a RUNX1-regulated protein.[24] Figure 2d clearly shows that while the RUNX1 binding site upstream granzyme B (GZMB) is occupied by the *ETV6/RUNX1* and RUNX1 proteins, the putative RUNX1 binding sites of the *hsa-mir-125b-2* cluster are not bound by the fusion protein.

Taken together these experiments suggest that the *hsa-mir-125b-2* cluster is *not* a direct target of *ETV6/RUNX1*, but rather an independent event occurring during leukemogenesis.

Hsa-miR-125b-2 has a pro-survival effect under growth inhibitory conditions

To test the hypothesis that the expression of the *hsa-mir-125b-2* cluster contributes to survival and growth of lymphoid progenitors, we performed forced expression experiments in IL-3-dependent Ba/F3 cells. Transformation of these pro-B cells is commonly used to identify activating mutations of kinases.[25] We decided to focus on *hsa-mir-125b-2* because of earlier studies implicating a function of this miRNA in human cancers.[10,14,26,27] In addition, the endogenous mmu-miR-99a and let-7c are expressed in Ba/F3 cells, whereas miR-125b is not expressed. Furthermore, the sequence of the mature miR-125b is identical in human and mouse. We transduced Ba/F3 cells with an empty retroviral vector, a vector expressing *hsa-mir-125b-2* or a construct encoding *hsa-mir-125b-2* mutated in the seed region (see Materials and methods; Supplementary Figure 7) and confirmed the expression of the mature miRNAs by northern blot analysis (Figure 3a). No differences in growth were observed under steady-state conditions (not shown). However, Ba/F3 cells expressing *hsa-mir-125b-2* were highly resistant to a transient removal of IL-3. On reintroduction of IL-3 to the growth medium only *hsa-mir-125b2*-transduced Ba/F3 cells, but not cells transduced with an empty vector or a mutated *hsa-mir-125b-2,* resumed their normal growth (Figure 3b). To examine the mechanism of resistance to IL-3 withdrawal, we performed a cell cycle analysis of Ba/F3 cells transduced with the different constructs before and after IL-3 withdrawal; 24 h after IL-3 deprivation most of the *hsa-mir-125b-2* transfected cells were arrested in G1 (71.7%), whereas most of the control Ba/F3 cells were apoptotic (73% in subG1 phase; Figure 4a). This relative protection from apoptosis conferred by *hsa-mir-125b-2* was evident at different time points during the first 24 h of IL-3 deprivation (Figure 4b). The anti-apoptotic activity of *hsa-mir-125b-2* was associated with a marked inhibition of caspase 3 activation and the cleavage of its substrate PARP (Figure 4c).

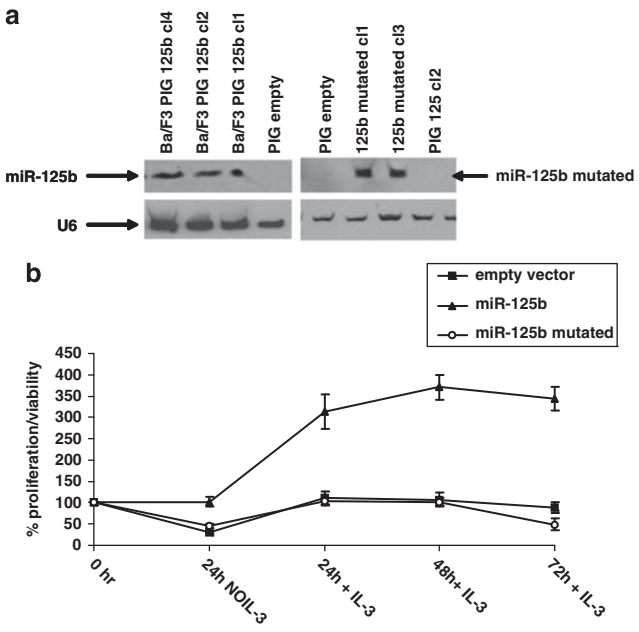

Figure 3 *Hsa-mir-125b-2* confers growth advantage in Ba/F3 cells after transient IL-3 deprivation. Ba/F3 cells were transduced with an empty vector, a vector expressing *mir-125b-2* or mutated *mir-125b-2*. (**a**) Northern blot analysis showing representative clones overexpressing *hsa-mir-125b-2* or mutated *hsa-mir-125b-2*. (**b**) Ba/F3 cells transduced with either empty vector, a vector expressing *hsa-mir-125b-2* or mutated *hsa-mir-125b-2* were cultured in the absence of IL-3 for 24 h. After 24 h, IL-3 was added to the medium and cell proliferation was measured by MTT every 24 h. The graph shows an average of at least three different clones and three experiments. Standard errors are indicated.

To examine how broad the anti-apoptotic phenotype observed in Ba/F3 cells overexpressing miR-125b is beyond the growth factor weaning, we exposed the cells to different apoptotic stimuli. Supplementary Figure 8 summarizes the percentage of living cells as has been quantified by FACS analysis of Annexin negative and 7AAD negative staining of four different treatments. As cytokine survival pathways involve activation of multiple kinases, we examined the effect of miR 125b on apoptosis induced by three kinase inhibitors with decreasing specificity: JAK Inhibitor I, AG490 and Staurosporine. Ba/F3 transduced with *hsa-mir-125b-2* were markedly resistant to each of these inhibitors in comparison with Ba/F3 cells transduced with mutated miR or with empty vector. Mild, but statistically significant resistance was also observed after treatment with Doxorubicin. Thus, miR125b provides survival advantage in response to multiple pro-apoptotic stimuli.

To test whether the survival advantage observed in Ba/F3 cells overexpressing miR-125b is relevant to *ETV6/RUNX1* leukemia, we used REH cells, a cell line derived from a patient with *ETV6/RUNX1* leukemia that highly expresses miR-125b. We knocked down the endogenous miR-125b by using LNA oligos labeled with FAM (Figure 5a) and measured the level of living cells of the FAM positive population (transfected with the LNA oligo) after treatment with either Doxorubicin or Staurosporine (see Materials and methods). Figure 5b and c shows that on knocking down miR-125b, the REH cells become more sensitive to Staurosporine and Doxorubicin treatments, respectively. These results indicate that the endogenous *mir-125b-2* provides partial protection from apoptosis induced by those agents similar to our observation in Ba/F3 cells.

A recent publication by Le *et al*.[15] suggested that miR-125b is a negative regulator of zebrafish and human (but not mouse) p53. We, therefore, asked whether the effects of miR-125b on apoptosis of Ba/F3 and REH cells could be explained by its regulation of p53 protein levels. Thus, we checked the levels of p53 and its main cellular protein target, p21, both under steady-state conditions and during apoptotic stress in both human and mouse models. The binding site of miR-125b on the 3′UTR of p53 is different between mouse and human particularly in the 'seed' area, an area considered to be the most significant for the recognition of miRNAs and their targets (Figure 6a). Therefore, it was not surprising that in the mouse Ba/F3 model, we have not observed any changes in the level of p53 neither under steady-state conditions nor under apoptotic conditions of IL-3 withdrawal (data not shown) or Doxorubicin treatment (Figure 6b and c). Surprisingly, knocking down miR-125b in the human REH cells did not alter p53 protein levels or p21 levels. Furthermore, treating the REH cells with Doxorubicin resulted in similar elevation of p53 levels in the cells transfected with a control LNA oligo or a miR-125b antisense LNA oligo, suggesting that p53 is not a target of miR-125b in these cells. This is further substantiated in the lack of alteration in the levels of p21 (Figure 6d and f). Similarly, there was no effect of miR-125b knockdown on p53 or p21 levels on treatment with Staurosporine (Figure 6e and f). Thus, p53 levels are not regulated by miR-125b in REH cells.

Discussion

Here, we describe that expression of the *hsa-mir-125b-2* cluster residing on chr 21 characterizes *ETV6/RUNX1* leukemias compared with other 'chr 21' leukemias. We show that this miRNA cluster is not regulated by the *ETV6/RUNX1* fusion protein and, therefore, hypothesize that its expression is an independent event occurring during the evolution of these leukemias. We further show by overexpression and knockdown studies that *mir-125b-2* provides a survival advantage by suppressing apoptosis and caspase 3 activation in response to growth inhibitory conditions.

This study was prompted by the hypothesis that increased expression of chr 21 miRNAs may explain the leukemogenic function of trisomy 21 in ALL of DS and in sporadic HHD leukemias (which uniformly contain either 3 or 4 copies of chr 21). This hypothesis was on the basis of our earlier observations that trisomies are usually associated with increased expression of multiple genes from the trisomic chromosomes[22] and by increased expression in DS AML of the miRNAs belonging to the *hsa-mir-125b-2* cluster.[28] Furthermore, increased expression of all chr 21 miRNAs has been recently reported in fetal heart and fetal hippocampus of DS patients.[29] Our findings that the expression of those miRNAs in B-cell precursor ALLs was *not* correlated to gene dosage but rather to the leukemia subtype were, therefore, unexpected. Increased expression levels of the *hsa-mir-125b-2* cluster were observed in *ETV6/RUNX1* ALL, whereas *hsa-miR-155* was similarly expressed in all subtypes. Furthermore, the expression of the *hsa-mir-125b-2* cluster was specific to the leukemic cells, as it was not observed in remission samples.

ETV6/RUNX1 is the most common translocation in childhood ALL. Similar to HHD ALL, these are B-cell precursor leukemias with excellent prognosis on contemporary treatment protocols.[30] The translocation is necessary for the initiation of a preleukemic clone, but insufficient for the evolution of leukemia.[7,8,31] Little is known about the acquired somatic

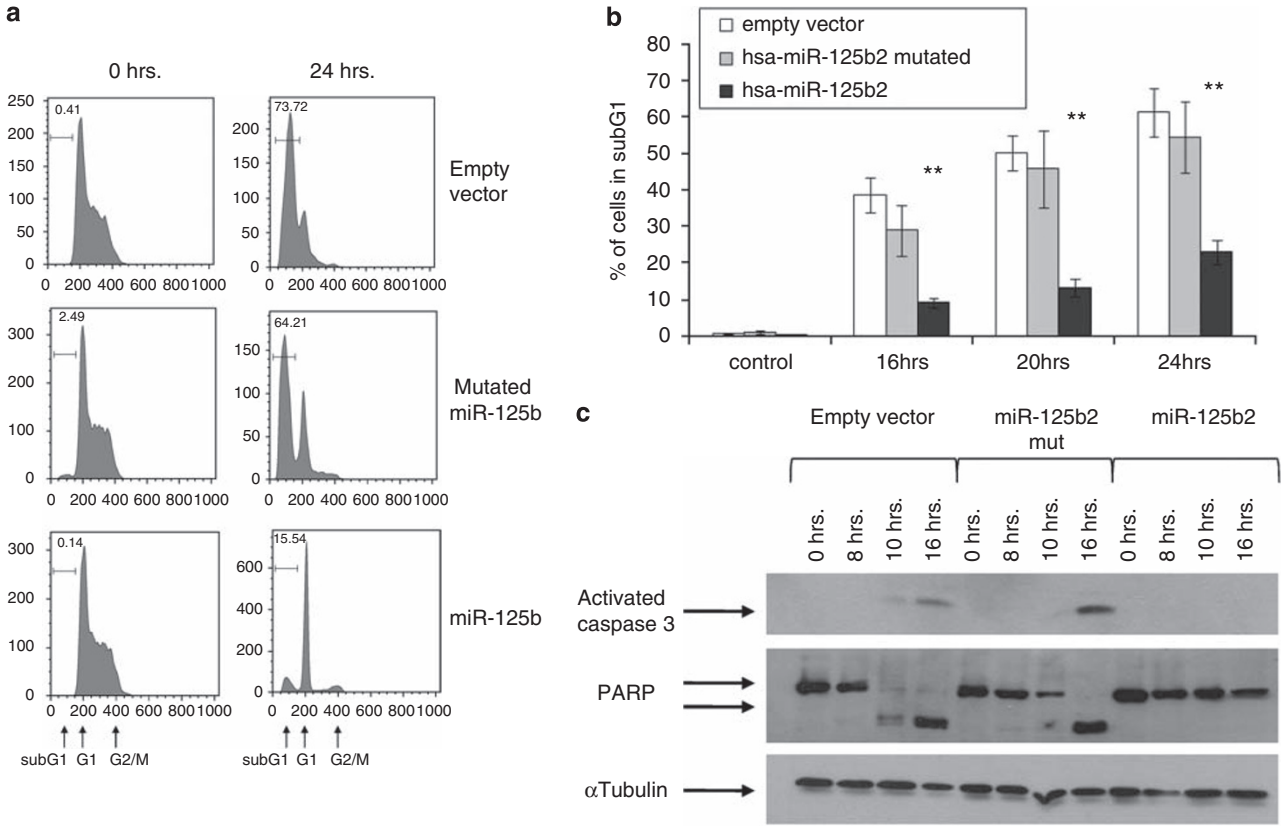

Figure 4 *Hsa-mir-125b-2* has an anti-apoptotic effect in Ba/F3 cells. (**a**, **b**) Quantification of apoptosis by measuring the subG1 fraction of Ba/F3 cells stained with propidum iodide, comparing wild-type cells, cells overexpressing *hsa-mir-125b-2* and cells overexpressing mutated *mir-125b-2*. (**a**) A representative example before (time 0) and 24 h after IL-3 withdrawal. (**b**) Kinetics of apoptosis with time after IL-3 withdrawal. Asterisks marks significance of $P<0.005$ as calculated by ANOVA. Standard errors are indicated. (**c**) Western blot analysis showing lack of activation of caspase 3 and cleavage of PARP after removal of IL-3 in Ba/F3 cells overexpressing *hsa-mir-125b-2* in comparison to wild-type Ba/F3 and those overexpressing mutated *hsa-mir-125b-2*. Experiments were repeated five times.

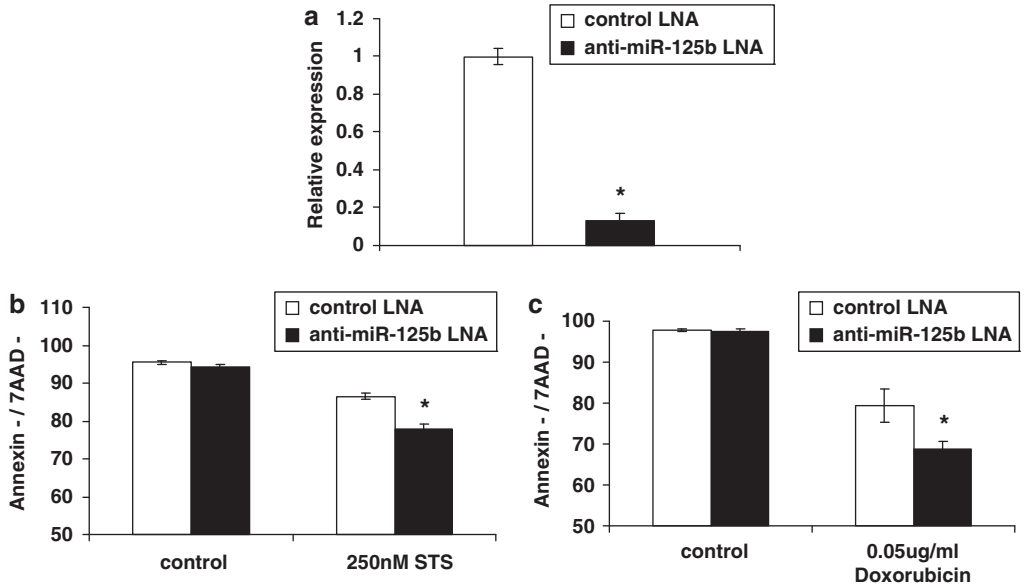

Figure 5 The endogenous *hsa-miR-125b* protects *ETV6/RUNX1* human leukemia cells from apoptosis. (**a**) qRT–PCR analysis of the knockdown efficiency of *hsa-miR-125b* in REH cells using a specific miR-125b antisense LNA oligo or a control oligo; *y* axis represents relative expression to the internal control RNU43. Eight independent experiments are shown. (**b, c**) Knockdown of miR-125b in REH cells increases the sensitivity to Staurosporine or Doxorubicin treatments, respectively, as indicated by decreased percentage of living cells (Annexin/7AAD negative). Data are means ± s.d. of four independent experiments for each treatment. *$P<0.05$ as calculated by *T*-test.

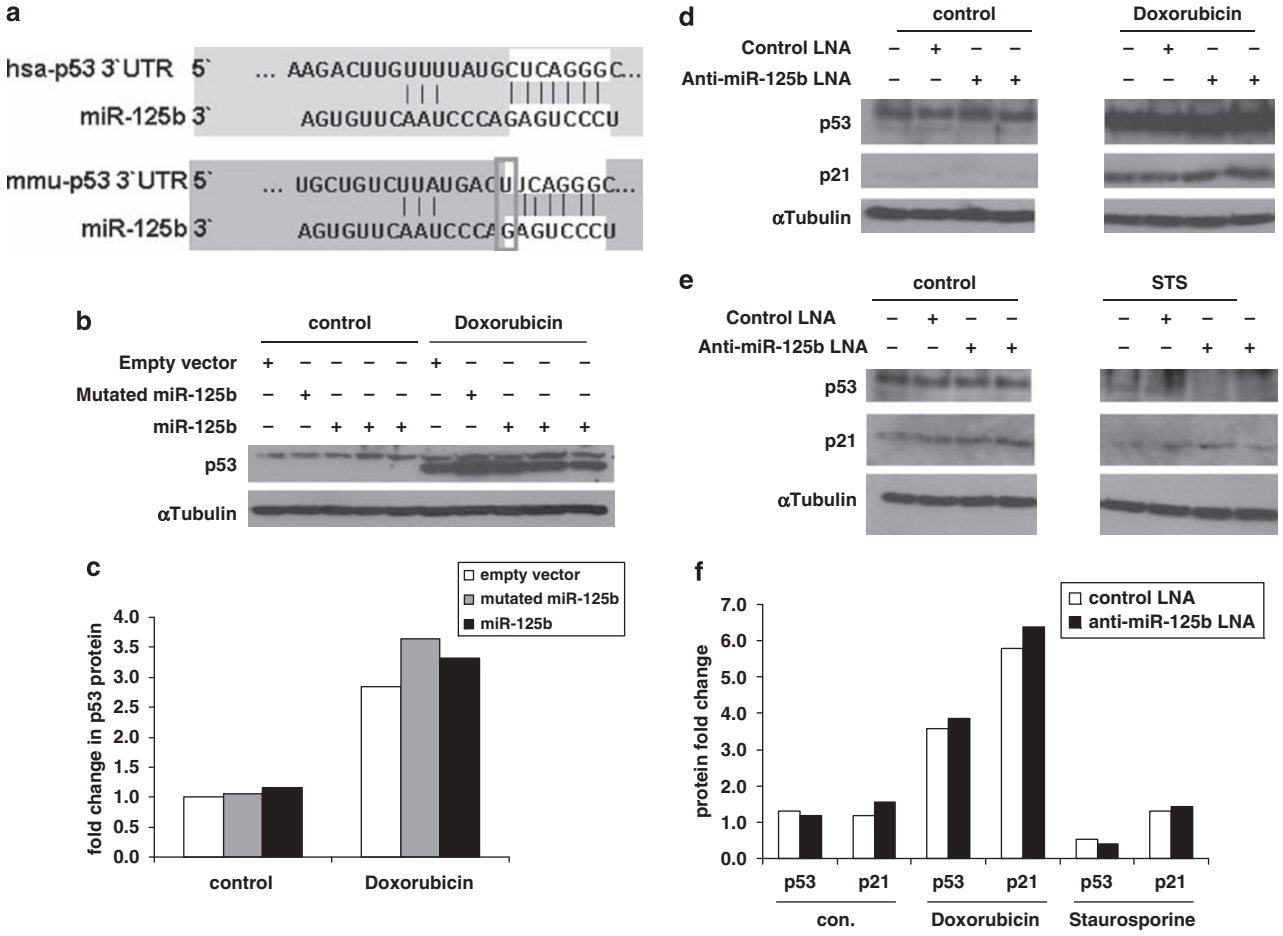

Figure 6 P53 is not a target of miR-125b in Ba/F3 and REH cells. (**a**) MiR-125b-binding site in the 3′UTR of the human and mouse p53 as predicted by TargetScan. Marked in white is the 'seed' area of miR-125b, also marked is the single different nucleotide in the potential miR-125b-binding site in the 3′UTR of the human and mouse p53. (**b**) Overexpression of miR-125b in mouse Ba/F3 cells does not down-regulate *endogenous* p53 levels. A representative western blot of *endogenous* p53 in Ba/F3 cells transduced with either the empty vector or the vector expressing mutated miR-125b or miR-125b. The cells were treated for 4 h with 0.2 μg/ml Doxorubicin. (**c**) Quantification of p53 protein level determined by western blot using the ImageJ software, normalized to αTubulin and presented as fold change relative to the level of p53 in Ba/F3 cells transduced with an empty vector. (**d**, **e**) *Endogenous* human p53 and p21 level after *endogenous* miR-125b knockdown in the human REH cells. After the knockdown, the cells were treated with either 0.05 μg/ml Doxorubicin (**d**) or Staurosporine (**e**). (**f**) Quantification of p53 and p21 protein levels determined by western blot using the ImageJ software, normalized to αTubulin level and presented as fold change relative to p53 or p21 levels, respectively, in REH cells transfected with a control LNA oligo.

oncogenic events that promote the progression of an *ETV6/RUNX1* preleukemic clone into a frank leukemia. The observation that the *hsa-mir-125b-2* cluster is not regulated by the *ETV6/RUNX1* fusion protein, suggests that its over-expression might be such an independent progression event.

MiRNAs have been shown to be dysregulated in cancer in tissue and cancer type-specific patterns. Although one miRNA acts as an oncogene in one type of cancer, the same miRNA serves as a tumor suppressor in another. In breast cancer, miR-125b has been found to suppress *ERBB2 (HER2)* and *ERBB3 (HER3)* expression[26] and thus functions as tumor suppressor. Conversely, a recent study suggested that miR-125b enhances growth and survival of prostate cancer and glioma cells.[12,27] To test the hypothesis that the increased expression of *mir-125b-2* in *ETV6/RUNX1* leukemia has a similar pro-survival function in hematopoietic cells, we used the IL-3-dependent pro-B Ba/F3 cells. These cells are considered as a standard screening tool to identify leukemia kinase oncogenes.[25,32–34] Functional analysis of *hsa-mir-125b-2* in Ba/F3 cells showed that this miRNA conferred growth factor independence by blocking apoptosis induced by IL3 withdrawal through delayed activation of caspase 3.

Cytokines such as IL3 promote cell survival through activation of JAK/STAT and related signal transduction pathways.[35–38] The function of mir-125b in protecting from death caused by silencing of pro-survival kinase regulated pathways is shown by the relative resistance it endowed Ba/F3 cells to three kinase inhibitors in decreasing specificity from JAK inhibitor 1 to Staurosporine. However, the anti-apoptotic effect of miR-125b is not limited to kinases as modest, but consistent and statistically significant resistance to apoptosis was also conferred to cells treated by the DNA damaging drug Doxorubicin. The anti-apoptotic phenotype was not an artifact of miRNA overexpression in Ba/F3 cells. Its relevance to *ETV6/RUNX1* leukemias is suggested by the sensitization to apoptosis induced by Staurosporine and Doxorubicin after knockdown of the endogenous miR-125b in REH cells.

Like most of the miRNAs, the precise targets of miR-125b are unknown. MiRNAs are believed to regulate many targets and currently bioinformatic target prediction algorithms are rather

limited.[39] A recent study suggested that miR-125b reduces the level of the pro-apoptotic protein BAK1,[27] thus blocking apoptosis. Though, we have not seen any reduction in BAK1 in either Ba/F3 or HEK293T cells overexpressing *hsa-mir-125b-2* (data not shown). We also have not detected any observable changes in several related pro-apoptotic proteins including BIM, BID, BAX and MCL-1 (data not shown). The recent report showing that p53 is negatively regulated by miR-125b[15] is intriguing as p53 is a major regulator of apoptosis in response to a variety of stresses including Doxorubicin. However, our experiments do not support that report. Similar to the observations by Le *et al*., and consistent with the lack of conservation of the miR-125b seed region in the 3′UTR region of mouse p53, we have not seen any alteration of the mouse p53 protein levels in Ba/F3 cells overexpressing miR-125b. Moreover, the very efficient knockdown conferred by specific LNA oligos in REH cells did not lead to any alterations in the human p53 levels or its target p21 before or after treatment with Doxorubicin. Thus, at least in these hematopoietic cells, p53 is not regulated by miR-25b.

Two provoking recent proteomic studies show that single miRNAs induce very small alterations in a large number of proteins and affect functional pathways by acting as sensitive 'Rheostats'.[40,41] Although such small alterations putatively induced by miR-125b in proteins that regulate cell survival may not be significant under steady-state conditions, they could provide growth advantage during periods of growth factor deprivation.

The pathogenesis of *ETV6/RUNX1* leukemias has been a mystery. *In vivo* modeling of *ETV6/RUNX1* leukemias by many laboratories has been proven experimentally challenging and resulting at most in a preleukemic condition.[31] A recent analysis of a 'knock-in' mouse model in which *ETV6/RUNX1* was expressed from the ETV6 promoter has shown an increase in hematopoietic stem cells. Intriguingly, the hematopoietic stem cells expressing the fusion protein were markedly more sensitive to apoptosis induced by cytokine withdrawal.[42] We propose that *hsa-mir-125b-2* and possibly the two other miRNAs in this cluster may collaborate with *ETV6/RUNX1* in the leukemogenic process by providing survival advantage under growth inhibitory conditions. It would be interesting to test this hypothesis in that mouse model.

Conflict of interest

The authors declare no conflict of interest.

Acknowledgements

We thank J Crispino, G Lavi and Y Sidi for providing reagents; M Oren for fruitful discussions and provision of reagents; the Department of Pediatric Hematology and Oncology, Dr von Haunersches Kinderspital, Munich, Germany, for providing clinical samples; members of SI and AB laboratories for helpful discussions and, in particular, P Landgraf for his excellent criticism and advice. SI, NG, VB and AB designed experiments. NG, VB, YL, MM, OW, MZ, JT, LE, NS, AN designed and performed experiments. LH analyzed data. NG, VB, AB, SI wrote the paper. This work was supported by National Institute of Health R01 CA120772-01A2 (SI), German Israeli Foundation (SI & AB), The Wolfson Foundation (SI, NS), Israel Science Foundation Morasha (SI), Children with Leukaemia UK (SI), Leukemia Research Fund UK (OW and MM), Curtis Katz (SI), MSM0021620813 and MZO00064203 (JT and MZ), Jewish National Fund, UK (SI), Claudine Galli Foundation (NG), Converging Technologies program (LH), Elterninitiative Kinderkrebsklinik Duesseldorf (AB). The study has been performed as partial fulfillment of the requirements for PhD degree of Nir Gefen and Libi Hertzberg, Sackler School of Medicine, Tel Aviv University.

References

1 Heerema NA, Sather HN, Sensel MG, Zhang T, Hutchinson RJ, Nachman JB *et al.* Prognostic impact of trisomies of chromosomes 10, 17, and 5 among children with acute lymphoblastic leukemia and high hyperdiploidy (>50 chromosomes). *J Clin Oncol* 2000; **18**: 1876–1887.
2 Moorman AV, Richards SM, Martineau M, Cheung KL, Robinson HM, Jalali GR *et al.* Outcome heterogeneity in childhood high-hyperdiploid acute lymphoblastic leukemia. *Blood* 2003; **102**: 2756–2762.
3 Hasle H. Pattern of malignant disorders in individuals with Down's syndrome. *Lancet Oncol* 2001; **2**: 429–436.
4 Strefford JC, van Delft FW, Robinson HM, Worley H, Yiannikouris O, Selzer R *et al.* Complex genomic alterations and gene expression in acute lymphoblastic leukemia with intrachromosomal amplification of chromosome 21. *Proc Natl Acad Sci USA* 2006; **103**: 8167–8172.
5 Pui CH, Relling MV, Downing JR. Acute lymphoblastic leukemia. *N Engl J Med* 2004; **350**: 1535–1548.
6 Romana SP, Mauchauffe M, Le Coniat M, Chumakov I, Le Paslier D, Berger R *et al.* The t(12;21) of acute lymphoblastic leukemia results in a tel-AML1 gene fusion. *Blood* 1995; **85**: 3662–3670.
7 Greaves MF, Wiemels J. Origins of chromosome translocations in childhood leukaemia. *Nat Rev Cancer* 2003; **3**: 639–649.
8 Hong D, Gupta R, Ancliff P, Atzberger A, Brown J, Soneji S *et al.* Initiating and cancer-propagating cells in TEL-AML1-associated childhood leukemia. *Science* 2008; **319**: 336–339.
9 Ambros V. The functions of animal microRNAs. *Nature* 2004; **431**: 350–355.
10 Lee YS, Kim HK, Chung S, Kim KS, Dutta A. Depletion of human micro-RNA miR-125b reveals that it is critical for the proliferation of differentiated cells but not for the down-regulation of putative targets during differentiation. *J Biol Chem* 2005; **280**: 16635–16641.
11 Iorio MV, Ferracin M, Liu CG, Veronese A, Spizzo R, Sabbioni S *et al.* MicroRNA gene expression deregulation in human breast cancer. *Cancer Res* 2005; **65**: 7065–7070.
12 Xia HF, He TZ, Liu CM, Cui Y, Song PP, Jin XH *et al.* MiR-125b expression affects the proliferation and apoptosis of human glioma cells by targeting Bmf. *Cell Physiol Biochem* 2009; **23**: 347–358.
13 Sonoki T, Iwanaga E, Mitsuya H, Asou N. Insertion of microRNA-125b-1, a human homologue of lin-4, into a rearranged immunoglobulin heavy chain gene locus in a patient with precursor B-cell acute lymphoblastic leukemia. *Leukemia* 2005; **19**: 2009–2010.
14 Bousquet M, Quelen C, Rosati R, Mansat-De Mas V, La Starza R, Bastard C *et al.* Myeloid cell differentiation arrest by miR-125b-1 in myelodysplastic syndrome and acute myeloid leukemia with the t(2;11)(p21;q23) translocation. *J Exp Med* 2008; **205**: 2499–2506.
15 Le MT, Teh C, Shyh-Chang N, Xie H, Zhou B, Korzh V *et al.* MicroRNA-125b is a novel negative regulator of p53. *Genes Dev* 2009; **23**: 862–876.
16 Metzler M, Wilda M, Busch K, Viehmann S, Borkhardt A. High expression of precursor microRNA-155/BIC RNA in children with Burkitt lymphoma. *Genes Chromosomes Cancer* 2004; **39**: 167–169.
17 van den Berg A, Kroesen BJ, Kooistra K, de Jong D, Briggs J, Blokzijl T *et al.* High expression of B-cell receptor inducible gene BIC in all subtypes of Hodgkin lymphoma. *Genes Chromosomes Cancer* 2003; **37**: 20–28.
18 Eis PS, Tam W, Sun L, Chadburn A, Li Z, Gomez MF *et al.* Accumulation of miR-155 and BIC RNA in human B cell lymphomas. *Proc Natl Acad Sci USA* 2005; **102**: 3627–3632.

19 Kluiver J, Poppema S, de Jong D, Blokzijl T, Harms G, Jacobs S *et al.* BIC and miR-155 are highly expressed in Hodgkin, primary mediastinal and diffuse large B cell lymphomas. *J Pathol* 2005; **207**: 243–249.
20 Costinean S, Zanesi N, Pekarsky Y, Tili E, Volinia S, Heerema N *et al.* Pre-B cell proliferation and lymphoblastic leukemia/high-grade lymphoma in E(mu)-miR155 transgenic mice. *Proc Natl Acad Sci USA* 2006; **103**: 7024–7029.
21 Hebert SS, De Strooper B. Alterations of the microRNA network cause neurodegenerative disease. *Trends Neurosci* 2009; **32**: 199–206.
22 Hertzberg L, Betts DR, Raimondi SC, Schafer BW, Notterman DA, Domany E *et al.* Prediction of chromosomal aneuploidy from gene expression data. *Genes Chromosomes Cancer* 2007; **46**: 75–86.
23 Morrow M, Horton S, Kioussis D, Brady HJ, Williams O. TEL-AML1 promotes development of specific hematopoietic lineages consistent with pre-leukemic activity. *Blood* 2004; **103**: 3890–3896.
24 Starkova J, Madzo J, Cario G, Kalina T, Ford A, Zaliova M *et al.* The identification of (ETV6)/RUNX1-regulated genes in lymphopoiesis using histone deacetylase inhibitors in ETV6/RUNX1-positive lymphoid leukemic cells. *Clin Cancer Res* 2007; **13**: 1726–1735.
25 Frohling S, Scholl C, Levine RL, Loriaux M, Boggon TJ, Bernard OA *et al.* Identification of driver and passenger mutations of FLT3 by high-throughput DNA sequence analysis and functional assessment of candidate alleles. *Cancer Cell* 2007; **12**: 501–513.
26 Scott GK, Goga A, Bhaumik D, Berger CE, Sullivan CS, Benz CC. Coordinate suppression of ERBB2 and ERBB3 by enforced expression of micro-RNA miR-125a or miR-125b. *J Biol Chem* 2007; **282**: 1479–1486.
27 Shi XB, Xue L, Yang J, Ma AH, Zhao J, Xu M *et al.* An androgen-regulated miRNA suppresses Bak1 expression and induces androgen-independent growth of prostate cancer cells. *Proc Natl Acad Sci USA* 2007; **104**: 19983–19988.
28 Klusmann J-H, Janikova K, Li Z, Orkin SH, Reinhardt D. Chromosome 21-encoded miR-125b and its role in the development of myeloid leukemia in children with Down's syndrome. ASH Annual Meeting Abstracts. 2007 November 16, 2007; **110**: 716.
29 Kuhn DE, Nuovo GJ, Martin MM, Malana GE, Pleister AP, Jiang J *et al.* Human chromosome 21-derived miRNAs are overexpressed in down syndrome brains and hearts. *Biochem Biophys Res Commun* 2008; **370**: 473–477.
30 Pui CH, Evans WE. Treatment of acute lymphoblastic leukemia. *N Engl J Med* 2006; **354**: 166–178.
31 Ford AM, Palmi C, Bueno C, Hong D, Cardus P, Knight D *et al.* The TEL-AML1 leukemia fusion gene dysregulates the TGF-beta pathway in early B lineage progenitor cells. *J Clin Invest* 2009; **119**: 826–836.
32 Sato T, Toki T, Kanezaki R, Xu G, Terui K, Kanegane H *et al.* Functional analysis of JAK3 mutations in transient myeloproliferative disorder and acute megakaryoblastic leukaemia accompanying Down syndrome. *Br J Haematol* 2008; **141**: 681–688.
33 Huntly BJ, Shigematsu H, Deguchi K, Lee BH, Mizuno S, Duclos N *et al.* MOZ-TIF2, but not BCR-ABL, confers properties of leukemic stem cells to committed murine hematopoietic progenitors. *Cancer Cell* 2004; **6**: 587–596.
34 Lacronique V, Boureux A, Monni R, Dumon S, Mauchauffe M, Mayeux P *et al.* Transforming properties of chimeric TEL-JAK proteins in Ba/F3 cells. *Blood* 2000; **95**: 2076–2083.
35 McCubrey JA, Steelman LS, Abrams SL, Bertrand FE, Ludwig DE, Basecke J *et al.* Targeting survival cascades induced by activation of Ras/Raf/MEK/ERK, PI3K/PTEN/Akt/mTOR and Jak/STAT pathways for effective leukemia therapy. *Leukemia* 2008; **22**: 708–722.
36 Ihle JN, Gilliland DG. Jak2: normal function and role in hematopoietic disorders. *Curr Opin Genet Dev* 2007; **17**: 8–14.
37 Liu CB, Itoh T, Arai K, Watanabe S. Constitutive activation of JAK2 confers murine interleukin-3-independent survival and proliferation of BA/F3 cells. *J Biol Chem* 1999; **274**: 6342–6349.
38 Bercovich D, Ganmore I, Scott LM, Wainreb G, Birger Y, Elimelech A *et al.* Mutations of JAK2 in acute lymphoblastic leukaemias associated with Down's syndrome. *Lancet* 2008; **372**: 1484–1492.
39 Hon LS, Zhang Z. The roles of binding site arrangement and combinatorial targeting in microRNA repression of gene expression. *Genome Biol* 2007; **8**: R166.
40 Baek D, Villen J, Shin C, Camargo FD, Gygi SP, Bartel DP. The impact of microRNAs on protein output. *Nature* 2008; **455**: 64–71.
41 Selbach M, Schwanhausser B, Thierfelder N, Fang Z, Khanin R, Rajewsky N. Widespread changes in protein synthesis induced by microRNAs. *Nature* 2008; **455**: 58–63.
42 Schindler JW, Van Buren D, Foudi A, Krejci O, Qin J, Orkin SH *et al.* TEL-AML1 corrupts hematopoietic stem cells to persist in the bone marrow and initiate leukemia. *Cell stem cell* 2009; **5**: 43–53.

Supplementary Information accompanies the paper on the Leukemia website (http://www.nature.com/leu)

A Novel mtDNA Large-Scale Mutation Clinically Exclusively Presenting With Refractory Anemia: Is There a Chance to Predict Disease Progression?

Vera Binder, MD, Laura Steenpass, PhD,* Hans-Juergen Laws, MD,* Jochen Ruebo, MD,† and Arndt Borkhardt, MD**

Summary: Because of the diversity of clinical symptoms, the diagnosis of mitochondrial DNA (mtDNA) deletion disorders can be difficult. Here, we describe an 8-month-old boy presenting clinically exclusively with refractory anemia. Mutation analysis in our patient revealed a large, novel deletion in his mtDNA encompassing ATPase 6, cytochrome oxidase subunit III, NADH dehydrogenase genes ND3 to ND6, and cytochrome b. Comparison with other cases from the literature showed that there is no genotype-phenotype correlation regarding hematologic features. It is not possible to predict whether our patient will develop additional features from Pearson syndrome or Kearns-Sayre syndrome, both syndromic mitochondrial disorders with hematological manifestations.

Key Words: Pearson syndrome, Kearns-Sayre syndrome, genotype-phenotype correlation, hematologic features

(*J Pediatr Hematol Oncol* 2012;34:283–292)

Mitochondrial disorders (MIDs) frequently manifest as a mono-organic problem but turn into multisystem disease in most of the cases. As a disorder of oxidative phosphorylation, MIDs might give rise to any symptom in any organ or tissue, including the central and peripheral nervous system, skeletal muscles, endocrine system, heart, eyes, ears, gastrointestinal tract, kidneys, dermis or the bone marrow, and thus the blood cells.[1,2] Syndromic MIDs with hematological manifestations, which are caused by large-scale deletions in mitochondrial DNA (mtDNA), are Pearson syndrome (PS) and Kearns-Sayre syndrome (KSS).

The PS is a rare, usually fatal mitochondrial disorder, first described in 1979[3] (MIM ID #557000), as a syndrome with refractory sideroblastic anemia with vacuolization of marrow precursors and exocrine pancreatic dysfunction. Most patients die before the age of 3 years. KSS (MIM ID #530000) is characterized by chronic, progressive external opthalmoplegia, pigmentary retinopathy, cardiac conduction defects, encephalomyopathy, endocrinopathies, and onset before 20 years of age.[4]

Received for publication March 15, 2011; accepted June 7, 2011.

From the *Department of Pediatric Oncology, Hematology and Clinical Immunology, Center for Child and Adolescent Health, Medical Faculty, Heinrich Heine University, Duesseldorf; and †St.-Antonius-Hospital Kleve, Clinic for Child and Adolescent Health and Neonatology, Kleve, Germany.

Disclosures: The authors have no conflicts of interest to disclose. Funding was partly provided by the Forschungskommission of the Medical Faculty of the Heinrich Heine University Duesseldorf and the Elterninitiative Kinderkrebsklinik e.V. Duesseldorf.

Reprints: Vera Binder, MD, Moorenstr. 5, 40225 Duesseldorf, Germany (e-mail: vera.binder@med.uni-duesseldorf.de).

Human mtDNA is a circular minichromosome of 16.5 kb; it is polyploid (up to several thousand mtDNA copies per cell[5]) and homoplasmic in healthy individuals (all mtDNA copies are identical). MtDNA displays its own genetic code[6] (*http://www.mitomap.org/MITOMAP/HumanMitoCode*,[7]) and is maternally inherited.[8] The propensity of mtDNA to mutate randomly results in the coexistence of wild-type mtDNA and mutant mtDNA in a single cell (heteroplasmy). Heteroplasmy is forwarded by the stochastic distribution of the mtDNA to daughter cells (mitotic segregation); hence, the level of heteroplasmy may vary between different cells, tissues, and individuals.[9] In general, the genotype-phenotype correlation in MIDs is poor, even for the same deletions in relatives.[10–16] Although it has been hypothesized that large-scale mtDNA deletions are the result of loop formation between direct repeat sequences (4 to 13 bp) during mtDNA replication in the developing oocyte,[17] the exact genomic mechanism of the deletion event is still unknown. Some nuclear gene defects predisposing to multiple deletions have been documented.[18,19] Here, we describe a patient presenting clinically exclusively with profound macrocytic anemia due to a large, novel mitochondrial deletion in his mtDNA. We put his hematologic and genetic features in context with all the case reports referenced in mitomap (*http://www.mitomap.org/bin/view.pl/MITOMAP/DeletionsSingle*[7]) to elicit potential genotype-phenotype correlations.

METHODS

Patient

The patient is the third child of healthy parents, originally from Russia, who moved to Germany 1 year before his birth. One elder brother also showed anemia in the newborn period, but treatment was not needed and a bone marrow aspirate was not performed. Pregnancy, delivery, and the first seven months of life ran normally; the patient received all recommended vaccinations, and besides vitamin D, no other medication was used. At the age of 8 months, he developed a cold with subfebrile temperatures. A notable pallor of skin and mucosa led to admission to the hospital and physical examination revealed mild tachycardia but only under excitement. Besides these symptoms, the physical examination was normal, without hepatosplenomegaly or lymphadenopathy. His growth curves showed deviation from percentile 90% (p90) down to p50 for weight and from p25 to p10 for head circumference (head circumference of the parents was not measured), but were stable along p50 for length. He showed normal psychomotor development, without any noticeable neurological problems.

Blood examination showed severe macrocytic anemia (hemoglobin 3.4 g/dL, MCV 101 fl, MCH 35.9 pg, MCHC 38.5 g/dL, normal levels of vitamin B12, and folic acid) with 6‰ reticuloytes. Normal leukocyte and thrombocyte levels indicated an isolated dysfunction in red blood cell production. The other biochemical parameters as electrolytes, renal retention parameters, liver enzymes, lipase, α-amylase, creatine kinase, lactate dehydrogenase, bilirubin, coagulation values, and iron metabolism were all within the normal range. Hemoglobin electrophoresis showed mild elevation of HbF (8.7%) with normal HbA and HbA2. Virus serology for Parvo B19, Epstein-Barr and cytomegalo virus was negative. Blood group serology was AB Rh positive, Kell positive with a negative direct Coombs test and negative antibody screening. The blood smear showed anisocytosis and poikylocytosis and some fragmentocytes, mild lymphocytosis, but no signs of malignancy. As the patient showed HHV-6 antibodies positive with 140 copies/g DNA, a transient erythroblastopenia was assumed and he received 2 times red blood cell transfusion until elevation of the hemoglobin to 8 g/dL. However, as the patient repeatedly showed transfusion-dependent anemia with hemoglobin going down to 6 g/dL with reticulocytopenia, a bone marrow puncture was performed at the age of 9 months. The bone marrrow aspirate showed a representative bone marrow with all maturation stages of hematopoiesis. Precursors of erythropoiesis and myelopoiesis showed characteristic vacuoles in the cytoplasm, which led to the diagnosis of the hematological manifestation of a mitochondriopathy (Fig. 1a). Iron staining showed no ringed sideroblasts. Further investigations revealed elevated alanine levels in blood (580 μmol/L, normal: 165 to 373 μmol/L) and an elevation of citric acid cycle intermediates in the urinary organic acid profile, both of which also suggested a mitochondriopathy.

Molecular Analysis

To confirm the diagnosis of a mitochondriopathy, molecular analysis of mtDNA of the patient and 2 healthy adult donors was performed, after informed consent was obtained. After preparation of total DNA from peripheral blood leukocytes using a DNA blood extraction kit (QIAamp DNA Blood Midi Kit, Qiagen, Hilden, Germany), amplification of mtDNA was performed by long-range polymerase chain reaction (PCR) as previously described[20] using a PCR long-range kit (Advantage Genomic LA Polymerase Mix, Clontech, Mountain View, CA). PCR primers were located at nucleotide (nt) positions 356 to 391 (F_CAAAAACAAAGAACCCTAACAC CAGCCTAACCAGAT) and 16018 to 15974 (R_ATTA GAATCTTAGCTTTGGGTGCTAATGGTGGAGT) of the mt genome, amplifying a 15662 DNA fragment, covering almost the whole mtDNA [16569 bp, GenBank: NC_012920.1 (2010)]. The initial melting step for 1 min at 94°C was followed by amplification for 28 cycles with denaturation at 94°C for 10 s and annealing and extension for 10 min at 68°C with a time extension of 15 s in the last 12 cycles.

We performed primer walking to further characterize the deletion site. With the following PCR primer set (P_F_new: aatctgttcgcttcattcattgcc, nt 8536-8559, P_R_new: ccccatcctccatatatccaaaca, nt 9698 to 9721), the fusion point was identified by DNA sequencing and subsequent alignment to the human mt reference genome [GenBank: NC_012920.1 (2010)].

Literature Review

We reviewed all the case reports referenced in mitomap (*http://www.mitomap.org/bin/view.pl/MITOMAP/DeletionsSingle*[7]) describing patients with large-scale deletions and analyzed the hematological features, other clinical features, type, size, and location of mtDNA mutation, and the level of heteroplasmy in different tissues (Table 1).

RESULTS

Detection of a Novel mtDNA Deletion With a Repetitive Motif at the Boundaries, Without Duplication or Deletion Dimerizations

As shown on the gel in Figure 1b, our patient had a mixture of deleted and healthy mtDNA and showed a deletion of approximately 6 kb. There are no bands running higher than the wtDNA band in the patient sample (lane 1), indicating that there is no duplication or deletion dimerization of his mtDNA. For analyzing his mtDNA in detail, we performed primer walking and detected a novel deletion of 5960 bp joining the nt at position 9100 (ATPase 6) to the nt at position 15061 (cytochrome b) of the reference human mtDNA. A repetitive motif of 5 nucleotides (ATCATC) was found at the boundaries of the deletion (Fig. 1c). The deletion joins the first nucleotide of the triplet encoding isoleucine 192 (ATC) from ATPase 6 to the A on position 3 of the triplet encoding for glycine 105 (GGA) from cytochrome b. This leads to a frameshift in the ATPase 6 protein, extending it for 18 amino acids after the breakpoint and terminating it at a TAG codon. No functional cytochrome b protein will be synthesized as its 5' part is deleted and the 3' part was fused to 3' truncated ATPase 6.

Hence, the deletion leads to an impaired function of ATPase 6 and cytochrome b and to a loss of cytochrome oxidase subunit III gene (COIII), a subunit of the cytochrome c oxidase (complex IV), and NADH dehydrogenase genes ND3 to ND6 (*http://mitowheel.org/mitowheel.html*,[33] *http://www.mitomap.org/MITOMAP*,[7] Fig. 2).

Literature Review

A review of the literature shows that PS and KSS could be associated with almost identical hematological features: with either isolated normocytic or macrocytic aplastic anemia and with or without sideroblasts in the bone marrow. The development of an additional thrombocytopenia or neutropenia, or even with panytopenia, may occur (Table 1). Bone marrow biopsy at the early stages in PS was described to be characterized by normal cellularity with vacuolization of precursor cells,[34,35] even from the neonatal period onward.[29]

Vacuolization of the hematopoietic precursor cells and ringed sideroblasts, previously described as distinctive for PS, were also present in patients, who presented with isolated hematopoietic symptoms in the beginning and who later developed KSS.[25,26] Bone marrow aspiration may show reduced to normal cell numbers, vacuolated erythroblasts, myeloblasts, megakayryoblasts, and ringed sideroblasts[22,34] at any stage in both syndromes.

Elevations of fetal hemoglobin (HbF) levels have also been observed in both syndromes, in PS[3,12,31] and in KSS,[11] where it was associated with a positive erythocyte i-antigen.[11] Elevation of the erythrocyte adenosine deaminase was also detected in one patient[12] as it is usually observed in Diamond-Blackfan anemia (Table 1).

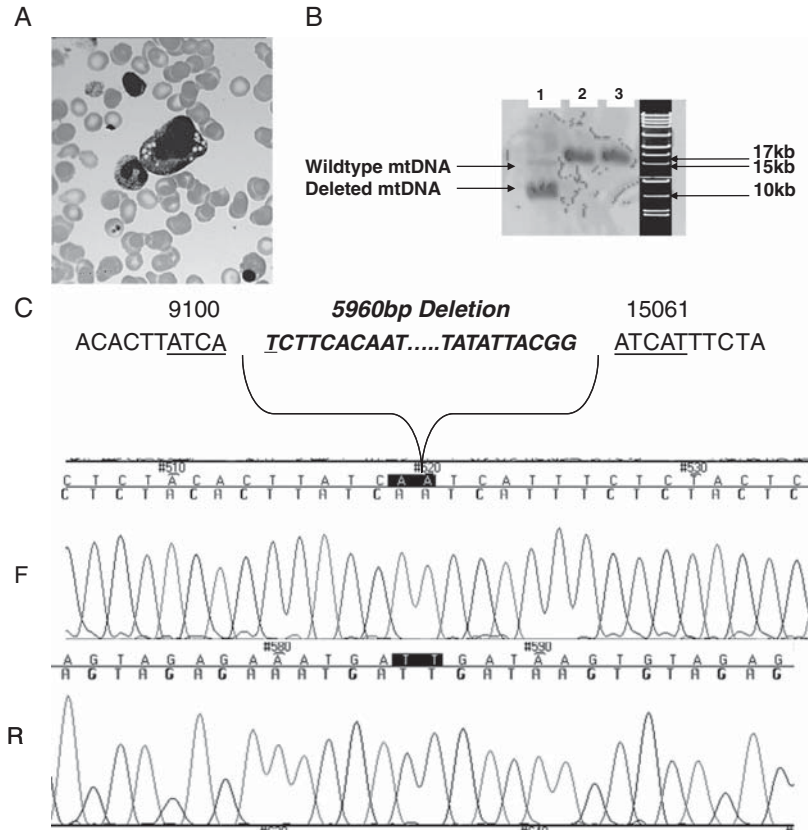

FIGURE 1. A, Bone marrow aspirate of our patient at the age of 9 months showing vacuolization of a proerythroblast. B, Agarose gel (0.8%) showing heteroplasmy of wt and deleted mtDNA of our patient (lane 1) in comparison with 2 healthy controls (lane 2 and 3). There are no bands running higher than the wtDNA band in the patient sample, indicating that there is no duplication or deletion dimerization of his mtDNA. C, Chromatogram of the DNA sequencing of the deletion site, fusing nt 9100 to nt 15061. F = sequenced with the forward primer, R = sequenced with the reverse primer. Underlined is the repetitive sequence at the boundaries of the 5960 bp deletion. The nucleotides that are lost due to the deletion are shown in bold letters.

There is no typical mtDNA region that has to be deleted to cause mainly hematologic features in the beginning of the disease, besides the short arc (nt 0 to 5511), which is not affected by mutations causing hematopoietic symptoms. Mutations between nt 5892 and nt 15576 were described causing hematologic features, with a wide size range and different times of occurrence. Single-point mutations in a subunit of the cytochrome c oxidase were described to cause sideroblastic anemia with no other features of a mitochondropathia,[24] most probably as a result of these point mutations being acquired in a self-renewing bone marrow stem cell. However as described for PS and KSS, congenital large scale mtDNA deletions (up to 7.6 kb[26]), also cause sideroblastic anemia. In contrast, even larger congenital deletions were described (up to 8.4 kb),[32] which were not associated with any hematological features (Fig. 2). The identification of 2 point mutations with very similar locations suggests that cytochrome c oxidase may play an important role in the pathogenesis of sideroblastic anemia and may be the physiologic site of iron reduction and transport through the inner mitochondrial membrane.[24] However, there were also literature reports from patients with sideroblastic anemia, in whom the cytochrome c oxidase was not included in the large-scale deletions[22,36] (Fig. 2).

The most common deletion, which was predescribed to cause phenotypically either PS or KSS, was variably associated with the complete absence of hematological features,[23] with pancytopenia, which spontaneously remitted at the age of 2 years,[28] and even with very early onset anemia at the age of 8 days[29] (Table 1).

High heteroplasmy levels (67% to 77%,[11,31,37]) in hematopoietic cells were associated with the classical hematologic features of PS. However, there were also cases described where 50% to 75% of heteroplasmy was not associated to any hematological features,[21,23] whereas only 16.5% of heteroplasmy was associated with mild hematologic features in others.[38]

DISCUSSION

Hematologic disorders are often the initial symptoms in KSS and PS[25,26,38] and are found in 1 out of 3 neonates with large-scale deletion syndromes of mtDNA.[39] As the metabolic disorders may present very mildly and may not be clinically observable as in our patient and others described before,[22] it is essential to consider mitochondriopathies in infants who present with persistent hematologic disorders. These may vary from normocytic or macrocytic anemia to pancytopenia.

As there is no strict correlation of heteroplasmy in blood cells to the severity of hematopoietic features,[21,23,38] the level of heteroplasmy was not determined in our

TABLE 1. Clinical and Molecular Genetic Findings in Patients with mtDNA Mutations

Diagnosis/Literature	Hematological Features	Other Clinical Features	mtDNA Mutation/Heteroplasmy
PS + KSS[16]	Until the age of 24 mo: Macrocytic anemia Neutropenia	Until the age of 8 y: Gradual development of encephalomyopathy (no exocrine pancreatic insufficiency, normal serum amino acids and urine organic acids)	Deletion (4.4 kb, nt 10,560-14,980, flanking repeats N/A) Heteroplasmy (8 y): blood 21%, hair follicles 38%, muscle 55%, buccal cells 57%
PS[37]	From the neonatal period on: Normocytic, sideroblastic anemia Neutropenia Vacuolization of granulocytic, monocytic, erythrocytic precursors, and megakaryocytes	At the age of 10 mo: Insulin-dependent diabetes mellitus (no clinical or biochemical evidence of exocrine pancreatic, liver or renal insufficiency)	No information on exact size and localization of the deletion Heteroplasmy (20 wk): bone marrow cells 77% (64% deleted and 13% duplicated)
PS[22]	With 5 mo: Severe macrocytic, sideroblastic anemia Recurrent neutropenia Thrombocytopenia Vacuolated hematopoietic precursors	Recurrent lactic acidemia Moderately increased pyruvate Elevated alanine concentrations in blood Abnormal urinary organic acid profile (no exocrine pancreas insufficiency)	Deletion (4.2 kb, nt 10,371-14,607, flanking repeats N/A) In DNA from blood cells Heteroplasmy N/A
PS + KSS[23]	No hematological features	Since the age of 3 y: Failure to thrive With 6 y Progressive hearing loss Visual impairment With 10 y: Insulin dependent diabetes mellitus Horizontal nystagmus Sensory deafness Pigmentary retinopathy Muscle atrophy Growth hormone deficiency With 14 y: Elevated levels of serum pyruvate and lactate Until the age of 21: Diffuse brain atrophy Elevated CSF protein and CSF lactate Red ragged fibers Ptosis, eye movement disturbance (no evidence for exocrine pancreatic insufficiency or hepatic dysfunction)	Deletion (4.9 kb, nt 8,482-13,460, common deletion, no duplication, flanking repeats 13 bp) Heteroplasmy (with 15, 16, and 21 y): muscle˜93%, blood˜50%
KSS[38]	With 2.5 y: Normocytic anemia 6 mo later: Pancytopenia Bone marrow: normal marrow precursors, cellularitiy less than 5%, no ringed sideroblasts During follow-up: Mild anemia	With 4 y: Hypoparathyroidism With 7 y: Short stature, partial growth hormone deficiency With 10 y: Proximal renal tubular dysfunction Ptosis Bilateral high-tone sensorineural deafness Gradual neurologivcal deterioration Metabolic acidosis Lactate peaks in brainstem, basal ganglia, lateral ventricles and frontal lobe Ragged red fibers No retinal or cardiac abnormalities, No pancreatic insufficiency	Deletion 4 kb, no information on exact localization or flanking repeats Heteroplasmy: peripheral blood 16.5%

TABLE 1. (*continued*)

AISA[24]	Patient 1 (50 y): Macrocytic anemia Ringed sideroblasts Patient 2 (50 y): Normal-microcytic anemia Ringed sideroblasts		Two distinct heteroplasmic point mutations (T6721C/T-C/M273T and T6742C/T-C/I280T) in cytochrome c oxidase In DNA from bone marrow, whole blood, isolated platelets, granulocytes, not in T and B lymphocytes, buccal cells, cultured skin fibroblasts
KSS[21]	No hematological features	With 1.5 y: Growth delay Delayed speech development With 6 y: Progressive hearing loss Learning deficit With 9 y: Mild ptosis, ophthalmoplegia Moderate retinal pigmentary degeneration General muscle weakness Ataxia Intention tremor	Deletion (7.4 kb, nt 7,194-14,595, no direct repeats) Heteroplasmy: peripheral blood 75%
PS[12]	From the neonatal period on: Hypoplastic anemia With 4 and 5 mo: Bone marrow: general hypocellularity with marked erythroblastopenia With 9 mo: Bone marrow: vacuolized hematopoietic precursors and sideroblasts With 15 mo: Macrocytic anemia Elevated HbF (30%) Elevated erythrocyte adenosine deaminase activity	From the neonatal period on: Failure to thrive Muscular hypotonia With 12 mo: Diabetes mellitus With 15 mo: Severe dystrophy Chronic diarrhea Severe progressive osteoporosis Renal Fanconi syndrome Lactic acidosis Complex organic aciduria Patient died with 19 mo due to severe metabolic acidosis	Deletion (6.3 kb, nt 9,238-15,576, flanking repeats 5 bp) half of the shortened mtDNA as circular dimers (20 kb). In DNA from the liver, kidney, muscle, and bone marrow Heteroplasmy, N/A
KSS[25]	With 3-7 mo: Sideroblastic anemia	With 2 y: Short stature With 7 y: Ptosis, external ophthalmoplegia, retinopathy Mild general wakness Gait ataxia Sensor-neural hearing loss No cardiac dysfunctions Patient died within 8 y due to severe metabolic acidosis	Deletion (7.7 kb, nt 7,669-15,437 bp, flanking repeats 8 bp) Heteroplasmy (post-mortem): lymphocytes 31%, muscle 74%, brain 69%, heart 24%, testis 69%, diaphragm 73%, liver 86%, kidney 65%
KSS[26]	With 6 mo: Macrocytic sideroblastic anemia Vacuolization of myeloid precursors cells, with normal degree of maturation and distribution With 2 y: Recovery from anemia Leukopenia Thromocytopenia With 4 y: Leukocyte counts normal Thrombocyte count slightly subnormal Vacuolization of megakaryocytes	With 8 y: Gait ataxia With 9 y: Retinal pigmentary degeneration, ptosis Ataxia, intention tremor With 13 y: Sensorineural hearing loss With 14 y: Atrio-ventricular block type III With 18 y Spasticity lower extremities Increased peripheral reflexes	Deletion (7.6 kb, between nt 6.204 and 14.148, flanking repeats N/A), Heteroplasmy: muscle 82%
Mitochondropathia[27]	With 3 mo: Severe anemia Reticulocytopenia Neutropenia Thrombocytopenia	From the neonatal period on: Metabolic acidosis High blood lactate Abnormal redox status in plasma	Deletion (no exact information on length, between nt 10,766 and 14,148, flanking repeats N/A) In DNA from lymphocytes Heteroplsamy N/A

TABLE 1. (*continued*)

	Bone marrow: normal cellularity, vacuolization and defective maturation of erythroid and myeloid precursors		
KSS[28]	With 2 y: Fe-refractory anemia Neutropenia Thrombocytopenia The pancytopenia remitted spontaneously	With 4 y Pancreas echo-dense in ultrasound With 7 y: Bilateral ptosis, atypical retinitis pigmentosa Lactate acidosis Muscular hypotonia Ataxia Increased protein in CSF	Common deletion (4.9 bp, nt 8,483-13,459, flanking repeats 13 bp) In DNA from leukocytes Heteroplasmy N/A
PS + KSS[29]	With 8 d: Hypoplastic anemia Bone marrow: sideroblasts, vacuolization of early and late myeloids and early lymphoids With 8 y: Macrocytic anemia Mild thrombocytosis (normal leukocytes)	With 1 y: Diarrhea Failure to thrive Pancreatic exocrine insufficiency With 2.5 y Hepatic dysfunction, mild fibrosis With 4 y: Fanconi renal tubular acidosis With 5 y: Visual impairment, bilateral ptosis, external ophthalmoplegia, pigmentary retinopathy Tremor Ataxia, Proximal muscle weakness CSF lactate and protein elevated Red ragged fibers	Common deletion (4.9 kb, nt 8,483-13459, flanking repeats 13 bp) Heteroplasmy (8 y): blood 63%, muscle 95%
PS + KSS[30]	Patient 1 (17 y) With 16 d: Anemia With 2 mo: Neutropenia With 6 mo: Thrombocytopenia Bone marrow: hypocellularity and vacuolated precursosrs With 7mo: No hematological features Patient 2 (5 y) With 3d: Anemia With 4 mo Bone marrow: vacuolization of hematopoietic precursors With 3 y No anemia Mild leukocytopenia Thrombocytopenia Patient 3 From the neonatal period on: Pancytopenia Bone marrow: ringed sideroblasts, vacuolated hematopoietic precursors	Patient 1 With 1 y: Hypoglycemia Walking difficulties No exocrine pancreas insufficiency With 9 y Retinitis pigmentosa With 16 y Left bundle branch block Patient 2 (5 y) With 3d: Metabolic acidosis Hypoglycemia Hyperkalaemia With 4 mo: Exocrine pancreatic dysfunction Patient 3 Severe metabolic acidosis Fatty deposits in stool Patient died with 14 days due to severe metabolic acidosis	Deletion (patient 1: 3.6 kb, nt 9,337-12,974, flanking repeats N/A, patient 2: 3.1 kb, nt 12,203-15,355, flanking repeats N/A, patient 3: 4.9 kb, nt 10,559-15,548, flanking repeats N/A) Heteroplasmy: peripheral blood and bone marrow cells: patient 1: 28%, patient 2: 63%, patient 3: 76% (in peripheral blood, patients with a higher proportion of deleted mitochondrial DNA had lower blood cell counts. In patient 2, the percentage of mutant mitochondrial DNA in bone marrow cells decreased as anaemia improved (from 99% to 80%))
PS + KSS[31]	With 6 mo: Anemia with megaloblasts Thrombocytopenia With 3.5 y Still megaloblastic anemia Bone marrow: normocellular pattern	With 2 y Left esotropia With 3.5 y Metabolic encephalopathy Mild intellectual delay Generalized weakness Decreased reflexes Impaired coordination Elevated blood lactate	Deletion (2.4 kb, nt 5,892-8,278, flanking repeats 10-12 bp) Heteroplasmy: liver 87%, muscle 75%, leukocytes 67%

TABLE 1. (*continued*)

		Patient died with 4 y due to sepsis and metabolic encephalopathy	
PS + KSS[11]	From the neonatal period on: Macrocytic anemia Low reticulocytes Granulocytopenia Thrombocytosis Bone marrow: hypoplastic, ringed sideroblasts, vacuolization of myeloid precursosrs With 7.5 mo Signs of bone marrow recovery With 20 mo Macrocytis anemia Positive erythrocyte i-antigen Elevated HbF Bone marrow: normocellular with vacuolization of nonerythroid precursors With 34 mo Nearly normal blood counts	From the neonatal period on: Failure to thrive With 10 mo: Diabetes mellitus With 17 mo Polyuria Metabolic acidosis Hypophosphatemia Hypocalcemia Hypomagnesemia Hyponatremia Hypokalemia Glucosuria Aminoaciduria With 20 mo Delayed motor development Cerebral atrophy Blood lactate + pyruvate elevated CSF lactate and protein elevated Exocrine pancreas insufficiency Renal tubular dysfunction	Deletion (~5.7 kb, between nt 8300 and 14,300, flanking repeats, N/A) Heteroplasmy: muscle 80%, leukocytes 75%, fibroblasts 35%
KSS[32]	No hematological features	Four patients with classical symptoms of KSS (17 y, 40 y, 30 y, 19 y) Patient 1 (17 y) With 3 y: Short stature With 10 y: Ptosis, limitation of eye movements, chorioretinal atrophy, constriction of visual field Perceptual deafness Myogenic pattern in electromyography Ragged-red fibers With 14 y: Diabetes mellitus Patient 2 (40 y) With 3 y: Chronic progressive external ophthalmoplegia and ptosis, chorioretinal atrophy Perceptual deafness Ragged-red fibers Patient 3 (30 y) With 19 y: Bilateral ptosis, limitations of ocular movement With 20 y: Muscle weakness Night blindness Chorioretinal atrophy With 21 y: Myogenic pattern in electromyography Ragged-red fibers With 24 y: Cardiac conduction block With 26 y: Tremor and ataxia Patient 4 (19 y) With 8 y: Short stature With 11 y: Reduction of visual acuity, chorioretinal atrophy With 13 y: Ptosis, limitation of eye movement Slurred speech	Deletion (patient 1: 8.4 kb, nt 6,023-14,423, patient 2: 7.2 kb, nt 6,226-13,447 (flanking repeats 9 bp), patient 3: 4.7 kb, nt 9,144-13,808 (flanking repeats 8 bp), patient 4: no abnormal fragments were amplified from mtDNA) In DNA from platelets Heteroplasmy N/A

TABLE 1. (*continued*)

	Cerebellar ataxia
	Ragged-red fibers
With 15 y:	
	Complete right bundle branch block
With 16 y:	
	Perceptual deafness
With 18 y:	
	Diabetes mellitus

PS and KSS cases and other mitochondriopathies, reported in the literature, were reviewed and analyzed regarding the hematological features, other clinical features, type, size and location of mtDNA mutation, and the level of heteroplasmy in different tissues.

AISA indicates acquired idiopathic sideroblastic anemia; bp, base pair; CSF, cerebrospinal fluid; kb, kilobases; KSS, Kearns-Sayre syndrome; N/A, not performed or not annotated; nt, nucleotide; PS, Pearson syndrome.

patient. The exact mechanism of how deleted mtDNA molecules spread to the whole body or how they are limited to specific cells or tissues and why some patients recover from the hematological features and others die of iron refractory anemia at the age 2 or 3 is not completely deciphered yet.

It was claimed that children with PS that have a mild phenotype, or are supported through bone marrow failure, often develop the encephalomyopathic features of KSS.[25,26,28,29,40] However, as it was shown, there are many cases in the literature describing patients showing symptoms of both syndromes throughout life [11,16,29,31,40] (Table 1). The length and location of deletion are highly variable in both syndromes, ranging in size from 1.1 to 14 kb mainly between tRNACyst and the D-loop.[39,41] As both syndromes could be caused by the same mutation, it seems to be obvious that PS and KSS are not 2 distinct entities but phenotypic differences of a common genetic background. These different phenotypic expressions of the same mtDNA mutations may be due to nuclear modifier genes, environmental factors, and polymorphisms.[42,43]

Yamashita et al,[41] who screened mainly muscle specimens from 136 Japanese patients with single large-scale deletions of their mtDNA, observed that the length of

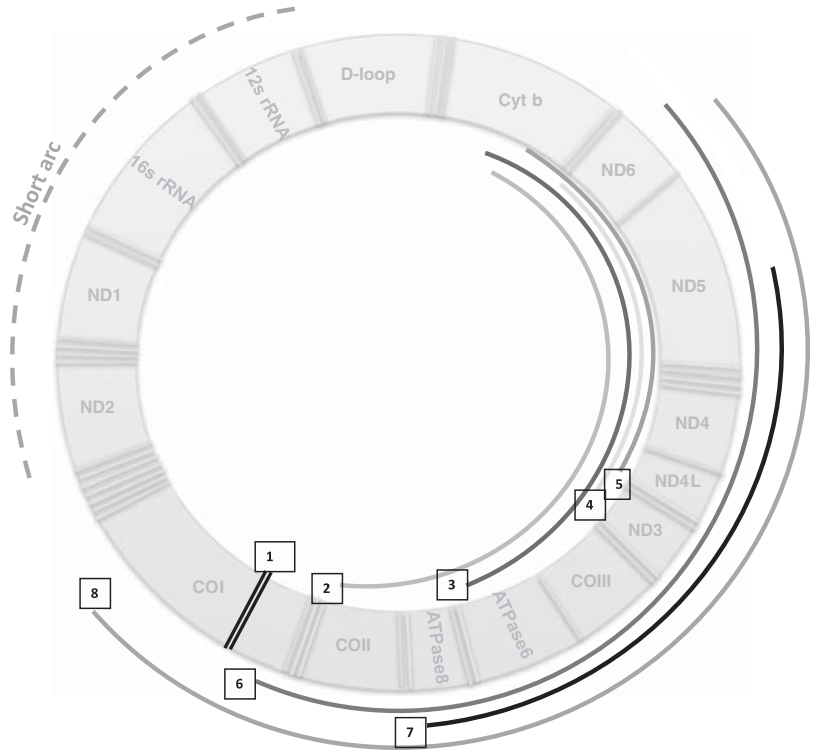

FIGURE 2. Schematic representation of mtDNA (modified from http://www.mitomap.org/pub/MITOMAP/MitomapFigures/mitomapgenome.pdf[7]) with size and location of different mtDNA deletions, associated with Pearson syndrome (PS) and Kearns-Sayre syndrome (KSS) and with or without hematologic features. (1) Two single-point mutations > acquired idiopathic sideroblastic anemia.[24] (2) Deletion from nt 7669 to 15437 > sideroblastic anemia (KSS).[25] **(3) Deletion from nt 9100 to 15061 > macrocytic anemia (patient of this study).** (4) Deletion from nt 10371 to 14607 > macrocytic anemia (PS).[22] (5) Deletion from nt 10560 to 14980 > macrocytic anemia (PS+KSS).[16] (6) Deletion from nt 7194 to 14595 > no hematologic phenotype (KSS).[21] (7) Deletion from nt 8469 to 13447>different or no hematologic phenotypes (common deletion in PS and KSS, Table 1). (8) Deletion from nt 6023 to 14423 > no hematologic phenotype (KSS).[32]

deletion and the number of deleted tRNAs showed a significant relationship with age at onset. Patients with deletions, including COX (cytochrome c oxidase) or ATPase subunits, showed earlier onset than those patients with the deletion limited to the region of ND and/or CYB subunits. This would fit our patient, whose deletion includes COIII and ATPase 6 and who presented with early onset of the disease. However, there were also patients described where the deletion started behind the COX genes (nt > 9990), also showing early onset of the disease and even death in early infancy[16,22,27,30] (Table 1).

After analyzing the clinical features of all reports regarding mtDNA deletions, no correlation could be found regarding the appearance of hematologic manifestations; this is besides the observation that there was no mutation described on the short arc of mtDNA, which was associated with hematologic features. Sideroblastic anemia was shown to be caused by single-point mutations up to large-scale deletions, affecting different parts of mtDNA.

In conclusion, we show that PS and KSS are associated with the same hematological features and that they are 2 syndromes with different phenotypes from the same genotype, which can change throughout life. There is no correlation to the size or location of deletion or the extent of heteroplasmy in blood cells. Therefore, it is not possible to give our patient, who presented with mainly hematologic features of an MID, a precise prognosis on how the disease will evolve. Treatment will be symptomatic, with red cell transfusions, alkalizing medications, reduction of further oxidative stress, and carbohydrate restriction.

As nuclear genes are probably responsible for different phenotypic expressions of the same mtDNA deletion, further large-scale genetic studies have to be performed.

REFERENCES

1. Zeviani M, Di Donato S. Mitochondrial disorders. *Brain*. 2004;127: 2153–272.
2. Munnich A, Rustin P. Clinical spectrum and diagnosis of mitochondrial disorders. *Am J Med Genet*. 2001;106:4–17.
3. Pearson HA, Lobel JS, Kocoshis SA, et al. A new syndrome of refractory sideroblastic anemia with vacuolization of marrow precursors and exocrine pancreatic dysfunction. *J Pediatr*. 1979;95:976–984.
4. Kearns TP, Sayre GP. Retinitis pigmentosa, external ophthalmophegia, and complete heart block: unusual syndrome with histologic study in one of two cases. *AMA Arch Ophthalmol*. 1958;60:280–289.
5. Robin ED, Wong R. Mitochondrial DNA molecules and virtual number of mitochondria per cell in mammalian cells. *J Cell Physiol*. 1988;136:507–513.
6. Barrell BG, Bankier AT, Drouin J. A different genetic code in human mitochondria. *Nature*. 1979;282:189–194.
7. MITOMAP: A Human Mitochondrial Genome Database. http://www.mitomap.org. Updated 2011.
8. Giles RE, Blanc H, Cann HM, et al. Maternal inheritance of human mitochondrial DNA. *Proc Natl Acad Sci U S A*. 1980;77:6715–6719.
9. Schapira AH. Primary and secondary defects of the mitochondrial respiratory chain. *J Inherit Metab Dis*. 2002;25:207–214.
10. Leonard JV, Schapira AH. Mitochondrial respiratory chain disorders I: mitochondrial DNA defects. *Lancet*. 2000;355:299–304.
11. Majander A, Suomalainen A, Vettenranta K, et al. Congenital hypoplastic anemia, diabetes, and severe renal tubular dysfunction associated with a mitochondrial DNA deletion. *Pediatr Res*. 1991;30:327–330.
12. Superti-Furga A, Schoenle E, Tuchschmid P, et al. Pearson bone marrow-pancreas syndrome with insulin-dependent diabetes, progressive renal tubulopathy, organic aciduria and elevated fetal haemoglobin caused by deletion and duplication of mitochondrial DNA. *Eur J Pediatr*. 1993;152:44–50.
13. Krauch G, Wilichowski E, Schmidt KG, et al. Pearson marrow-pancreas syndrome with worsening cardiac function caused by pleiotropic rearrangement of mitochondrial DNA. *Am J Med Genet*. 2002;110:57–61.
14. Shanske S, Tang Y, Hirano M, et al. Identical mitochondrial DNA deletion in a woman with ocular myopathy and in her son with Pearson syndrome. *Am J Hum Genet*. 2002;71:679–683.
15. Casademont J, et al. Multiple deletions of mtDNA in two brothers with sideroblastic anemia and mitochondrial myopathy and in their asymptomatic mother. *Hum Mol Genet*. 1994;3:1945–1949.
16. Lacbawan F, Tifft CJ, Luban NL, et al. Clinical heterogeneity in mitochondrial DNA deletion disorders: a diagnostic challenge of Pearson syndrome. *Am J Med Genet*. 2000;95: 266–268.
17. Mita S, Rizzuto R, Moraes CT, et al. Recombination via flanking direct repeats is a major cause of large-scale deletions of human mitochondrial DNA. *Nucleic Acids Res*. 1990;18: 561–567.
18. Van Goethem G, Dermaut B, Lofgren A, et al. Mutation of POLG is associated with progressive external ophthalmoplegia characterized by mtDNA deletions. *Nat Genet*. 2001;28:211–212.
19. Spelbrink JN, Li FY, Tiranti V, et al. Human mitochondrial DNA deletions associated with mutations in the gene encoding Twinkle, a phage T7 gene 4-like protein localized in mitochondria. *Nat Genet*. 2001;28:223–231.
20. Kreuder J, Repp R, Borkhardt A, et al. Rapid detection of mitochondrial deletions by long-distance polymerase chain reaction. *Eur J Pediatr*. 1995;154:996.
21. Fischel-Ghodsian N, Bohlman MC, Prezant TR, et al. Deletion in blood mitochondrial DNA in Kearns-Sayre syndrome. *Pediatr Res*. 1992;31:557–560.
22. Knerr I, Metzler M, Niemeyer CM, et al. Hematologic features and clinical course of an infant with Pearson syndrome caused by a novel deletion of mitochondrial DNA. *J Pediatr Hematol Oncol*. 2003;25:948–951.
23. Mohri I, Taniike M, Fujimura H, et al. A case of Kearns-Sayre syndrome showing a constant proportion of deleted mitochondrial DNA in blood cells during 6 years of follow-up. *J Neurol Sci*. 1998;158:106–109.
24. Gattermann N, Retzlaff S, Wang YL, et al. Heteroplasmic point mutations of mitochondrial DNA affecting subunit I of cytochrome c oxidase in two patients with acquired idiopathic sideroblastic anemia. *Blood*. 1997;90:4961–4972.
25. Nelson I, Bonne G, Degoul F, et al. Kearns-Sayre syndrome with sideroblastic anemia: molecular investigations. *Neuropediatrics*. 1992;23:199–205.
26. Larsson NG, Holme E, Kristiansson B, et al. Progressive increase of the mutated mitochondrial DNA fraction in Kearns-Sayre syndrome. *Pediatr Res*. 1990;28:131–136.
27. Rotig A, Colonna M, Blanche S, et al. Deletion of blood mitochondrial DNA in pancytopenia. *Lancet*. 1988;2:567–568.
28. Simonsz HJ, Barlocher K, Rotig A. Kearns-Sayre's syndrome developing in a boy who survived Pearson's syndrome caused by mitochondrial DNA deletion. *Doc Ophthalmol*. 1992;82: 73–79.
29. McShane MA, Hammans SR, Sweeney M, et al. Pearson syndrome and mitochondrial encephalomyopathy in a patient with a deletion of mtDNA. *Am J Hum Genet*. 1991;48:39–42.
30. Muraki K, Nishimura S, Goto Y, et al. The association between haematological manifestation and mtDNA deletions in Pearson syndrome. *J Inherit Metab Dis*. 1997;20:697–703.
31. Akman CI, Sue CM, Shanske S, et al. Mitochondrial DNA deletion in a child with megaloblastic anemia and recurrent encephalopathy. *J Child Neurol*. 2004;19:258–261.
32. Ota Y, Tanaka M, Sato W, et al. Detection of platelet mitochondrial DNA deletions in Kearns-Sayre syndrome. *Invest Ophthalmol Vis Sci*. 1991;32:2667–2675.

33. Gábor Zsurka AC. MitoWheel 1.2, http://mitowheel.org/mitowheel.html. Updated on July 6th, 2008.
34. Morikawa Y, Matsuura N, Kakudo K, et al. Pearson's marrow/pancreas syndrome: a histological and genetic study. *Virchows Arch A Pathol Anat Histopathol*. 1993;423:227–231.
35. Schapira AH, Cock HR. Mitochondrial myopathies and encephalomyopathies. *Eur J Clin Invest*. 1999;29:886–898.
36. Muraki K, Sakura N, Ueda H, et al. Clinical implications of duplicated mtDNA in Pearson syndrome. *Am J Med Genet*. 2001;98:205–209.
37. Smith OP, Hann IM, Woodward CE, et al. Pearson's marrow/pancreas syndrome: haematological features associated with deletion and duplication of mitochondrial DNA. *Br J Haematol*. 1995;90:469–472.
38. Leung TF, Hui J, Shoubridge E, et al. Aplastic anaemia in association with Kearns-Sayre syndrome. *J Inherit Metab Dis*. 1999;22:86–87.
39. Manea EM, Leverger G, Bellmann F, et al. Pearson syndrome in the neonatal period: two case reports and review of the literature. *J Pediatr Hematol Oncol*. 2009;31:947–951.
40. Becher MW, Wills ML, Noll WW, et al. Kearns-Sayre syndrome with features of Pearson's marrow-pancreas syndrome and a novel 2905-base pair mitochondrial DNA deletion. *Hum Pathol*. 1999;30:577–581.
41. Yamashita S, Nishino I, Nonaka I, et al. Genotype and phenotype analyses in 136 patients with single large-scale mitochondrial DNA deletions. *J Hum Genet*. 2008;53:598–606.
42. Limongelli A, Schaefer J, Jackson S, et al. Variable penetrance of a familial progressive necrotising encephalopathy due to a novel tRNA(Ile) homoplasmic mutation in the mitochondrial genome. *J Med Genet*. 2004;41:342–349.
43. Bernes SM, Bacino C, Prezant TR, et al. Identical mitochondrial DNA deletion in mother with progressive external ophthalmoplegia and son with Pearson marrow-pancreas syndrome. *J Pediatr*. 1993;123:598–602.

METHODS

Human Mutation

OFFICIAL JOURNAL HGVS HUMAN GENOME VARIATION SOCIETY www.hgvs.org

A New Workflow for Whole-Genome Sequencing of Single Human Cells

Vera Binder,[1*†‡] Christoph Bartenhagen,[2‡] Vera Okpanyi,[1] Michael Gombert,[1] Birte Moehlendick,[3] Bianca Behrens,[3] Hans-Ulrich Klein,[2] Harald Rieder,[4] Pina Fanny Ida Krell,[1] Martin Dugas,[2] Nikolas Hendrik Stoecklein,[3*‡] and Arndt Borkhardt[1‡]

[1]*Department of Pediatric Oncology, Hematology and Clinical Immunology, Medical Faculty, University of Duesseldorf, Duesseldorf, Germany;* [2]*Institute of Medical Informatics, University of Muenster, Muenster, Germany;* [3]*Department of General, Visceral and Pediatric Surgery, Medical Faculty, University of Duesseldorf, Duesseldorf, Germany;* [4]*Institute of Human Genetics and Anthropology, University of Duesseldorf, Duesseldorf, Germany*

Communicated by Paolo Fortina

Received 20 December 2013; accepted revised manuscript 30 June 2014.
Published online 27 July 2014 in Wiley Online Library (www.wiley.com/humanmutation). DOI: 10.1002/humu.22625

ABSTRACT: Unbiased amplification of the whole-genome amplification (WGA) of single cells is crucial to study cancer evolution and genetic heterogeneity, but is challenging due to the high complexity of the human genome. Here, we present a new workflow combining an efficient adapter-linker PCR-based WGA method with second-generation sequencing. This approach allows comparison of single cells at base pair resolution. Amplification recovered up to 74% of the human genome. Copy-number variants and loss of heterozygosity detected in single cell genomes showed concordance of up to 99% to pooled genomic DNA. Allele frequencies of mutations could be determined accurately due to an allele dropout rate of only 2%, clearly demonstrating the low bias of our PCR-based WGA approach. Sequencing with paired-end reads allowed genome-wide analysis of structural variants. By direct comparison to other WGA methods, we further endorse its suitability to analyze genetic heterogeneity.

Hum Mutat 35:1260–1270, 2014.

KEY WORDS: whole-genome amplification; single cell; CNV; LOH; allele dropout rate

Introduction

The analysis of genetic heterogeneity among single cancer cells is key to understand cancer evolution and failure of systemic cancer therapy [Stoecklein and Klein, 2010; Anderson et al., 2011; Navin et al., 2011]. So far, genome-wide single cell approaches were limited by their low resolution [Klein et al., 1999; Stoecklein et al., 2002; Stoecklein et al., 2008]. With the advent of second-generation sequencing, the bias of whole-genome amplification (WGA) methods could be analyzed in a comprehensive manner, for example, high-resolution analysis with a coverage of up to 99% was achieved in single low-complexity genomes after WGA [Parkhomchuk et al., 2009; Rodrigue et al., 2009; Woyke et al., 2009, 2010; Chitsaz et al., 2011]. More recently, different methods for the challenging amplification of the complex human genome were proposed and characterized. Navin et al. (2011) described the first analysis of single human cells by next-generation sequencing. Although sequence coverage by their PCR-based WGA method was low (6% of human genome), it allowed them to comprehensively compare copy-number variations (CNVs) in these regions and study tumor evolution in single cells. Hou et al. (2012) showed a sufficient coverage of the human genome with a commercially available kit based on multiple displacement amplification (MDA). Zong et al. (2012) compared MDA with their multiple annealing and looping-based amplification cycles (MALBAC) method and showed that MALBAC provides a more reproducible and uniform amplification of up to 93% of the human genome. By utilizing the paired-end (PE) read approach, Voet et al. (2013) recently reported the ability to detect structural variations (SVs) after amplification of genomes of single human cells. MIDAS (microwell displacement amplification system), a strategy for conducting MDA reactions in very small reaction volumes, allowed the detection of single copy-number changes in human neurons at 1–2 Mb resolution [Gole et al., 2013]. Currently existing methods of WGA of single cells were recently comprehensively reviewed by Macaulay and Voet (2014) and commented on in a recent issue of *Nature Methods* [Blainey and Quake, 2014; Chi, 2014; Eberwine et al., 2014; Nawy, 2014].

Here, we used an adapter-linker PCR-based WGA method developed by Klein et al. (1999) and precharacterized by us [Stoecklein et al., 2008; Mohlendick et al., 2013], which is now commercialized as AMPLI1 WGA Kit by Silicon Biosystems (Bologna, Italy). We combined it with second-generation sequencing and analyzed extensively whether this approach leads to a sufficient and uniform amplification of the complex human genome and whether it enables us to discover genetic heterogeneity among individual leukemic cells at single base pair resolution.

To test the reproducibility of single cell sequencing, a permanent cell line with a defined, stable genomic alteration pattern was used.

Additional Supporting Information may be found in the online version of this article.

†Vera Binder's present address is Stem Cell Program and Division of Hematology/Oncology, Boston Children's Hospital, Harvard Stem Cell Institute, Harvard Medical School, Boston, Massachusetts

‡These authors contributed equally to this work.

*Correspondence to: Vera Binder E-mail: vbinder@enders.tch.harvard.edu; Nikolas Hendrik Stoecklein. E-mail: nikolas.stoecklein@uni-duesseldorf.de

Contract grant sponsors: German-Israeli Foundation (GIF); German Consortium for Translational Cancer Research (DKTK); German Childhood Cancer Research Foundation; DFG (STO464/2-2); Krebsstiftung NRW; Krebsgesellschaft NRW; Forschungskommission University Duesseldorf; Elterninitiative Kinderkrebsklinik e.V; COST Action EuGESMA; Carreras Foundation (project Leukemia Gene Atlas).

As pediatric leukemias were shown to present only a limited number of mutations and copy-number alterations [Mullighan et al., 2007; Lilljebjorn et al., 2010, 2011], we used the well-characterized REH cell line, resembling a pediatric ETV6/RUNX1 positive precursor B cell leukemia. By comparing single cell sequencing results with data obtained from sequencing-pooled genomic DNA (gDNA) without preamplification, we assessed the allele dropout (ADO) rate introduced by our amplification method and were able to analyze the accuracy of our method to identify CNVs, loss of heterozygosity (LOH), and allele frequencies of mutations. Applying PE read sequencing to the amplified single cell genomes allowed us to detect breakpoints and delineate SVs such as translocations, inversions, deletions, insertions, and tandem duplications.

Material and Methods

WGA

REH cells were cultured under standard conditions (ATCC no. CRL-8286, http://www.atcc.org) and three individual cells were isolated under optical control using a 1-μl pipette. Cells were transferred into a PCR reaction tube containing 2 μl of lysis buffer (10 mmol/l Tris–acetate, pH 7.5, 10 mmol/l Mg–acetate, 50 mmol/l K–acetate, 0.67% Tween 20 (Sigma, Deisenhofen, Germany), 0.67% Igepal (Sigma), and 1.3 mg/ml proteinase K]. Proteinase K digestion was carried out for 10 hr in a PCR machine equipped with a heated lid. After inactivation of proteinase K at 80°C for 10 min, WGA was exactly performed as described by Klein et al. (1999) (PNAS 1999) with the exception of the adapter oligonucleotides (Lib1-primer: 5′-AGT GGG ATT CCT GCT GTC AGT-3′; ddMse-primer: 5′-TAA CTG ACA GCdd-3′) [Stoecklein et al., 2002, 2008]. This approach is now commercialized as AMPLI1 WGA Kit by Silicon Biosystems.

gDNA

gDNA extraction from pooled REH (100,000 cells) cells from the same passage of REH cells for sequencing-pooled gDNA and breakpoint PCR analysis was performed using the AllPrep kit (Qiagen, Hilden, Germany). DNA quality was assessed on a 0.8% agarose gel.

Library Preparation

Library preparation for amplified single cell genomes and pooled gDNA was performed according to the "Paired-End Sample Preparation Guide" February 2010 from Illumina: DNA fragments were randomly fragmented to 100 bp (run 2), 250 bp (run 1 and 3), and 350 bp (pooled gDNA), respectively, with the Covaris© system according to the manufacturer's protocol. Material was purified with the MinElute PCR Purification kit from Qiagen. End repair, adenylation of the 3′-ends, ligation of the PE adapters, and purification of the ligation product were performed in an automated manner (Beckman Coulter SPRI works system; SPRI-works I kits for Illumina GA; Beckman Coulter, Krefeld, Germany) including a size-exclusion step for fragments <200 bp (only for run 1, run 3, and pooled gDNA). The purified ligation product was PCR amplified according to the protocol for low amounts of DNA. DNA libraries ran on a 1.5% agarose gel and were purified with the MinElute Gel Extraction kit from Qiagen. Quality control and quantification was performed on the Bioanalyzer from Agilent (Agilent Technologies, Santa Clara, CA, USA). Libraries were adjusted to a final concentration of 8 pM. PE sequencing was performed on the Illumina GAIIx for run 1 and on an Illumina HiSeq2000 for run 3 and pooled gDNA with a read length of 2 × 100 bp. Run 2 was performed on the GAIIx with a read length of 2 × 75 bp.

Preprocessing of Sequencing Reads

Sequencing data is accessible on Sequencing Read Archive (SRA) under the accession number ERP001296.

The LIB1 adapters, ligated during WGA, were cut off from the 5′-end of the reads (if present). The small insert size of run 2 allowed overlapping PE reads leading to short fractions of Illumina's PE adapters at the 3′ end, which had to be trimmed as well. In comparison to the first two runs, base qualities in run 3 decreased significantly toward the 3′ end. The last 10 bases of every read got trimmed to achieve a better overall read quality and thus a more accurate alignment. The program FASTQC (www.bioinformatics.bbsrc.ac.uk/projects/fastqc) generated the statistics about base qualities and GC content, based on the raw sequences after trimming.

Alignment and Reference Genomes

The alignment against the human reference genome (hg19/GRCh 37) was performed with the Burrows–Wheeler Alignment (BWA) Tool (version 0.5.8c) [Li and Durbin, 2009] using mostly the default settings. Only the allowed number of mismatches was set to 5, 4, and 4 according to the different read lengths in run 1, 2, and 3, respectively. The alignment consists of two consecutive steps: (1) the global alignment against the reference genome for every end of a read pair individually; (2) the assembly of both alignments of every pair with respect to their insert size. This may include a local alignment of previously unmapped reads if the mate could be mapped properly.

All BWA alignments were given in Sequence Alignment/Map (SAM) format [Li et al., 2009] that was converted into its binary equivalent, the BAM format, for all downstream analyses.

Postprocessing of Sequencing Reads

Duplicated reads were excluded from all subsequent analyses. The function MarkDuplicates from the Picard utilities (version 1.46) (www.picard.sourceforge.net) was used to remove reads having identical 5′ mapping coordinates (both ends of a PE read) and orientation. Sorting of the alignment, either by mapping coordinate or by read name, was done with Picard as well.

Coverage and Insert Size Statistics

The sequence and fragment coverage and depth statistics are based on the coverage histograms created with BEDTools (version 2.10.1) [Quinlan and Hall, 2010]. The coverage plot (Fig. 1B) shows the mean sequence depth over 100 kb windows for chromosome 3, 16, and 21. The fragment coverage as noted in Supp. Table S1a only refers to proper pairs, that is, read pairs having the correct insert size and orientation. The coverage information does not include duplicated read pairs.

To compute the cumulative fraction of genome coverage and total read number for the Lorenz curve in Figure 1C, the number of bases and corresponding number of reads from the coverage histograms were added successively and divided by the genome length and total number of reads, respectively.

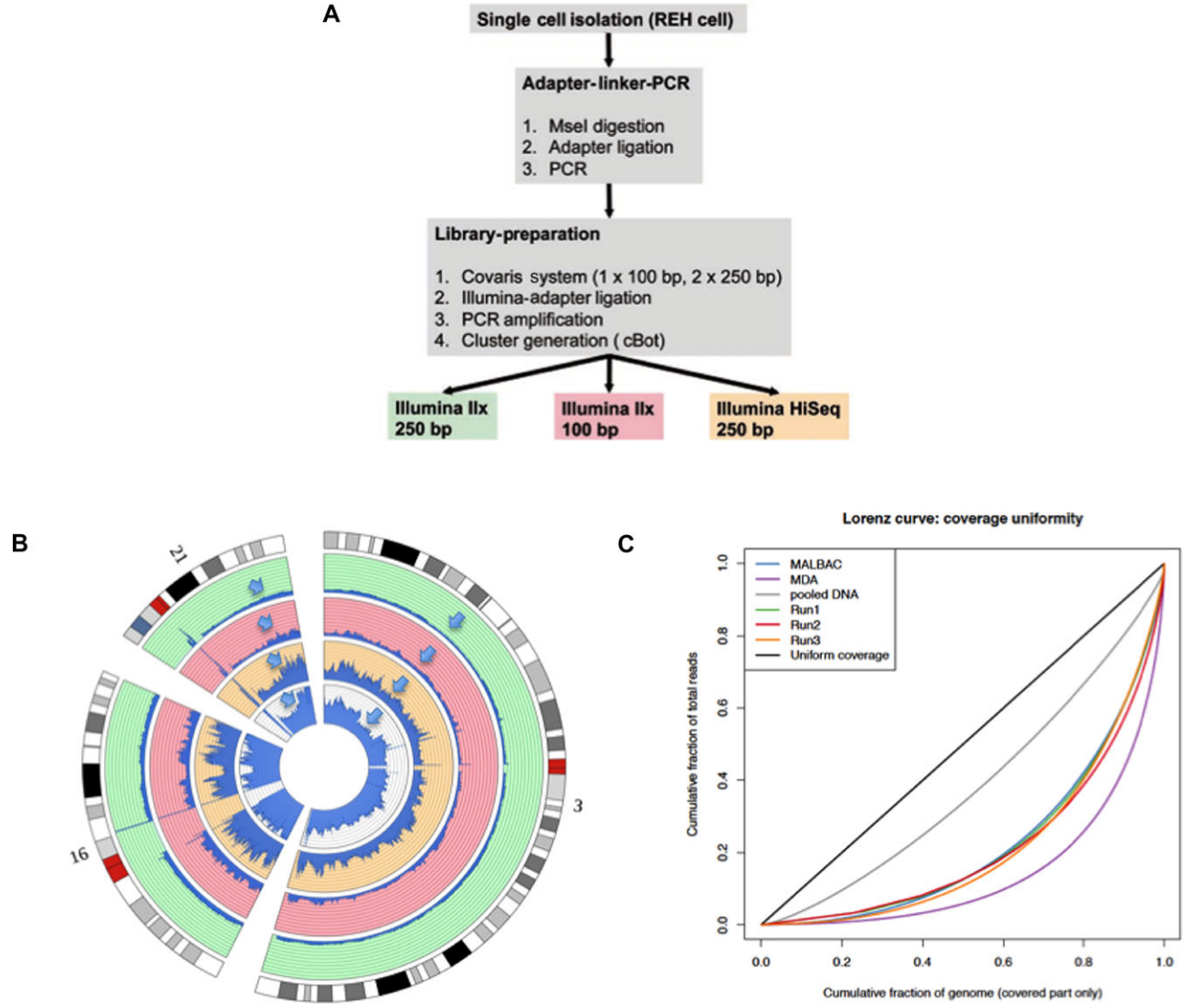

Figure 1. Overview of the workflow for single cell sequencing, sequence coverage, and coverage uniformity. **A**: Three individual REH cells were isolated. gDNA was digested by MseI prior to adapter-linker PCR. WGA products were further fragmented to 100 bp (run 2) and 250 bp (run 1 and 3) to make them suitable for Illumina-adapter annealing, PCR amplification, and cluster generation. After loading one amplified single cell genome per flow cell, DNA was sequenced with PE reads (2 x 75 bp or 2 x 100 bp) on a GA IIx (run 1 and run 2) or a HiSeq 2000 (run 3). **B:** Circos plot of sequence coverage for three single cell sequencing runs (green, run 1; red, run 2; yellow, run 3) and for pooled gDNA (white), depicted for chromosome 3, 16, and 21. Sequence coverage plots clearly depict loss of genomic material on chromosome 3p, the additional chromosome 16, and gain on chromosome 21q according to the consensus karyotype (highlighted by blue arrows). Resolution 100 kb. Scale for y-axis for all runs: minimum, 0 reads; maximum, 55 reads. **C:** Lorenz curves to evaluate coverage uniformity along the genome. Cumulative fraction of total reads that cover a given cumulative fraction of the genome was plotted for pooled gDNA and the single cell runs. Sequencing of pooled gDNA led to most uniform coverage. Single cell genomes 1–3, amplified by our PCR-based method, showed similar coverage uniformity as single cell genomes amplified with MALBAC. Both PCR-based amplification methods clearly outperformed MDA. As the quality of the Lorenz curves depends on coverage, we only compared the regions covered in all runs.

The coverage statistics in Supp. Table S1a and b (for sequences and fragments) and Figure 1C were normalized to the 91% sequence coverage of the pooled DNA sequencing data.

To estimate the coverage of the MseI fragments (Supp. Fig. S2A and B), an in silico digestion of the reference genome (hg19) was performed by cutting the sequences at the restriction site TTAA. The coverage was computed for every single fragment and summed up into results for groups of fragments having a size of 50–100, 100–250 bp, 250 bp–2 kb, and so on. Not annotated regions, for example, telomeres and centromeres, were left out from the in silico digestion. The statistics concerning coding sequence are based on the track from the Consensus Coding Sequence Project (CCDS) [Pruitt et al., 2009] downloaded from the UCSC browser (http://genome.ucsc.edu/).

Copy-Number Analysis with Sequencing Data

The program FREEC (version 3.92) [Boeva et al., 2011] was used to estimate CNVs. It normalizes the data according to a precomputed GC content profile and a mappability track (see GEM toolbox www.gemlibrary.sourceforge.net) without requiring a control dataset. After normalization, copy-number ratios over 10 and 100 kb windows were computed. The following segmentation step used LASSO regression [Tibshirani, 1996] to merge the windows into

larger, contiguous regions showing copy-number gains or losses. Except for the window sizes, all other parameters were set to FREEC's default settings.

Reads having a mapping quality below 10 were excluded before copy-number analysis.

To evaluate sensitivity and specificity for the Relative (or Receiver) Operating Characteristic ROC curves (Fig. 2B; Supp. Table S2a), the threshold for the copy-number ratio, that separates a loss or gain from a normal region, was increased stepwise from 0.5 to 2 (1 = normal copy number). True positive rate and false positive rate were calculated for every such copy-number profile in comparison to the reference profile of pooled gDNA. The ROC curves were computed and plotted with R (www.R-project.org).

Genotyping

The Genome Analysis Toolkit (GATK, version 1.0.4705) [DePristo et al., 2011] was used for SNP detection and genotyping. The analysis followed the suggested pipeline for GATK release 1.0. Only minor adjustments were made with respect to our single sample scenario and the relatively low coverage in run 1 and 2.

The pipeline consists of four steps including preprocessing and postprocessing. (1) A local realignment of the raw BWA mapping around known indels from dbSNP and new indels in our mapping and clusters of mismatches, within intervals of maximal 500 bp, corrects misinterpretations of such mismatches as SNPs. (2) the base quality score recalibration considers a base's relative position within the read, its neighboring bases, and the probability of mismatching to the reference genome to achieve more accurate scores than provided by the sequencer. This becomes crucial, when filtering low-quality SNPs in subsequent steps. (3) The actual SNP calling and genotyping is done using GATK's Unified Genotyper. Calls having a confidence score of at least 30 were accepted (scores within 10–30 were marked as filtered) when base quality and mapping quality were higher than 20 and 17, respectively. (4) The VariantFiltrationWalker finally marks SNPs lying in regions of high SNP density (three SNPs within 10 bp windows) or of low-mapping quality, that is, regions having more than 10% reads of mapping quality zero, for example, regions of highly repetitive sequences. All SNPs, which were marked as filtered in steps (3) and (4), were excluded from further analysis.

GATK outputs the SNP and genotype calls in the Variant Call Format (VCF) (www.vcftools.sourceforge.net/specs.html).

We used SNPs and the associated genotypes passing the filter described in (3) and (4) for comparisons between the single cell runs and pooled gDNA, estimation of ADO, and for the detection of regions of LOH.

The genotyping and its statistics and comparisons to pooled DNA were computed repeatedly for downsampled versions of single cell run 3. Therefore, reads were removed randomly until lower mean sequencing depths of 10× and 5× were achieved.

ADO Rate

The ADO rate for diploid genomes of a single cell run compared with pooled DNA can be computed with the following statistics from the GATK Unified Genotyper:

S, # of heterozygous calls in a single cell; P, # of heterozygous calls in pooled DNA with call at the same position in single cell run (homozygous or heterozygous); M, # of calls that are heterozygous calls in pooled DNA, but homozygous in single cell.

Then a is defined such that $M = Pa\,(1 - a)$ and $S = P\,(1 - a)\,(1 - a)$

Thus, a can be computed as $a = \sqrt{M^2/SP}$

The distribution of MseI fragments related to ADO in the single cell runs is based on the subset of fragments that contains only SNPs called as homozygous in the single cell but heterozygous in the pooled DNA.

LOH

We adapted the LOH detection algorithm implemented in Affymetrix' Genotyping Console 2.0 for the GATK SNP calls of our sequencing experiments: regions are called LOH, if the number of heterozygous SNPs among a fixed window of SNPs falls below a certain threshold. Window size and threshold are estimated automatically from the data as described in detail in Affymetrix (2008). This sliding window approach returns contiguous LOH regions of varying size depending on the number of SNPs in the windows and the distance between the SNPs. The algorithm may tend to overcall small regions of LOH; thus, regions below a maximum resolution were excluded. Resolutions between 100 bp and 500 kb for the sequencing data and the SNP array were tested and results are compared in Supp. Table S4. In both the genotyping console and our adaption of its LOH algorithm, only calls at known SNP sites reported in the dbSNP database (http://www.ncbi.nlm.nih.gov/projects/SNP, dbSNP Build 132) were used for LOH detection. The exact base overlap was calculated with R using the IRanges and Ringo packages.

Detection of SVs

SVs comprise deletions and insertions significantly larger than indels, inversions, tandem duplications, and translocations. Two programs were used for SV detection, both with a different approach:

(1) Pindel [Ye et al., 2009] performs a split-read alignment of unmapped reads around mapped mate reads (so-called anchor reads) within a default distance of 10 kb. This way, it can detect SV breakpoints of deletions, inversions, short and long insertions, and tandem duplications with single-nucleotide resolution.

(2) GASV [Sindi et al., 2009] detects PE reads with an aberrant insert size and/or read orientation and clusters reads that belong to the same SV. This approach gives only an estimate of the breakpoint up to a few hundred base pairs (depending on insert size of the library and the number of reads in the breakpoint cluster).

The analysis of deletions, insertions (short and long), inversions, and tandem duplications was carried out with Pindel. GASV was used to either support its results (as described below) or to detect translocations, deletions, and inversions larger than 10 kb, which could not be detected with Pindel (when using its default settings). Pindel analyzed all three single cell runs and the pooled DNA at once. Except for insertions, only deletions, inversions, and tandem duplications with a size of at least 200 bp were used for further analysis. Minimum mapping quality was set to 20, and SVs closer than 1 Mb to telomeres and centromeres were excluded. To count the overlaps with pooled DNA, SVs in pooled DNA were required to have a minimum read support of five reads, whereas one read was sufficient in the single cell runs.

For the statistics of SV calls in single cell run 3 alone, the minimum read support was set to five. The SV annotations refer to SV calls found with Pindel (short/long insertions, tandem duplications), a combination of Pindel and GASV (deletions and inversions <10 kb) or GASV only (deletions and inversions >10 kb, translocations). The

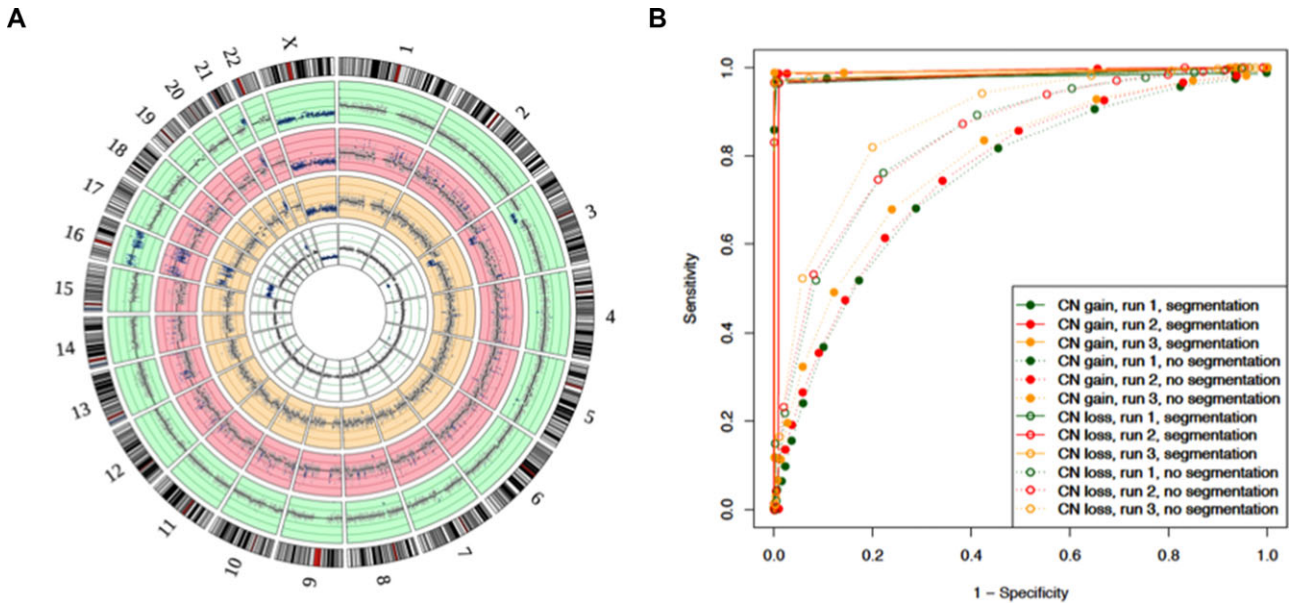

Figure 2. CNVs. **A:** Circos plot of copy-number analysis of pooled gDNA (white inner ring) and three independent single cell genome sequencing runs (green, run 1; red, run 2; yellow, run 3) depicted for each chromosome. Copy numbers from one to four are illustrated by the lines within each ring. Alterations of copy numbers compared with the hg19 reference genome are highlighted in blue. According to the consensus karyotype of REH cells, the plots show loss of one chromosome X, loss of genomic material on chromosome 3p, gain of an additional chromosome 16, and gain of genomic material on chromosome 21q for pooled gDNA and all three single cell sequencing runs. Resolution 100 kb. **B:** Relative (or receiver) operating characteristic (ROC) curves to depict sensitivity (true positive rate) and specificity (1-false positive rate) for the detection of copy-number gains and losses of sequencing run 1–3 in comparison to pooled gDNA with and without segmentation. After segmentation, copy-number detection improves dramatically. Copy-number losses were detected with a sensitivity of 96.9% and specificity of 99.8%, and copy-number gains with a sensitivity of 98.9% and specificity of 99.4% after segmentation. The false positive rate is depicted on the x-axis, and the true positive rate on the y-axis. Resolution 10 kb.

minimum read support is the same as described above. In case of the Pindel–GASV combination, minimum support was five split reads detected by Pindel and 1 PE read detected by GASV. An overlap between both approaches was counted, if an exact breakpoint by Pindel fell into an approximated breakpoint region by GASV.

Supp. Table S5d lists translocations, deletions, and large deletions (>10 kb), which are likely the result of MseI fragment fusions. Those SVs occur exclusively in single cell runs, not in pooled DNA, with an MseI restriction site localized in both breakpoint regions (i.e., the breakpoint estimation by GASV).

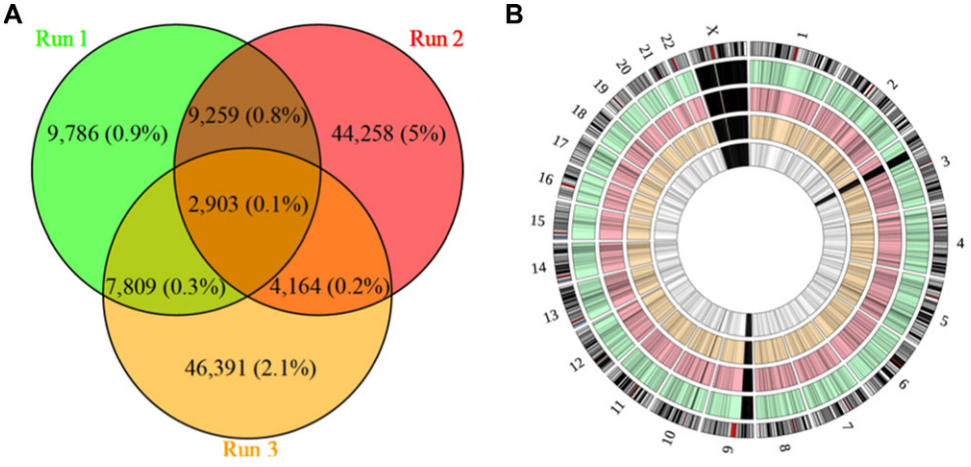

Figure 3. Regions of LOH, exclusive SNPs in single cell sequencing runs and allele frequencies. **A:** Venn diagram of exclusive SNPs detected in single cell runs and not found in pooled gDNA. Indicated are absolute numbers and percentages relating to total number of SNPs detected per single cell run. Only 2.7% of all SNPs detected in run 3 were exclusive and could not be found in pooled gDNA. The percentage of overlapping exclusive SNPs in all three single cell runs was only 0.1% (relating to run 3). Highest overlap of exclusive SNPs was shown for run 1 and run 2 (0.9% relating to run 1). **B:** Circos plot of LOH analysis of pooled gDNA (white inner ring) and three independent single cell sequencing runs (green, run 1; red, run 2; yellow, run 3) depicted for each chromosome. The three major regions of LOH in REH are the region of loss of genomic material on chromosome 3p, the loss of one chromosome X, and the loss of a copy-number neutral region on chromosome 9p. Regions of LOH could be retraced in all three single cell runs with high overlap to pooled gDNA. Resolution 100 kb.

Visualization

The circular plots were created with Circos (version 0.54) [Krzywinski et al., 2009]. The point mutation in Supp. Figure S10 has been visualized with the Integrated Genomics Viewer (version 2.0) [Robinson et al., 2011]. All other plots, if not noted differently in the sections before, were created with R (www.R-project.org).

Spectral Karyotyping Fluorescence in situ hybridization

Spectral karyotyping (SKY) of the cell line REH was performed with the Human SkyPaint Kit (Applied Spectral Imaging, Migdal Ha´Emek, Israel) in line with the manufacturer's protocol. In short, metaphase chromosomes were prepared following standard procedures; chromosomes were labeled with five fluorescent dyes in different colors and analyzed with a fluorescence microscope equipped with a multiple band pass filter set. The karyotype was described according to the ISCN 2009 (http://atlasgeneticsoncology.org/ISCN09/ISCN09.html).

Breakpoint PCR ETV6/RUNX1 Breakpoint

As the exact genomic breakpoint for t(12;21) is known for the REH cell line, its presence in all WGA products was confirmed by nested PCR prior to sequencing (Supp. Fig. S13). Nested primers were designed using Primer blast (http://www.ncbi.nlm.nih.gov/tools/primer-blast/) (inner pair: Pr4: tgtggctcacgcctgtaatc, Pr5: ACTGTGGCGGACCTCTGAGG; outer pair: Pr4ex: TCATTTTTCAggctgggtactgtg, Pr5ex: GAAATAGCTGTGCATTCCTGCC), and the PCR product was conventionally sequenced using the outer PCR primer pair.

Results

Alignment and Sequence Coverage

The described WGA method combines enzymatic genomic digest with MseI and subsequent adapter linker PCR. MseI recognizes a motif of four bases (TTAA), highly abundant throughout the genome. In silico digestion of the human reference genome hg19 with MseI showed a peak of DNA fragment length between 100 and 300 bp (Supp. Fig. S1), with the longest fragments exceeding 10 kb (data not shown). The length distribution of in silico segments made an additional fragmentation step necessary for efficient library preparation. WGA products of three individually isolated REH cells were fragmented to 100 bp (run 2) or 250 bp (runs 1 and 3) by adaptive focused acoustics (Covaris). After loading one amplified single cell genome per flow cell, DNA was sequenced with PE reads (2×75 or 2×100 bp, respectively) on an Illumina Genome Analyzer IIx (GA IIx) (runs 1 and 2) or a HiSeq 2000 (run 3) (Fig. 1A).

For run 1 and 2, we obtained 119 and 149 million mapped reads after duplicate removal, with normalized sequence coverage of 49% and sequencing depth of 3.1×. For run 3, we achieved over 600 million mappable reads after removal of duplicates. This yielded normalized sequence coverage of 74%. Sequence depth was 15.9× (Supp. Table S1a).

Pooled gDNA was sequenced on four lanes with DNA insert size of 300 bp and read length of 2×100 bp on a HiSeq 2000. About 830 million mapped reads led to sequence coverage of 91% with a sequencing depth of 35× (Supp. Table S1a). Sequence coverage is depicted exemplary for chromosomes 3, 16, and 21 in Figure 1B for each run.

To evaluate coverage uniformity along the genome, we plotted the cumulative fraction of total reads that cover a given cumulative fraction of the genome as Lorenz curves for pooled gDNA and the single cell runs (Fig. 1C). In addition, the plot shows the curves of MALBAC [Zong et al., 2012] and MDA [Hou et al., 2012] data that we downloaded and aligned in the same fashion as our single cell PE reads. Perfectly uniform coverage would result in a diagonal line, whereas deviation from the diagonal is indicative of biased coverage. As expected, sequencing of pooled gDNA led to most uniform coverage. Single cell genomes 1–3, amplified by our PCR-based method, showed similar coverage uniformity as single cell genomes amplified with MALBAC [Zong et al., 2012]. Both PCR-based amplification methods clearly outperformed MDA [Hou et al., 2012].

Fragment Coverage

In silico digested MseI fragments were subdivided in different size categories to analyze how fragment length influences PCR-based WGA and therefore fragment coverage. As expected, best fragment coverage was obtained for segment sizes between 100 bp and 5 kb sizes, most applicable for PCR amplification (Supp. Fig. S2A). But in silico MseI fragments up to 10 kb also were covered up to 15% by sequencing reads. As these large fragments are mainly located in complex regions of the genome, including not annotated regions, additional MseI restriction sites were most likely masked and not applicable for in silico analysis. MseI fragments >10 kb were only sequenced in ≤0.1%, since they were not accessible for PCR amplification during WGA. Overall, normalized fragment coverage was 76% for run 3 (Supp. Table S1a and b).

Coverage of Coding Sequence

In silico analysis revealed that 20% of coding sequence is represented in the fragment size categories from 50–250 bp. As the intended DNA insert size for run 1 was 250 bp, fragments smaller than 200 bp were size-excluded during library preparation. After random fragmentation of the WGA products at the beginning of library preparation, this fraction is supposed to be even larger, though not calculable. Only 1% of the coding sequence in the fragment category from 50 to 100 bp and 22.7% in the category from 100 to 250 bp was covered by run 1 (Supp. Fig. S2B). This was the rationale to lower mean DNA insert size from 250 to 100 bp for run 2. As expected, we gained coverage of coding sequence in the small fractions from 50 to 100 bp (5.7%), but in the fraction of 100–250 bp, the coverage of coding sequence was comparable to run 1 (22.7%). The coverage of the fragment sizes from 50 to 100 bp (9.3%) as well as for fragments from 100 to 250 bp (68.2%) was highest in run 3, although library preparation excluded this fragment sizes similar to library preparation for run 1 (Supp. Fig. S2B). This indicates that the high-sequencing coverage of run 3 exceeded the use of smaller DNA fragments for library preparation in terms of coverage of coding sequence, also depicted by the highest coverage for coding sequence overall (77%) (Supp. Table S1a) and per chromosome (Supp. Fig. S3).

CNVs

To validate that our PCR-based WGA method with subsequent second-generation sequencing of single cells is accurate enough for

CNV detection, we compared the copy-number profiles of the single cell runs with the profile derived from pooled gDNA.

All major regions of copy-number changes identified by sequencing-pooled genomic DNA could be detected in all three single cell sequencing runs as depicted for each chromosome in Figure 2A and as linear heat map for chromosome 3, 16, and 21 (Supp. Fig. S4). Segmentation of the copy-number windows reduced the impact of noise caused by overamplified and nonamplified regions (Fig. 2B; Supp. Table S2a). To analyze overlaps in the detection of CNVs between single cell run 3 and pooled gDNA, we compared them (1) by segments of copy-number changes, (2) segments of copy-number changes plus absolute copy numbers, and by (3) overlapping base pairs (Supp. Table S2a and b). When we compared by segments of copy-number gains, we calculated an overlap of 62.5%, with a high false negative rate of 77.3% and a false positive rate of 37.5%. By comparing run 3 and pooled gDNA based on segments of copy-number gains and absolute copy number, we calculated an even lower overlap (37.5%). But when we calculated the overlap based on an analysis by base pairs (3), we saw that the overlap was 99.7% for gains of genomic material, and only slightly lower (99.3%) when the criterion of overlap of absolute copy number was added to the analysis. This clearly indicates that the nonoverlapping segments from analysis (1) and (2) were very small as they accounted for only 0.3% of actual genomic sequence (Supp. Table S2b). For losses of genomic material, we observed a similar phenomenon: whereas the overlap based on segment analysis was only 66.7%, the overlap based on base pair analysis was 97%.

In summary, copy-number losses were detected with a sensitivity of 96.9% and a specificity of 99.8% in single cell run 3 compared with pooled gDNA. Copy-number gains were detected with a sensitivity of 98.9% and specificity 99.4% (Supp. Table S2a). Normal copy numbers (CN = 2) were detected with an overlap up to 100% (data not shown).

Interestingly, when we analyzed how precise breakpoints overlap between pooled gDNA and the single cell runs, we very rarely observed differences in the breakpoint locations (maximum difference 10.8 Mb). The vast majority of breakpoints were detected at exactly the same position in the genome (minimum and median for breakpoint distance: zero; Supp. Table S2b).

As an additional quality control, we compared our results after WGA combined with next-generation sequencing to a dataset obtained by combining WGA of a single genome of the REH cell line with array comparative genomic hybridization (aCGH) [Mohlendick et al., 2013]. The smallest fragments of copy-number changes we were able to detect in run 3 were 160 kb with the chosen CNV calling settings (10 kb windows). This was less sensitive than single cell aCGH based on the same WGA method (56 kb) or pooled gDNA (10 kb). However, a 56-kb deletion detected on chromosome 7 by aCGH could be retraced not only in pooled gDNA, but also in single cell run 1–3 when illustrated in IGV (Supp. Fig. S5). But after subsequent segmentation, the deletion was only "called" in pooled gDNA. This demonstrates that higher sequence coverage influences sensitivity for the detection of small CNVs (Supp. Table S2b and c). However, the overlap between a single cell genome of the REH cell line analyzed by aCGH or next-generation sequencing was high (99.6% for copy-number gains and 88.1% for losses based on base pair analysis). The overlap of single cell aCGH to aCGH on pooled gDNA was 91.9% for copy-number gains and 89.7% for losses. This indicates that both single cell analysis methods are highly suitable for the detection of CNVs, but that analyzing single cell genomes by second-generation sequencing is more accurate, as the overlap to pooled gDNA was shown to be higher (Supp. Table S2c). The smaller-sized segments that were not detected by the single cell runs accounted for negligible genomic regions in terms of base pairs (Supp. Table S2a and c).

Genotyping and ADO Rate

To analyze the accuracy of our WGA approach for genotyping, we compared SNP positions covered by sequencing-pooled gDNA with all SNP positions covered by the single cell sequencing runs. In total, we detected 3,689,179 SNPs in pooled gDNA of REH cells; 2,308,408 were heterozygous and 1,380,771 were homozygous. Run 3 covered 1,437,631 of the heterozygous SNP positions, with 1,324,918 matching in genotype and position to pooled gDNA. This indicates a sensitivity of 62%, mainly due to the lower sequence coverage in the single cell runs, with a high detection precision of 92% for heterozygous SNPs. For homozygous SNPs, although sensitivity was only 53%, detection precision was 99% for run 3 (Supp. Table S3a), clearly demonstrating that genotypes can be determined accurately after WGA.

To determine the ADO rate, we assessed the number of heterozygous SNPs detected in pooled gDNA that were called as homozygous in the single cell runs. These discrepancies are potentially introduced during WGA, when only one of the two alleles gets amplified. We calculated an overall ADO rate of 3% for run 3. We further categorized allele coverage ratios as a function of sequence coverage (Supp. Table S3a and Supp. Fig. S6A and B). The ADO rate decreases below 2% with higher coverage (>20 reads) due to better genotyping quality.

To analyze how ADO relates to MseI fragment length, we compared the size distribution of all MseI fragments with ADO fragments. The peaks of the fragment length distribution for ADO fragments were shifted toward larger sizes between 300 and 500 bp, with an additional relative peak ≥2 kb, suggesting that SNPs within larger fragments exhibit more ADO (Supp. Fig. S7).

To test how sequence coverage influences detection sensitivity, detection precision, and ADO rate, we downsampled run 3 to lower sequence coverage (10×, 5×) by randomly deleting reads. We observed a decrease in detection sensitivity to 43% for 5× coverage, but stable detection precision (92%), and ADO (3%), respectively (Supp. Table S3b).

Genomic Heterogeneity Between Single Cells: Single-Nucleotide Variations

Biological differences acquired during cell division would display as exclusive SNPs detected in only very few or single cells and would therefore not be detectable in pooled gDNA due to underrepresentation. The number of exclusive SNPs per single cell is expected to be low in a permanent cell line. Indeed, only 2.7% of all SNPs detected in run 3 were exclusive and could not be found in pooled gDNA. The percentage of overlapping exclusive SNPs in all three single cell runs was only 0.1% (relating to run 3). Highest overlap of exclusive SNPs was shown for run 1 and run 2 (0.9% relating to run 1) (Fig. 3A; Supp. Table S3a).

92% of SNPs detected by sequencing pooled gDNA and 85%–89% of SNPs in single cell runs were published in the dbSNP database (http://www.ncbi.nlm.nih.gov/projects/SNP/) (Supp. Table S3c) and therefore are more likely real biological variants than introduced by systematic or random amplification or sequencing errors. Up to 12% of the SNPs exclusively detected in single cell runs were also published (Supp. Table S3c), further suggesting that they were not introduced by technical errors.

To investigate the characteristics of exclusive SNPs more deeply, we determined the two types of nucleotide substitution in single cell genomes compared with pooled gDNA. Transitions are interchanges of two-ring purines (A<>G) or of one-ring pyrimidines (C<>T). Transversions are interchanges of purine for pyrimidine bases, which therefore involve exchange of one-ring and two-ring structures. Normally, the transition–transversion ratio for whole-genome sequencing of human DNA is 2–2.1, which means that transitions are twice as frequent as transversions [Abecasis et al., 2010]. We could confirm a transition–transversion ratio of 2.03–2.05 for all SNPs of pooled gDNA and single cell runs (Supp. Table S3c). For SNPs exclusively detected in pooled gDNA (not listed in dbSNP), the ratio was lower (1.72). The transition–transversion ratio for exclusively detected SNPs in single cells from our cell line is only 0.74 in average for all single cell runs and suggests dependency on sequence coverage: it is 1.3 for run 2 with the lowest sequence coverage, whereas the ratio is 0.43 for run 3, the run with the highest coverage (Supp. Table S3c). This indicates that in newly acquired SNPs of single cells of our cell line, transversions are more frequent than transitions.

We listed all novel SNPs (no overlap with dbSNP) in or near coding region (within 2 kb) detected in pooled gDNA and/or in single cell amplicons with genotype and allele coverage (Supp. Table S3d).

Table 1. Overlap for the Detection of SVs by PE Read Analysis Between Pooled gDNA and Single Cell Run 3

	Pooled gDNA	Run 3 overlap	Run 3, no overlap	Run 3 SV+ MseI site	Run 3, no overlap/ MseI corrected
Deletions	1,864	646 = 35%	543	118 = 22%	425
Inversions	158	60 = 38%	1,176	n/a	n/a
Tandem duplications	282	139 = 49%	223	n/a	n/a
Short insertions	187,362	90,946 = 49%	60,899	n/a	n/a
Long insertions	1,141	797 = 70%	14,649	n/a	n/a
Deletions >10kb	114	41 = 36%	116	100 = 86%	16
Inversions >10kb	44	20 = 45%	252	n/a	n/a
Translocations	28	9 = 32%	2,071	1,789 = 86%	282

Table 1 highlights the major findings regarding the detection of SVs by PE read analysis comparing sequencing of pooled gDNA to single cell genomes of a permanent leukemic cell line amplified by adapter-linker PCR. The highest overlap was observed for long insertions, and the lowest for translocations. An important reason for the detection of false positive SVs is the generation of DNA chimeras during the adapter ligation step of WGA, but also in the adapter ligation step during library preparation and amplification. The false positive detection of SVs based on DNA chimeras after library preparation is not traceable (because fragmentation during library preparation is random), whereas DNA chimeras generated during WGA are supposedly generated at MseI restriction sites in the genome. To address this point, we analyzed the number of SVs located at MseI restriction sites for deletions, large deletions (≥10 kb), and translocations, which are variations presumably most likely prone to this type of error. We analyzed variations detected in single cell runs that did not show an overlap to pooled gDNA. For smaller deletions, MseI chimeras only accounted for 22%, whereas for larger deletions and translocations, the incidence for MseI chimeras was 86%. We have listed the data summarized here in detail in Supp. Table S5a–l.

LOH

As a further quality control, we compared regions with LOH detected by sequencing-pooled gDNA and single cell genomes. All major regions of LOH in REH cells detected by sequencing-pooled gDNA were also found in the three single cell runs (e.g., chromosome 3, 9, and X), as depicted in Figure 3B.

LOH regions were analyzed in different resolutions from 500 kb up to 100 bp. Absolute numbers of detected LOH regions increased with resolution: 799 Mb at a resolution of 100 bp compared with 194 Mb at a resolution of 500 kb for pooled gDNA (Supp. Table S4). The overlap between LOH regions detected in pooled gDNA compared with single cell runs showed the opposite trend and decreased with higher resolution. At a resolution of 500 kb, the overlap between pooled gDNA and run 3 was 94%, whereas at a resolution of 100 bp, the overlap was only 86%. This indicates an increasing false positive rate for high resolutions, with 10–50 kb serving as a good compromise between sensitivity and resolution.

Breakpoint Analysis: Structural and Quantitative Variations

To be able to analyze the genotype of the studied cell line, we verified the consensus karyotype for REH cells [Uphoff et al., 1997] by SKY [Schrock et al., 1997] in 100 metaphases, also validating the genomic homogeneity of this cell line (Supp. Fig. S8).

Targeted sequencing approaches in REH cells revealed two point mutations (*MLH1, TP53*) and one deletion (*CDKN2A*) (http://www.sanger.ac.uk/genetics/CGP/CellLines/).

The described deletion in *CDKN2A*, residing in the region on chromosome 9p21, could be identified in all three single cell sequencing runs (Supp. Fig. S9). The point mutation in *TP53* was published to be heterozygous. This could be confirmed in run 3, but not in run 1 and run 2, demonstrating again that allele frequencies are preserved after PCR-based WGA (Supp. Fig. S10), and can be accurately assessed when sequencing is performed with sufficient sequencing depth.

PE sequencing enables the identification of structural and quantitative variations based on insert size and orientation of two paired reads. Variations were detected by two different algorithms: a base-exact split-read alignment with Pindel [Ye et al., 2009] and an approximate detection from aberrant PE reads with GASV [Sindi et al., 2009] (see *Material and Methods*). Variations found in pooled gDNA were compared with variations identified in single cell amplicons. Best overlap for all types of variations was detected for run 3, the run with the highest coverage. Translocations were detected with the lowest overlap to pooled gDNA of only 32%, whereas the detection of long insertions showed the highest overlap with 70% (Table 1; Supp. Table S5a). Overlap between single cell runs is highest for run1 and run 3, with 82% for tandem duplications, and up to 100% for translocations (Supp. Table S5a).

Exclusive variations were found in single cells compared with pooled gDNA, with the highest percentage for short (94%) and long (96%) inversions and the lowest for short insertions (10%) in run 3 (Table 1; Supp. Table S5b). Overlap of exclusive variations between single cell runs is highest for run 1 and 3 for short and long insertions, but low overall (Supp. Table S5b).

To further quality control the detection of variations with PE read analysis, we compared large deletions >10 kb detected by GASV with deletions detected by copy-number analysis for pooled gDNA and run 3. Of the 114 large deletions detected in pooled gDNA by PE read distance (GASV), only 35 could also be detected by copy-number analysis. Of these 35 overlapping deletions, only six could also be detected in run 3 by PE read analysis, eight by copy-number analysis, with an overlap of four between the algorithms (Supp. Table S5c and Supp. Fig. S11). This low overlap between algorithms together with the high number of detected variations by PE read analysis suggests a high false positive rate.

DNA chimeras generated during WGA are a potential reason for the detection of false positive SVs and would supposedly be generated at MseI restriction sites. We therefore analyzed the number of SVs located at MseI restriction sites for deletions, large deletions (≥10 kb), and translocations. We analyzed variations only detected

in single cell runs but not in pooled gDNA and found that for smaller deletions MseI chimeras accounted for only 22%, whereas for larger deletions and translocations the prevalence of MseI chimeras was 86% (Table 1; Supp. Table S5d).

According to the consensus karyotype, the REH cell line harbors several translocations (t[4;12], t[5;12], t[4;16], t[16;21], and t[12;21]) [Uphoff et al., 1997] that could be detected by SKY (Supp. Fig. S8). All known translocations were detected by sequencing-pooled gDNA (data not shown). Out of the five known translocations, one could be detected in run 1 and 3 (t[5;12]), another only in run 3 (t[4;12]). Three translocations were detected in pooled gDNA and run 3, which were not identified by SKY (t[2;19], t[6;17], and t[6;22]) (Supp. Fig. S12). For t(12;21), the exact genomic breakpoint is known in REH cells and its presence was confirmed by PCR in all WGA products prior to sequencing (Supp. Fig. S13). The translocation could be verified in single cell analysis by split-read alignment of initially unmapped reads directly to the breakpoint region (run 1). The translocation t(12;21) includes one *RUNX1* allele, whereas the other allele is supposed to be deleted in the REH cell line [Uphoff et al., 1997]. Surprisingly, we could not detect a deletion in the wild-type *RUNX1* allele, neither in pooled gDNA nor in any of the single cell amplicons. However, we found a 20-bp long insertion in the wild-type *RUNX1* allele in pooled gDNA, run 1 and run 3. We listed all SVs detected by PE read mapping or split-read analysis in pooled gDNA and at least one single cell run. We highlighted the ones that were also detected in samples of patients with ETV6/RUNX1 leukemia, if applicable (Supp. Table S5e–l).

Discussion

Here, we describe a new workflow for genome-wide analysis of single human cell genomes combining a very robust and efficient WGA method, based on adapter-linker PCR, with next-generation sequencing. The WGA protocol was well precharacterized by other methods such as aCGH and is widely used for the analysis of single cancer cells [Klein et al., 1999; Stoecklein et al., 2002; Stoecklein et al., 2008; Stoecklein and Klein, 2010; Mohlendick et al., 2013; Steinert et al., 2014]. However, with the advent of second-generation sequencing biases of WGA methods could be analyzed in a more comprehensive manner. By comparing sequencing results of single REH cells to matched pooled gDNA, we extensively analyzed the accuracy of the adapter-linker WGA method and showed that the workflow presented here allows accurate detection of SNPs, copy-number alterations, and regions with LOH at the single cell level.

The percentage of genomic sequence amplified by our approach is twice as high as for other PCR-based methods (36% sequence coverage for PicoPlex [Voet et al., 2013] vs. 74%). We calculated a much lower ADO rate (2%) for the adaptor-linker PCR-based method compared with MDA (65%), where DNA is amplified in a linear manner in the first cycles [Hou et al., 2012]. WGA using the MALBAC method led to a slightly lower ADO rate of 1% [Zong et al., 2012]. Coverage uniformity along the genome showed similar performance for the PCR-based WGA method used by us when compared with MALBAC [Zong et al., 2012], and clearly outperformed MDA [Hou et al., 2012]. Another advantage of our workflow is that important components of the WGA method are known, as adapter sequences and restriction sites [Klein et al., 1999; Mohlendick et al., 2013]. This highly facilitates the bioinformatic analysis, the alignment process in particular, for example, WGA adapter sequences can easily be trimmed in silico and therefore would not interfere with accurate read mapping.

Alignment of reads from single cell sequencing runs showed a higher percentage of read pairs with an aberrant insert size or orientation (37%–59%) compared with pooled gDNA (7%) (Supp. Table S1a). Deviations in insert size could be due to real biological variations or technical errors. Such artifacts could be caused by mismapping of sequencing reads or synthesis of chimeric DNA fragments during the adapter ligation step of WGA. This problem could be minimized by optimization of the molar ratios between DNA fragments and adapters, but not completely avoided. Chimeras are hard to distinguish from true variations because they get sequenced with normal read depth like any other DNA fragment. As it is not likely that single cells acquired large numbers of additional variations in a permanent cell line, the higher number of aberrant insert sizes after WGA potentially indicate an accumulation of artificial chimeras. This is also reflected in lower overlaps of SVs detected by breakpoint analysis in pooled gDNA and single cells compared with variations detected by copy-number analysis. This matches observations from Voet et al. (2013), who sequenced single HCC38 cells after MDA WGA with PE reads and reported high numbers of SV not only due to mismapping, but also due to false synthesis of chimeric DNA fragments during WGA. However, we also detected a high number of SVs by breakpoint analysis in not preamplified gDNA that could not be retraced by copy-number analysis or conventional karyotyping. Potential reasons are the generation of similar DNA chimeras in the adapter ligation step during library preparation and amplification, as well as mapping ambiguity during the alignment process due to the relatively short read length (maximum 100 bp for Illumina). These are general technical challenges of next-generation sequencing that might be optimized in following years by improving the sensitivity of next-generation sequencing making amplification steps unnecessary. Future techniques enabling sequencing with longer sequencing reads ($\geq$1 kb) will help to overcome read mapping ambiguity.

The false positive detection of SVs based on DNA chimeras after library preparation is not traceable because fragmentation during library preparation is random, but DNA chimeras generated during WGA are supposedly generated at MseI restriction sites in the genome. We therefore analyzed the number of SVs located at MseI sites and observed a high prevalence for MseI chimeras (up to 86%) for some SVs. This type of analysis provides a good tool for quality control of SV data generated by our workflow.

Normally, the transition–transversion ratio for whole-genome sequencing of human DNA is 2:2.1, which means that transitions are twice as frequent as transversions [Abecasis et al., 2010]. Zong et al. (2012) observed that the transition–transversion ratio of newly acquired SNVs in single cells was lower (0.3), indicating that transitions were not favored over transversions for newly acquired SNVs in the cell line they studied. We made a similar observation since the transition–transversion ratio of exclusive SNPs in single cells was 0.74 in average. Also, SNPs in pooled gDNA that were not previously published in the dbSNP database and are therefore presumably newly acquired SNPs had a lower transition–transversion ratio of 1.72. It is unclear whether this represents a real biological phenomenon or introduced artifacts. Interestingly, the transition–transversion ratio in our single cell runs was dependent on sequence coverage: run 3 with the highest coverage showed the lowest transition–transversion ratio of 0.43, whereas run 2 with the lowest coverage showed a higher ratio of 1.32. This suggests a more methodological origin for this observation.

As for SVs, SNPs private to the single cell genomes could represent real biological differences acquired during cell division, but might also be introduced by amplification or sequencing errors. However, if SNPs were introduced by a systematic technical error during WGA,

the overlap of exclusive SNPs between single cells would be high, but the overlap to not preamplified pooled gDNA low. A systematic technical error during sequencing would result in high overlap of SNPs between single cells, and to pooled gDNA. Arbitrarily introduced SNPs or real biological differences would not be detectable in pooled gDNA due to under-representation, and should not overlap in three randomly picked cells. Thus, the low number of exclusive SNPs in the three single cell amplicons and their low overlap suggest that artificial SNPs were not systematically introduced by our WGA approach. The high overlap of the majority of SNPs detected in single cell amplicons with pooled gDNA clearly demonstrates that our WGA method enables accurate SNP profiling in single cells.

The ratio of read length compared with DNA insert size was influential for PE read mapping. Run 2 showed the lowest number of detected SVs (1–2) and the lowest overlap of variations detected by breakpoint analysis compared with pooled gDNA. This single cell amplicon was sequenced with the lowest DNA insert size compared with read length and was therefore inferior for the detection of breakpoints. The shorter read length of 75 bp also made it disadvantageous for split-read analysis. Run 2 also turned out to have the lowest detection sensitivity and detection precision for CNVs, and a higher ADO rate (Supp. Table S3a). The workflow as followed for run 3 was shown to be the most powerful, as it provides sufficient sequence coverage of the genome, allowing analysis in single base resolution including the assessment of allele frequencies, and is suitable for breakpoint analysis with insert sizes around 250–300 bp and long PE reads (100 bp).

Taken together, we developed an effective and robust single cell sequencing workflow based on adapter-linker PCR combined with second-generation sequencing, which allowed analysis at single nucleotide resolution. High coverage uniformity and low ADO rate make our method sufficient for comprehensive SNP and copy-number analysis. The described workflow should be most suitable to analyze cancer cell heterogeneity and clonality.

Acknowledgments

We thank Silke Furlan and Ina Bachmann for excellent technical assistance.

Disclosure statement: The authors declare that there are no conflicts of interest.

References

Abecasis GR, Altshuler D, Auton A, Brooks LD, Durbin RM, Gibbs RA, Hurles ME, McVean GA. 2010. A map of human genome variation from population-scale sequencing. Nature 467:1061–1073.

Affymetrix. 2008. Affymetrix White Paper: the loss of heterozygosity algorithm in genotyping console 2.0. http://media.affymetrix.com/support/technical/whitepapers/loh_algorithm_gtc2_whitepaper.pdf Revision 1, February 11, 2008.

Anderson K, Lutz C, van Delft FW, Bateman CM, Guo Y, Colman SM, Kempski H, Moorman AV, Titley I, Swansbury J, Kearney L, Enver T, et al. 2011. Genetic variegation of clonal architecture and propagating cells in leukaemia. Nature 469:356–361.

Blainey PC, Quake SR. 2014. Dissecting genomic diversity, one cell at a time. Nat Methods 11:19–21.

Boeva V, Zinovyev A, Bleakley K, Vert JP, Janoueix-Lerosey I, Delattre O, Barillot E. 2011. Control-free calling of copy number alterations in deep-sequencing data using GC-content normalization. Bioinformatics 27:268–269.

Chi KR. 2014. Singled out for sequencing. Nat Methods 11:13–17.

Chitsaz H, Yee-Greenbaum JL, Tesler G, Lombardo MJ, Dupont CL, Badger JH, Novotny M, Rusch DB, Fraser LJ, Gormley NA, Schulz-Trieglaff O, Smith GP, et al. 2011. Efficient de novo assembly of single-cell bacterial genomes from short-read data sets. Nat Biotechnol 29:915–921.

DePristo MA, Banks E, Poplin R, Garimella KV, Maguire JR, Hartl C, Philippakis AA, del Angel G, Rivas MA, Hanna M, McKenna A, Fennell TJ, et al. 2011. A framework for variation discovery and genotyping using next-generation DNA sequencing data. Nat Genet 43:491–498.

Eberwine J, Sul JY, Bartfai T, Kim J. 2014. The promise of single-cell sequencing. Nat Methods 11:25–27.

Gole J, Gore A, Richards A, Chiu YJ, Fung HL, Bushman D, Chiang HI, Chun J, Lo YH, Zhang K. 2013. Massively parallel polymerase cloning and genome sequencing of single cells using nanoliter microwells. Nat Biotechnol 31:1126–1132.

Hou Y, Song L, Zhu P, Zhang B, Tao Y, Xu X, Li F, Wu K, Liang J, Shao D, Wu H, Ye X, et al. 2012. Single-cell exome sequencing and monoclonal evolution of a JAK2-negative myeloproliferative neoplasm. Cell 148:873–885.

Klein CA, Schmidt-Kittler O, Schardt JA, Pantel K, Speicher MR, Riethmuller G. 1999. Comparative genomic hybridization, loss of heterozygosity, and DNA sequence analysis of single cells. Proc Natl Acad Sci USA 96:4494–4499.

Krzywinski M, Schein J, Birol I, Connors J, Gascoyne R, Horsman D, Jones SJ, Marra MA. 2009. Circos: an information aesthetic for comparative genomics. Genome Res 19:1639–1645.

Li H, Durbin R. 2009. Fast and accurate short read alignment with Burrows–Wheeler transform. Bioinformatics 25:1754–1760.

Li H, Handsaker B, Wysoker A, Fennell T, Ruan J, Homer N, Marth G, Abecasis G, Durbin R. 2009. The sequence alignment/map format and SAMtools. Bioinformatics 25:2078–2079.

Lilljebjorn H, Rissler M, Lassen C, Heldrup J, Behrendtz M, Mitelman F, Johansson B, Fioretos T. 2011. Whole-exome sequencing of pediatric acute lymphoblastic leukemia. Leukemia 26:1602–1607.

Lilljebjorn H, Soneson C, Andersson A, Heldrup J, Behrendtz M, Kawamata N, Ogawa S, Koeffler HP, Mitelman F, Johansson B, Fontes M, Fioretos T. 2010. The correlation pattern of acquired copy number changes in 164 ETV6/RUNX1-positive childhood acute lymphoblastic leukemias. Hum Mol Genet 19:3150–3158.

Macaulay IC, Voet T. 2014. Single cell genomics: advances and future perspectives. PLoS Genet 10:e1004126.

Mohlendick B, Bartenhagen C, Behrens B, Honisch E, Raba K, Knoefel WT, Stoecklein NH. 2013. A robust method to analyze copy number alterations of less than 100 kb in single cells using oligonucleotide array CGH. PLoS One 8:e67031.

Mullighan CG, Goorha S, Radtke I, Miller CB, Coustan-Smith E, Dalton JD, Girtman K, Mathew S, Ma J, Pounds SB, Su X, Pui CH, et al. 2007. Genome-wide analysis of genetic alterations in acute lymphoblastic leukaemia. Nature 446:758–764.

Navin N, Kendall J, Troge J, Andrews P, Rodgers L, McIndoo J, Cook K, Stepansky A, Levy D, Esposito D, Muthuswamy L, Krasnitz A, et al. 2011. Tumour evolution inferred by single-cell sequencing. Nature 472:90–94.

Nawy T. 2014. Single-cell sequencing. Nat Methods 11:18.

Parkhomchuk D, Amstislavskiy V, Soldatov A, Ogryzko V. 2009. Use of high throughput sequencing to observe genome dynamics at a single cell level. Proc Natl Acad Sci USA 106:20830–20835.

Pruitt KD, Harrow J, Harte RA, Wallin C, Diekhans M, Maglott DR, Searle S, Farrell CM, Loveland JE, Ruef BJ, Hart E, Suner MM, et al. 2009. The consensus coding sequence (CCDS) project: identifying a common protein-coding gene set for the human and mouse genomes. Genome Res 19:1316–1323.

Quinlan AR, Hall IM. 2010. BEDTools: a flexible suite of utilities for comparing genomic features. Bioinformatics 26:841–842.

Robinson JT, Thorvaldsdottir H, Winckler W, Guttman M, Lander ES, Getz G, Mesirov JP. 2011. Integrative genomics viewer. Nature Biotechnol 29:24–26.

Rodrigue S, Malmstrom RR, Berlin AM, Birren BW, Henn MR, Chisholm SW. 2009. Whole genome amplification and de novo assembly of single bacterial cells. PLoS One 4:e6864.

Schrock E, Veldman T, Padilla-Nash H, Ning Y, Spurbeck J, Jalal S, Shaffer LG, Papenhausen P, Kozma C, Phelan MC, Kjeldsen E, Schonberg SA, et al. 1997. Spectral karyotyping refines cytogenetic diagnostics of constitutional chromosomal abnormalities. Hum Genet 101:255–262.

Sindi S, Helman E, Bashir A, Raphael BJ. 2009. A geometric approach for classification and comparison of structural variants. Bioinformatics 25:i222–i230.

Steinert G, Scholch S, Niemietz T, Iwata N, Garcia SA, Behrens B, Voigt A, Kloor M, Benner A, Bork U, Rahbari NN, Buchler MW, et al. 2014. Immune escape and survival mechanisms in circulating tumor cells of colorectal cancer. Cancer Res 74:1694–1704.

Stoecklein NH, Erbersdobler A, Schmidt-Kittler O, Diebold J, Schardt JA, Izbicki JR, Klein CA. 2002. SCOMP is superior to degenerated oligonucleotide primed-polymerase chain reaction for global amplification of minute amounts of DNA from microdissected archival tissue samples. Am J Pathol 161:43–51.

Stoecklein NH, Hosch SB, Bezler M, Stern F, Hartmann CH, Vay C, Siegmund A, Scheunemann P, Schurr P, Knoefel WT, Verde PE, Reichelt U, et al. 2008. Direct genetic analysis of single disseminated cancer cells for prediction of outcome and therapy selection in esophageal cancer. Cancer Cell 13:441–453.

Stoecklein NH, Klein CA. 2010. Genetic disparity between primary tumours, disseminated tumour cells, and manifest metastasis. Int J Cancer 126:589–598.

Tibshirani R. 1996. Regression shrinkage and selection via the lasso. J Roy Statist Soc Ser B 58:267–288.

Uphoff CC, MacLeod RA, Denkmann SA, Golub TR, Borkhardt A, Janssen JW, Drexler HG. 1997. Occurrence of TEL-AML1 fusion resulting from (12;21) translocation in human early B-lineage leukemia cell lines. Leukemia 11:441–447.

Voet T, Kumar P, Van Loo P, Cooke SL, Marshall J, Lin ML, Zamani Esteki M, Van der Aa N, Mateiu L, McBride DJ, Bignell GR, McLaren S, et al. 2013. Single-cell paired-end genome sequencing reveals structural variation per cell cycle. Nucleic Acids Res 41:6119–6138.

Woyke T, Tighe D, Mavromatis K, Clum A, Copeland A, Schackwitz W, Lapidus A, Wu D, McCutcheon JP, McDonald BR, Moran NA, Bristow J, et al. 2010. One bacterial cell, one complete genome. PLoS One 5:e10314.

Woyke T, Xie G, Copeland A, Gonzalez JM, Han C, Kiss H, Saw JH, Senin P, Yang C, Chatterji S, Cheng JF, Eisen JA, et al. 2009. Assembling the marine metagenome, one cell at a time. PLoS One 4:e5299.

Ye K, Schulz MH, Long Q, Apweiler R, Ning Z. 2009. Pindel: a pattern growth approach to detect break points of large deletions and medium sized insertions from paired-end short reads. Bioinformatics 25:2865–2871.

Zong C, Lu S, Chapman AR, Xie XS. 2012. Genome-wide detection of single-nucleotide and copy-number variations of a single human cell. Science 338:1622–1626.

LETTER

doi:10.1038/nature14569

Epoxyeicosatrienoic acids enhance embryonic haematopoiesis and adult marrow engraftment

Pulin Li[1,2]*, Jamie L. Lahvic[1]*, Vera Binder[1,3]*, Emily K. Pugach[1], Elizabeth B. Riley[1], Owen J. Tamplin[1], Dipak Panigrahy[4], Teresa V. Bowman[1], Francesca G. Barrett[1], Garrett C. Heffner[1], Shannon McKinney-Freeman[5], Thorsten M. Schlaeger[1], George Q. Daley[1], Darryl C. Zeldin[6] & Leonard I. Zon[1,2]

Haematopoietic stem and progenitor cell (HSPC) transplant is a widely used treatment for life-threatening conditions such as leukaemia; however, the molecular mechanisms regulating HSPC engraftment of the recipient niche remain incompletely understood. Here we develop a competitive HSPC transplant method in adult zebrafish, using *in vivo* imaging as a non-invasive readout. We use this system to conduct a chemical screen, and identify epoxyeicosatrienoic acids (EETs) as a family of lipids[1,2] that enhance HSPC engraftment. The pro-haematopoietic effects of EETs were conserved in the developing zebrafish embryo, where 11,12-EET promoted HSPC specification by activating a unique activator protein 1 (AP-1) and *runx1* transcription program autonomous to the haemogenic endothelium. This effect required the activation of the phosphatidylinositol-3-OH kinase (PI(3)K) pathway, specifically PI(3)Kγ. In adult HSPCs, 11,12-EET induced transcriptional programs, including AP-1 activation, which modulate several cellular processes, such as migration, to promote engraftment. Furthermore, we demonstrate that the EET effects on enhancing HSPC homing and engraftment are conserved in mammals. Our study establishes a new method to explore the molecular mechanisms of HSPC engraftment, and discovers a previously unrecognized, evolutionarily conserved pathway regulating multiple haematopoietic generation and regeneration processes. EETs may have clinical application in marrow or cord blood transplantation.

To our knowledge, a screen-based forward-genetic approach to understand transplantation biology has never been attempted. In an effort to quantify HSPC activity, we developed a competitive transplantation system in a transparent mutant zebrafish, *casper*[3], which allows direct visualization of engraftment *in vivo*. We co-injected whole kidney marrow (WKM) cells from two ubiquitous GFP and DsRed2 transgenic donors into *casper* (Fig. 1a), and calculated relative engraftment as the ratio of GFP/DsRed2 intensity (*G*/*R*) within the same kidney region (Fig. 1b). We validated the quantitative potential of this imaging-based approach by comparing with flow cytometry-based analysis of WKM from the same recipient (Fig. 1c). The assay was also sensitive to changes in the relative number of green-to-red donor cells (Fig. 1d). Additionally, our system successfully detected the effects of two known chemical modulators of HSPC engraftment: $dmPGE_2$ (16,16-dimethyl-prostaglandin E_2), a stabilized derivative of PGE_2 (ref. 4), and BIO (6-bromoindirubin-3′-oxime), a GSK-3β inhibitor[5]. We used our assay to screen 480 compounds with known bioactivities, which had been selected to cover diverse signalling pathways (Extended Data Fig. 1a). Ten compounds significantly increased the *G*/*R* ratio reproducibly, including PGE_2 and Ro 20-1724, which activates the cAMP pathway downstream of PGE_2 (refs 4 and 5). The other hits target pathways that previously have not been linked to HSPC engraftment, including 11,12-EET and 14,15-EET (Fig. 1e). These are arachidonic-acid-derived eicosanoids that are synthesized through the cytochrome P450 epoxygenase pathway[1,2] (Extended Data Fig. 1b).

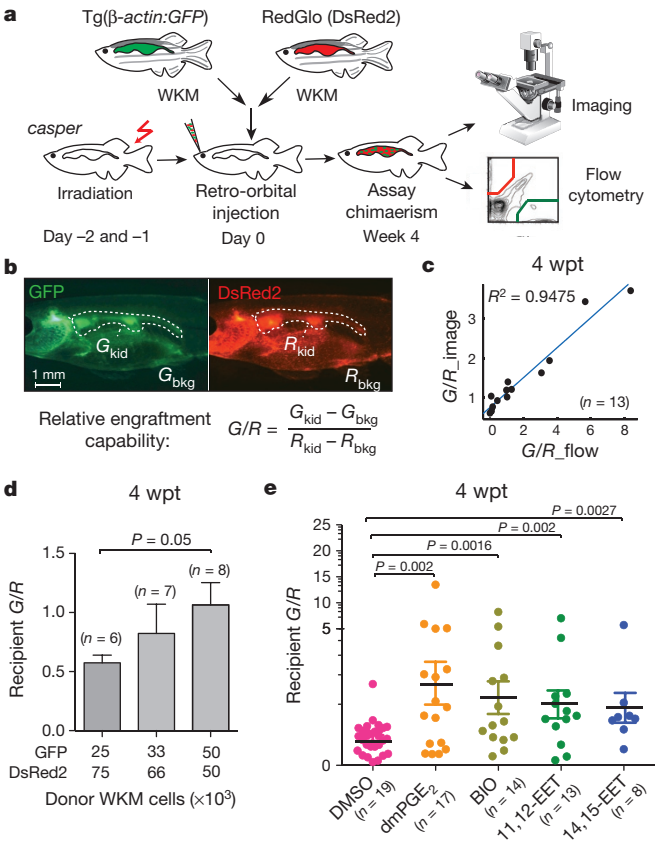

Figure 1 | Zebrafish whole kidney marrow competitive transplantation-based chemical screen identifies EETs as enhancers of marrow engraftment. **a**, Schematic of zebrafish whole kidney marrow (WKM) competitive transplantation. **b**, Calculation of relative engraftment capability (*G*/*R*). White dashed line denotes kidney. G_{kid}/R_{kid}, kidney fluorescence intensity; G_{bkg}/R_{bkg}, background fluorescence intensity. **c**, The *G*/*R* ratios from imaging linearly correlated with flow cytometry analysis of the same recipients (linear regression). wpt, weeks post-transplant. **d**, Serial dilution competitive transplantation with varying donor GFP/DsRed2 ratios. **e**, Four-hour transient chemical treatment increased WKM engraftment. 11,12- and 14,15-EET, 0.5 μM. Unpaired two-tailed *t*-test; mean and s.e.m. (**d**, **e**).

[1]Stem Cell Program and Division of Haematology/Oncology, Boston Children's Hospital and Dana-Farber Cancer Institute, Howard Hughes Medical Institute, Harvard Stem Cell Institute, Harvard Medical School, Boston, Massachusetts 02115, USA. [2]Chemical Biology Program, Harvard University, Cambridge, Massachusetts 02138, USA. [3]Department of Hematology and Oncology, Dr. von Hauner Children's Hospital, Ludwig-Maximilians University, 80337 Munich, Germany. [4]Center for Vascular Biology Research, Beth Israel Deaconess Medical Center, Harvard Medical School, Boston, Massachusetts 02115, USA. [5]Department of Haematology, St Jude Children's Research Hospital, Memphis, Tennessee 38105-3678, USA. [6]Division of Intramural Research, National Institute of Environmental Health Sciences, National Institutes of Health, Research Triangle Park, North Carolina 27709, USA.
*These authors contributed equally to this work.

A gene expression study previously reported mouse *Cyp2j6*, a cytochrome P450 epoxygenase, as one of the 93 genes enriched in long-term haematopoietic stem cells[6].

Despite years of research on the potent effects of EETs in numerous physiological processes[7–9,22], knowledge about their direct target(s) and downstream pathway(s) is still very limited. To tackle this problem, a robust system allowing easy genetic perturbation is crucial. As adult regeneration often reactivates pathways important for development, we decided to probe the effects of EETs on haematopoiesis during embryo development. Analogous to mammalian development, zebrafish HSPCs form from a *flk1*+ population, named haemogenic endothelium, at 24 hours post fertilization (hpf), and become *runx1*+ at 36 hpf in the evolutionarily conserved aorta–gonad–mesonephros (AGM) region[10–12]. HSPCs enter the circulation after they emerge from the AGM[11–13], and seed the caudal haematopoietic tissue (CHT), a secondary haematopoietic site equivalent to the mammalian fetal liver[14,15] (Fig. 2a). The 11,12-EET treatment between 24 and 36 hpf strongly increased the HSPC marker *runx1* in the AGM, and surprisingly induced *runx1* in a non-haematopoietic region of the tail mesenchyme, where *runx1* is not normally expressed (Fig. 2b). This indicates 11,12-EET might be inducing a conserved transcriptional program. We confirmed this AGM phenotype with *in vivo* time-lapse imaging of HSPC birth from the haemogenic endothelium. Tg(*CD41:GFP; flk1:DsRed2*) embryos treated with 11,12-EET starting at 24 hpf showed a significant increase in the number of double-positive HSPCs in the AGM from 30 to 46 hpf (Fig. 2c, d). Single-cell analysis showed that this change is mainly due to a significant increase in the frequency of HSPCs directly specified from the haemogenic endothelium, while no increase in the rate of cell division or AGM retention was observed (Extended Data Fig. 2). The additional HSPCs produced after 11,12-EET treatment successfully homed to their next niche, resulting in increased numbers of HSPCs in the CHT, which was verified by *in situ* hybridization for the HSPC marker *cmyb* (Fig. 2e and Extended Data Fig. 3). Time-lapse imaging of Tg(*Runx1+23:GFP*) zebrafish showed that 11,12-EET treatment between 24 and 48 hpf increased the rate of arrival of GFP$^+$ HSPCs to the CHT (Fig. 2f and Supplementary Videos 1 and 2), presumably owing to enhanced HSPC specification in the AGM.

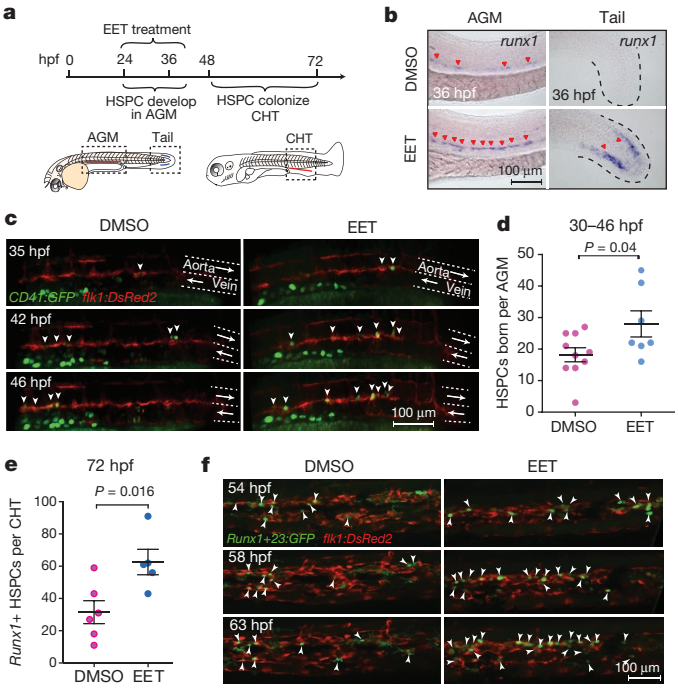

Figure 2 | 11,12-EET enhances HSPC specification in the zebrafish embryo AGM. **a**, Schematic of HSPC development in zebrafish embryos. **b**, Representative images of whole-mount *in situ* hybridization showing 11,12-EET (24–36 hpf treatment) induced HSPC marker *runx1* in the AGM and a tail non-haematopoietic tissue (>8 independent experiments, $n > 100$). **c**, **d**, 11,12-EET (24–46 hpf) enhanced *CD41:GFP/flk1:DsRed2* double-positive HSPCs (white arrowheads) emerging in the AGM. Arrows indicate blood flow. **e**, **f**, Same treatment increased the number of HSPCs in the CHT. **e**, mCherry$^+$ HSPCs quantified in the Tg(*Runx1+23:mCherry*) CHT. **f**, Representative montage images of *Runx1+23:GFP* HSPCs (white arrowheads) engrafting CHT. *flk1:DsRed2*, endothelial cells. Unpaired two-tailed *t*-test, mean and s.e.m. (**d**, **e**).

To dissect the molecular mechanism leading to *runx1* induction further, we performed microarray analysis on 11,12-EET-treated 36-hpf embryos (Supplementary Table 3). The upregulation of multiple activator protein 1 (AP-1) family transcription factors, including *fosl2*, and duplicated orthologues of human JUNB, *junb* and *junbl*, were among the most prominent changes. Whole-mount *in situ* hybridization confirmed the induction both in the AGM and the non-haematopoietic region of the tail mesenchyme (Fig. 3d, top two rows). AP-1 messenger RNA transcripts were detectable within 1 h of 11,12-EET treatment and insensitive to the protein translation inhibitor cycloheximide (Extended Data Fig. 4a, b), indicating that AP-1 members are immediate targets of EET signalling. By contrast, *runx1* induction required at least 4 h of 11,12-EET treatment and was completely blocked by cycloheximide (Extended Data Fig. 4c). Therefore, we proposed that EET-induced AP-1 expression is necessary for increasing *runx1* transcription.

To test this hypothesis genetically, we globally knocked down AP-1 with anti-sense morpholinos targeting *junb* and *junbl*, which blocked *runx1* expression without affecting endothelial cells of the AGM (Extended Data Fig. 5), suggesting that AP-1 might be required for HSPC specification from haemogenic endothelium. To test whether *AP-1* function is autonomous to the haemogenic endothelium, we delivered a dominant-negative form of JunB protein (dnJUNB) specifically to the *flk1*+ endothelial cells, before the induction of *runx1*, to functionally inhibit all AP-1 activity. Although *flk1:dnJUNB* did not significantly reduce the expression of *runx1* in DMSO-treated embryos, it suppressed the EET-induced increase of *runx1* in the AGM (Fig. 3a, b). Combined with the gene expression data, these genetic analyses showed that 11,12-EET activates an AP-1 and *runx1* transcriptional cascade of cell-fate specification autonomous to the haemogenic endothelium.

In an effort to define downstream signalling events for 11,12-EET, we performed a chemical suppressor screen in zebrafish embryos by examining the capability of various chemicals to suppress the 11,12-EET-induced AP-1 and *runx1* gene signature (Fig. 3c). Several PI(3)K inhibitors completely blocked the signature without detrimental effects to overall embryonic development (Fig. 3d, e and Extended Data Fig. 6a). To interrogate specific PI(3)K catalytic subunits, we assayed subunit-specific chemical inhibitors and morpholinos targeting individual class I PI(3)K subunits. Among α-, β-, γ- and δ-subunits of PI(3)K, only PI(3)Kγ loss of function specifically abrogated the *runx1* induction in the AGM and tail non-haematopoietic tissue (Extended Data Fig. 6b, c). Furthermore, 11,12-EET enhanced PI(3)K activity in immortalized human umbilical vein endothelial cells, assayed by Akt phosphorylation (data not shown). No such increase was seen in human umbilical cord blood CD34$^+$ HSPCs, although EET-induced gene expression changes could be partially blocked in these cells by co-treatment with PI(3)K inhibitors. This indicates PI(3)K functions either directly downstream of 11,12-EET or as a parallel pathway, depending on the cellular context. In either case, PI(3)K activity is required for inducing the AP-1 and *runx1* transcription cascade in the AGM.

To understand how 11,12-EET treatment leads to increased engraftment in already-specified HSPCs, we performed RNA-sequencing in human umbilical cord blood CD34$^+$ HSPCs and a human myeloid cell line (U937), and used Ingenuity Pathway Analysis (IPA) to decipher the biological pathways regulated by 11,12-EET in both cell types

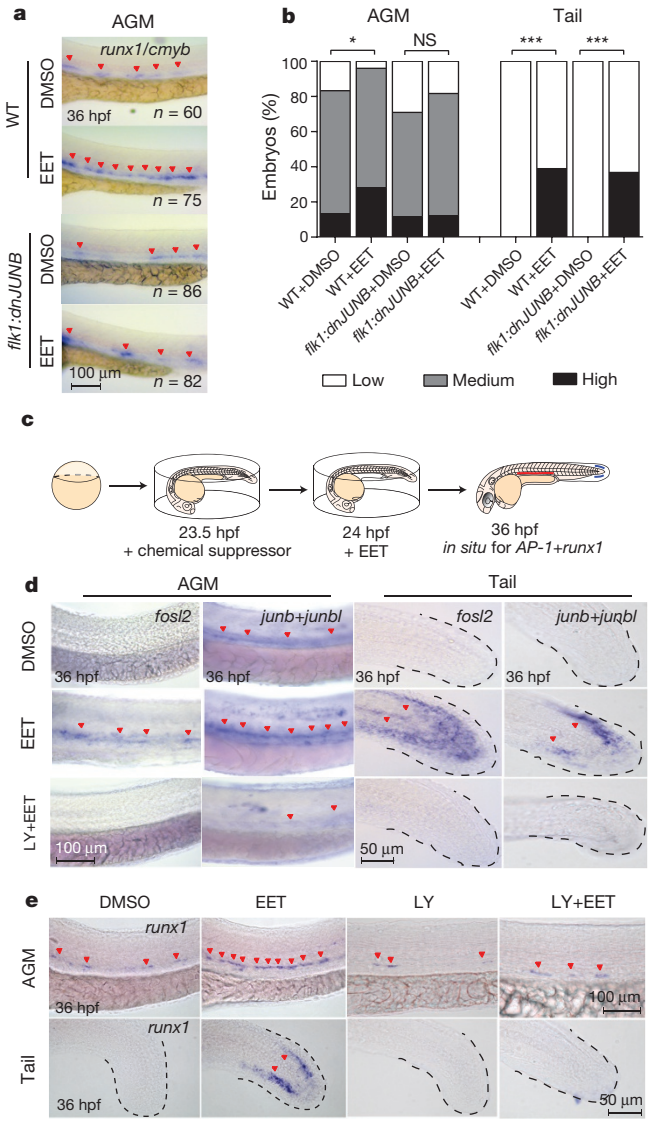

Figure 3 | 11,12-EET induces a PI(3)K-dependent AP-1/*runx1* transcriptional program to increase HSPC specification. **a**, **b**, Stable *flk1:dnJUNB-2A-GFP* expression blocking AP-1 function suppressed 11,12-EET-enhanced HSPCs in the AGM. Representative images of *runx1* and *cmyb in situ* hybridization (**a**) and quantification (**b**) after 11,12-EET treatment (24–36 hpf). Embryos scored as high, medium or low *runx1* and *cmyb*, summed across 4 experiments. $*P = 0.01$, $***P < 0.0001$, Chi-square. NS, not significant; WT, wild-type. **c**, Schematic of chemical screen for EET signalling pathway suppressors. **d**, **e**, 11,12-EET induced AP-1 family transcription factors (*fosl2*, *junb* and *junbl*) (**d**) and *runx1* (**e**), suppressed by cotreatment with the PI(3)K inhibitor LY294002 (LY), in the AGM and tail (**d**, **e**) (three independent experiments, $n > 40$). Same images from Fig. 2b were used as staining controls (**e**).

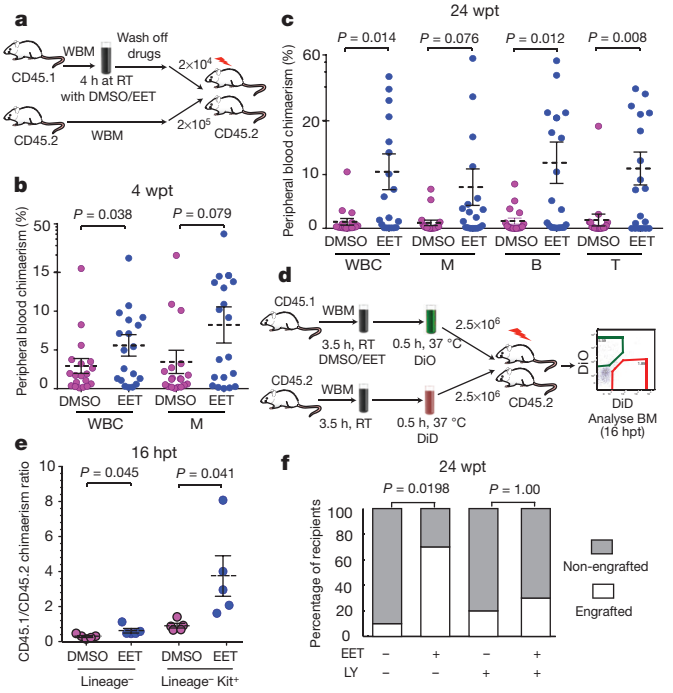

Figure 4 | 11,12-EET enhances HSPC engraftment and homing in mammals. **a**, Schematic of mouse WBM competitive transplantation. RT, room temperature. **b**, **c**, Four hours of 11,12-EET treatment promoted short-term WBM engraftment at 4 wpt (**b**) and long-term multilineage engraftment at 24 wpt (**c**). B, B cells; M, myeloid cells; T, T cells; WBC, white blood cells. Two independent experiments combined, $n = 20$ total. **d**, Schematic of WBM competitive homing assay. DiD and DiO denote cell-labelling solutions. **e**, 11,12-EET increased homing efficiency of Lin^- cells and Lin^- Kit^+ HSPCs ($n = 5$). **f**, PI(3)K activation is required for EET-enhanced mouse WBM engraftment ($n = 10$). LY, 10 μM LY294002. Recipients characterized as engrafted or non-engrafted based on peripheral blood WBC chimaerism, two-tailed Fisher's exact test (**b**, **f**); unpaired two-tailed *t*-test (**c**, **e**), mean and s.e.m.

(Extended Data Fig. 7 and Supplementary Table 4). Cell-to-cell signalling and cellular movement networks topped the list of activated biological pathways, including the AP-1 members, which have been shown to modulate cell migration in many cell types[16,17]. AP-1 thus seems to be a common target of EET signalling, which leads to the induction of *runx1* in the haemogenic endothelium (Fig. 3), and probably supports cell migration and cell–cell signalling of already-specified haematopoietic cells. By contrast, *RUNX1* is not upregulated in already-specified HSPCs, which is consistent with previous studies showing that *Runx1* is dispensable for HSPCs to engraft later haematopoietic sites[18]. Several cytokines, such as *CXCL8*, *OSM* and *CCL2*, were also upregulated and involved in the cell migration network.

These data show that besides promoting HSPC specification from the haemogenic endothelium, 11,12-EET can also directly induce gene expression programs beneficial for engraftment in already-specified HSPCs. Similarly, 11,12-EET treatment of zebrafish embryos after 48 hpf, when AGM HSPC production has already completed, leads to increased HSPCs in the CHT in a PI(3)Kγ-dependent manner, without affecting cell apoptosis or proliferation (Extended Data Fig. 8). Our data strongly suggest that 11,12-EET modulates cell migration and cell–cell interaction during HSPC engraftment.

To test the evolutionary conservation of EET-induced haematopoietic phenotypes, we examined the effect of 11,12-EET on HSPC engraftment in mammalian bone marrow competitive transplantation. Consistently, 11,12-EET promoted greater short-term chimaerism by 4 weeks post-transplant compared to control-treated cells (Fig. 4a, b). Even up to 24 weeks, EET-treated marrow maintained greater multi-lineage contribution (Fig. 4c). Enhanced short- and long-term engraftment suggests that 11,12-EET may affect both stem and progenitor cells, perhaps by establishing a competitive advantage at the early stage of engraftment. In a whole-bone-marrow (WBM) homing assay, we found 11,12-EET promoted the initial seeding of progenitor cells in the bone marrow (Fig. 4d, e). The early effect could be due to an enhanced cell migration and cell–cell signalling program, since assaying cell proliferation or apoptosis in whole marrow immediately after 11,12-EET treatment did not show significant changes (Extended Data Fig. 9). However, this does not exclude the possibility of a later onset of anti-apoptotic effects on transplantation. Finally we found transient inhibition of PI(3)K partially blocked EET-induced enhancement of long-term, multi-lineage engraftment after mouse

bone marrow transplant (Fig. 4f). Thus, the EET effect on enhancing HSPC engraftment is evolutionarily conserved in fish and mammals.

Our unbiased chemical genetic studies establish a new eicosanoid pathway for haematopoiesis, which increases HSPC specification in the AGM by inducing AP-1 and *runx1*, and also enhances HSPC engraftment by modulating several biological pathways, such as migration and cell–cell signalling. Previous work in our laboratory discovered a different eicosanoid, PGE_2, could also enhance marrow engraftment[4,5]. Both PGE_2 and EETs are arachidonic-acid-derived eicosanoids that are locally produced near wounds, and may facilitate progenitor recruitment, engraftment and proliferation. Despite their common origin, the underlying molecular signalling mechanisms and activities of PGE_2 and EETs are different (Supplementary Table 5). Although the direct receptor for EETs is unknown, several studies have provided biochemical evidence that EETs bind to a G-protein-coupled receptor (GPCR)[19,20]. GPCRs signal through various Gα subunits[21]. Previously, we showed that PGE_2 signals through the cAMP-dependent Gαs-coupled PGE_2 receptor for its pro-haematopoietic effects[5]. Using chemical inhibition and genetic loss-of-function approaches, we screened all families of zebrafish Gα subunits. Notably, we found that *gna12* and *gna13* are specifically required for EET-induced AP-1 and *runx1* expression (Extended Data Fig. 10). Inhibiting Gαs did not suppress the EET phenotypes, indicating that EETs and PGE_2 have different signalling mechanisms.

During marrow transplantation, the achieved chimaerism over time is critical, and the time to adequate neutrophil engraftment is an important milestone for treatment success. In addition to improving long-term repopulation, EETs seem to have a prominent effect on progenitor engraftment, as shown by increased chimaerism early after transplantation. Our studies highlight the importance of lipid mediators in regulating HSPC engraftment, and the manipulation of these pathways could have clinical impact for patients undergoing transplantation.

Online Content Methods, along with any additional Extended Data display items and Source Data, are available in the online version of the paper; references unique to these sections appear only in the online paper.

Received 31 October 2012; accepted 11 May 2015.

1. Spector, A. A. & Kim, H.-Y. Y. Cytochrome P450 epoxygenase pathway of polyunsaturated fatty acid metabolism. *Biochim. Biophys. Acta* **1851,** 356–365 (2015).
2. Node, K. *et al.* Anti-inflammatory properties of cytochrome P450 epoxygenase-derived eicosanoids. *Science* **285,** 1276–1279 (1999).
3. White, R. M. *et al.* Transparent adult zebrafish as a tool for *in vivo* transplantation analysis. *Cell Stem Cell* **2,** 183–189 (2008).
4. North, T. E. *et al.* Prostaglandin E2 regulates vertebrate haematopoietic stem cell homeostasis. *Nature* **447,** 1007–1011 (2007).
5. Goessling, W. *et al.* Genetic interaction of PGE2 and Wnt signaling regulates developmental specification of stem cells and regeneration. *Cell* **136,** 1136–1147 (2009).
6. Forsberg, E. C. *et al.* Molecular signatures of quiescent, mobilized and leukemia-initiating hematopoietic stem cells. *PLoS ONE* **5,** e8785 (2010).
7. Panigrahy, D., Greene, E. R., Pozzi, A., Wang, D. W. & Zeldin, D. C. EET signaling in cancer. *Cancer Metastasis Rev.* **30,** 525–540 (2011).
8. Pfister, S. L., Gauthier, K. M. & Campbell, W. B. Vascular pharmacology of epoxyeicosatrienoic acids. *Adv. Pharmacol.* **60,** 27–59 (2010).
9. Wang, Y. *et al.* Arachidonic acid epoxygenase metabolites stimulate endothelial cell growth and angiogenesis via mitogen-activated protein kinase and phosphatidylinositol 3-kinase/Akt signaling pathways. *J. Pharmacol. Exp. Ther.* **314,** 522–532 (2005).
10. Lam, E. Y., Hall, C. J., Crosier, P. S., Crosier, K. E. & Flores, M. V. Live imaging of Runx1 expression in the dorsal aorta tracks the emergence of blood progenitors from endothelial cells. *Blood* **116,** 909–914 (2010).
11. Bertrand, J. Y. *et al.* Haematopoietic stem cells derive directly from aortic endothelium during development. *Nature* **464,** 108–111 (2010).
12. Kissa, K. & Herbomel, P. Blood stem cells emerge from aortic endothelium by a novel type of cell transition. *Nature* **464,** 112–115 (2010).
13. Boisset, J. C. *et al. In vivo* imaging of haematopoietic cells emerging from the mouse aortic endothelium. *Nature* **464,** 116–120 (2010).
14. Murayama, E. *et al.* Tracing hematopoietic precursor migration to successive hematopoietic organs during zebrafish development. *Immunity* **25,** 963–975 (2006).
15. Tamplin, O. J. *et al.* Hematopoietic stem cell arrival triggers dynamic remodeling of the perivascular niche. *Cell* **160,** 241–252 (2015).
16. Renaud, S. J., Kubota, K., Rumi, M. A. & Soares, M. J. The FOS transcription factor family differentially controls trophoblast migration and invasion. *J. Biol. Chem.* **289,** 5025–5039 (2014).
17. Gilan, O. *et al.* PR55α-containing protein phosphatase 2A complexes promote cancer cell migration and invasion through regulation of AP-1 transcriptional activity. *Oncogene* **34,** 1333–1339 (2015).
18. Chen, M. J., Yokomizo, T., Zeigler, B. M., Dzierzak, E. & Speck, N. A. Runx1 is required for the endothelial to haematopoietic cell transition but not thereafter. *Nature* **457,** 887–891 (2009).
19. Chen, Y., Falck, J. R., Manthati, V. L., Jat, J. L. & Campbell, W. B. 20-Iodo-14,15-epoxyeicosa-8(Z)-enoyl-3-azidophenylsulfonamide: photoaffinity labeling of a 14,15-epoxyeicosatrienoic acid receptor. *Biochemistry* **50,** 3840–3848 (2011).
20. Yang, W. *et al.* Characterization of epoxyeicosatrienoic acid binding site in U937 membranes using a novel radiolabeled agonist, 20–125i-14,15-epoxyeicosa-8(Z)-enoic acid. *J. Pharmacol. Exp. Ther.* **324,** 1019–1027 (2008).
21. Lappano, R. & Maggiolini, M. G protein-coupled receptors: novel targets for drug discovery in cancer. *Nature Rev. Drug Discov.* **10,** 47–60 (2011).
22. Frömel, T. *et al.* Soluble epoxide hydrolase regulates hematopoietic progenitor cell function via generation of fatty acid diols. *Proc. Natl Acad. Sci. USA* **109,** 9995–10000 (2012).

Supplementary Information is available in the online version of the paper.

Acknowledgements We thank C. R. Lee, M. L. Edin and N. Gray for providing reagents; Y. Zhou, A. Dibiase, S. Yang, S. Datta, P. Manos, R. Mathieu and M. Ammerman for technical assistance; H. Huang for providing graphic illustration; R. M. White, T. E. North and C. Mosimann for discussion. Microarray studies were performed by the Molecular Genetics Core Facility at Boston Children's Hospital, supported by NIH-P50-NS40828 and NIH-P30-HD18655. S. Li in Y. Zhang's laboratory at the Longwood HHMI joint core facility helped with RNA-seq. L.I.Z. and G.Q.D. are Howard Hughes Medical Institute (HHMI) investigators. This work was supported by HHMI and National Institutes of Health (NIH) grants R01 HL04880, P015PO1HL32262-32, 5P30 DK49216, 5R01 DK53298, 5U01 HL10001-05, R24 DK092760, and 1R01HL097794-04 (to L.I.Z.). This work was also funded, in part, by the Intramural Research Program of the NIH, National Institute of Environmental Health Sciences (Z01 ES025034 to D.C.Z.), the National Cancer Institute grant ROCA148633-01A5 (D.P.), and DFG and Care-for-Rare Foundation (V.B.).

Author Contributions P.L. and L.I.Z. designed the study, analysed data and wrote the manuscript, with help from J.L.L. and V.B. P.L. developed the zebrafish competitive transplantation and performed the chemical screen with technical help from E.K.P. P.L. performed the mouse experiments with technical help from T.V.B., S.M. and G.C.H. P.L. performed the zebrafish microarray and embryo chemical/genetic suppressor screens with technical help from E.B.R. J.L.L. performed zebrafish embryo genetic studies and AGM timelapse imaging. V.B. performed RNA-seq and analysis on human cells with technical help from F.G.B. O.J.T. performed CHT time-lapse imaging. T.M.S. provided the chemical library. D.P. and D.C.Z. offered reagents and information related to the EET study. All authors discussed the results and commented on the manuscript.

Author Information The gene expression profiling data have been deposited in the Gene Expression Omnibus (GEO) under the accession code GSE66767. Reprints and permissions information is available at www.nature.com/reprints. The authors declare competing financial interests: details are available in the online version of the paper. Readers are welcome to comment on the online version of the paper. Correspondence and requests for materials should be addressed to L.I.Z. (zon@enders.tch.harvard.edu).

METHODS

Zebrafish strains. Zebrafish were maintained in accordance with Animal Research Guidelines at Boston Children's Hospital (BCH). The following transgenic zebrafish were used in this study: Tg(*β-actin:GFP*)[23], *casper*[3], RedGlo (ubiquitous *DsRed2* transgenic)[24], Tg(*flk1:DsRed2*)[25], Tg(*CD41:GFP*)[26], Tg(*Runx1+23:mCherry*)[15] and Tg(*Runx1+23:GFP*)[15]. The +23 enhancer region of mouse *Runx1* was used to drive HSPC-specific expression[27]. Tg(*flk1:dnJUNB-2A-GFP*) was constructed by cloning a human JUNBΔN into a *tol2* transgenesis vector[28].

Chemical treatment. The ICCB Known Bioactive Library was purchased from BIOMOL (Enzo Life Sciences) and used for the adult zebrafish transplantation-based chemical screen. Chemicals were diluted at a 1:200 ratio. Chemicals used for the secondary round of screening for confirmation were from a different aliquot of the library, independent of the primary screen plate. 11,12-EET (Cayman Chemical, 50511) was resuspended in DMSO with original organic solvent evaporated. AS605240 (Sigma-Aldrich A0233) was resuspended in DMSO. The following chemicals were used for zebrafish marrow treatment: $dmPGE_2$ (Cayman, 14750), 10 μM; BIO (EMD), 0.5 μM. 0.5 μM 11,12-EET and 14,15-EET were used for zebrafish WKM treatment (Fig. 1e); 2 μM 11,12-EET for all mouse WBM treatment (Fig. 4); and 5 μM 11,12-EET for all zebrafish embryo treatment (Figs 2 and 3). The concentrations were chosen based on dose titration pilot experiments with doses spanning 0.1 to 50 μM. For the chemical suppressor screen, the suppressors were added 30 min before 11,12-EET. Zebrafish embryos were incubated with inhibitors at three different concentrations. The highest effective concentrations tested without causing general toxicity are listed in Supplementary Table 1.

Adult zebrafish kidney marrow transplantation and chemical screen. Adult zebrafish transplantation-based chemical screen was done at the human embronyic stem cell core at BCH. Three-month-old *casper* recipients (both male and female) received split-dose irradiation of 15 Gy each two days and one day before transplantation. Adult zebrafish kidney marrow cells from multiple donors were dissected, pooled together, processed into single-cell suspension and injected retro-orbitally as described previously[29]. Tg(*β-actin:GFP*) WKM cells were incubated with DMSO control or chemicals in 0.9× DPBS plus 5% heat-inactivated FBS for 4 h at room temperature, at a density of 1,000 cells μl^{-1}. Chemicals were washed off before 20,000 treated Tg(*β-actin:GFP*) WKM and 80,000 untreated RedGlo WKM were mixed together and co-injected into irradiated *casper* recipients. The number of recipients per treatment condition in the chemical screen ($n = 10$) was estimated based on preliminary experiments comparing the WKM treated with DMSO or the positive control chemical, $dmPGE_2$. In each experiment, recipients were randomly assigned to each treatment group. All primary hits were cherry-picked and tested in a secondary round of screening ($n = 10$ each). Recipients that died before 4 wpt, mostly owing to infection, were excluded from the analysis. No statistically significant association was observed between recipients' survival rate and a particular drug treatment.

Adult zebrafish fluorescence imaging and quantification. All zebrafish WKM transplantation results shown were obtained at 4 wpt. Transplanted adult *casper* recipients were anaesthetized with 0.2% Tricaine and imaged using a Zeiss Discovery V8 fluorescence stereomicroscope with GFP/RFP filters. To quantify the relative engraftment level in adult zebrafish, the kidney region was manually annotated for each fish, and the average fluorescence intensity of GFP and DsRed2 within the same region was measured (G_{kid} and R_{kid}) using ImageJ. The average background fluorescence intensity (G_{bkg} and R_{bkg}) was measured in a region outside the fish and a mean from multiple images within an experiment was used for all the background subtraction. The relative engraftment level was calculated as $G/R = (G_{kid} - G_{bkg})/(R_{kid} - R_{bkg})$. The investigator analysing the data was blinded to the chemical treatment conditions. For the chemical treatment and screen results (Fig. 1e), the mean G/R in the DMSO group was normalized to 1, and all other groups were normalized to the mean G/R of DMSO. Normalized results from 2–3 independent experiments were pooled for the same chemical.

Zebrafish embryo live imaging. For live imaging, zebrafish embryos were embedded in agarose as described before[11,15]. Single-frame images or time-lapse movies were taken on a spinning disk confocal microscope with an incubation chamber. Images of HSPC birth in the AGM were taken every 10 min. Images of the CHT engraftment process were taken every 2 min. Image post-processing and the creation of the supplementary videos were done with Fluorender, ImageJ, and Imaris.

Zebrafish embryo whole-mount *in situ* hybridization, anti-sense morpholino knockdown and mRNA overexpression. Whole-mount mRNA *in situ* hybridization experiments were performed based on the standard protocol with some modifications (http://zfin.org/zf_info/zfbook/chapt9/9.8.html). Embryos were scored blindly. All of the morpholinos were initially tested at 2, 4 and 6 ng to decide the effective dosage. If the morpholino did not produce a phenotype at 6 ng, additional higher doses were tested (8, 12 ng), until the morpholino caused toxicity. See Supplementary Table 2 for morpholino sequences. *PtxA* (pertussis toxin A, Gαi inhibitor) mRNA (Addgene, plasmid 16678)[30] was *in vitro* transcribed with SP6 RNA polymerase (Ambion, mMESSAGE mMACHINE SP6, AM1340) and injected into one-cell stage zebrafish embryos at 3 pg per embryo, causing morphological defects but no general toxicity.

Zebrafish embryo proliferation and apoptosis assays. Zebrafish embryos were chemically treated between 48 and 72 hpf, and fixed at 72 hpf. For proliferation analysis, embryos were permeablized and stained with primary antibody against phospho-histone H3, and FITC-conjugated secondary antibody. Embryos were imaged and phospho-H3-positive cells in the CHT were manually counted. Secondary antibody-only control showed no nonspecific staining. For apoptosis analysis, embryos were stained using the colorimetric TUNEL staining kit (Promega).

Cell culture. Human $CD34^+$ cells were isolated from fresh umbilical cord blood by Ficoll separation of mononuclear cells and subsequent positive selection of $CD34^+$ cells using magnetic beads (Miltenyi). Cells were treated in serum-free IMDM media (Sigma-Aldrich) with either DMSO or 5 μM 11,12-EET for 2 h at 37 °C. U937 cells[31] were cultured in RPMI-1640 Medium (Sigma-Aldrich) and 10% FBS at 5% CO_2 in air atmosphere according to the protocol (purchased from ATCC without additional confirmation or examination for mycoplasma contamination). For *in vitro* treatment, cells were serum-starved for 1 h and then treated with either DMSO or 5 μM 11,12-EET for 2 h at 37 °C. The conditions for use of human umbilical cord blood $CD34^+$ cells are governed by the associated institution's Internal Review Board (IRB) on behalf of the DF/HCC in accordance with Department of Health and Human Services regulations at 45 CFR Part 46. Informed consent was obtained from all subjects.

Mouse bone marrow transplant. All mice were maintained according to IACUC approved protocols in accordance with BCH animal research guidelines. Nine-week-old CD45.1 and CD45.2 (C57/BL6) male mice were purchased from Jackson Laboratories and housed for 2–3 weeks before the experiments. All CD45.2 recipients received an 11 Gy split dose of γ-irradiation before transplantation, and were randomly assigned to each treatment group. 20,000 CD45.1 WBM cells from age- and gender-matched BL6 donors were treated in DMEM plus 2% FBS at room temperature for 4 h with 2 μM 11,12-EET. For the suppressor experiment (Fig. 4f), 10 μM LY294002 was added to the cells 30 min before the addition of 11,12-EET. Chemicals were washed off before cells were resuspended in PBS and mixed with 200,000 fresh CD45.2 mouse WBM cells. Donor cells were retro-orbitally injected into CD45.2 recipients. Each treatment condition included 10 recipients per experiment. The 12-week survival rate in each experiment was 90–95%, and recipients that died before 12 wpt were excluded from the analysis.

Mouse peripheral blood chimaerism analysis. Peripheral blood was stained with lineage-specific antibodies and analysed on LSRII (BD Biosciences) to assess engraftment. The following antibodies were used: Gr1 (RB6-8C5), Mac1 (M1/70), B220 (RA3-B2), CD3 (145-2C11) and Ter119 from eBioscience; CD45.1 and CD45.2 from BD Biosciences. The CD45.1 chimaerisms in non-irradiated, untransplanted CD45.2 mice were used as a negative staining control. Recipients with multi-lineage chimaerism above the average negative-control chimaerism plus 3 standard deviations were considered to have multi-lineage engraftment (Fig. 4f).

Mouse competitive homing assay. The mouse competitive homing experiment was performed as described, with modifications[32]. In brief, CD45.1 mouse WBM were treated with either DMSO or 2 μM 11,12-EET at room temperature for 3.5 h at a density of 2×10^6 cells per ml. DiO dye was added to the cell suspension (1:200) and incubated at 37 °C for 30 min. At the same time, WBM from CD45.2 mice were incubated at room temperature for 3.5 h without chemical treatment, then labelled with DiD dye (1:200) at 37 °C for 30 min. After the incubation and labelling, the chemicals and dyes were washed off. The DiO-labelled CD45.1 bone marrow and DiD-labelled CD45.2 WBM were mixed at a 1:1 ratio and competitively transplanted into CD45.2 recipients (2.5×10^6 from each donor). Recipients received total body irradiation of 11 Gy one day before transplantation. 16 h after transplant, the recipients were euthanized and bone marrow was analysed by flow cytometry for both DiO/DiD and surface lineage markers (Gr1, Mac1, B220, CD3, Ter119, from Ebioscience) and c-Kit (2B8, BD Biosciences). The ratio between the percentages of DiO^+ (donor) and DiD^+ (competitor) cells within different cell populations was quantified. DiO and DiD are from Vybrant Multicolor Cell-Labelling Kit (Molecular Probes, V-22889).

Mouse bone marrow apoptosis and proliferation assays. For apoptosis analysis, mouse WBM cells were treated with DMSO or 2 μM 11,12-EET for 4 h *in vitro* and stained using the AnnexinV apoptosis kit (BD Biosciences), together with antibodies against lineage markers, Sca-1 (E13-161.7) and c-Kit (2B8). The 7-AAD^-/annexinV^+ cells are the apoptotic population. For proliferation analysis, mouse WBM were treated with DMSO or 2 μM 11,12-EET for 4 h *in vitro*, in the presence

of 10 μM BrdU, then fixed, permeabilized and stained with anti-BrdU antibody (BD Pharmingen BrdU Flow Kits)[33], together with antibodies against lineage markers, Sca-1 and c-Kit.

Gene expression profiling and IPA analysis. Gene expression profiling data are available in GEO (accession numbers GSE39707 and GSE66767). For the zebrafish embryo gene expression study, total RNA was extracted from 36 hpf zebrafish embryos treated with DMSO or 5 μM 11,12-EET between 24 and 36 hpf, with three biological replicates each and $n = 25$ in each group. Microarray hybridization was performed with the Affymetrix GeneChip Zebrafish Genome Array. Hybridized microarray was background-corrected, normalized and multiple-tested using Goldenspike (http://www2.ccr.buffalo.edu/halfon/spike/) in R/Bioconductor[34]. Genes with $q < 0.1$ by SNR test were considered differentially expressed (Supplementary Table 3). For RNaseq analysis on human cells, total RNA was extracted from treated $CD34^+$ and U937 cells with the RNeasy mini plus kit from Qiagen. After quality control on the Bioanalyzer (Agilent), total RNA was depleted of ribosomal RNA with the RiboZero gold kit (Epicentre). Enriched mRNA was applied to library preparation according to manufacturer's protocol (NEBNext Ultra). After repeated quality control for average DNA input size of 300 base pairs (bp), samples were sequenced on a HiSeq Illumina sequencer with 2×100-bp paired-end reads. Quality control of RNA-Seq data sets was performed by FastQC (http://www.bioinformatics.babraham.ac.uk/projects/fastqc/) and Cutadapt[35] to remove adaptor sequences and low quality regions. The high-quality reads were aligned to UCSC build hg19 of the human genome using Tophat 2.0.11 without novel splicing form calls[36]. Transcript abundance and differential expression were calculated with Cufflinks 2.2.1 (ref. 37). FPKM values were used to normalize and quantify each transcript. $\log_2$(fc) ($\log_2$ fold change), P and q values were calculated. As the experiment was not performed in biological replicates, the P and q values were not taken into consideration for further analysis of the data. Results are listed with a cutoff of $\log_2(\text{fc}) > 0.5$ for upregulated genes and $\log_2(\text{fc}) < -0.5$ for downregulated genes in Supplementary Table 4. Analysis of overlapping upregulated genes in both cell types after EET treatment was done using Venny (http://bioinfogp.cnb.csic.es/tools/venny/index.html). The list of overlapping genes was analysed using IPA (QIAGEN) to map enriched bio-functions.

Statistics. The comparison of multi-lineage engraftment in Fig. 4b and f were done by two-tailed Fisher's exact test by comparing the number of engrafted versus non-engrafted recipients. Using the mean chimaerism plus 2× s.e.m. in the DMSO control group as the cutoff, recipients with a chimaerism higher than the cutoff were considered engrafted (Fig. 4b). Embryos in the *in situ* hybridization experiments were scored blindly and analysed by Chi-square tests or two-tailed Fisher's exact test in the case of small sample sizes. The rest of the statistics were done with unpaired two-tailed t-test. Graphs show mean with s.e.m. No statistical methods were used to predetermine sample size. All the zebrafish embryos, adult zebrafish and mice for transplantation were randomized into each treatment group.

23. Traver, D. *et al.* Transplantation and *in vivo* imaging of multilineage engraftment in zebrafish bloodless mutants. *Nature Immunol.* **4,** 1238–1246 (2003).
24. Blake, A., Crockett, R., Essner, J., Hackett, P. & Nasevicius, A. Recombinant constructs and transgenic fluorescent ornamental fish therefrom. US patent US7,700,825 B2 (2010).
25. Kikuchi, K. *et al.* Retinoic acid production by endocardium and epicardium is an injury response essential for zebrafish heart regeneration. *Dev. Cell* **20,** 397–404 (2011).
26. Ma, D., Zhang, J., Lin, H. F., Italiano, J. & Handin, R. I. The identification and characterization of zebrafish hematopoietic stem cells. *Blood* **118,** 289–297 (2011).
27. Bee, T. *et al.* The mouse *Runx1 +23* hematopoietic stem cell enhancer confers hematopoietic specificity to both *Runx1* promoters. *Blood* **113,** 5121–5124 (2009).
28. Ikebe, D., Wang, B., Suzuki, H. & Kato, M. Suppression of keratinocyte stratification by a dominant negative JunB mutant without blocking cell proliferation. *Genes Cells* **12,** 197–207 (2007).
29. Pugach, E. K., Li, P., White, R. & Zon, L. Retro-orbital injection in adult zebrafish. *J. Vis. Exp.* **34,** 1645 (2009).
30. Slusarski, D. C., Corces, V. G. & Moon, R. T. Interaction of Wnt and a Frizzled homologue triggers G-protein-linked phosphatidylinositol signalling. *Nature* **390,** 410–413 (1997).
31. Sundstrom, C. & Nilsson, K. Establishment and characterization of a human histiocytic lymphoma cell line (U-937). *Int. J. Cancer* **17,** 565–577 (1976).
32. Lam, B. S., Cunningham, C. & Adams, G. B. Pharmacologic modulation of the calcium-sensing receptor enhances hematopoietic stem cell lodgment in the adult bone marrow. *Blood* **117,** 1167–1175 (2011).
33. Challen, G. A., Boles, N., Lin, K. K. & Goodell, M. A. Mouse hematopoietic stem cell identification and analysis. *Cytometry A* **75,** 14–24 (2009).
34. Choe, S. E., Boutros, M., Michelson, A. M., Church, G. M. & Halfon, M. S. Preferred analysis methods for Affymetrix GeneChips revealed by a wholly defined control dataset. *Genome Biol.* **6,** R16 (2005).
35. Martin, M. Cutadapt removes adapter sequences from high-throughput sequencing reads. *EMBnet J.* **17,** 1 (2011).
36. Trapnell, C., Pachter, L. & Salzberg, S. L. TopHat: discovering splice junctions with RNA-Seq. *Bioinformatics* **25,** 1105–1111 (2009).
37. Trapnell, C. *et al.* Transcript assembly and quantification by RNA-Seq reveals unannotated transcripts and isoform switching during cell differentiation. *Nature Biotechnol.* **28,** 511–515 (2010).
38. Lee, C. R. *et al.* Endothelial expression of human cytochrome P450 epoxygenases lowers blood pressure and attenuates hypertension-induced renal injury in mice. *FASEB J.* **24,** 3770–3781 (2010).

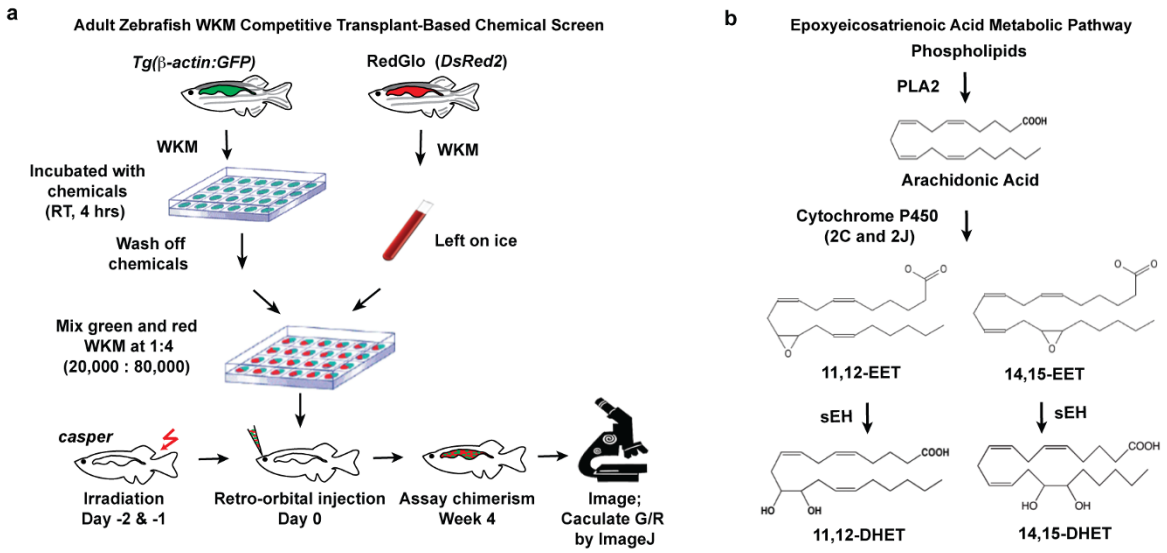

Extended Data Figure 1 | Zebrafish WKM competitive transplantation-based chemical screen identifies EETs as enhancers of marrow engraftment. **a**, WKM from Tg(*β-actin:GFP*) donors were dissected, dissociated as single-cell suspension, and incubated with chemicals at room temperature for 4 h in a round-bottom 96-well plate. Meanwhile, WKM were dissected from RedGlo zebrafish, counted and kept on ice. After the drug treatment, chemicals were washed off and cells were resuspended in 0.9× PBS plus 5% FBS. Approximately 20,000 treated green WKM and 80,000 untreated red WKM were co-injected retro-orbitally into sublethally irradiated *casper* zebrafish ($n = 10$ per chemical). For every independent screening day, negative control (DMSO) and positive control (10 μM $dmPGE_2$) treatments were used for normalization and quality assurance. The engraftment was measured at 4 wpt by fluorescence imaging and ImageJ quantification as described in Fig. 1b. **b**, EET metabolic pathway: arachidonic acid is released by phospholipase A_2 (PLA_2) from the membrane lipid bilayer. EETs are synthesized directly from arachidonic acid by the cytochrome P450 family of epoxygenases, especially 2C and 2J in human[38], and get degraded by soluble epoxide hydrolase (sEH), generating dihydroxyeicosatrienoic acids (DiHET). Four isomers of EET exist *in vivo*: 5,6-, 8,9-, 11,12- and 14,15-EET.

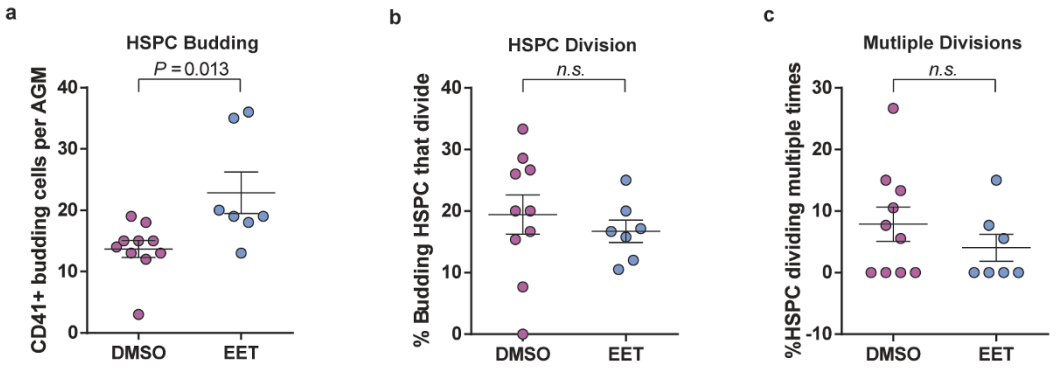

Extended Data Figure 2 | 11,12-EET enhances HSPC specification in the AGM in zebrafish embryos. Tg(*CD41:GFP/flk1:DsRed2*) embryos were treated with DMSO or 5 μM 11,12-EET starting at 24 hpf, then mounted for spinning disc confocal timelapse imaging from 30–46 hpf in the presence of the chemicals. Data are mean and s.e.m., unpaired two-tailed *t*-tests, $n = 10$ for DMSO, $n = 7$ for EET. **a**, More HSPCs are directly specified in EET-treated AGM. Graph shows HSPCs born by direct specification/budding only, excluding cells born by division of an already-budding cell. **b**, **c**, 11,12-EET does not influence the rate of HSPC division in the AGM, shown by per movie, percentage of budding HSPCs that divide at least once (**b**) and divide twice or more (**c**) before leaving the AGM or before the end of timelapse recording.

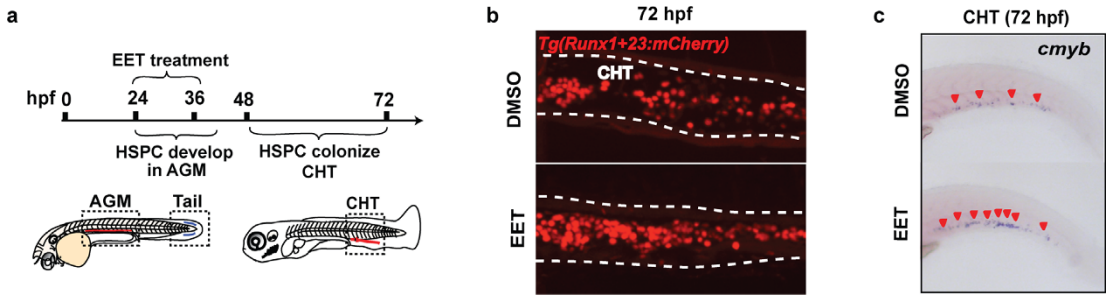

Extended Data Figure 3 | 11,12-EET treatment between 24 and 48 hpf increases the number of HSPCs in the CHT. **a**, Embryos were treated between 24 and 48 hpf with either DMSO or 5 μM 11,12-EET. Chemicals were washed off at 48 hpf, and embryos grew in drug-free environment for another 24 h. **b**, 11,12-EET treatment increased the number of mCherry^{+} HSPCs in the CHT in Tg(*Runx1+23:mCherry*) embryos (see also Fig. 2e). Representative images of the CHT from the two groups. **c**, The same chemical treatment increased the staining of *cmyb*, a HSPC marker, by whole-mount RNA *in situ* hybridization. Representative images from each group (a total of $n > 60$ from three independent experiments).

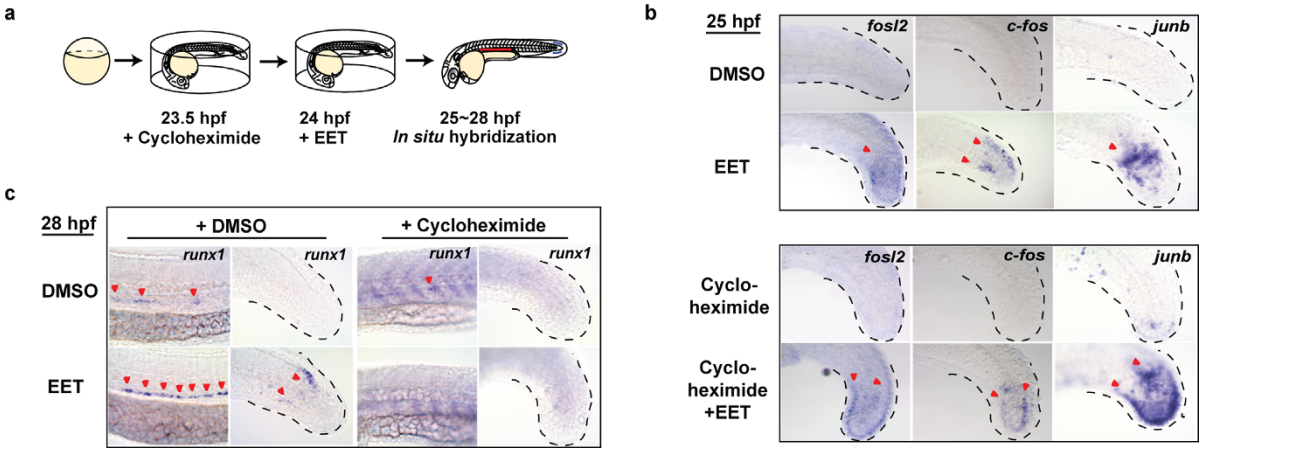

Extended Data Figure 4 | EET signalling pathway activates AP-1 family members as primary transcriptional targets, and *runx1* as a secondary transcriptional target. **a**, Wild-type embryos were incubated with 300 μM cycloheximide, a translation blocker, for 30 min before the addition of 5 μM 11,12-EET at 24 hpf. Embryos were fixed for *in situ* hybridization at 25 hpf or 28 hpf. **b**, AP-1 transcription was induced after 1 h treatment with 11,12-EET, insensitive to cycloheximide inhibition. This means AP-1 induction does not depend on *de novo* protein synthesis, indicating AP-1 members are primary transcriptional targets of the EET signalling pathway. **c**, *runx1* transcription was induced after 4 h treatment with EET (two columns on the left) and cycloheximide completely blocked EET-induced *runx1* expression (two columns on the right). This suggests *runx1* transcription depends on *de novo* protein synthesis of an upstream factor(s) upon EET stimulation, indicating that *runx1* is a secondary transcriptional target of the EET signalling pathway. Representative images from each group (a total of $n > 30$ from two independent experiments).

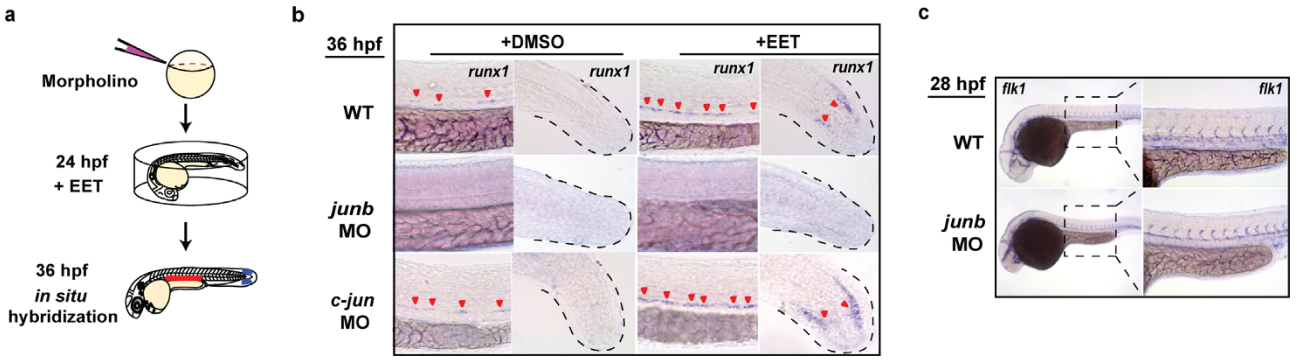

Extended Data Figure 5 | Knocking down *junb* and *junbl* inhibits HSPC specification in the AGM. **a**, Wild-type embryos were injected with antisense morpholinos at the one-cell stage, and treated with DMSO or 5 μM 11,12-EET starting from 24 hpf. Embryos were fixed at 36 hpf for *in situ* hybridization of *runx1*. **b**, Knocking down *junb* completely blocked *runx1* expression at 36 hpf both in the AGM and the tail non-haematopoietic tissue (middle row). By contrast, knocking down *c-jun* did not block the increase of *runx1* (bottom row), consistent with the lack of *c-jun* upregulation in EET-treated embryos (data not shown). **c**, *junb* morphants still developed normal vascular structure in the AGM at 28 hpf, as shown by endothelial marker *flk1*. Representative images from each group (a total of $n > 40$ from three independent experiments).

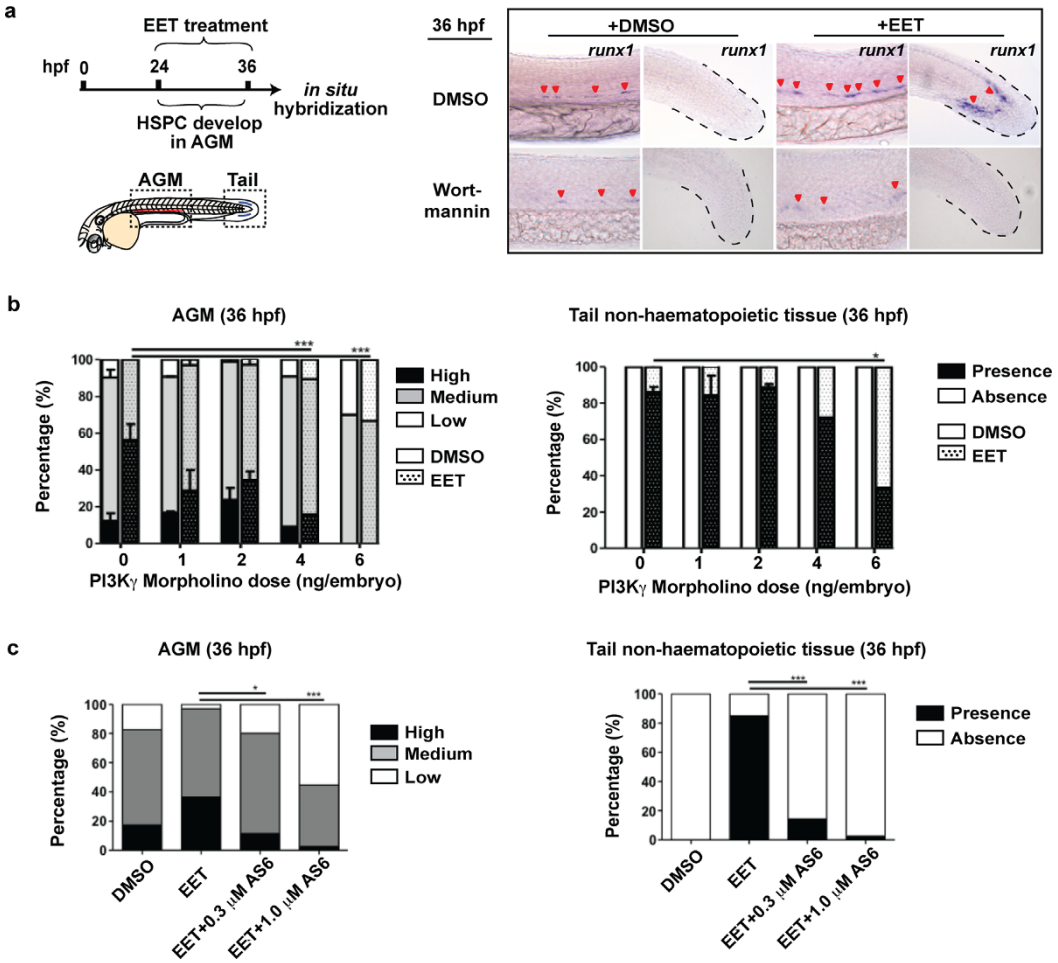

Extended Data Figure 6 | PI(3)Kγ activation is specifically required for EET-induced gene expression signature. **a**, Similar to LY294002 (Fig. 3d–e), another pan-PI(3)K/AKT inhibitor, wortmannin (1 μM), blocked EET-induced *runx1* expression both in the AGM and tail. Representative images from each group (a total of $n > 60$ from three independent experiments). **b**, Morpholinos specific to PI(3)Kγ, but not α, β and δ subunits (data not shown), prevented EET-induced *runx1* in the AGM and tail. Embryos were injected at 1–2-cell stage with the indicated amount of morpholino and treated with DMSO or 5 μM 11,12-EET from 24–36 hpf. *In situ* hybridization for *runx1* performed at 36 hpf and percentages of embryos having high, medium or low expression in the AGM and present or absent expression in the tail are shown. Graph summarizes three experiments, $n \geq 10$ embryos for each condition (0, 1 and 2 ng, data are mean and s.e.m.) or one experiment $n \geq 9$ for all conditions (4 and 6 ng). **c**, The PI(3)Kγ-specific inhibitor AS605240 (AS6) recapitulates the morpholino phenotype. Embryos treated from 24 to 36 hpf with DMSO or 5 μM 11,12-EET, with or without 0.3–1.0 μM AS6, then fixed and stained for *runx1* at 36 hpf. DMSO, $n = 23$; EET, $n = 33$; EET+0.3 μM AS6, $n = 35$; EET+1.0 μM AS6, $n = 38$. $^{*}P < 0.05$, $^{***}P < 0.001$, two-tailed Fisher's exact test.

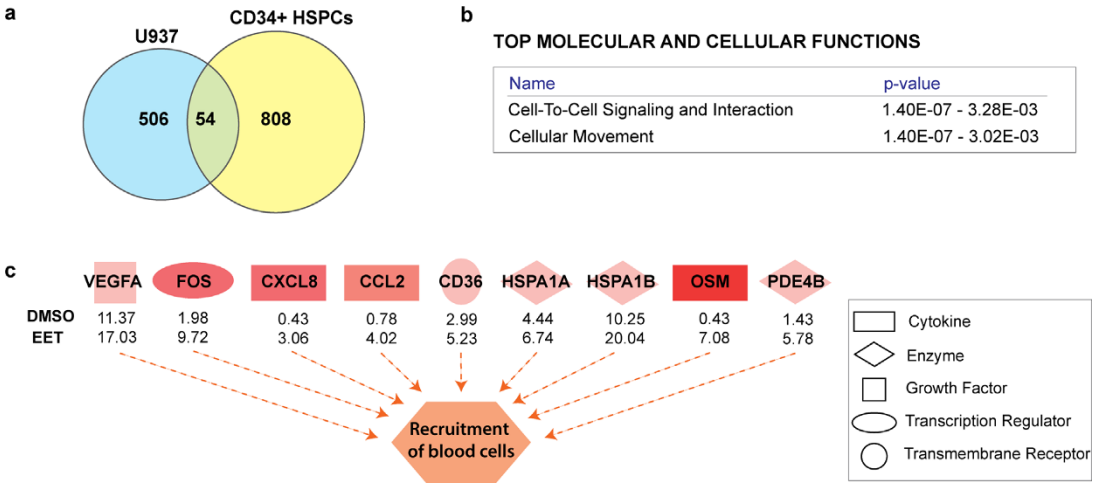

Extended Data Figure 7 | 11,12-EET upregulates genes involved in cell-to-cell signalling and cellular movement in haematopoietic progenitors. **a**, Venn diagram showing a common set of 54 genes upregulated ($\log_2$(fc) > 0.5) after 2 h of 11,12-EET treatment (5 μM), both in human myeloid U937 cells and human umbilical cord $CD34^+$ HSPCs (see also Supplementary Table 4 for lists of up- and downregulated genes). **b**, **c**, Ingenuity Pathway Analysis (IPA) of the overlapping gene set between the two cell types for enrichment of bio-functions. **b**, Biological processes, such as cell-to-cell signalling and cellular movement, were highly enriched, supporting the capability of EETs in enhancing engraftment (see also Supplementary Table 4 for a comprehensive list of all biological functions predicted to be activated or suppressed based on the same gene set). **c**, Activation of recruitment of blood cells is caused by upregulation of chemokines and cytokines such as CXCL8 and OSM after EET treatment, as well as by upregulation of transcription factors, such as AP-1 genes (FOS). Orange dashed arrows depict activation. Shades of red represent the level of activation. Numbers underneath factors show RNaseq FPKM (fragments per kilobase of exon per million reads mapped) values in U937 cells.

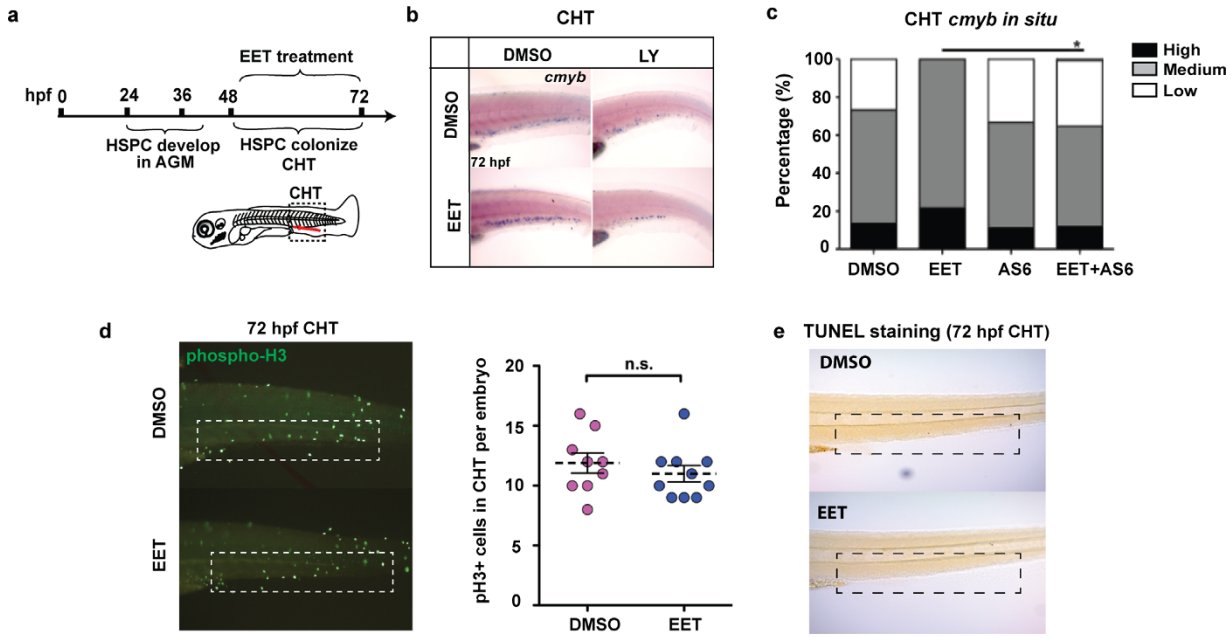

Extended Data Figure 8 | 11,12-EET treatment after HSPC specification still enhances the number of HSPCs in the CHT. **a**, Embryos were treated with DMSO or 5 μM 11,12-EET between 48 and 72 hpf to bypass the HSPC specification process in the AGM. 72-hpf embryos were fixed and tested on the following assays. **b**, *In situ* hybridization for *cmyb*, a marker for HSPCs. EET treatment significantly increased the staining, while LY294002, a pan-PI(3)K inhibitor, suppressed the effect. Representative images from each group (a total of $n > 60$ from four independent experiments). **c**, A PI(3)Kγ-specific inhibitor AS605240 (AS6) also blocked the EET-induced increase of *cmyb* staining. Percentage of embryos having high, medium or low expression in the CHT is shown. $n \geq 11$ for all conditions. Chi-square analysis. **d**, The increase of HSPCs in the CHT is not due to effects on proliferation. Immunofluorescence staining for phospho-histone H3 (pH3) as a marker for proliferating cells. The number of pH3-positive cells was manually counted. Two-tailed *t*-test showed no significant difference between DMSO- versus EET-treated embryos. $n = 9$ for DMSO, $n = 10$ for EET. **e**, TUNEL staining as an assay for apoptotic cells. Apoptosis was minimal in the CHT at 72 hpf. As a staining control, obvious apoptosis was detected in the same embryos in the brain region, and was comparable between DMSO- and EET-treated embryos (data not shown).

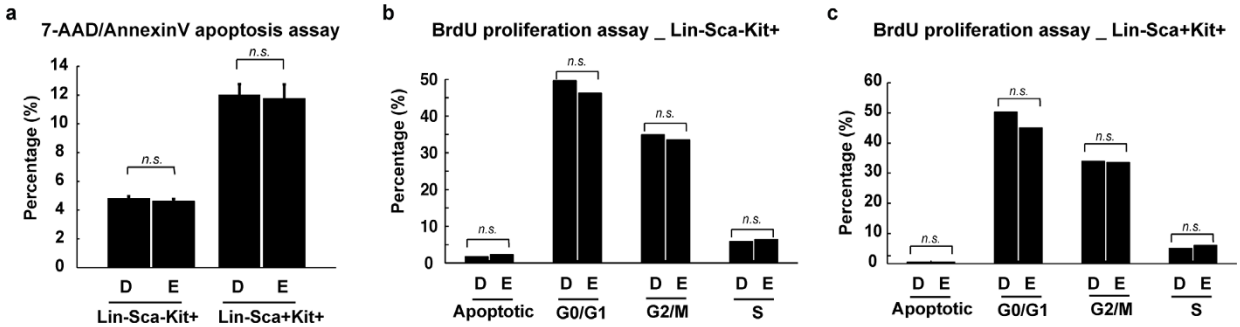

Extended Data Figure 9 | 11,12-EET treatment of mouse WBM does not lead to immediate changes in cell proliferation or apoptosis. **a**, *In vitro* apoptosis assay on WBM treated with DMSO or 2 μM 11,12-EET for 4 h. The 7-AAD-negative and annexinV-positive population are the cells undergoing apoptosis. No significant differences between the two groups were observed either in $Lin^{-}Sca^{-}Kit^{+}$ or $Lin^{-}Sca^{+}Kit^{+}$ progenitor populations ($n = 4$ each), mean and s.e.m. **b**, **c**, *In vitro* proliferation assay on WBM treated with DMSO or 2 μM 11,12-EET for 4 h, in the presence of 10 μM BrdU. No significant differences between the two groups were observed either in $Lin^{-}Sca^{-}Kit^{+}$ (**b**) or $Lin^{-}Sca^{+}Kit^{+}$ populations (**c**) for any cell cycle stage. Unpaired two-tailed *t*-test, $n = 4$ each, bar denotes the mean. D, DMSO; E, EET.

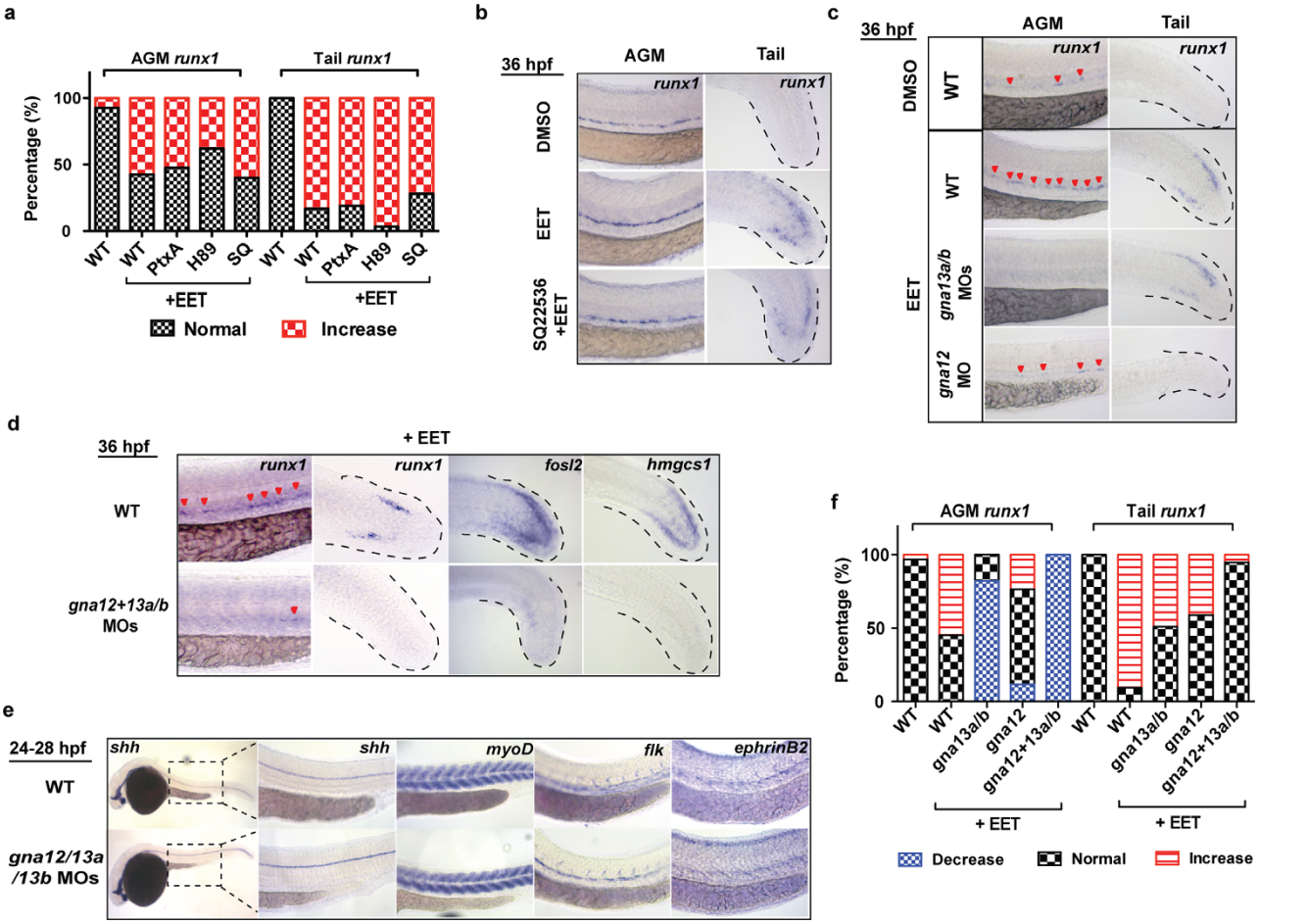

Extended Data Figure 10 | Gα12/13 is specifically required for EET-induced phenotypes in zebrafish embryos. All embryos were treated with DMSO or 5 μM 11,12-EET between 24 and 36 hpf. Chemical inhibitors were added 30 min before EET. mRNA or morpholinos (MO) were injected at the one-cell stage. **a**, **b**, Inhibiting Gαs or Gαi had no effect on EET-induced *runx1* expression. Embryos were categorized into two groups with either normal or increased *runx1* expression level ($n > 20$ each). PtxA, pertussis toxin A, 3 pg, inhibiting Gαi (ref. 30); H89, 5 μM, PKA inhibitor downstream of Gαs[5]; SQ, SQ22536, 50 μM, adenylate cyclase inhibitor downstream of Gαs[5]. Representative images from each group (**b**) (a total of $n > 40$ from two independent experiments). **c**–**f**, Synergistic effects of *gna12/13a/13b* knockdown on suppressing *runx1* expression. Knocking down *gna13a/b* or *gna12* alone partially inhibited EET-induced *runx1* expression in the AGM and tail (**c**). *gna12* MO: 2 ng; *gna13a/13b* MOs: 1 ng each. Triple morpholinos against *gna12*, *gna13a* and *gna13b* (0.67 ng each) completely blocked EET-induced multiple gene expression, including *runx1*, genes in regeneration (*fosl2*) and cholesterol metabolism (*hmgcs1*) (**d**), while other major tissue development processes were not significantly affected, such as notochord (*shh*), muscle (*myoD*), and blood vessels (*flk*, *ephrinB2*) (**e**). **f**, The results were quantified. Embryos were categorized as having decreased, normal or increased *runx1* expression. The bar graph represents the percentage of embryos in each group ($n > 30$).

PLOS | ONE

RESEARCH ARTICLE

Variant rs1801157 in the 3'UTR of SDF-1β Does Not Explain Variability of Healthy-Donor G-CSF Responsiveness

Miriam Schulz[1☯], Darja Karpova[2☯], Gabriele Spohn[2], Annette Damert[2¤a], Erhard Seifried[1,2], Vera Binder[3☯¤b], Halvard Bönig[1,2,4☯*]

1 German Red Cross Blood Service Baden-Württemberg-Hesse, Frankfurt, Germany, **2** Institute for Transfusion Medicine and Immunohematology, Goethe University, Frankfurt, Germany, **3** Department of Pediatric Oncology, Hematology and Clinical Immunology, Medical Faculty, University of Duesseldorf, Duesseldorf, Germany, **4** University of Washington, Department of Medicine, Division of Hematology, Seattle, WA, United States of America

☯ These authors contributed equally to this work.
¤a Current address: Babes-Bolyai University Interdisciplinary Research Institute on Bio-Nano-Sciences, Molecular Biology Center, Cluj-Napoca, Romania
¤b Current address: Stem Cell Program and Division of Hematology/Oncology, Boston Children's Hospital, Harvard Stem Cell Institute, Harvard Medical School, Boston, MA, United States of America
* h.boenig@blutspende.de

OPEN ACCESS

Citation: Schulz M, Karpova D, Spohn G, Damert A, Seifried E, Binder V, et al. (2015) Variant rs1801157 in the 3'UTR of SDF-1ß Does Not Explain Variability of Healthy-Donor G-CSF Responsiveness. PLoS ONE 10(3): e0121859. doi:10.1371/journal.pone.0121859

Academic Editor: Federico Quaini, University-Hospital of Parma, ITALY

Received: December 16, 2014

Accepted: January 26, 2015

Published: March 24, 2015

Data Availability Statement: All relevant data are included within the paper.

Funding: MS is the recipient of a clinician-scientist scholarship, ES and HB are members of the LOEWE Cell and Gene Therapy Frankfurt faculty, funded by Hessian Ministry of Higher Education, Research and the Arts ref.no.: III L 4 518/17.004 (2010/2013). The funders had no role in study design, data collection and analysis, decision to publish, or preparation of the manuscript.

Abstract

The genetics responsible for the inter-individually variable G-CSF responsiveness remain elusive. A single nucleotide polymorphism (SNP) in the 3'UTR of CXCL12, rs1801157, was implicated in X4-tropic HiV susceptibility and later, in two small studies, in G-CSR responsiveness in patients and donors. The position of the SNP in the 3'UTR together with *in-silico* predictions suggested differential binding of micro-RNA941 as an underlying mechanism. In a cohort of 515 healthy stem cell donors we attempted to reproduce the correlation of the CXCL12 3'UTR SNP and mobilization responses and tested the role of miR941 in this context. The SNP was distributed with the expected frequency. Mobilization efficiency for CD34 + cells in WT, heterozygous and homozygous SNP individuals was indistinguishable, even after controlling for gender. miR941 expression in non-hematopoietic bone marrow cells was undetectable and miR941 did not interact with the 3' UTR of CXCL12. Proposed effects of the SNP rs1801157 on G-CSF responsiveness cannot be confirmed in a larger cohort.

Introduction

Allogeneic G-CSF mobilized peripheral blood stem/progenitor cells from healthy volunteer donors have become the source of choice for allogeneic "stem cell" transplantation.[1–3] A hundred-fold difference in G-CSF responsiveness between poorly and well mobilizing donors was noticed early on, but except for an arguable, if anything weak effect of gender no predictors of mobilization response have been identified.[4–6] Several examples suggest that mobilization response is genetically determined: Humans subjected to successive cycles of G-CSF responded

Competing Interests: The authors have declared that no competing interests exist.

with similar mobilization both times.[5] In mice, strain-specific differences in G-CSF responsiveness have been appreciated for decades.[7, 8] The responsible genes remain elusive, however, despite significant efforts. Recently three small studies on autologous donors or healthy volunteer donors suggested a correlation between a single-nucleotide polymorphism (SNP) in the 3'URT of CXCL12ß, rs1801157, and G-CSF mobilization efficiency, which promised to be a break-through discovery in this field.[9–11]

This SNP had previously been described to mediate susceptibility for X4-tropic strains of HiV.[12] Because of the great significance of this observation, it was carefully followed up and in more adequately-sized cohorts shown to be unreproducible.[13] Sparse and contradictory observations have been reported about effects of this SNP on CXCL12 production.[14–17] However, those reports and the position of SNP rs1801157 in the CXCL12 3'UTR suggested a possible influence of miRNAs, as these are known to mediate gene expression by binding to an mRNA's 3'UTR. A seven bases long homologous sequence to the predicted seed of miR941 in the region of SNP rs1801157 was predicted by Target Scan Human (http://www.targetscan.org/) as a putative binding site, although this interaction was not predicted by any other microRNA web-tools. The 4th base of this sequence being the polymorphic one, loss of the miRNA941 binding site of the SNP variant was predicted (Fig. 1A).

We therefore tested the correlation of SNP rs1801157 and G-CSF responsiveness in a representatively sized cohort of healthy volunteer donors. We also tested two prerequisites for miR941 mediated modulation of G-CSF induced mobilization, i.e. expression of miR941 in primary bone marrow (BM) stroma cells and differential interaction by miR941 with the WT- and SNP-variant of the CXCL12 3'UTR.

Material and Methods

Healthy volunteer stem cell donors were subjected to G-CSF induced stem cell mobilization as described (7.5–10 µg/kgBW*d in two divided doses q12h),[18–20] in preparation for stem cell donation. Circulating CD34+ cells were enumerated 2–3 h after the ninth dose of G-CSF, just prior to apheresis, using commercial single-platform flow cytometry assays.[21] With written informed donor consent and permission from the Ethics Committee of Johann Wolfgang Goethe University School of Medicine (permit #190/12), DNA was isolated from pseudonymized left-over blood samples (Qiagen, Hilden, Germany). Circulating CD34+ cell concentration and gender were extracted from our stem cell donor data base. An SSP-PCR was established that distinguishes between WT- and SNP-variants (Fig. 1B). Samples were additionally genotyped for the SNP using Sanger sequencing (Fig. 1C), i.e. all genotyping analyses were performed with two independent methods. Mobilization data were sorted by 3'UTR genotype and gender. miR941 expression in non-hematopoietic BM stroma cells was tested in 20 anonymized CD45-purged BM samples from healthy volunteer donors using miR expression arrays (Miltenyi Biotec, Bergisch Gladbach, Germany) and taqMan qPCR (stem-loop RT primers and assay: Applied Biosystems, Darmstadt, Germany). miR941 binding to the WT- or SNP variant CXCL12 3'UTR was tested by cloning premiR941 (Eurofins, Hamburg, Germany) or SNP-premiR941 (premiR941 mutated in the 4th position of the seed by site directed mutagenesis (Agilent technologies, Böblingen, Germany), to match the sequence of the SNP) into plasmid pSUPER.retro.puro (Oligoengine, Seattle, WA) and cloning of the whole 3'UTR of WT or SNP CXCL12ß (3285 bp) into the dual-luciferase plasmid pmirGLO (Promega, Mannheim, Germany). Plasmids were co-expressed in HEK 293 cells via lipofectamine (Life Technologies, Darmstadt, Germany). Transfection efficiency and expression of miR941 were tested by TaqMan qPCR (Applied Biosystems). Firefly and renilla luciferase activity were measured with the Dual-Glo Luciferase Assay System (Promega). In addition to miR941 expression by p.SUPER.

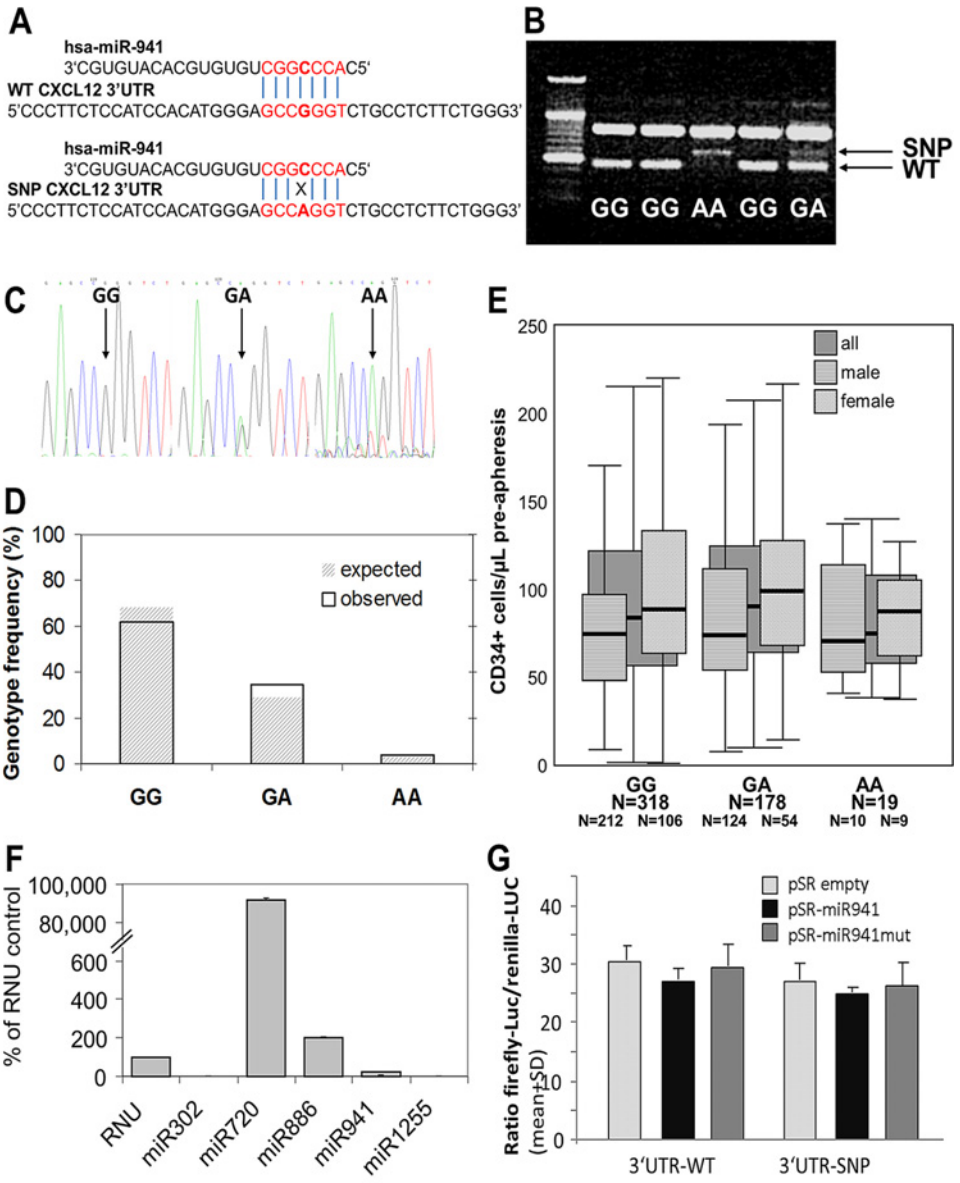

Fig 1. Variant rs1801157 of the SDF-1ß 3'UTR, miRNA941 and G-CSF responsiveness of healthy stem cell donors. (A) Sequence alignment of miR941 with WT- and SNP-variants of the 3'UTR of CXCL12. (**B)** Representative results from the sequence-specific PCR established to distinguish between WT- and SNP-variant. (**C)** Representative sequencing results from the 3'UTR genotyping. (**D)** Expected and observed frequencies of WT, heterozygous and homozygous SNP genotypes. (**E)** Circulating CD34+ cells after 9 doses q12h of G-CSF by CXCL12 3'UTR genotype. Mobilization efficiency for WT, heterozygous SNP and homozygous SNP donors was 94.9±2.9, 101.6±4.3 and 88.0±10.0 CD34+ cells/µl (mean±SEM), respectively. All donors combined are shown in dark grey bars, separate analyses by gender are overlaid. (**F)** miRNA expression in non-hematopoietic BM cells from healthy volunteer donors was tested by global miR expression arrays; individual highly and lowly expressed miRNAs were further tested by real-time PCR. miR941 expression was barely detectable. (**G)** The interaction between miR941 and the 3'UTR was assessed by dual luciferase assays. Luciferase activity was the same for the WT- and SNP-variant of the CXCL12 3'UTR, in the presence or absence of WT or mutated miR941. Hsa-miR1255 served as positive control for miRNA-mediated down-regulation of luciferase activity (not shown).

doi:10.1371/journal.pone.0121859.g001

Table 1. Custom oligonucleotides used for these studies. PCR conditions are available from the authors upon request.

Primer name	Nucleotide sequence
SSP/Sequencing fwd	5' GTCAGCCCTAGGGTGGAGAG 3'
SSP/Sequencing rev	5' CCTGCTTGGTGCACAGTTTA 3'
SSP fwd	5' CATCCACATGGGAGCCA 3'
SSP rev	5' TCCCAGAAGAGGCAGACCC 3'
SNP miR941 fwd	5' GAAGAGGACGCACCTGGCTGTGTGCACAT 3'
SNP miR941 rev	5' ATGTGCA CACAGCCAGGTGCGTCCTCTTC 3'
3'UTR fwd	5' GAGCTCGAGGGTCAGACGCCTGAGGAAC 3'
3'UTR rev	5' TCTAGATGCCCTGTTTTCCATGAACCACTGT 3'

doi:10.1371/journal.pone.0121859.t001

retro.puro, synthetic miR941 and SNP-miR941 (Qiagen) were alternatively co-transfected with the pmirGLO 3'UTR variants. Cross-over analyses for WT- or SNP-3'UTR variant and WT- or mutated miR941were performed. Experiments were performed with commercial kits according to manufacturers' instructions. Custom oligonucleotides are listed in Table 1. Descriptive statistics and t-tests (Student's t-test or one-way ANOVA) were calculated using SPSS for Windows, version 11.0 (Statcon, Witzenhausen, Germany). A $p<0.05$ was considered statistically significant.

Results and Discussion

These studies had been triggered by visibly published reports of SNP rs1801157 effects on CXCL12 protein levels and, likely in consequence thereof, on infectivity of X4-tropic HiV strains.[12, 14–16] These data were later refuted by appropriately-sized studies.[13] Nevertheless, two studies containing 63 patients [9] or 65 donors [10] suggesting effects of the SNP on HSPC mobilization were published. Samples from 515 consecutive donors, i.e. an eight-fold larger cohort than in above-referenced studies, were tested. Mobilization efficiency on the 5th day of G-CSF was 97.0±2.4 CD34+ cells/μl (mean±SEM), in agreement with published data for split-dose G-CSF.[18–20] Distribution of genotypes was in agreement with expected frequencies (Fig. 1D). Mobilization was equally efficient in all genotypes (Fig. 1E). The same analyses were repeated after controlling for gender (Fig. 1E) and by analyzing together donors heterozygous and homozygous for the SNP (not shown), with the same outcome. Importantly, the first study connecting SNP rs1801157 with mobilization deals with patients undergoing autologous donation. By the time patients undergo mobilization and autologous stem cell collection, they have received considerable cumulative doses of myelotoxic chemotherapy.[22–24] Chemotherapy-induced mobilopathy due to impaired stem cell reserve is a well-recognized confounder of autologous mobilization responses far in excess of that of the genetically determined variability.[25] Moreover, given the role of the CXCL12/CXCR4 axis in stem cell maintenance, if indeed the SNP genotype was associated with altered CXCL12 expression in BM, then the same chemotherapy could cause different degrees of stem cell depletion depending on SNP genotype. Thus alternative hypotheses to explain the observations must be considered, although they are not raised, let alone explored by the authors.[9] Further autologous cohorts were not tested. Bogunia-Kubik et al. [10] claimed to support the notion of the SNP conveying a good-mobilizer phenotype in healthy volunteer stem cell donors. However, mobilization efficiency (CD34 + cells/μl) was not actually analyzed in that study. Instead, conclusions are based on the number of CD34+ cells in the apheresis product. In the study, men were two-fold overrepresented among the SNP carriers. Of relevance to the authors' conclusions, gender has a very strong effect on apheresis outcomes: The two factors determining (and often limiting) blood throughput

in donors are ACD-A infusion rate ($\leq$1.2 ml/L total blood volume*min) and venous capacity. As a consequence, much greater blood flow rates and hence, apheresis process volumes are achieved in the (on average heavier) male. In donors with the same mobilization response (CD34+ cells/μL), this difference results, on average, in one-third greater stem cell harvests in men than in women (own unpublished data). Clearly, the observed differences in the parameters presented by Bogunia-Kubik et al.,[10] such as number of aphereses required to achieve target dose and CD34+ cell dose collected per kgBW, can be explained by this effect alone instead of effects of SNP rs1801157. Moreover, several studies report greater G-CSF responsiveness of males compared to females,[4, 6, 26] but this one as well as a previous one of ours does not.[5] In agreement with our data, analysis of a large donor cohort recently also showed no effect of the CXCL12 3'UTR genotype on mobilization.[6]

A putative binding site for hsa-miR-941 was predicted by Target Scan Human (http://www.targetscan.org/) in the region of SNP rs1801157 and loss thereof in the SNP variant was predicted. Even though none of several other commonly used miRNA search engines (Ensembl version 69, miRBase version 18, MICRORNA.ORG, MIRDB, RNA22-HSA, TARGETMINER, TARGETSCAN-VERT) predicted this interaction, to end the discussions about putative roles of SNP rs1801157 in mobilization responses, we explored whether the CXCL12 3'UTR polymorphism quantitatively affects mRNA expression and what is the role, if any, of miR941 in this context. For miR941 to differentially influence CXCL12 expression depending on the CXCL12 3'UTR genotype, the expectation would be that it must be expressed in BM stroma cells, the main source of CXCL12 in BM. miRNA expression arrays in non-hematopoietic BM cells, corroborated by qPCR, detected several highly expressed miRNAs, but no expression of miR941 (Fig. 1F). We also assessed (differential) association of miR941 with the SNP-region of the 3'UTR of CXCL12, as *in silico* analyses had suggested. Direct evidence was sought using dual luciferase assays. As we are showing, luciferase expression was not affected by co-expression of miR941, nor were differential effects on the different genotypes or differential effects of miR941 and mutant-miR941 observed (Fig. 1G). Linkage of SNP rs1801157 with other SNPs in the CXCL12 gene was not suggested by database searches. These data are in complete agreement with our observation that SNP rs1801157 does not affect mobilization responses.

In summary, our studies definitively contradict previous reports about effects of the SNP rs1801157 on G-CSF responsiveness in donors, just as previous reports of an effect of this polymorphism on susceptibility towards X4-tropic HI virus were unhinged when sufficiently large cohorts of HIV patients were analyzed.[13] We propose that unaccounted for confounders, poorly balanced within the very small cohorts, are responsible for the unreproducible data that were previously published.[9, 10] Of note, another study, similarly sized as ours, comes to the same conclusions.[6] The computer-predicted miRNA binding site in the CXCL12 3'UTR could not be confirmed, underscoring the necessity to experimentally confirm computer algorithm-predicted molecular interactions. The genetics underlying G-CSF responsiveness remain elusive.

Acknowledgments

The unselfish gift of stem cells by our volunteer donors is acknowledged. The staff of the cellular therapy laboratory is acknowledged for pseudonymization of samples.

Author Contributions

Conceived and designed the experiments: ES VB HB MS DK. Performed the experiments: MS DK GS AD. Analyzed the data: MS HB. Wrote the paper: MS HB.

References

1. Russell NH, Byrne JL (2001) Allogeneic transplantation using peripheral blood stem cells. Best Pract Res Clin Haematol. 14:685–700. PMID: 11924916
2. Favre G, Beksaç M, Bacigalupo A, Ruutu T, Nagler A, Gluckman E, et al (2003) European Group for Blood and Marrow Transplantation (EBMT). Differences between graft product and donor side effects following bone marrow or stem cell donation. Bone Marrow Transplant. 32:873–80. PMID: 14561987
3. Motabi IH, DiPersio JF (2012) Advances in stem cell mobilization. Blood Rev. 26:267–78. doi: 10.1016/j.blre.2012.09.003 PMID: 23068307
4. Holig K, Kramer M, Kroschinsky F, Bornhauser M, Mengling T, Schmidt AH, et al (2009) Safety and efficacy of hematopoietic stem cell collection from mobilized peripheral blood in unrelated volunteers: 12 years of single-center experience in 3928 donors. Blood 114:3757–63. doi: 10.1182/blood-2009-04-218651 PMID: 19666868
5. Mueller MM, Bialleck H, Bomke B, Brauninger S, Varga C, Seidl C, et al (2013) Safety and efficacy of healthy volunteer stem cell mobilization with filgrastim G-CSF and mobilized stem cell apheresis: results of a prospective longitudinal 5-year follow-up study. Vox Sang. 104:46–54. doi: 10.1111/j.1423-0410.2012.01632.x PMID: 22827736
6. Lenk J, Bornhauser M, Kramer M, Holig K, Poppe-Thiede K, Schmidt H, et al (2013) Sex and body mass index but not CXCL12 801 G/A polymorphism determine the efficacy of hematopoietic cell mobilization: a study in healthy volunteer donors. Biol Blood Marrow Transplant. 19:1517–21. doi: 10.1016/j.bbmt.2013.07.018 PMID: 23891749
7. Phillips RL, Couzens MS, Van ZG (1995) Genetic factors influencing murine hematopoietic productivity in culture. J Cell Physiol. 164:99–107. PMID: 7790403
8. de Haan G, Nijhof W, van Zandt G (1997) Mouse strain-dependent changes in frequency and proliferation of hematopoietic stem cells during aging: correlation between lifespan and cycling activity. Blood 89:1543–50. PMID: 9057635
9. Benboubker L, Watier H, Carion A, Georget MT, Desbois I, Colombat P, et al (2001) Association between the SDF1-3'A allele and high levels of CD34(+) progenitor cells mobilized into peripheral blood in humans. Br J Haematol. 113:247–50. PMID: 11328308
10. Bogunia-Kubik K, Gieryng A, Dlubek D, Lange A (2009) The CXCL12-3'A allele is associated with a higher mobilization yield of CD34 progenitors to the peripheral blood of healthy donors for allogeneic transplantation. Bone Marrow Transplant. 44:273–8. doi: 10.1038/bmt.2009.30 PMID: 19252530
11. Ben Nasr M, Reguaya Z, Berraies L, Maamar M, Ladeb S, Ben Othmen T, et al. (2011) Association of stromal cell-derived factor-1-3'A polymorphism to higher mobilization of hematopoietic stem cells CD34 + in Tunisian population. Transplant Proc. 43:635–8. doi: 10.1016/j.transproceed.2011.01.016 PMID: 21440782
12. Winkler C, Modi W, Smith MW, Nelson GW, Wu X, Carrington M, et al (1998) Genetic restriction of AIDS pathogenesis by an SDF-1 chemokine gene variant. ALIVE Study, Hemophilia Growth and Development Study (HGDS), Multicenter AIDS Cohort Study (MACS), Multicenter Hemophilia Cohort Study (MHCS), San Francisco City Cohort (SFCC). Science 279:389–93. PMID: 9430590
13. McLaren PJ, Coulonges C, Ripke S, van den Berg L, Buchbinder S, Carrington M, et al (2013) Association study of common genetic variants and HIV-1 acquisition in 6,300 infected cases and 7,200 controls. PLoS Pathog. 2013; 9(7):e1003515. doi: 10.1371/journal.ppat.1003515 PMID: 23935489
14. Xiao Q, Ye S, Oberhollenzer F, Mayr A, Jahangiri M, Willeit J, et al. (2008) SDF1 gene variation is associated with circulating SDF1alpha level and endothelial progenitor cell number: the Bruneck Study. PLoS One. 3:e4061. doi: 10.1371/journal.pone.0004061 PMID: 19115008
15. Arya SK, Ginsberg CC, Davis-Warren A, D'Costa J (1999) In vitro phenotype of SDF1 gene mutant that delays the onset of human immunodeficiency virus disease in vivo. J Hum Virol. 2:133–8. PMID: 10413364
16. Soriano A, Martínez C, García F, Plana M, Palou E, Lejeune M, et al. (2002) Plasma stromal cell-derived factor (SDF)-1 levels, SDF1-3'A genotype, and expression of CXCR4 on T lymphocytes: their impact on resistance to human immunodeficiency virus type 1 infection and its progression. J Infect Dis. 186:922–31. PMID: 12232832
17. Zhang Y, Yang P, Sun T, Li D, Xu X, Rui Y, et al. (2013) miR-126 and miR-126* repress recruitment of mesenchymal stem cells and inflammatory monocytes to inhibit breast cancer metastasis. Nat Cell Biol. 15:284–94. doi: 10.1038/ncb2690 PMID: 23396050
18. Ings SJ, Balsa C, Leverett D, Mackinnon S, Linch DC, Watts MJ (2006) Peripheral blood stem cell yield in 400 normal donors mobilised with granulocyte colony-stimulating factor (G-CSF): impact of age, sex, donor weight and type of G-CSF used. Br J Haematol. 134:517–25. PMID: 17018030

19. Arbona C, Prosper F, Benet I, Mena F, Solano C, Garcia-Conde J (1998) Comparison between once a day vs twice a day G-CSF for mobilization of peripheral blood progenitor cells (PBPC) in normal donors for allogeneic PBPC transplantation. Bone Marrow Transplant. 22:39–45. PMID: 9678794

20. Kröger N, Renges H, Krüger W, Gutensohn K, Löliger C, Carrero I, et al. (2000) A randomized comparison of once versus twice daily recombinant human granulocyte colony-stimulating factor (filgrastim) for stem cell mobilization in healthy donors for allogeneic transplantation. Br J Haematol. 111:761–5. PMID: 11122135

21. Dauber K, Becker D, Odendahl M, Seifried E, Bonig H, Tonn T (2011) Enumeration of viable CD34(+) cells by flow cytometry in blood, bone marrow and cord blood: results of a study of the novel BD™ stem cell enumeration kit. Cytotherapy. 13:449–58. doi: 10.3109/14653249.2010.529894 PMID: 21077730

22. Clark RE, Brammer CG (1998) Previous treatment predicts the efficiency of blood progenitor cell mobilisation: validation of a chemotherapy scoring system. Bone Marrow Transplant. 22:859–63. PMID: 9827813

23. Tournilhac O, Cazin B, Leprètre S, Diviné M, Maloum K, Delmer A, et al. (2004) Impact of frontline fludarabine and cyclophosphamide combined treatment on peripheral blood stem cell mobilization in B-cell chronic lymphocytic leukemia. Blood 103:363–5. PMID: 12969985

24. Noach EJ, Ausema A, van Os R, Akkerman I, Koopal S, Weersing E, et al. (2003) Chemotherapy prior to autologous bone marrow transplantation impairs long-term engraftment in mice. Exp Hematol. 31:528–34. PMID: 12829029

25. Morton J, Morton A, Bird R, Hutchins C, Durrant S (1997) Predictors for optimal mobilization and subsequent engraftment of peripheral blood progenitor cells following intermediate dose cyclophosphamide and G-CSF. Leuk Res. 21:21–7. PMID: 9029182

26. Bertani G, Santoleri L, Martino M, Fedele R, Moscato T, Marenco P, et al. (2014) Identification of hematopoietic progenitor cell donor characteristics predicting successful mobilization: results of an Italian multicenter study. Transfusion 54:2028–33. doi: 10.1111/trf.12612 PMID: 24588265

Cell Reports

Article

Microenvironmental control of hematopoietic stem cell fate via CXCL8 and protein kinase C

Graphical abstract

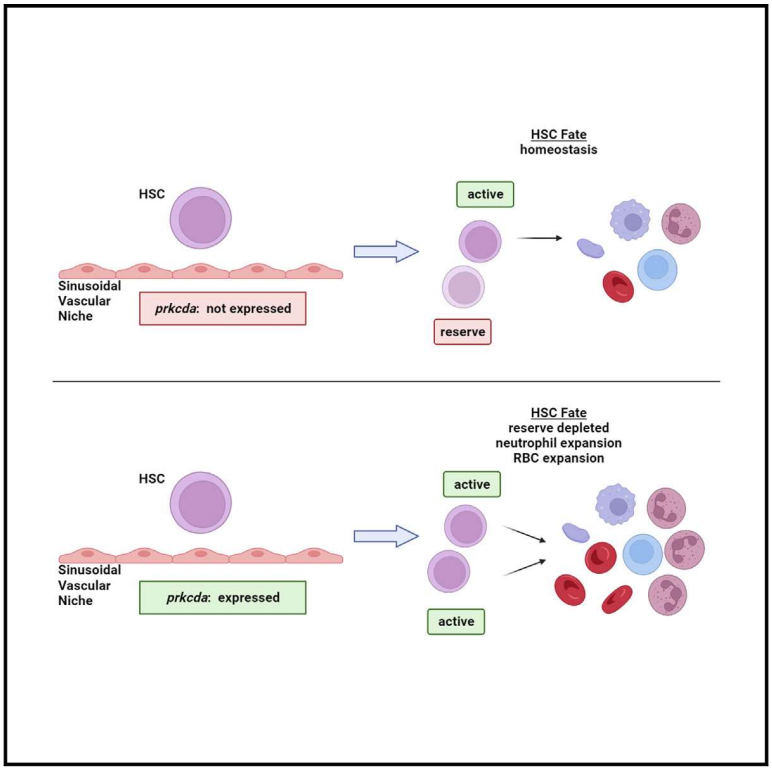

Authors

Vera Binder, Wantong Li, Muhammad Faisal, ..., Rosa Lapalombella, Leonard I. Zon, Bradley W. Blaser

Correspondence

bradley.blaser@osumc.edu

In brief

Binder et al. show that *prkcda*, encoding PKC-δ, is transcriptionally regulated in the sinusoidal vascular hematopoietic niche. Dysregulated expression within the niche alters hematopoietic stem cell (HSC) clonal evolution and phenotypic fate. This provides insight into how the microenvironment maintains a reserve capacity of HSCs for regeneration and stress responses.

Highlights

- Lineage tracing reveals microenvironmental control of HSC clonal evolution
- Expression of *prkcda* is regulated to maintain HSC reserve capacity
- Cxcl8 signals via *prkcda*/pkc-δ and promotes HSC competition for niche residency
- Microenvironmental control of HSC fate has implications for hematologic disorders

Binder et al., 2023, Cell Reports *42*, 112528
May 30, 2023
https://doi.org/10.1016/j.celrep.2023.112528

CellPress

Cell Reports

CellPress
OPEN ACCESS

Article

Microenvironmental control of hematopoietic stem cell fate via CXCL8 and protein kinase C

Vera Binder,[1,11] Wantong Li,[2,3,11] Muhammad Faisal,[2,3] Konur Oyman,[2,3] Donn L. Calkins,[2,3] Jami Shaffer,[2,3] Emily M. Teets,[2,3] Steven Sher,[2,3] Andrew Magnotte,[2,3] Alex Belardo,[2,3] William Deruelle,[2,3] T. Charles Gregory,[2,3,4] Shelley Orwick,[2,3] Elliott J. Hagedorn,[5] Julie R. Perlin,[6] Serine Avagyan,[7] Asher Lichtig,[6] Francesca Barrett,[6] Michelle Ammerman,[6] Song Yang,[6] Yi Zhou,[6] William E. Carson,[3] Heather R. Shive,[8] James S. Blachly,[2,3,4] Rosa Lapalombella,[2,3] Leonard I. Zon,[6,7,9,10] and Bradley W. Blaser[2,3,12,*]

[1]Dr. von Hauner Childrens' Hospital, University Hospital Ludwig Maximillian's University, Department of Pediatric Hematology/Oncology, 80337 Munich, Germany

[2]The Ohio State University College of Medicine, Department of Internal Medicine, Division of Hematology, Columbus, OH 43210, USA

[3]The Ohio State University Comprehensive Cancer Center, James Cancer Hospital and Solove Research Institute, Columbus, OH 43210, USA

[4]The Ohio State University College of Medicine, Department of Biomedical Informatics, Columbus, OH 43210, USA

[5]Boston University School of Medicine, Department of Medicine, Boston, MA 02118, USA

[6]Stem Cell Program, Division of Hematology/Oncology, Boston Children's Hospital and Dana Farber Cancer Institute, Boston, MA 02115, USA

[7]Dana-Farber/Boston Children's Hospital Cancer and Blood Disorders Center, Boston, MA 02115, USA

[8]Laboratory of Cancer Biology and Genetics, Center for Cancer Research, National Cancer Institute, Bethesda, MD 20892, USA

[9]Howard Hughes Medical Institute, Chevy Chase, MD 20815, USA

[10]Stem Cell and Regenerative Biology Department, Harvard University, Cambridge, MA 02138, USA

[11]These authors contributed equally

[12]Lead contact

*Correspondence: bradley.blaser@osumc.edu

https://doi.org/10.1016/j.celrep.2023.112528

SUMMARY

Altered hematopoietic stem cell (HSC) fate underlies primary blood disorders but microenvironmental factors controlling this are poorly understood. Genetically barcoded genome editing of synthetic target arrays for lineage tracing (GESTALT) zebrafish were used to screen for factors expressed by the sinusoidal vascular niche that alter the phylogenetic distribution of the HSC pool under native conditions. Dysregulated expression of protein kinase C delta (PKC-δ, encoded by *prkcda*) increases the number of HSC clones by up to 80% and expands polyclonal populations of immature neutrophil and erythroid precursors. PKC agonists such as *cxcl8* augment HSC competition for residency within the niche and expand defined niche populations. CXCL8 induces association of PKC-δ with the focal adhesion complex, activating extracellular signal-regulated kinase (ERK) signaling and expression of niche factors in human endothelial cells. Our findings demonstrate the existence of reserve capacity within the niche that is controlled by CXCL8 and PKC and has significant impact on HSC phylogenetic and phenotypic fate.

INTRODUCTION

Hematopoiesis is a cellular developmental program influenced by hematopoietic stem and progenitor cell (HSPC)-intrinsic genetic programs and HSPC-extrinsic factors from the surrounding microenvironment.[1,2] In hematologic neoplasms, the actions of mutated transcription factors, histone and DNA modifiers, and signaling receptors are appreciated to be the primary forces driving clonal expansion, loss of phylogenetic diversity, and adoption of a malignant cell fate.[3–9] However, the mechanisms by which the hematopoietic microenvironment regulates hematopoietic stem cell (HSC) clonal diversity and cell fate remain poorly understood.

The hematopoietic microenvironment can be regarded as a collection of specialized cellular niches with overlapping functions depending on the developmental context or presence of external stresses.[2] The sinusoidal vascular niche is found in developing or regenerative microenvironment tissue and is critical for hematopoietic recovery after transplantation because of its expression of Notch ligands, CXCL12, stem cell factor (SCF), and other angiocrine growth factors.[10–18] Overexpression of the angiogenic chemokine receptor *cxcr1* in embryonic zebrafish increases the three-dimensional volume of the caudal hematopoietic tissue (CHT), a transient sinusoidal vascular niche present from 3 to 7 days post fertilization (dpf), increases expression of *cxcl12a*, and enhances colonization by phenotypic HSPCs.[19,20] Conversely, zebrafish with homozygous null mutations in *cxcl8*, the ligand for *cxcr1*, have reduced colonization of the CHT by phenotypic HSPCs.[20] Given the importance of the sinusoidal niche in the development and regeneration of the hematopoietic system, we hypothesized that perturbations in downstream components of *cxcl8/cxcr1* signaling would

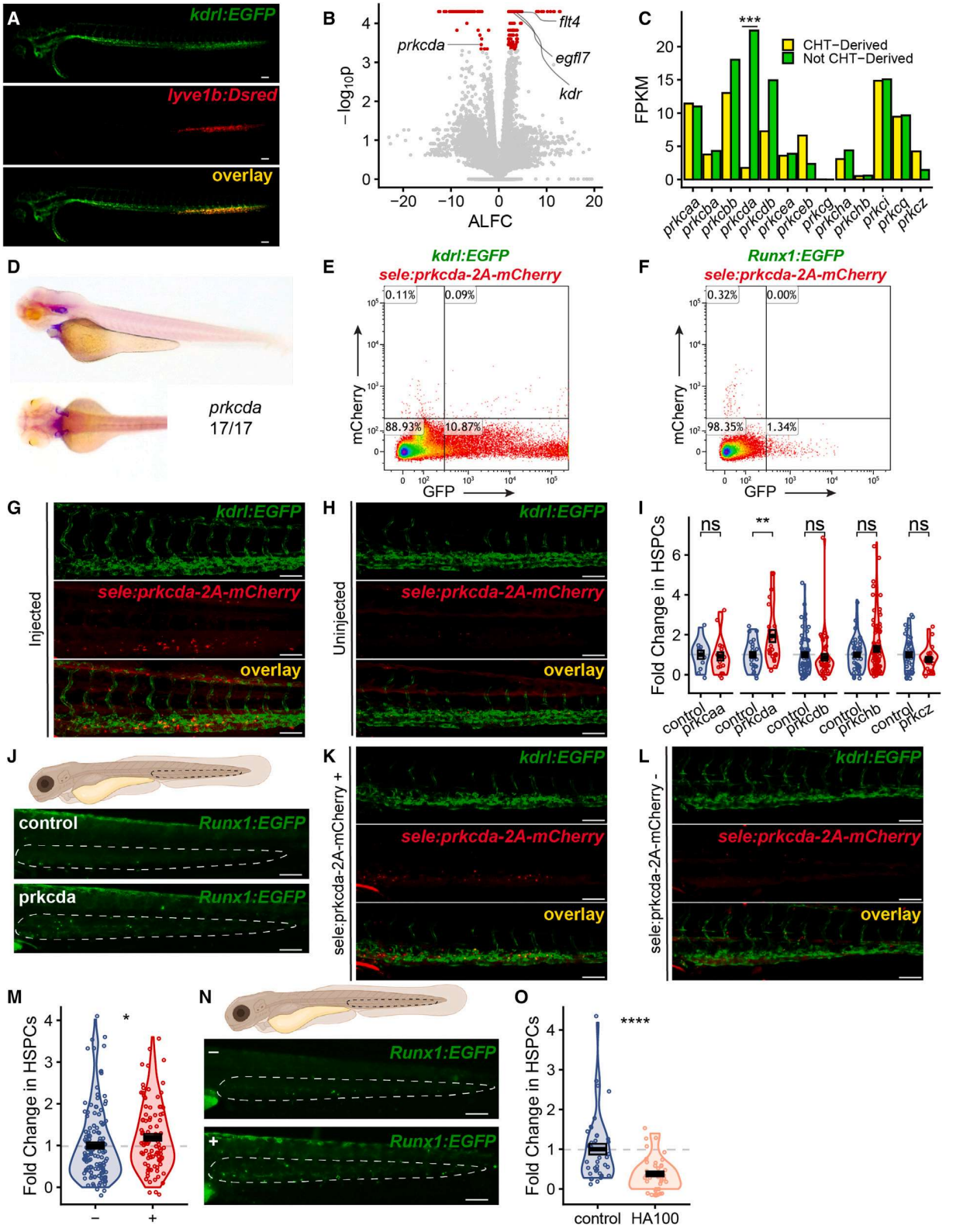

(legend on next page)

alleviate or exacerbate natural evolutionary bottlenecks, thereby altering the fate of the HSC pool. Using genetic lineage tracing techniques and single-cell RNA sequencing (scRNA-seq) analysis to map the fate of native HSC clones, we demonstrate involvement of protein kinase C (PKC) and *cxcl8* in regulating the capacity of the sinusoidal endothelial niche to support a phylogenetically and phenotypically diverse hematopoietic system.

RESULTS

Differential expression of *prkcda* in the vascular niche

We aimed to identify downstream components of *cxcl8* signaling with a specific pattern of expression relative to CHT-derived sinusoidal endothelial cells and non-CHT-derived arteriovenous endothelial cells. *Kdrl:EGFP;lyve1b:DsRed* zebrafish embryos (Figure 1A) were dissociated at 72 h post fertilization (hpf).[21,22] Kdrl:EGFP(+) lyve1b:DsRed(+) CHT-derived sinusoidal endothelial cells and kdrl:EGFP(+) lyve1b:dDsRed(−) non-CHT-derived arteriovenous endothelial cells were purified by fluorescence-activated cell sorting (FACS), bulk RNA sequencing (RNA-seq) was performed, and 219 significantly differentially regulated genes were identified (Figure 1B; Table S1). Genes known to be expressed at high levels in sinusoidal vascular tissues such as *kdr (vegfr2b)*, *flt4* (vegfr3), and *egfl7* were among the significantly upregulated genes in CHT-derived sinusoidal endothelial cells.[18,23] The list of significantly downregulated genes in CHT-derived sinusoidal endothelial cells included *prkcda*, which encodes the novel PKC isozyme, PKC-δ. Of all annotated zebrafish PKC isoforms, only *prkcda* was differentially regulated in CHT-derived sinusoidal endothelial cells and non-CHT-derived arteriovenous endothelial cells (Figure 1C). Whole-mount *in situ* hybridization of 72 hpf embryos confirmed these findings by showing expression of *prkcda* mRNA in the region of the heart and hindbrain (Figure 1D).[24] PKC is a downstream component of *cxcl8/cxcr1* signaling, although a role for the delta isoform in this pathway has not been described.[25,26] The pattern of expression observed suggested that *prkcda* expression may be tightly controlled in order to properly regulate responses to *cxcl8*-expressing cells within the CHT.

Ectopic expression of *prkcda* in the vascular niche expands phenotypic HSPCs

Given the tight transcriptional control on *prkcda* expression in the CHT and since upstream *cxcl8/cxcr1* signaling is a positive regulator of HSPC colonization, we hypothesized that dysregulated expression of *prkcda* would alter CHT colonization by HSPCs. E-selectin (*sele*) is a specific marker for CHT endothelial cells; a 798-bp enhancer/promoter element from *sele*, was used to drive expression of *prkcda* or other zebrafish PKC family members in CHT endothelial cells by microinjecting expression constructs into embryos at the single-cell stage to generate F_0 mosaic transgenics. *Kdrl:EGFP* and *Runx1:EGFP* zebrafish carry reporter transgenes that are highly specific for endothelial cells and embryonic HSPCs, respectively.[27,28] Dissociated *kdrl:EGFP;sele:prkcda-2A-mCherry* F_0 transgenics showed co-expression of these transgenes by flow cytometry, whereas *Runx1:EGFP;sele:prkcda-2A-mCherry* F_0 transgenics did not (Figures 1E, 1F, S1A, and S1B). Confocal imaging of the CHT in *kdrl:EGFP;sele:prkcda-2A-mCherry* F_0 transgenics showed mCherry expression in a subset of CHT endothelial cells (Figure 1G), in contrast to uninjected clutchmates (Figure 1H). Together these data show specific expression of the *sele*-driven transgene in CHT endothelial cells but not HSPCs. To determine the effect of dysregulated prkcda expression by CHT endothelial cells on HSPC numbers, *Runx1:EGFP;sele:prkcda-2A-mCherry* transgenics were compared to negative control clutchmates microinjected with expression constructs containing an empty multiple cloning site (control). Expression of the prkcda transgene caused significantly greater colonization of the CHT by EGFP(+) HSPCs at 72 hpf compared to clutchmate controls (Figures 1I and 1J). By contrast, there was no significant difference in CHT colonization in *prkcaa*, *prkcdb*, *prkchb*, or *prkcz* transgenics compared to clutchmate controls (Figure 1I).

Figure 1. Transcription of *prkcda* is repressed in the vascular niche and dysregulated expression of *prkcda* expands phenotypic HSPCs

(A) Representative images of the *kdrl:EGFP; lyve1b:DsRed* transgenic line. Bar, 100 μm.

(B) Volcano plot indicating genes with significantly differentially regulated genes in red; *prkcda* and selected CHT-specific genes are shown. Positive absolute log fold change (ALFC) indicates upregulation in CHT-derived sinusoidal endothelial cells compared to non-CHT-derived arteriovenous endothelial cells.

(C) Differential expression of PKC-family genes in CHT-derived and non-CHT-derived endothelial cells. Values represent average fragments per kilobase of exon per million mapped fragments (FPKM) from three biological replicates. For *prkcda*, p = 0.00035.

(D–F) Whole-mount *in situ* hybridization for *prkcda* in 72-hpf zebrafish embryos. (E and F) Flow cytometric analysis of kdrl:EGFP;*sele:prkcda-2A-mCherry* (E) and *Runx1:EGFP;sele:prkcda-2A-mCherry* (F) embryos.

(G and H) Representative images of kdrl:EGFP zebrafish embryos injected (G) or not (H) with the *sele:prkcda-2A-mCherry* expression construct. Bar, 100 μm.

(I) Dysregulated expression of *prkcda* in *Runx1:EGFP;sele:prkcda-2A-mCherry* embryos expands HSPCs. Each PKC family member is compared to clutchmates injected with a vector containing an empty multiple cloning site (control). Data are presented as fold change relative to control for each clutch (two or three clutches analyzed per PKC family member; each point represents a biological replicate). Boxes represent mean ± SEM. Prkcda vs. control: 1.94 ± 0.3-fold increase, p = 0.0092, Welch's t test.

(J) Representative images of CHT colonization in control and prkcda groups. Dotted lines indicate the CHT. Bar, 100 μm.

(K and L) Representative images of kdrl:EGFP(+) sele:prkcda-2A-mCherry(+) (K) and kdrl:EGFP(+); sele:prkcda-2A-mCherry(−) (L) transgenics. Bar, 100 μm.

(M) Phenotypic HSPCs were quantified in stable Runx1:EGFP;sele:prkcda-2A-mCherry transgenics (+) and Runx1:EGFP clutchmates (−) at 72 hpf. Data are pooled from two independent clutches and are represented as fold change relative to (−). Boxes represent mean ± SEM; each point represents a biological replicate. + vs. −: 1.19 ± 0.08-fold increase, p = 0.014, Wilcoxon rank-sum test.

(N) Representative images of CHT colonization for the (−) and (+) animals from Figure 1G. Dotted lines indicate CHT.

(O) Phenotypic HSPCs were quantified in Runx1:EGFP transgenics treated with HA-100 or an equivalent volume of DMSO as a vehicle control. Data are pooled from two independent experiments and are shown as fold change relative to control. Box represents mean ± SEM; each point represents a biological replicate. HA-100 vs. control: 0.38 ± 0.06-fold decrease, $p = 8.3 \times 10^{-6}$, Wilcoxon rank-sum test. See also Figure S1 and Table S1.

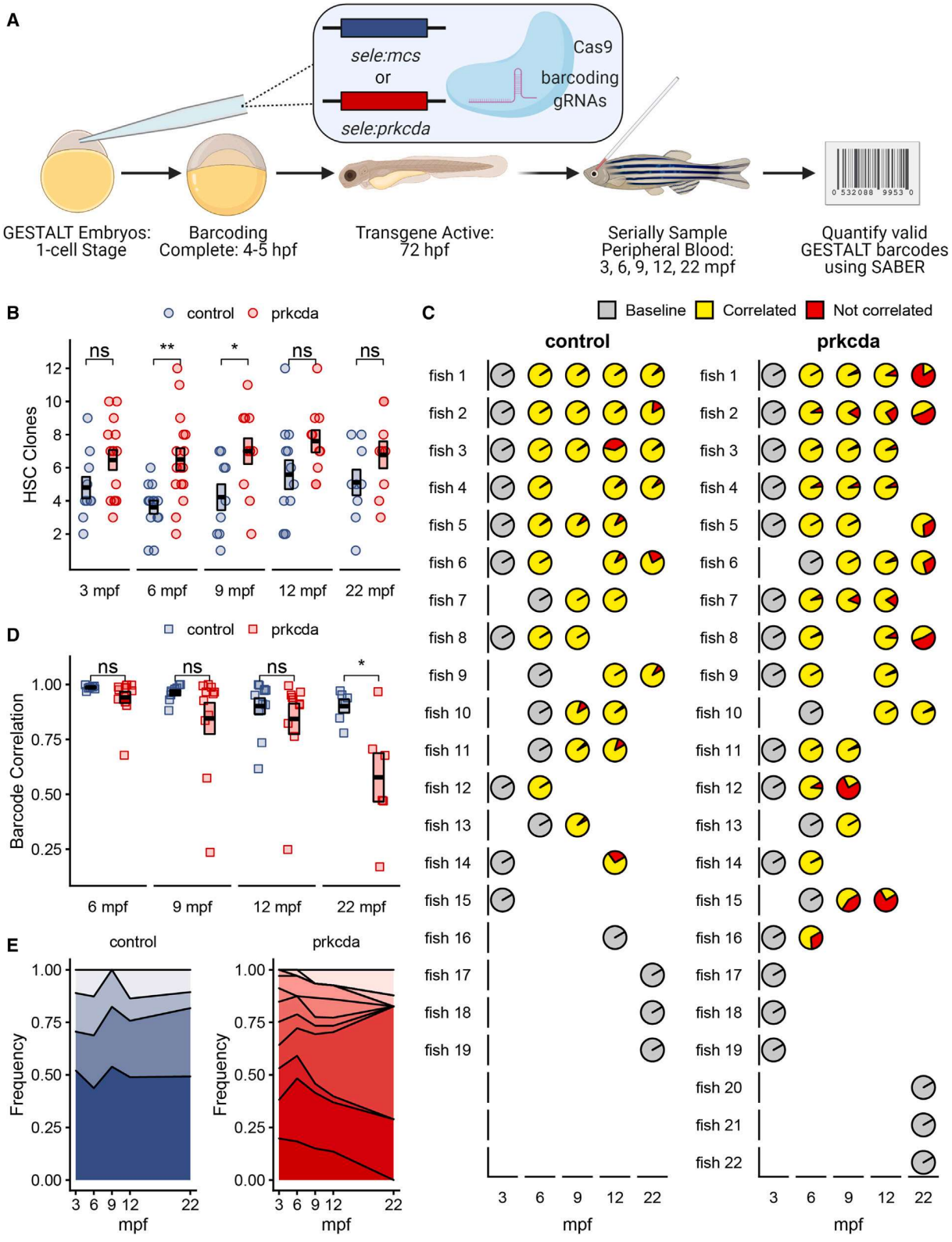

(legend on next page)

A stable *sele:prkcda-2A-mCherry* transgenic line was generated and crossed to the *kdrl:EGFP* endothelial cell reporter line; kdrl:EGFP(+) sele:prkcda-2A-mCherry(+) transgenics demonstrated specific expression in a subset of CHT endothelial cells compared to kdrl:EGFP(+) sele:prkcda-2A-mCherry(−) clutchmates (Figures 1K and 1L). The *sele:prkcda-2A-mCherry* line was crossed to *Runx1:EGFP* HSPC reporter zebrafish. Sele:prkcda-2A-mcherry(+) zebrafish showed greater CHT colonization by HSPCs compared to sele:prkcda-2A-mcherry(−) clutchmates (Figures 1M and 1N). HA-100 dihydrochloride (HA-100) is a selective inhibitor of PKC enzymes that is soluble in water and does not fluoresce in the emission spectrum of GFP. *Runx1:EGFP* embryos treated at the maximum tolerated dose of HA-100 (50 μM) had lower CHT colonization by HSPCs compared to control-treated clutchmates (Figure 1O). These data suggest that, as a class, PKC family enzymes positively regulate HSPC colonization of the embryonic vascular niche. Transcriptional dysregulation of PKC family members with non-specific patterns of expression with respect to endothelial cell of origin (sinusoidal versus arteriovenous), including conventional (*prkcaa*) and atypical (*prkcz*) subtypes, did not affect CHT engraftment. However, dysregulated expression of *prkcda*, which is transcribed at a lower level in CHT-derived sinusoidal endothelial cells, was sufficient to increase CHT engraftment. This is consistent with a possible role in regulating responses to *cxcl8* signaling within the vascular niche.

Vascular niche expression of *prkcda* increases the number of long-term HSC clones

The genome editing of synthetic target arrays for lineage tracing (GESTALT) lineage tracing system[29] was used to interrogate the effect of dysregulated vascular niche expression of *prkcda* on long-term HSC fate in the setting of otherwise unperturbed, native hematopoiesis. GESTALT embryos were microinjected with Cas9, barcoding sgRNAs, and either *sele:prkcda-2A-mCherry* (prkcda) or empty vector (*sele:mcs-2a-mCherry*, control) expression constructs (Figure 2A). Barcoded zebrafish were grown to 3 months post fertilization (mpf), peripheral blood was sampled, GESTALT barcodes were sequenced, and the number of HSC clones contributing to peripheral blood was quantified using an unsupervised algorithm for selecting informative amplicon barcodes from experimental replicates (SABER).[30] Peripheral blood was serially resampled at 6, 9, 12, and 22 mpf. Accounting for repeated measures across all serial samples, animals in the *sele:prkcda-2A-mCherry* group had more HSC clones contributing to the peripheral blood compared to control clutchmates from 3 to 22 mpf (Figure 2B). *Post hoc* testing showed significantly more HSC clones in the prkcda group compared to control at 6 and 9 mpf.

We sought to determine the stability of HSC clonal output over time. Since zebrafish are housed in groups, GESTALT barcodes were used to identify longitudinal blood samples derived from the same fish. Sixteen *sele:prkcda-2A-mCherry* fish and 14 clutchmate controls could be identified at two or more time points. To measure stability of clonal output in individual fish, GESTALT barcode frequencies at each time point were correlated with baseline (Pearson correlation shown in Figures 2C and 2D). There was no difference in GESTALT barcode correlation at the 6, 9, and 12 mpf time points compared to baseline (Figure 2D). However, at the 22 mpf time point, the GESTALT barcode correlation was significantly lower for *sele:prkcda-2A-mCherry* transgenics compared to clutchmate controls (Figure 2D). Representative plots of allele frequency over time are shown in Figure 2E. These findings show that dysregulated expression of *prkcda* expands the capacity of the hematopoietic niche and allows it to support more phylogenetically distinct HSC clones that can contribute to hematopoiesis through at least 12 months of life. From 12 to 22 mpf, the effect of *prkcda* dysregulation in the vascular niche led to changes in the phylogenetic makeup of the HSC pool that were not observed in control clutchmates.

Polyclonal expansion of erythroid precursors and immature neutrophils in zebrafish with dysregulated expression of *prkcda*

scRNA-seq was performed on *sele:prkcda-2A-mCherry* transgenic zebrafish to identify phenotypic changes occurring in the hematopoietic compartment concurrent with the changes observed in HSC phylogenetic diversity. Kidney marrow was harvested at 22 mpf and 10,995 cells (6,346 from *sele:prkcda-2A-mCherry* and 4,649 from clutchmate controls) were isolated without pre-enrichment using 10X Genomics 3′-capture technology. Unsupervised clustering revealed eight clusters of hematopoietic cells (Figures 3A–3C; see Figure S2A for all cell populations). The identity of individual hematopoietic clusters was assigned by gene module Gene Ontology (GO)-term analysis and inspection of top specific cluster markers (Tables S2–S4). A group of hematologic cell clusters was identified with specific expression of canonical hematopoietic genes (Figure 3C). Initial cluster assignments could be made on the basis of these genes, including myeloid progenitors (*csf1rb*, *gata2b*), lymphoid progenitors (*ccr9a*, *cd81a*, *gata2a*), erythroid progenitors (*gata1a*, *lmo2*), and three neutrophil populations (*lyz*, *mpx*).[31–37] A very small cluster was identified that expressed high levels of

Figure 2. Vascular niche expression of *prkcda* increases the number of long-term HSC clones

(A) Schematic outline of the long-term fate-mapping experiment.

(B) GESTALT barcodes were amplified from peripheral blood samples and quantified using SABER. The number of HSC clones at each time point is shown for *sele:prkcda-2A-mCherry* transgenics (prkcda) and clutchmate controls. Representative data from one of two experiments is shown. Boxes indicate mean ± SEM; each point represents a biological replicate. For 3 mpf to 22 mpf, prkcda vs. control: $p = 0.0008$, robust two-way mixed ANOVA. *Post hoc* testing for prkcda vs. control at 6 and 9 mpf: 6.5 ± 0.7 vs. 3.6 ± 0.4 HSC clones, $p = 0.001$ and 7.0 ± 0.8 vs. 4.2 ± 0.8 HSC clones, $p = 0.02$, Welch's t test.

(C) Correlation of serial samples to baseline for GESTALT barcode-identified fish. Each row per column represents a biological replicate.

(D) The Pearson correlation for each fish is plotted by group and by time point (6 mpf and later). Boxes represent mean ± SEM; each point represents a biological replicate. For prkcda vs. control: mean Pearson coefficient of 0.58 ± 0.11 vs. 0.90 ± 0.03, $p = 0.03$, Welch's t test.

(E) Representative plots showing HSC clonal dynamics in control and prkcda groups. The height of each polygon at the indicated time points is proportional the measured frequency of alleles derived from uniquely-barcoded HSC clones. Only HSC clones with a contribution of 2% or greater are included.

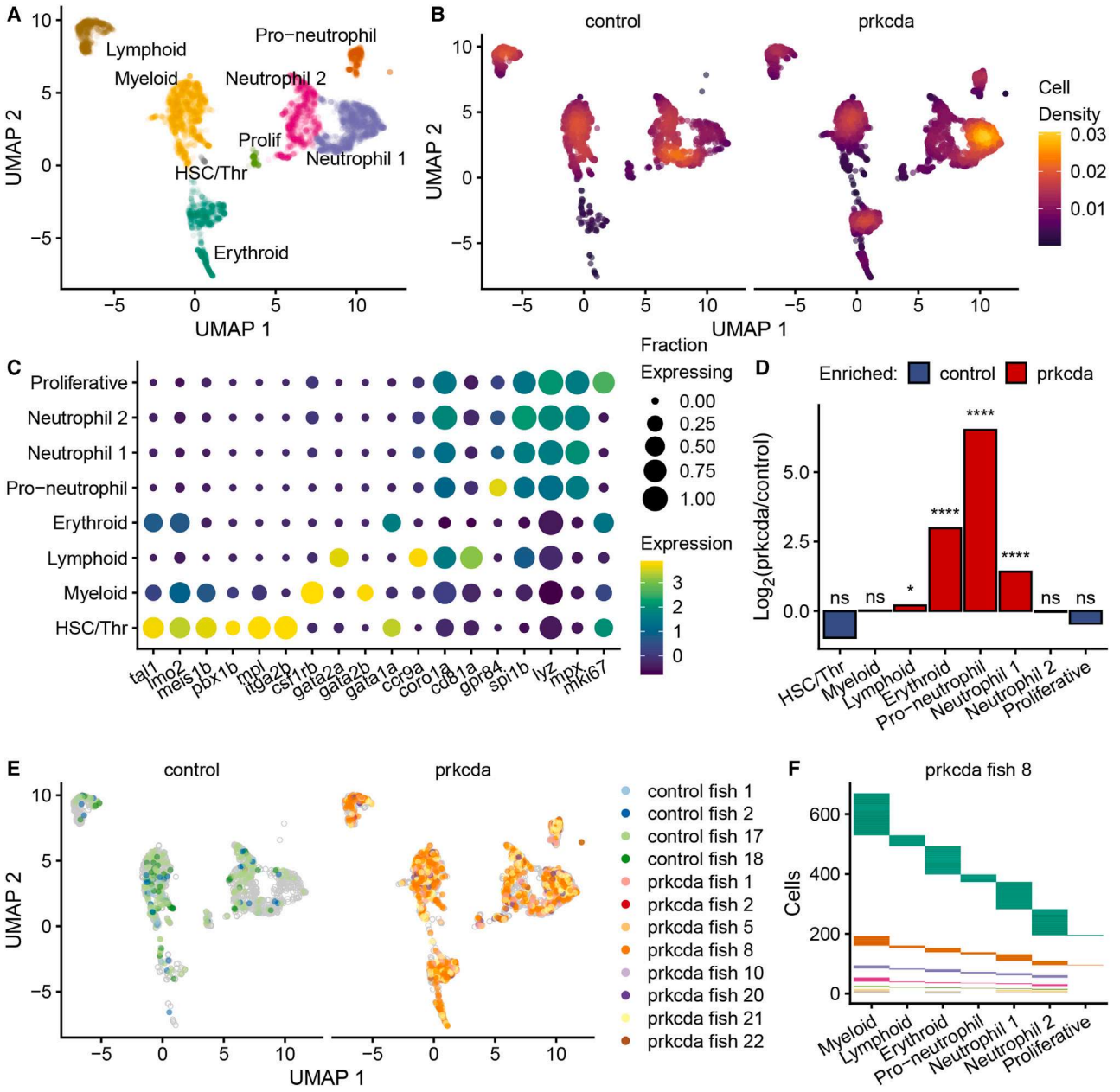

Figure 3. Polyclonal expansion of erythroid precursors and immature neutrophils in zebrafish with dysregulated expression of *prkcda*

(A) Uniform Manifold Approximation and Projection (UMAP) plot of hematologic cell clusters. All data points for the indicated clusters are shown; data are from n = 9 (control) and n = 10 (prkcda) pooled kidney marrows.

(B) UMAP plot of hematologic cell clusters stratified by experimental group; colors indicated local cell density in two-dimensional UMAP space.

(C) Expression of selected canonical genes within each hematopoietic cell cluster.

(D) Differential representation of experimental groups by hematologic cell cluster. Values were normalized to the number of cells recovered for each experimental group. For prkcda compared to control by cluster: lymphoid, 1.15-fold expansion, p = 0.049; erythroid, 7.99-fold expansion, $p = 3.3 \times 10^{-111}$; neutrophil 1, 2.68-fold expansion, $p = 4.56 \times 10^{-91}$; and pro-neutrophil, 137-fold expansion, $p = 3.82 \times 10^{-88}$, Fisher's exact test.

(E) UMAP representation of GESTALT barcodes mapped to single hematopoietic cells. Colored points indicate biological replicates. Gray circles indicate cells without barcoding data.

(F) Clonal contribution to the hematologic cell clusters is indicated by the colored bars. Each color represents a uniquely defined GESTALT clone. See also Figure S2 and Tables S2–S4.

markers characteristic of HSCs (*tal1*, *lmo2*, *meis1b*, *pbx1b*) and thrombocyte precursors (*mpl*, *itga2b*). To confirm identities to hematopoietic cell clusters, these data were compared to three reference scRNA-seq datasets (two mouse, one zebrafish), using defined zebrafish orthologs for cross-species comparisons (Figures S2B and S2C).[38–40] A normalized aggregate expression score was calculated for each reference gene set within each hematopoietic cell cluster and cluster identities assigned according to the highest aggregate scores. Stratification by experimental group showed significant selective expansion of lymphoid, erythroid, and neutrophil 1 clusters and the presence of a highly specific pro-neutrophil cluster in *sele:prkcda-2A-mCherry* transgenic zebrafish (Figure 3D).

We wished to understand the clonal distribution of expanded cell populations observed in kidney marrow from *sele:prkcda-2A-mCherry* animals. Expansion of monoclonal cell populations arising from experimentally altered niche tissue have been reported, but polyclonal cell populations have not.[41] The latter would support a broad increase in the capacity of the vascular niche to support hematopoiesis. In the GESTALT system, barcode sequences are expressed as poly-adenylated mRNA under control of a ubiquitous enhancer/promoter element.[29] Expressed GESTALT barcodes were amplified from 10X cell-barcoded cDNA and mapped onto the scRNA-seq data. Cells from the control group could be assigned to four fish and cells from the prkcda group could be assigned to eight fish. Multiple identifiable fish were represented in each of the hematopoietic cell clusters (Figure 3E). Each cluster contained cells with multiple distinct GESTALT barcodes and most GESTALT barcodes could be identified in multiple cell clusters (Figure 3F). These data show that dysregulated expression of *prkcda* within the vascular niche expands its capacity to support a polyclonal population of HSPCs, increasing the phylogenetic diversity of the HSC pool and specifically expanding erythroid and immature neutrophil subsets. Together, these findings describe a change in HSC fate resulting from dysregulated expression of *prkcda* in the vascular niche.

Expression of *prkcda in vivo* is controlled by defined *cis*-acting regulatory elements

Observing altered HSC fates in zebrafish with dysregulated expression of *prkcda* in the vascular niche led us to hypothesize the existence of specific epigenetic mechanisms, i.e., one or more definable *cis*-acting regulatory elements, controlling *prkcda* expression. scRNA-seq expression profiles showed specific expression of *prkcda* in kidney marrow neutrophils (Figure 4A). Single-cell assay for transposase-accessible chromatin with sequencing sequencing (scATAC-seq) performed on kidney marrow cells from the same animals identified five unique cell clusters based on global chromatin accessibility (Figures 4B and S3A). We established cell cluster identities by label transfer from scRNA-seq data obtained from the same samples, using Cicero gene activity scores as a surrogate for gene expression in the scATAC-seq data.[42,43] These identities were confirmed by plotting top specific gene activity scores and chromatin accessibility at putative lineage-defining transcription factor binding sites. (Figures S3B–S3G). Top specific gene activity markers for the neutrophil cluster included *prkcda*. Plotting chromatin accessibility at the *prkcda* locus identified an intronic peak approximately 7 kb from the transcription start site that was most prominent in the neutrophil cluster and interacted strongly with the *prkcda* promoter (link score 0.73; Figure 4C). To understand whether this putative regulatory sequence was conserved across species and tissue types, we used a comparative approach and transduced human umbilical vein endothelial cells (HUVEC) with the adenovirus E4ORF1 gene to generate E4-HUVEC cells, a well-defined model of the human sinusoidal vascular niche.[44,45] Similar to the zebrafish kidney marrow scATAC-seq data, bulk ATAC sequencing identified a peak of accessible chromatin in an intronic region approximately 6 kb from the *PRKCD* transcriptional start site (Figures 4D and S3H). Find individual motif occurrences (FIMO)[46] analysis of putative transcription factor binding sites in the zebrafish and human enhancer sequences identified nine with $q < 0.05$ in both datasets (Figures 4E and S3I). These included the pluripotency factor KLF4 and WT1, a zinc-finger transcription factor expressed during hematopoiesis,[47] in the endocardium during development and after infarction,[48] and in tumor neo-vasculature, where it supports endothelial cell proliferation, migration, and tube formation via binding at the vascular endothelial growth factor (VEGF) promoter.[49,50] We tested the function of this intronic sequence by generating an *mClover* reporter construct and microinjecting this into zebrafish embryos. Fluorescence was observed in bulbus arteriosus endothelial cells of 72-hpf zebrafish embryos using live imaging (Figures 4F; Video 1) and confirmed by immunofluorescence for the vascular marker Fli1 and transgenic mClover (Figure 4G). This indicates the intronic sequence is an enhancer of *prkcda* expression in neutrophils and endothelial cells and identifies a *cis*-regulatory element with the potential to influence HSC fate.

PKC agonists augment HSPC engraftment and niche colonization in competition assays

We wished to understand the cellular and molecular mechanisms by which PKC enzymes, including *prkcda*, facilitate HSC colonization of the vascular niche. A chemical screen was performed to identify positive regulators of HSC engraftment in a zebrafish kidney marrow transplant assay. The experimental approach has been previously described[51]; briefly, kidney marrow from *ubi:GFP* transgenic zebrafish was treated at room temperature for 4 h prior to competitive transplantation into conditioned *casper* zebrafish recipients. Treated marrow was transplanted in a 1:2 ratio with untreated marrow from *ubi:mCherry* transgenic zebrafish (40,000 and 80,000 cells, respectively, per recipient). Short- and long-term readouts were performed at 4 and 12 weeks post transplantation (wpt) using two-color fluorescent imaging of the kidney marrow or FACS analysis of peripheral blood chimerism (Figure 5A). Marrow treated with 1,2-didecanoyl-sn-glycerol (DDG, a stabilized analog of diacylglycerol [DAG]; Millipore Sigma) significantly outcompeted control-treated marrow at the 4 wpt time point (Figure 5B). DAG is an activator of PKC family enzymes.[52] In particular, the subfamily of novel PKC enzymes (including PKC-δ) are strictly activated by DAG and do not require calcium release for activation.[53,54] To confirm this finding, the competitive transplant experiment was repeated using 12-O-tetradecanoylphorbol-13-acetate (TPA, also known as phorbol

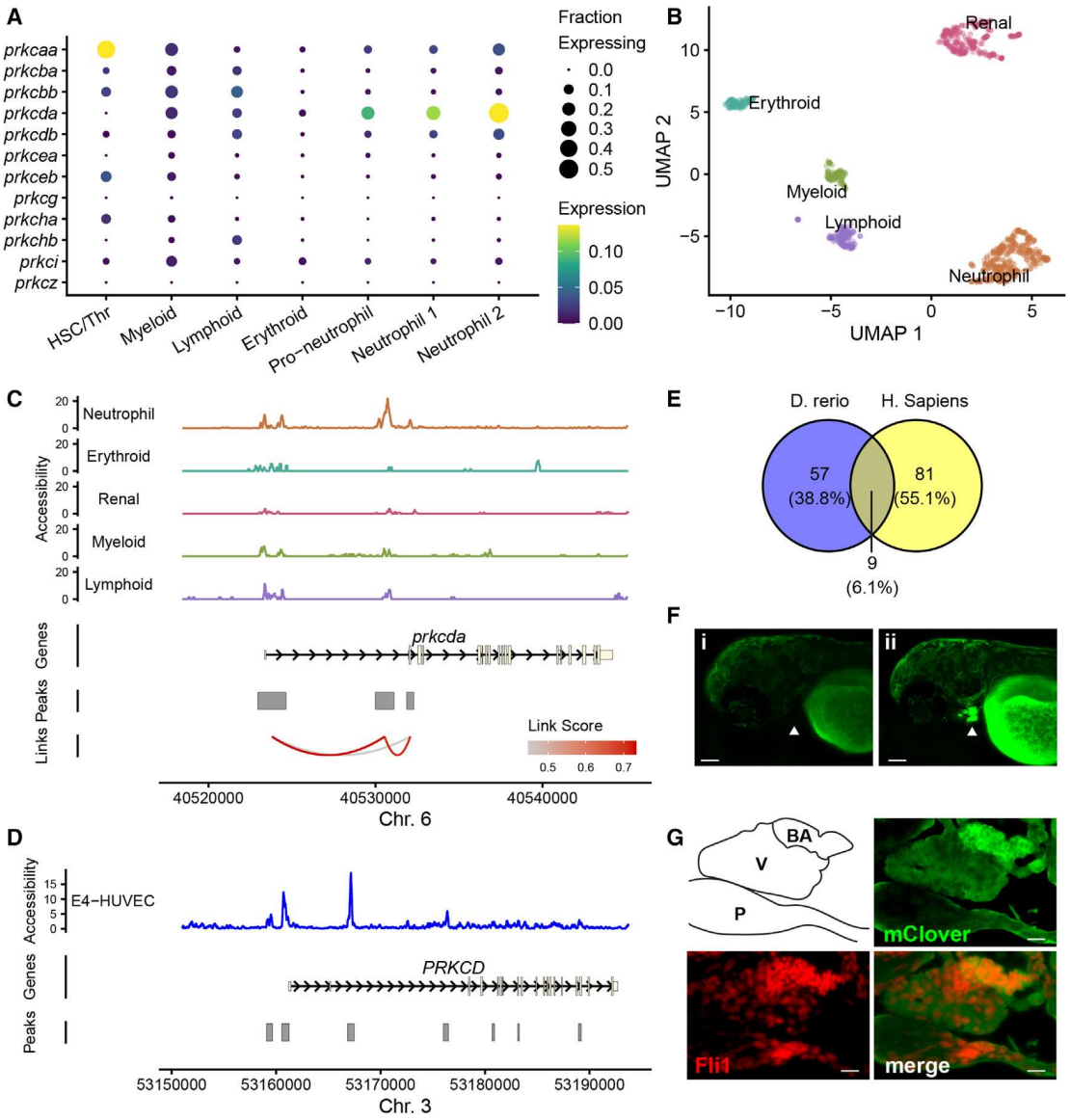

Figure 4. Regulation of *prkcda* expression by an intronic enhancer element

(A) Expression of PKC isoforms in kidney marrow cell clusters identified in Figure 3.

(B) UMAP representation of global chromatin accessibility in single zebrafish kidney marrow cells. Samples are from the same kidney marrow pools shown in Figure 3.

(C) Chromatin accessibility at the *prkcda* locus in kidney marrow cells by cluster. Peaks of chromatin accessibility and Cicero links identifying co-accessible peaks are shown.

(D) Bulk ATAC sequencing showing chromatin accessibility at the human PRKCD locus in E4-HUVEC cells. Peaks were identified using MACS2.

(E) FIMO analysis of zebrafish and human intron enhancer peak sequences. The number of putative binding sites with $q < 0.05$ in each set is indicated.

(F) Expression of an *mClover* reporter construct driven by the zebrafish *prkcda* intronic enhancer in uninjected (i) and injected (ii) animals. Arrowhead indicates the bulbus arteriosus. Bar, 25 μm.

(G) Immune fluorescence in a 72 hpf zebrafish embryo expressing the prkcda intronic enhancer reporter. Cryosections were probed with anti-GFP/mClover and anti-Fli1 antibodies and fluorescent secondaries (see STAR Methods). The outline indicates pericardium (P), ventricle (V), and bulbus arteriosus (BA, cardiac outflow tract). Bar, 10 μm. See also Figure S3 and Video S1.

12-myristate 13-acetate [PMA]), another DAG structural analog and PKC activator.[55] Marrow treated with TPA significantly outcompeted control-treated marrow relative to competitor at 4 and 12 wpt (Figure 5C). To identify downstream signaling dependencies for the enhanced engraftment observed after treatment with these PKC agonists, the competitive transplant assay was performed using TPA in combination with inhibitors of PKC (AEB071, PKCi) and mitogen-activated protein kinase kinase

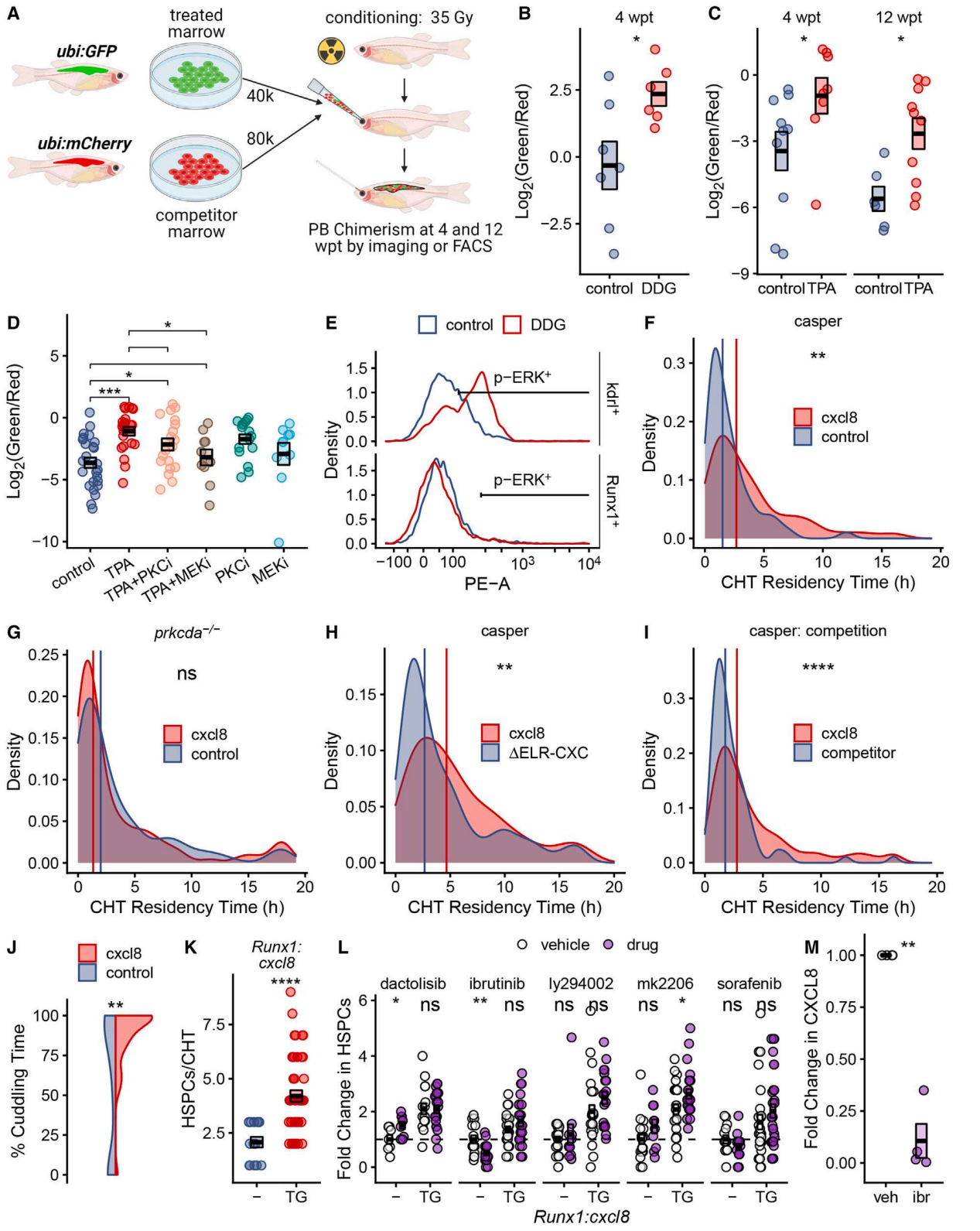

(legend on next page)

(MEK) (AZD6244, MEKi) signaling. Co-treatment with PKCi blunted the competitive advantage in engraftment conferred by TPA at 4 wpt, while co-treatment with MEKi significantly reduced the competitive advantage conferred by TPA (Figure 5D). These data suggested a role for PKC and mitogen-activated protein kinase (MAPK) in responding to cell-extrinsic signaling factors present in the hematopoietic microenvironment. To identify whether HSPCs, endothelial cells, or both respond to PKC stimulation, these cell types were FACS-sorted separately from *kdrl:mCherry;Runx1:EGFP* dual-reporter transgenics, treated *ex vivo* with DDG for 15 min, and assayed for ERK phosphorylation by intracellular flow cytometry. Kdrl+ endothelial cells showed a 38% increase in p-ERK+ cells, whereas no increase was observed in Runx1+ HSPCs (Figures 5E and S1). Since MEK/ERK inhibition blocked the engraftment advantage conferred by PKC signaling, these data support a model in which the vascular niche mediates HSPC engraftment via PKC and ERK.

A genetic approach was used to identify mechanisms by which *cxcl8*, a PKC agonist, might augment colonization of the vascular niche by HSPCs. Tol2-based zebrafish expression constructs were generated to enforce expression of a zebrafish *cxcl8a* (ENSDARG00000104795, *cxcl8*) minigene under control of the Runx1+23 HSC-specific enhancer,[27] with either P2A-GFP or P2A-mCherry co-expressed from the same transcript. These constructs (or controls expressing the fluorescent protein alone) were microinjected into single-cell *casper* zebrafish embryos and time-lapse fluorescence microscopy was used to quantify the dynamics of HSPC colonization of the CHT in F_0 transgenics (Figure S4A). Compared to HSPCs from clutchmate controls, HSPCs from *Runx1:cxcl8* transgenics had a significantly longer residency time within the CHT (Figure 5F).

We hypothesized that the low level of *prkcda* expression observed in the sinusoidal endothelial cells of the CHT might be required downstream of cxcl8 signaling in order to prolong HSPC residency time in the CHT. We generated a homozygous zebrafish line with a 4-bp deletion in the third exon of *prkcda* leading to loss of mRNA expression (*prkcda(−/−)*; Figures S4B and S4C). *Prkcda(−/−)* embryos microinjected with a *Runx1:cxcl8-2A-mCherry* expression construct showed no difference in CHT residency time compared with *prkcda(−/−)* animals microinjected with a control expression construct (Figure 5G). The effect of *cxcl8* on HSPC residency time was dependent upon the ELR-CXC amino acid motif, which is responsible for its engagement with cxcr1/cxcr2[56]; *Runx1:cxcl8* transgenics had significantly longer CHT residency time compared to clutchmates injected with a similar construct lacking this motif (Figure 5H).

Next, we designed an assay to directly observe *in vivo* competition between HSPCs with and without enforced expression of *cxcl8* within the same animal. *Runx1:cxcl8-2A-GFP* and *Runx1:mCherry* (or alternatively *Runx1:EGFP* and *Runx1:cxcl8-2A-mCherry*) expression constructs were co-injected into *casper* zebrafish embryos at a 1:1 molar ratio. HSPCs expressing only the control construct were identified as competitor HSPCs and those expressing the *Runx1:cxcl8* construct with or without expression of the control construct were identified as cxcl8-expressing HSPCs within each co-injected embryo. CHT residency time was significantly longer for *cxcl8*-expressing HSPCs compared to competitor HSPCs (Figure 5I).

Figure 5. PKC agonists augment HSPC engraftment and niche colonization in competition assays

(A) Schematic illustration of competitive marrow transplant experiments.

(B–D) Competitive transplant data are presented as Log_2(green/red) where green/red is the calculated ratio of drug- or control-treated marrow to untreated competitor marrow. Boxes represent mean ± SEM; each point is a biological replicate. (B) DDG vs. vehicle control at 4 wpt: DDG:competitor ratio 6.58 ± 2.18 vs. control:competitor ratio 2.11 ± 1.12, p = 0.026, Welch's t test. (C) TPA vs. vehicle control at 4 wpt: TPA:competitor ratio 0.99 ± 0.31 vs. control:competitor ratio 0.24 ± 0.07, p = 0.027, Wilcoxon rank-sum test. 12 wpt: TPA:competitor ratio 0.34 ± 0.11 vs. control:competitor ratio 0.03 ± 0.01, p = 0.016, Wilcoxon rank-sum test. (D) TPA treatment in the presence or absence of PKC and MEK inhibitors, vs. control. TPA vs. TPA+MEKi: TPA:competitor ratio 0.71 ± 0.13 vs. TPA+MEKi:competitor ratio 0.22 ± 0.08, p = 0.018, Wilcoxon rank-sum test.

(E) ERK phosphorylation was assessed by intracellular flow cytometry in sorted kdrl+ endothelial cells and Runx1+ HSPCs.

(F) Distribution of CHT residency times for n = 46 HSPCs from *Runx1:cxcl8* transgenics and n = 62 HSPCs from control clutchmates. Vertical lines indicate the median for each group. Representative data from one of four similar experiments is shown. For cxcl8 vs. control: median of 2.67 vs. 1.5 h, p = 0.003, Wilcoxon rank-sum test.

(G) Distribution of CHT residency times for *Runx1:cxcl8* transgenics and control clutchmates in the prkcda(−/−) mutant background. n = 108 HSPCs for *Runx1:cxcl8* and n = 111 HSPCs for control in 10 fish per group.

(H) Distribution of CHT residency times for n = 110 HSPCs from *Runx1:cxcl8* transgenics and n = 223 HSPCs from ΔELR-CXC clutchmates. Vertical lines indicate the median for each group. For cxcl8 vs. ΔELR-CXC; median of 4.66 vs. 2.66 h, p = 0.002, Wilcoxon rank-sum test.

(I) Distribution of CHT residency times for n = 404 HSPCs for *Runx1:cxcl8* and n = 174 HSPCs for competitor. Vertical lines indicated the median for each group. For cxcl8 vs. competitor: median of 2.75 vs. 1.75 h, $p = 1 \times 10^{-9}$, Wilcoxon rank-sum test.

(J) Violin plots represent the percentage of time individual HSPCs were cuddled by endothelial cells within the CHT. n = 32 HSPCs for *Runx1:cxcl8* and n = 108 HSPCs for control. For cxcl8 vs. control: median of 97.7% vs. 79.3% cuddling time, p = 0.0013, Wilcoxon rank-sum test.

(K) Quantification of Runx1:EGFP$^+$ HSPCs in *Runx1:EGFP;Runx1:cxcl8-2A-mCherry* transgenics (TG) and *Runx1:EGFP* clutchmates (−). Data are from one of two representative zebrafish clutches. Boxes represent mean ± SEM; each point is a biological replicate. For TG vs. −: 4.2 ± 0.27 vs. 2.1 ± 0.25 HSPCs per CHT, $p = 5.5 \times 10^{-7}$, Welch's t test.

(L) Quantification of Runx1:EGFP(+) HSPCs in *Runx1:cxcl8-2A-mCherry*transgenics (TG) and cxcl8 transgene-negative control clutchmates (−) treated with the indicated drugs or vehicle control. Data are presented as fold change relative to control-treated, transgene-negative clutchmates and are pooled from eight independent experiments. Boxes represent mean ± SEM; each point is a biological replicate. For ibrutinib-treated cxcl8 transgene-negative zebrafish: 0.51 ± 0.08-fold relative to vehicle-treated clutchmates, p = 0.0067, Welch's t test.

(M) Quantitative RT-PCR for CXCL8 mRNA expression by THP-1 cells treated with ibrutinib or vehicle control. Four biological replicates were performed per condition; each point is the mean of three technical replicates. For ibrutinib-treated cells: 0.11 ± 0.08-fold decrease relative to vehicle control, p = 0.002, Welch's t test. See also Figure S4.

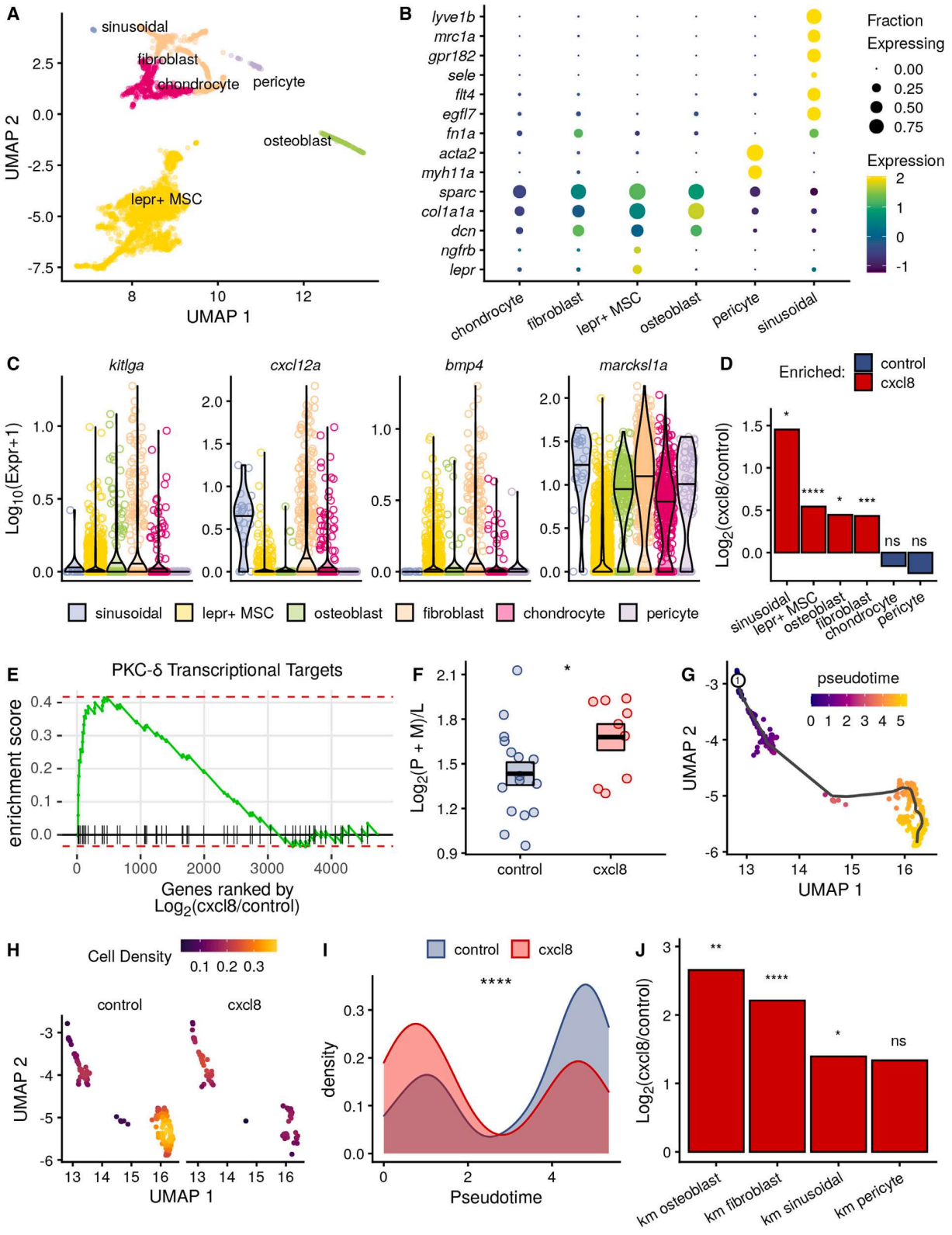

(legend on next page)

It was important to distinguish and quantify two types of HSPC behavior observed in the time-lapse imaging: prolonged interactions between relatively immobile HSPCs and a single pocket of endothelial cells ("cuddling") and persistent HSPC migration throughout the CHT. HSPCs from control transgenic animals showed a bimodal distribution of these behaviors with many cells migrating through the CHT without cuddling. By contrast, a large majority of HSPCs in *Runx1:cxcl8* transgenic animals spent most of their CHT residency time cuddling with endothelial cells (Figures 5J and S4D).

In order to quantify the effect of enforced expression of cxcl8 on HSPC colonization of the CHT in terms of absolute numbers, a stable *Runx1:cxcl8-2A-mCherry* transgenic line was generated and crossed to the established *Runx1:EGFP* transgenic reporter line. Enforced expression of *cxcl8* by HSPCs in this transgenic line increased CHT colonization 2-fold compared to *cxcl8* transgene-negative clutchmates (Figure 5K). Taken together, these findings show that *cxcl8* signals through *cxcr1/cxcr2* and *prkcda*, augmenting HSPC residency within the vascular niche via increased endothelial cell cuddling and expanding HSPC numbers.

We aimed to understand the upstream signaling mechanisms driving *cxcl8* expression by HSPCs in the zebrafish embryo and screened a panel of small-molecule inhibitors to identify those that reduced CHT colonization. We hypothesized that inhibition of these upstream mechanisms would reduce GFP(+) HSPC numbers in *Runx1:EGFP* embryos but would be rescued in *Runx1:cxcl8-2A-mCherry; Runx1:EGFP* embryos in which *cxcl8* expression is transgene-driven. Hemizygous *Runx1:cxcl8-2A-mCherry* transgenics were crossed to homozygous *Runx1:EGFP* transgenics, clutches were treated from 48 to 72 hpf, embryos were genotyped by mCherry expression, and HSPCs were enumerated by GFP expression. Treatment of zebrafish embryos with dactolisib (phosphoinositide 3-kinase [PI3K]/mammalian target of rapamycin [mTOR]), ly294002 (PI3K), mk2206 (AKT), and sorafenib (multikinase) at maximum tolerated doses did not significantly decrease CHT colonization in zebrafish embryos at 72 hpf, whereas treatment with the BTK/Tec family kinase inhibitor ibrutinib did significantly reduce CHT colonization in *Runx1:cxcl8-2A-mCherry(−);Runx1:EGFP(+)* transgenics (Figure 5L). However, enforced expression of *cxcl8* in *Runx1:cxcl8-2A-mCherry(+);Runx1:EGFP(+)* transgenics rescued CHT colonization by HSPCs in the presence of ibrutinib. Ibrutinib treatment significantly reduced *CXCL8* expression in the human myeloid cell line, THP-1 (Figure 5M). These results implicate BTK/Tec family kinase signaling upstream of *cxcl8* signaling in HSPCs as they colonize the vascular niche.

Cxcl8 expression by HSPCs expands hematopoietic niche populations

In order to understand how *cxcl8* signaling by HSPCs modifies the hematopoietic niche, we performed scRNA-seq on *Runx1:cxcl8-2A-mCherry* zebrafish embryos and clutchmate controls. We recovered 17,699 cells, and gene module analysis was used to define niche cell clusters (Figures 6A and S5A–S5D). Module 3 included many recognized niche genes, including *cxcl12a*, *kitlg*, *lepr*, *bmp4*, WNT factors, and Notch ligands (Figure S5D). Enriched GO terms for genes in module 3 compared to other modules included cell migration, cell communication, response to growth factor, and developmental processes (Table S3).

Niche cell clusters were individually identified as sinusoidal endothelial cell, osteoblast, fibroblast, chondrocyte, pericyte, and lepr+ mesenchymal stem cell (MSC) populations based on canonical gene expression and comparison with published datasets (Figures 6A, 6B, and S5E–S5I). To identify pericyte, fibroblast, and chondrocyte populations, murine niche cluster gene sets were converted to zebrafish orthologs and used to calculate aggregate gene scores (Figure S5G).[57] Expression of *cxcl12a* and the proliferative markers *cdk1*, *mki67*, *cenpf*, and *myca* were mutually exclusive between fibroblasts and pericytes/chondrocytes, respectively (Figures S5H and S5I). Expression of *kitlga*, *cxcl12a*, and *bmp4* within the six defined niche clusters is shown in Figure 6C. Also shown is expression of *marcksl1a*, the immediate downstream target of PKC signaling. Sinusoidal endothelial cells had the highest per-cell expression of *cxcl12a* and *marcksl1a*. Cluster membership according to experimental group was normalized according to total number of cells recovered and plotted for

Figure 6. Cxcl8 expression by HSPCs expands niche populations and favors early-pseudotime hematopoietic cells

(A) UMAP plot showing cellular populations from 96-hpf zebrafish embryos. Data are pooled from four samples derived from two clutches of *Runx1:cxcl8-2A-mCherry* transgenics and clutchmate controls. Each sample was a pool of 15–20 dissociated embryos.

(B) Expression of population-defining niche genes.

(C) Expression of selected hematopoietic and signaling factors by niche cell clusters.

(D) Differential representation of niche cell clusters according to experimental group. Positive values indicate enrichment in the *Runx1:cxcl8-2A-mCherry* group relative to clutchmate controls. Values were normalized according to the number of cells recovered per group. Sinusoidal, $p = 0.03$; lepr+ MSC, $p = 6.0 \times 10^{-18}$; osteoblast, $p = 0.03$; fibroblast, $p = 0.0005$; Fisher's exact test.

(E) GSEA enrichment plot for PKC-δ transcriptional targets. Expression data are ranked by differential expression in sinusoidal endothelial cells from *Runx1:cxcl8-2A-mCherry* embryos compared to control.

(F) The log-transformed ratio of precursor and myeloid cells to lymphoid cells is shown. Boxes indicate mean ± SEM. For cxcl8 vs. control, 3.25 ± 0.19 vs. 2.76 ± 0.16, $p = 0.049$, Welch's t test.

(G) Pseudotime trajectory in the hematopoietic cell partition. The root node is indicated.

(H) Stratification of progenitor/myeloid cells by experimental group.

(I) Distribution of progenitor/myeloid cells from *Runx1:cxcl8* transgenics and control clutchmates according to pseudotime. For cxcl8 vs. control, $p = 3.4 \times 10^{-5}$, two-sample Kolmogorov-Smirnov test.

(J) Differential representation of niche cell clusters according to experimental group. Positive values indicate enrichment in the *Runx1:cxcl8-2A-mCherry* group relative to clutchmate controls. Values were normalized according to the number of cells recovered per group. Osteoblast, $p = 0.0029$; fibroblast, $p = 2.7 \times 10^{-5}$; sinusoidal endothelial cells, $p = 0.013$; Fisher's exact test. See also Figures S5 and S6 and Tables S2–S4.

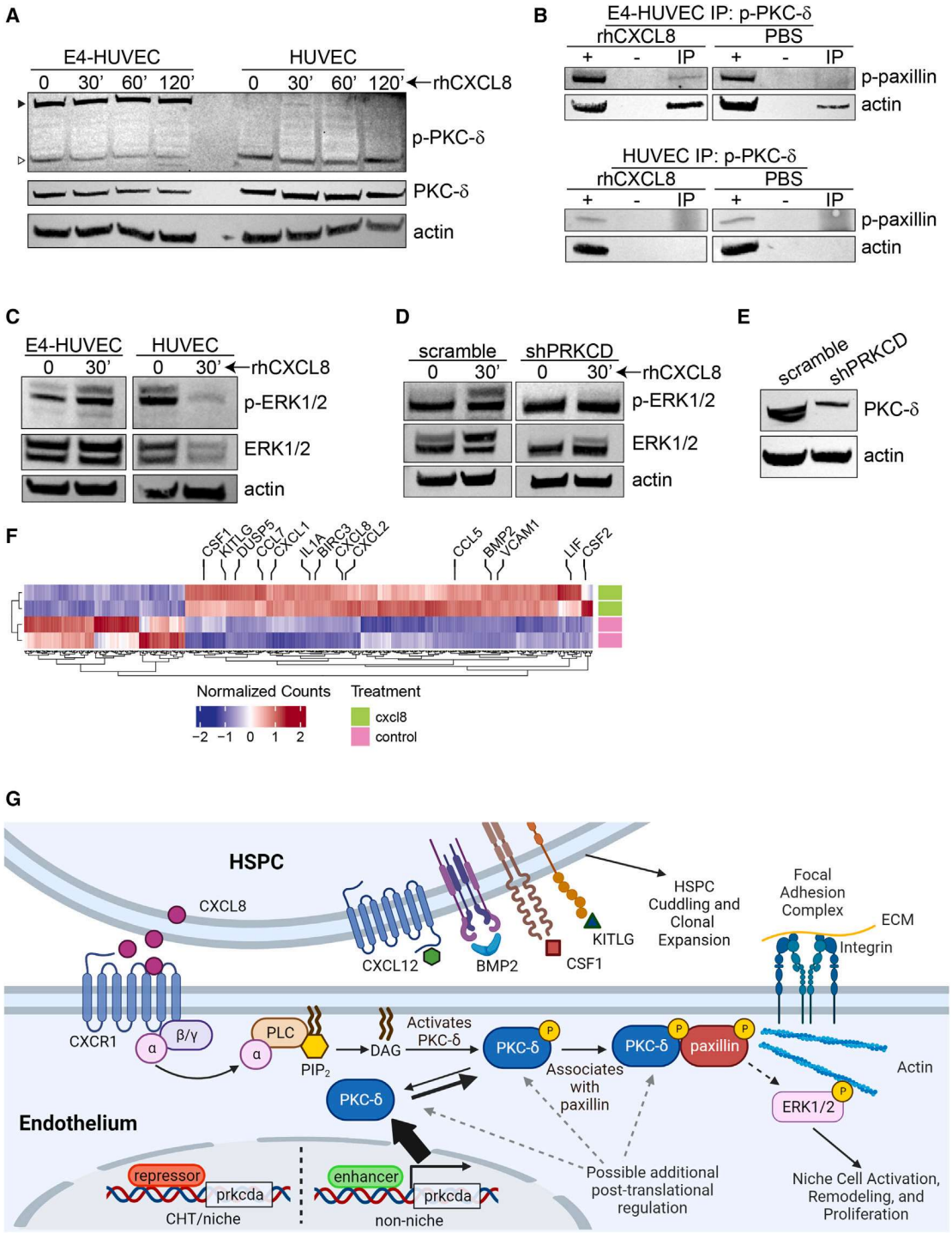

Figure 7. CXCL8 links PKC-δ to the focal adhesion complex

(A) E4-HUVEC and parental HUVEC cells were treated with rhCXCL8 (10 ng/mL) for the indicated times. The black triangle indicates the ~130-kDa form of p-PKC-δ and the white triangle indicates the ~78-kDa form.

(B) Immunoprecipitation (IP) for p-PKC-δ with immunoblotting for p-paxillin and actin is shown. Input lysate is indicated by (+); (−) indicates beads-only control. Treatment was with 10 ng/mL rhCXCL8 or PBS for 30 min.

(C) E4-HUVEC or parental HUVEC cells were treated with 10 ng/mL rhCXCL8 for the indicated times and immunoblotting for p-ERK1/2 and ERK1/2 was performed.

(legend continued on next page)

each niche population (Figure 6D). Sinusoidal endothelial cell, lepr+ MSC, osteoblast, and fibroblast populations were all significantly more abundant in *Runx1:cxcl8-2A-mCherry* embryos compared to clutchmate controls. To identify a signature of PKC-δ activation, pseudobulk differential expression analysis was performed on sinusoidal endothelial cells identified in *Runx1:cxcl8-2A-mCherry* and clutchmate control embryos. A list of PKC-δ-specific transcriptional targets has previously been reported.[58,59] Gene set enrichment analysis (GSEA) showed significant enrichment of PKC-δ transcriptional targets in genes upregulated in sinusoidal endothelial cells from *Runx1:cxcl8-2A-mCherry* embryos (normalized enrichment score [NES] 1.97; adjusted p = 0.0003, Figure 6E). This analysis shows that *cxcl8* expression by HSPCs leads to selective expansion of important niche cellular subsets with high levels of expression of factors supporting hematopoiesis.

Cxcl8 expression by HSPCs skews hematopoiesis in favor of immature populations and expands marrow niche populations

Next, we wished to understand the impact of long-term enforced *cxcl8* expression on the hematopoietic compartment. Kidney marrow was harvested from adult *Runx1:cxcl8-2A-mCherry* zebrafish at 3 mpf, analyzed by flow cytometry, and the relative proportion of myeloid, lymphoid, and precursor cells determined by forward- and side-scatter characteristics (Figures S6A and S6B).[60–62] The ratio of precursor plus myeloid cells to lymphoid cells was significantly greater in adult *Runx1:cxcl8-2A-mCherry* zebrafish compared to clutchmate controls (Figure 6F). At 12 mpf, kidney marrow was harvested from *Runx1:cxcl8-2A-mCherry* zebrafish and control clutchmates and scRNA-seq was performed. Progenitor/myeloid cells expressing *tal1*, *gata2b*, *mpx*, and *lyz* and lymphoid cells expressing *gata2a*, *ccr9a*, and *cd81a* were identified (Figures S6C and S6D). A pseudotime trajectory was plotted for the hematopoietic cells (Figure 6G). Root and leaf nodes were identified by expression of genes characteristic of HSPCs and mature myeloid cells (*tal1*, *spi1b*, and *mpx*; Figure S6E). Compared to control clutchmates, *Runx1:cxcl8-2A-mCherry* animals showed a relative expansion of early-pseudotime cells (Figures 6H and 6I). Consistent with the FACS experiment, the ratio of progenitor/myeloid cells to lymphoid cells was increased in *Runx1:cxcl8-2A-mCherry* zebrafish (18.0 vs. 7.8), suggesting the development of a "myeloid bias" seen in aged and diseased hematopoiesis.

We hypothesized that enforced expression of *cxcl8* in *Runx1:cxcl8-2A-mCherry* animals might expand niche-like cell populations as was observed in the embryo scRNA-seq experiments. A group of cells expressing *cxcl12a*, *dcn*, *fn1a*, and *col1a1a* was identified as the niche partition (Table S4; Figure S6D), and four sub-populations were identified by Louvain clustering (Figure S6F). Identities of these sub-populations were established using aggregate gene scores for the top markers from the embryonic niche (Figure S6G). The osteoblast, fibroblast, and sinusoidal cell populations were significantly over-represented in *Runx1:cxcl8-2A-mCherry* animals compared to clutchmate controls (Figure 6J). Thus, in concordance with our findings in zebrafish embryos, enforced expression of *cxcl8* in *Runx1:cxcl8-2A-mcherry* transgenics expands specific niche populations in the adult marrow.

CXCL8 links PKC-δ to the focal adhesion complex

We sought to identify molecular mechanisms by which CXCL8 activates the vascular niche to support hematopoiesis and how these might depend on PKC-δ. Immunoblotting HUVEC and E4-HUVEC cell lysates showed expression of total PKC-δ at the anticipated molecular weight of 78 kDa (middle panel, Figure 7A). Immunoblotting E4-HUVEC cell lysates for p-PKC-δ (phosphorylated Thr-505, Cell Signaling Technology) demonstrated a prominent high-molecular-weight band (approximately 130 kDa) that was not observed in HUVEC cells (black triangle, top panel, Figure 7A). By contrast, p-PKC-δ migrated at 78 kDa in HUVEC cells (white triangle, top panel, Figure 7A). Treatment of E4-HUVECs with recombinant human (rh) CXCL8 changed the relative intensity of the p-PKC-δ bands in favor of the 130-kDa form but had little effect on HUVEC cells (Figures 7A and S7A–S7C). A high-molecular weight form of PKC-δ was previously shown to associate with the signal transduction adapter protein paxillin as part of the focal adhesion complex.[63,64] To determine whether this was also the case in the vascular niche-like E4-HUVEC cells, we performed immunoprecipitation for p-PKC-δ, probed for p-paxillin, and found no association in the absence of rhCXCL8. However, in the presence of rhCXCL8, co-immunoprecipitation of p-PKC-δ and p-paxillin was observed (Figures 7B and S7D). Treatment with rhCXCL8 also increased association of p-PKC-δ with actin, the cytoskeletal component of the focal adhesion complex (Figures 7B and S7D). Parental HUVEC cells expressed comparatively low levels of p-paxillin; co-immunoprecipitation of p-PKC-δ and p-paxillin or actin was not observed in either the presence or absence of rhCXCL8 (Figures 7B and S7D). Together, these findings show that CXCL8 treatment preferentially stabilizes the high-molecular-weight form of p-PKC-δ, allowing its recruitment to focal adhesion complexes that may be induced upon HSC-niche interaction.

PKC-δ signals via ERK activation and ERK1/2 have been shown to associate with the focal adhesion complex.[65,66] Since

(D) E4-HUVEC cells were transduced with lentivirus expressing shRNA against PRKCD or scramble control. Immunoblotting for p-ERK1/2 and ERK1/2 was performed.
(E) shRNA knockdown of PKC-δ expression.
(F) Bulk RNA sequencing was performed in E4-HUVEC cells treated with rhCXCL8 for 6 h or PBS as a control. Significantly differentially regulated genes are shown with key hematopoietic factors highlighted. Each row indicates a biological replicate.
(G) Proposed model for HSPC remodeling of the niche via CXCL8 and PKC-δ. HSPCs produce CXCL8 upon encountering the vascular niche, which signals via CXCR1, releases DAG, and activates PKC family members. Transcription of PKC-δ is normally tightly controlled in order to maintain a reserve capacity to support HSPCs. CXCL8 signaling induces association of PKC-δ with the focal adhesion complex, activating niche functions such as HSPC cuddling and growth factor production. See also Figure S7 and Table S5 and S6.

our competitive transplant assay had shown that the advantage conferred by PKC agonists was dependent on MEK/ERK signaling (Figure 5D) and intracellular flow cytometry showed ERK phosphorylation in DDG-treated zebrafish endothelial cells (Figure 5E), we hypothesized that there would be induction of p-ERK in E4-HUVEC cells treated with rhCXCL8. This was indeed the case, and, by contrast, parental HUVEC cells treated with rhCXCL8 did not show induction of p-ERK (Figures 7C and S7E). This observation was dependent on PKC-δ since E4-HUVEC cells transduced with PRKCD short hairpin RNA (shRNA) did not show induction of p-ERK upon rhCXCL8 treatment (Figures 7D, 7E, S7F, and S7G). Bulk RNA-seq was performed on rhCXCL8-treated E4-HUVEC cells and showed transcriptional upregulation of anti-apoptotic factors, chemokines, and hematopoietic growth factors (Figures 7F; Table S5). GSEA demonstrated induction of gene programs associated with HSC differentiation, cytokine-cytokine receptor interactions, and ERK phosphorylation (Figures S7H–S7J; Table S6). These findings show that CXCL8 promotes association of p-PKC-δ with the focal adhesion complex, activating the MEK/ERK signaling cascade and expression of key hematopoietic growth factors.

DISCUSSION

Here we have shown that transcriptional dysregulation of PKC-δ increases the number of HSC clones that contribute to hematopoiesis and that PKC agonists such as CXCL8 or TPA enhance the ability for hematopoietic stem cells to compete for colonization or engraftment of the vascular niche. Based on these data, we propose the following model (Figure 7G): HSPCs produce CXCL8 upon encountering the vascular niche, signal via CXCR1, release DAG, and activate PKC family members. CXCL8 itself is likely induced by nuclear factor κB (NF-κB), the activity of which is positively regulated by BTK.[67,68] Transcription of PKC-δ is normally tightly regulated to keep the available pool of PKC in a tonic state and thereby maintain a reserve capacity to support additional HSCs. CXCL8 stabilizes association of phosphorylated PKC-δ with the focal cell adhesion complex, facilitating cytoskeletal reorganization, HSPC cuddling, and downstream activation of ERK1/2. This induces niche cell proliferation and expression of chemotactic factors, hematopoietic growth factors, and inflammatory signals that support the cuddled HSPC. The result of this cascade of intra- and intercellular signaling events is a change in fate of the cuddled HSC: HSCs that engage with the niche in this way actively contribute to hematopoiesis and those that do not are maintained in reserve or are pruned altogether from the HSC phylogenetic tree. The network of the epigenetic regulators that limits *prkcda* transcription in the vascular niche of the CHT but enhances its transcription in other endothelial cells is unclear and awaits further study. Understanding this regulatory network and how CXCL8 and other post-translational regulators of PKC-δ control its activity in the vascular niche may be relevant for hematologic diseases and engraftment after HSCT.

Using genetic barcoding techniques to study native hematopoiesis, we were able to experimentally isolate the effect of PKC-δ overexpression on HSC fate from any potential artifact of transplantation. HSPCs cycle rapidly in the CHT[19,20] and its murine cognate, the fetal liver,[69–71] in part to meet the needs of the developing organism. This degree of proliferation may be necessary to compensate for a population bottleneck observed in lineage tracing studies related to colonization of the fetal liver.[72] It was therefore quite surprising to find that a positive regulator of stem cell colonization (*prkcda*) is transcriptionally repressed in this tissue. Using ATAC sequencing in humans and zebrafish, we were able to identify intronic enhancer elements within PKC-δ sufficient to drive expression of a fluorescent reporter transgene in zebrafish vascular tissues. This points to a defined reserve capacity within the HSC pool that is maintained by active repression of epigenetic enhancer elements within niche cells and represents a mechanism by which the vascular niche regulates HSC fate. Dysregulation of this mechanism in *sele:prkcda-2A-mCherry* transgenic zebrafish pulls HSCs from the reserve pool, which may become prematurely exhausted, leading to their replacement by 12 mpf. Alternatively, *prkcda* expression may permit additional reserve short-term HSCs to survive the transition to adult hematopoiesis and thereby contribute their progeny to the peripheral blood. Expanded marrow cellular populations observed in *sele:prkcda-2A-mCherry* transgenics show that *prkcda* expression regulates HSC phenotypic fate as well. Future studies with refined transgenic lines and more sensitive fate recorders will be required to further define the progenitor and precursor populations and epigenetic elements involved.[73]

Altered HSC fate defines the natural history of hematopoietic disorders such as myelodysplasia and acute myeloid leukemia. Patients whose HSCs acquire a leukemic cell fate through a lengthy process of evolution and clonal selection have a dismal prognosis with all modern therapies.[74,75] Single-cell sequencing, phylogenetic barcoding, and time-lapse imaging have allowed insights into the cellular and molecular mechanisms by which the hematopoietic niche shapes long-term HSC fate. Understanding more about the reserve capacity of the hematopoietic niche could provide new therapeutic avenues for preserving HSC clonal diversity in patients with hematopoietic disorders.

Limitations of the study

In order to confirm the cell autonomy of the effects of *prkcda* and *cxcl8* on HSPC colonization and niche interactions, we attempted to make a series of knockouts using a tissue-specific CRISPR system but were unable to do so effectively. As is widely recognized, tissue-specific gene disruption is not easily achieved in the zebrafish model. Tissue-specific CRISPR, in particular, requires a strong transgenic driver. We believe the *sele* enhancer/promoter element used here is insufficiently strong for this method.

Experiments with enforced expression of *cxcl8* showed expansion of sinusoidal endothelial cells but also other well-defined niche cell types. Therefore, we cannot exclude a role for other niche cells in the effects observed in these experiments.

Although our E-selectin-based transgenics showed specific expression in CHT endothelial cells and not in HSPCs, it is

possible that some unrecognized off-target expression has occurred in our experiments.

STAR★METHODS

Detailed methods are provided in the online version of this paper and include the following:

- KEY RESOURCES TABLE
- RESOURCE AVAILABILITY
  - Lead contact
  - Materials availability
  - Data and code availability
- EXPERIMENTAL MODEL AND SUBJECT DETAILS
  - Zebrafish
  - Cell lines and primary cultures
- METHOD DETAILS
  - FACS
  - Microscopy
  - Quantitative image analysis
  - Transgenesis and GESTALT barcoding
  - Single cell RNA sequencing
  - Bulk GESTALT barcode sequencing
  - Single cell GESTALT sequencing
  - Single cell ATAC sequencing
  - Bulk RNA sequencing
  - Bulk ATAC sequencing
  - Embryo drug treatments
  - Kidney marrow treatments
  - Kidney marrow transplantation
  - Lentivirus
  - Immunoprecipitation and immunoblotting
  - *Whole-mount in situ hybridization*
  - Immunofluorescence
- QUANTIFICATION AND STATISTICAL ANALYSIS
  - ScRNA-seq data preprocessing and quality control
  - Dimensionality reduction
  - Cell clustering
  - Dataset reanalysis
  - Gene expression, gene module analysis, and aggregated gene scores
  - Pseudotime analysis
  - GO-term analysis
  - Single cell GESTALT barcode analysis
  - Single cell ATAC-seq analysis
  - General statistical analysis

SUPPLEMENTAL INFORMATION

Supplemental information can be found online at https://doi.org/10.1016/j.celrep.2023.112528.

ACKNOWLEDGMENTS

The authors would like to thank S. Cabrera for animal husbandry and members of the Zon Laboratory for critical reading of the manuscript.

This work was supported by NIH R01 DK128238 (B.W.B.), K08 DK111920 (B.W.B.), a Young Investigator Award from the Pelotonia Foundation (B.W.B.), UM1 CA186712 (W.E.C.), U01 HL134812 (L.I.Z.), P01 HL032262 (L.I.Z.), P01 HL131477, R01 HL144780 (L.I.Z.), RC2 DK120535 (L.I.Z.), an Alex's Lemonade Stand Crazy 8 Initiative Award (L.I.Z.), and research fellowships from the German Research Foundation and the Care-for-Rare Foundation (both to V.B.).

AUTHOR CONTRIBUTIONS

Conceptualization, B.W.B. and V.B.; methodology, B.W.B. and L.I.Z.; software, B.W.B., W.L., and T.C.G.; investigation, V.B., W.L., M.F., K.O., D.L.C., J.S., E.M.T., S.S., A.M., A.B., W.D., S.O., E.H., J.R.P., S.A., A.L., F.B., M.A., S.Y., and Y.Z.; resources, B.W.B., H.R.S., R.L., and L.I.Z.; data curation, B.W.B.; writing – original draft, B.W.B. and V.B.; writing – review and editing, S.A., E.M.T., J.S.B., W.E.C., and L.I.Z., supervision, B.W.B.; project administration, B.W.B.; funding acquisition, B.W.B. and L.I.Z.

DECLARATION OF INTERESTS

L.I.Z. is a founder and stockholder of Fate Therapeutics, CAMP4 Therapeutics, Amagma Therapeutics, Scholar Rock, and Branch Biosciences. He is a consultant for Celularity and Cellarity.

Received: March 13, 2022
Revised: March 19, 2023
Accepted: May 2, 2023
Published: May 18, 2023

REFERENCES

1. Perlin, J.R., Robertson, A.L., and Zon, L.I. (2017). Efforts to enhance blood stem cell engraftment: recent insights from zebrafish hematopoiesis. J. Exp. Med. *214*, 2817–2827. https://doi.org/10.1084/jem.20171069.
2. Pinho, S., and Frenette, P.S. (2019). Haematopoietic stem cell activity and interactions with the niche. Nat. Rev. Mol. Cell Biol. *20*, 303–320. https://doi.org/10.1038/s41580-019-0103-9.
3. Abelson, S., Collord, G., Ng, S.W.K., Weissbrod, O., Mendelson Cohen, N., Niemeyer, E., Barda, N., Zuzarte, P.C., Heisler, L., Sundaravadanam, Y., et al. (2018). Prediction of acute myeloid leukaemia risk in healthy individuals. Nature *559*, 400–404. https://doi.org/10.1038/s41586-018-0317-6.
4. Genovese, G., Kähler, A.K., Handsaker, R.E., Lindberg, J., Rose, S.A., Bakhoum, S.F., Chambert, K., Mick, E., Neale, B.M., Fromer, M., et al. (2014). Clonal hematopoiesis and blood-cancer risk inferred from blood DNA sequence. N. Engl. J. Med. *371*, 2477–2487. https://doi.org/10.1056/NEJMoa1409405.
5. Jaiswal, S., Fontanillas, P., Flannick, J., Manning, A., Grauman, P.V., Mar, B.G., Lindsley, R.C., Mermel, C.H., Burtt, N., Chavez, A., et al. (2014). Age-related clonal hematopoiesis associated with adverse outcomes. N. Engl. J. Med. *371*, 2488–2498. https://doi.org/10.1056/NEJMoa1408617.
6. Jaiswal, S., Natarajan, P., Silver, A.J., Gibson, C.J., Bick, A.G., Shvartz, E., McConkey, M., Gupta, N., Gabriel, S., Ardissino, D., et al. (2017). Clonal hematopoiesis and risk of atherosclerotic cardiovascular disease. N. Engl. J. Med. *377*, 111–121. https://doi.org/10.1056/NEJMoa1701719.
7. Meisel, M., Hinterleitner, R., Pacis, A., Chen, L., Earley, Z.M., Mayassi, T., Pierre, J.F., Ernest, J.D., Galipeau, H.J., Thuille, N., et al. (2018). Microbial signals drive pre-leukaemic myeloproliferation in a Tet2-deficient host. Nature *557*, 580–584. https://doi.org/10.1038/s41586-018-0125-z.
8. Nagata, Y., Makishima, H., Kerr, C.M., Przychodzen, B.P., Aly, M., Goyal, A., Awada, H., Asad, M.F., Kuzmanovic, T., Suzuki, H., et al. (2019). Invariant patterns of clonal succession determine specific clinical features of myelodysplastic syndromes. Nat. Commun. *10*, 5386. https://doi.org/10.1038/s41467-019-13001-y.
9. Avagyan, S., Henninger, J.E., Mannherz, W.P., Mistry, M., Yoon, J., Yang, S., Weber, M.C., Moore, J.L., and Zon, L.I. (2021). Resistance to inflammation underlies enhanced fitness in clonal hematopoiesis. Science *374*, 768–772. https://doi.org/10.1126/science.aba9304.
10. Butler, J.M., Nolan, D.J., Vertes, E.L., Varnum-Finney, B., Kobayashi, H., Hooper, A.T., Seandel, M., Shido, K., White, I.A., Kobayashi, M., et al.

(2010). Endothelial cells are essential for the self-renewal and repopulation of Notch-dependent hematopoietic stem cells. Cell Stem Cell *6*, 251–264. https://doi.org/10.1016/j.stem.2010.02.001.

11. Himburg, H.A., Termini, C.M., Schlussel, L., Kan, J., Li, M., Zhao, L., Fang, T., Sasine, J.P., Chang, V.Y., and Chute, J.P. (2018). Distinct bone marrow sources of pleiotrophin control hematopoietic stem cell maintenance and regeneration. Cell Stem Cell *23*, 370–381.e5. https://doi.org/10.1016/j.stem.2018.07.003.
12. Winkler, I.G., Barbier, V., Nowlan, B., Jacobsen, R.N., Forristal, C.E., Patton, J.T., Magnani, J.L., and Lévesque, J.P. (2012). Vascular niche E-selectin regulates hematopoietic stem cell dormancy, self renewal and chemoresistance. Nat. Med. *18*, 1651–1657. https://doi.org/10.1038/nm.2969.
13. Kobayashi, H., Butler, J.M., O'Donnell, R., Kobayashi, M., Ding, B.S., Bonner, B., Chiu, V.K., Nolan, D.J., Shido, K., Benjamin, L., and Rafii, S. (2010). Angiocrine factors from Akt-activated endothelial cells balance self-renewal and differentiation of haematopoietic stem cells. Nat. Cell Biol. *12*, 1046–1056. https://doi.org/10.1038/ncb2108.
14. Poulos, M.G., Guo, P., Kofler, N.M., Pinho, S., Gutkin, M.C., Tikhonova, A., Aifantis, I., Frenette, P.S., Kitajewski, J., Rafii, S., and Butler, J.M. (2013). Endothelial Jagged-1 is necessary for homeostatic and regenerative hematopoiesis. Cell Rep. *4*, 1022–1034. https://doi.org/10.1016/j.celrep.2013.07.048.
15. Itkin, T., Gur-Cohen, S., Spencer, J.A., Schajnovitz, A., Ramasamy, S.K., Kusumbe, A.P., Ledergor, G., Jung, Y., Milo, I., Poulos, M.G., et al. (2016). Distinct bone marrow blood vessels differentially regulate haematopoiesis. Nature *532*, 323–328. https://doi.org/10.1038/nature17624.
16. Ding, L., Saunders, T.L., Enikolopov, G., and Morrison, S.J. (2012). Endothelial and perivascular cells maintain haematopoietic stem cells. Nature *481*, 457–462. https://doi.org/10.1038/nature10783.
17. Ding, L., and Morrison, S.J. (2013). Haematopoietic stem cells and early lymphoid progenitors occupy distinct bone marrow niches. Nature *495*, 231–235. https://doi.org/10.1038/nature11885.
18. Hooper, A.T., Butler, J.M., Nolan, D.J., Kranz, A., Iida, K., Kobayashi, M., Kopp, H.G., Shido, K., Petit, I., Yanger, K., et al. (2009). Engraftment and reconstitution of hematopoiesis is dependent on VEGFR2-mediated regeneration of sinusoidal endothelial cells. Cell Stem Cell *4*, 263–274. https://doi.org/10.1016/j.stem.2009.01.006.
19. Murayama, E., Kissa, K., Zapata, A., Mordelet, E., Briolat, V., Lin, H.F., Handin, R.I., and Herbomel, P. (2006). Tracing hematopoietic precursor migration to successive hematopoietic organs during zebrafish development. Immunity *25*, 963–975. https://doi.org/10.1016/j.immuni.2006.10.015.
20. Blaser, B.W., Moore, J.L., Hagedorn, E.J., Li, B., Riquelme, R., Lichtig, A., Yang, S., Zhou, Y., Tamplin, O.J., Binder, V., and Zon, L.I. (2017). CXCR1 remodels the vascular niche to promote hematopoietic stem and progenitor cell engraftment. J. Exp. Med. *214*, 1011–1027. https://doi.org/10.1084/jem.20161616.
21. Beis, D., Bartman, T., Jin, S.W., Scott, I.C., D'Amico, L.A., Ober, E.A., Verkade, H., Frantsve, J., Field, H.A., Wehman, A., et al. (2005). Genetic and cellular analyses of zebrafish atrioventricular cushion and valve development. Development *132*, 4193–4204. https://doi.org/10.1242/dev.01970.
22. Okuda, K.S., Astin, J.W., Misa, J.P., Flores, M.V., Crosier, K.E., and Crosier, P.S. (2012). lyve1 expression reveals novel lymphatic vessels and new mechanisms for lymphatic vessel development in zebrafish. Development *139*, 2381–2391. https://doi.org/10.1242/dev.077701.
23. Rossi, A., Kontarakis, Z., Gerri, C., Nolte, H., Hölper, S., Krüger, M., and Stainier, D.Y.R. (2015). Genetic compensation induced by deleterious mutations but not gene knockdowns. Nature *524*, 230–233. https://doi.org/10.1038/nature14580.
24. Munson, M.J., Mathai, B.J., Ng, M.Y.W., Trachsel-Moncho, L., de la Ballina, L.R., Schultz, S.W., Aman, Y., Lystad, A.H., Singh, S., Singh, S., et al. (2021). GAK and PRKCD are positive regulators of PRKN-independent mitophagy. Nat. Commun. *12*, 6101. https://doi.org/10.1038/s41467-021-26331-7.
25. Liu, Q., Li, A., Tian, Y., Wu, J.D., Liu, Y., Li, T., Chen, Y., Han, X., and Wu, K. (2016). The CXCL8-CXCR1/2 pathways in cancer. Cytokine Growth Factor Rev. *31*, 61–71. https://doi.org/10.1016/j.cytogfr.2016.08.002.
26. Lang, K., Niggemann, B., Zanker, K.S., and Entschladen, F. (2002). Signal processing in migrating T24 human bladder carcinoma cells: role of the autocrine interleukin-8 loop. Int. J. Cancer *99*, 673–680. https://doi.org/10.1002/ijc.10424.
27. Tamplin, O.J., Durand, E.M., Carr, L.A., Childs, S.J., Hagedorn, E.J., Li, P., Yzaguirre, A.D., Speck, N.A., and Zon, L.I. (2015). Hematopoietic stem cell arrival triggers dynamic remodeling of the perivascular niche. Cell *160*, 241–252. https://doi.org/10.1016/j.cell.2014.12.032.
28. Jin, S.W., Beis, D., Mitchell, T., Chen, J.N., and Stainier, D.Y.R. (2005). Cellular and molecular analyses of vascular tube and lumen formation in zebrafish. Development *132*, 5199–5209. https://doi.org/10.1242/dev.02087.
29. McKenna, A., Findlay, G.M., Gagnon, J.A., Horwitz, M.S., Schier, A.F., and Shendure, J. (2016). Whole-organism lineage tracing by combinatorial and cumulative genome editing. Science *353*, aaf7907. https://doi.org/10.1126/science.aaf7907.
30. Teets, E.M., Gregory, C., Shaffer, J., Blachly, J.S., and Blaser, B.W. (2020). Quantifying hematopoietic stem cell clonal diversity by selecting informative Amplicon barcodes. Sci. Rep. *10*, 2153. https://doi.org/10.1038/s41598-020-59119-8.
31. Baron, C.S., Barve, A., Muraro, M.J., van der Linden, R., Dharmadhikari, G., Lyubimova, A., de Koning, E.J.P., and van Oudenaarden, A. (2019). Cell type purification by single-cell transcriptome-trained sorting. Cell *179*, 527–542.e19. https://doi.org/10.1016/j.cell.2019.08.006.
32. Huang, Y., Lu, Y., He, Y., Feng, Z., Zhan, Y., Huang, X., Liu, Q., Zhang, J., Li, H., Huang, H., et al. (2019). Ikzf1 regulates embryonic T lymphopoiesis via Ccr9 and Irf4 in zebrafish. J. Biol. Chem. *294*, 16152–16163. https://doi.org/10.1074/jbc.RA119.009883.
33. Lawir, D.F., Iwanami, N., Schorpp, M., and Boehm, T. (2017). A missense mutation in zbtb17 blocks the earliest steps of T cell differentiation in zebrafish. Sci. Rep. *7*, 44145. https://doi.org/10.1038/srep44145.
34. Lu, X., Zhang, Y., Liu, F., and Wang, L. (2020). Rac2 regulates the migration of T lymphoid progenitors to the thymus during zebrafish embryogenesis. J. Immunol. *204*, 2447–2454. https://doi.org/10.4049/jimmunol.1901494.
35. Zlotoff, D.A., Sambandam, A., Logan, T.D., Bell, J.J., Schwarz, B.A., and Bhandoola, A. (2010). CCR7 and CCR9 together recruit hematopoietic progenitors to the adult thymus. Blood *115*, 1897–1905. https://doi.org/10.1182/blood-2009-08-237784.
36. Carter, R.H., and Barrington, R.A. (2004). Signaling by the CD19/CD21 complex on B cells. Curr. Dir. Autoimmun. *7*, 4–32. https://doi.org/10.1159/000075685.
37. Oren, R., Takahashi, S., Doss, C., Levy, R., and Levy, S. (1990). TAPA-1, the target of an antiproliferative antibody, defines a new family of transmembrane proteins. Mol. Cell Biol. *10*, 4007–4015. https://doi.org/10.1128/mcb.10.8.4007-4015.1990.
38. Muench, D.E., Olsson, A., Ferchen, K., Pham, G., Serafin, R.A., Chutipongtanate, S., Dwivedi, P., Song, B., Hay, S., Chetal, K., et al. (2020). Mouse models of neutropenia reveal progenitor-stage-specific defects. Nature *582*, 109–114. https://doi.org/10.1038/s41586-020-2227-7.
39. Tusi, B.K., Wolock, S.L., Weinreb, C., Hwang, Y., Hidalgo, D., Zilionis, R., Waisman, A., Huh, J.R., Klein, A.M., and Socolovsky, M. (2018). Population snapshots predict early haematopoietic and erythroid hierarchies. Nature *555*, 54–60. https://doi.org/10.1038/nature25741.
40. Tang, Q., Iyer, S., Lobbardi, R., Moore, J.C., Chen, H., Lareau, C., Hebert, C., Shaw, M.L., Neftel, C., Suva, M.L., et al. (2017). Dissecting hematopoietic and renal cell heterogeneity in adult zebrafish at single-cell resolution using RNA sequencing. J. Exp. Med. *214*, 2875–2887. https://doi.org/10.1084/jem.20170976.
41. Raaijmakers Marc, H.G.P., Mukherjee, S., Guo, S., Zhang, S., Kobayashi, T., Schoonmaker, J.A., Ebert, B.L., Al-Shahrour, F., Hasserjian, R.P., Scadden, E.O., et al. (2010). Bone progenitor dysfunction induces

myelodysplasia and secondary leukaemia. Nature *464*, 852–857. https://doi.org/10.1038/nature08851.

42. Pliner, H.A., Packer, J.S., McFaline-Figueroa, J.L., Cusanovich, D.A., Daza, R.M., Aghamirzaie, D., Srivatsan, S., Qiu, X., Jackson, D., Minkina, A., et al. (2018). Cicero predicts cis-regulatory DNA interactions from single-cell chromatin accessibility data. Mol. Cell *71*, 858–871.e8. https://doi.org/10.1016/j.molcel.2018.06.044.
43. Hao, Y., Hao, S., Andersen-Nissen, E., Mauck, W.M., 3rd, Zheng, S., Butler, A., Lee, M.J., Wilk, A.J., Darby, C., Zager, M., et al. (2021). Integrated analysis of multimodal single-cell data. Cell *184*, 3573–3587.e29. https://doi.org/10.1016/j.cell.2021.04.048.
44. Seandel, M., Butler, J.M., Kobayashi, H., Hooper, A.T., White, I.A., Zhang, F., Vertes, E.L., Kobayashi, M., Zhang, Y., Shmelkov, S.V., et al. (2008). Generation of a functional and durable vascular niche by the adenoviral E4ORF1 gene. Proc. Natl. Acad. Sci. USA. *105*, 19288–19293. https://doi.org/10.1073/pnas.0805980105.
45. Ramalingam, R., Rafii, S., Worgall, S., Brough, D.E., and Crystal, R.G. (1999). E1(-)E4(+) adenoviral gene transfer vectors function as a "pro-life" signal to promote survival of primary human endothelial cells. Blood *93*, 2936–2944.
46. Grant, C.E., Bailey, T.L., and Noble, W.S. (2011). FIMO: Scanning for occurrences of a given motif. Bioinformatics *27*, 1017–1018.
47. Ellisen, L.W., Carlesso, N., Cheng, T., Scadden, D.T., and Haber, D.A. (2001). The Wilms tumor suppressor WT1 directs stage-specific quiescence and differentiation of human hematopoietic progenitor cells. EMBO J. *20*, 1897–1909. https://doi.org/10.1093/emboj/20.8.1897.
48. Duim, S.N., Kurakula, K., Goumans, M.J., and Kruithof, B.P.T. (2015). Cardiac endothelial cells express Wilms' tumor-1: Wt1 expression in the developing, adult and infarcted heart. J. Mol. Cell. Cardiol. *81*, 127–135. https://doi.org/10.1016/j.yjmcc.2015.02.007.
49. Wagner, N., Michiels, J.F., Schedl, A., and Wagner, K.D. (2008). The Wilms' tumour suppressor WT1 is involved in endothelial cell proliferation and migration: expression in tumour vessels in vivo. Oncogene *27*, 3662–3672. https://doi.org/10.1038/sj.onc.1211044.
50. McCarty, G., Awad, O., and Loeb, D.M. (2011). WT1 protein directly regulates expression of vascular endothelial growth factor and is a mediator of tumor response to hypoxia. J. Biol. Chem. *286*, 43634–43643. https://doi.org/10.1074/jbc.M111.310128.
51. Li, P., Lahvic, J.L., Binder, V., Pugach, E.K., Riley, E.B., Tamplin, O.J., Panigrahy, D., Bowman, T.V., Barrett, F.G., Heffner, G.C., et al. (2015). Epoxyeicosatrienoic acids enhance embryonic haematopoiesis and adult marrow engraftment. Nature *523*, 468–471. https://doi.org/10.1038/nature14569.
52. Steinberg, S.F. (2008). Structural basis of protein kinase C isoform function. Physiol. Rev. *88*, 1341–1378. https://doi.org/10.1152/physrev.00034.2007.
53. Kikkawa, U., Matsuzaki, H., and Yamamoto, T. (2002). Protein kinase C delta (PKC delta): activation mechanisms and functions. J. Biochem. *132*, 831–839. https://doi.org/10.1093/oxfordjournals.jbchem.a003294.
54. Ogita, K., Miyamoto, S., Yamaguchi, K., Koide, H., Fujisawa, N., Kikkawa, U., Sahara, S., Fukami, Y., and Nishizuka, Y. (1992). Isolation and characterization of delta-subspecies of protein kinase C from rat brain. Proc. Natl. Acad. Sci. USA. *89*, 1592–1596. https://doi.org/10.1073/pnas.89.5.1592.
55. Zhang, G., Kazanietz, M.G., Blumberg, P.M., and Hurley, J.H. (1995). Crystal structure of the cys2 activator-binding domain of protein kinase C delta in complex with phorbol ester. Cell *81*, 917–924. https://doi.org/10.1016/0092-8674(95)90011-x.
56. Falsone, A., Wabitsch, V., Geretti, E., Potzinger, H., Gerlza, T., Robinson, J., Adage, T., Teixeira, M.M., and Kungl, A.J. (2013). Designing CXCL8-based decoy proteins with strong anti-inflammatory activity in vivo. Biosci. Rep. *33*, e00068. https://doi.org/10.1042/BSR20130069.
57. Baryawno, N., Przybylski, D., Kowalczyk, M.S., Kfoury, Y., Severe, N., Gustafsson, K., Kokkaliaris, K.D., Mercier, F., Tabaka, M., Hofree, M., et al. (2019). A cellular taxonomy of the bone marrow stroma in homeostasis and leukemia. Cell *177*, 1915–1932.e16. https://doi.org/10.1016/j.cell.2019.04.040.
58. Garg, R., Caino, M.C., and Kazanietz, M.G. (2013). Regulation of transcriptional networks by PKC isozymes: identification of c-Rel as a key transcription factor for PKC-regulated genes. PLoS One *8*, e67319. https://doi.org/10.1371/journal.pone.0067319.
59. Caino, M.C., von Burstin, V.A., Lopez-Haber, C., and Kazanietz, M.G. (2011). Differential regulation of gene expression by protein kinase C isozymes as determined by genome-wide expression analysis. J. Biol. Chem. *286*, 11254–11264. https://doi.org/10.1074/jbc.M110.194332.
60. North, T.E., Goessling, W., Walkley, C.R., Lengerke, C., Kopani, K.R., Lord, A.M., Weber, G.J., Bowman, T.V., Jang, I.H., Grosser, T., et al. (2007). Prostaglandin E2 regulates vertebrate haematopoietic stem cell homeostasis. Nature *447*, 1007–1011. https://doi.org/10.1038/nature05883.
61. Goessling, W., North, T.E., Loewer, S., Lord, A.M., Lee, S., Stoick-Cooper, C.L., Weidinger, G., Puder, M., Daley, G.Q., Moon, R.T., and Zon, L.I. (2009). Genetic interaction of PGE2 and Wnt signaling regulates developmental specification of stem cells and regeneration. Cell *136*, 1136–1147. https://doi.org/10.1016/j.cell.2009.01.015.
62. Traver, D., Paw, B.H., Poss, K.D., Penberthy, W.T., Lin, S., and Zon, L.I. (2003). Transplantation and in vivo imaging of multilineage engraftment in zebrafish bloodless mutants. Nat. Immunol. *4*, 1238–1246. https://doi.org/10.1038/ni1007.
63. Robertson, J., Jacquemet, G., Byron, A., Jones, M.C., Warwood, S., Selley, J.N., Knight, D., Humphries, J.D., and Humphries, M.J. (2015). Defining the phospho-adhesome through the phosphoproteomic analysis of integrin signalling. Nat. Commun. *6*, 6265. https://doi.org/10.1038/ncomms7265.
64. Rosales, J.L., and Isseroff, R.R. (1995). Increased expression of a high molecular weight (130 KD) protein kinase C isoform in a differentiation-defective ras-transfected keratinocyte line. J. Cell. Physiol. *164*, 509–521. https://doi.org/10.1002/jcp.1041640309.
65. Ueda, Y., Hirai, S.i., Osada, S.i., Suzuki, A., Mizuno, K., and Ohno, S. (1996). Protein kinase C activates the MEK-ERK pathway in a manner independent of Ras and dependent on Raf. J. Biol. Chem. *271*, 23512–23519. https://doi.org/10.1074/jbc.271.38.23512.
66. López-Colomé, A.M., Lee-Rivera, I., Benavides-Hidalgo, R., and López, E. (2017). Paxillin: a crossroad in pathological cell migration. J. Hematol. Oncol. *10*, 50. https://doi.org/10.1186/s13045-017-0418-y.
67. Petro, J.B., Rahman, S.M., Ballard, D.W., and Khan, W.N. (2000). Bruton's tyrosine kinase is required for activation of IkappaB kinase and nuclear factor kappaB in response to B cell receptor engagement. J. Exp. Med. *191*, 1745–1754. https://doi.org/10.1084/jem.191.10.1745.
68. Shinners, N.P., Carlesso, G., Castro, I., Hoek, K.L., Corn, R.A., Woodland, R.T., Scott, M.L., Wang, D., and Khan, W.N. (2007). Bruton's tyrosine kinase mediates NF-kappa B activation and B cell survival by B cell-activating factor receptor of the TNF-R family. J. Immunol. *179*, 3872–3880. https://doi.org/10.4049/jimmunol.179.6.3872.
69. Morrison, S.J., Hemmati, H.D., Wandycz, A.M., and Weissman, I.L. (1995). The purification and characterization of fetal liver hematopoietic stem cells. Proc. Natl. Acad. Sci. USA. *92*, 10302–10306. https://doi.org/10.1073/pnas.92.22.10302.
70. Fleming, W.H., Alpern, E.J., Uchida, N., Ikuta, K., Spangrude, G.J., and Weissman, I.L. (1993). Functional heterogeneity is associated with the cell cycle status of murine hematopoietic stem cells. J. Cell Biol. *122*, 897–902. https://doi.org/10.1083/jcb.122.4.897.
71. Bowie, M.B., McKnight, K.D., Kent, D.G., McCaffrey, L., Hoodless, P.A., and Eaves, C.J. (2006). Hematopoietic stem cells proliferate until after birth and show a reversible phase-specific engraftment defect. J. Clin. Invest. *116*, 2808–2816. https://doi.org/10.1172/JCI28310.
72. Ganuza, M., Hall, T., Finkelstein, D., Chabot, A., Kang, G., and McKinney-Freeman, S. (2017). Lifelong haematopoiesis is established by hundreds

of precursors throughout mammalian ontogeny. Nat. Cell Biol. *19*, 1153–1163. https://doi.org/10.1038/ncb3607.

73. McKenna, A., and Gagnon, J.A. (2019). Recording development with single cell dynamic lineage tracing. Development *146*. https://doi.org/10.1242/dev.169730.
74. Dohner, H., Wei, A.H., Appelbaum, F.R., Craddock, C., DiNardo, C.D., Dombret, H., Ebert, B.L., Fenaux, P., Godley, L.A., Hasserjian, R.P., et al. (2022). Diagnosis and management of AML in adults: 2022 ELN recommendations from an international expert panel. Blood. https://doi.org/10.1182/blood.2022016867.
75. Wong, T.N., Ramsingh, G., Young, A.L., Miller, C.A., Touma, W., Welch, J.S., Lamprecht, T.L., Shen, D., Hundal, J., Fulton, R.S., et al. (2015). Role of TP53 mutations in the origin and evolution of therapy-related acute myeloid leukaemia. Nature *518*, 552–555. https://doi.org/10.1038/nature13968.
76. White, R.M., Sessa, A., Burke, C., Bowman, T., LeBlanc, J., Ceol, C., Bourque, C., Dovey, M., Goessling, W., Burns, C.E., and Zon, L.I. (2008). Transparent adult zebrafish as a tool for in vivo transplantation analysis. Cell Stem Cell *2*, 183–189. https://doi.org/10.1016/j.stem.2007.11.002.
77. Raj, B., Wagner, D.E., McKenna, A., Pandey, S., Klein, A.M., Shendure, J., Gagnon, J.A., and Schier, A.F. (2018). Simultaneous single-cell profiling of lineages and cell types in the vertebrate brain. Nat. Biotechnol. *36*, 442–450. https://doi.org/10.1038/nbt.4103.
78. Schneider, C.A., Rasband, W.S., and Eliceiri, K.W. (2012). NIH Image to ImageJ: 25 years of image analysis. Nat. Methods *9*, 671–675. https://doi.org/10.1038/nmeth.2089.
79. Lawrence, C., Best, J., Cockington, J., Henry, E.C., Hurley, S., James, A., Lapointe, C., Maloney, K., and Sanders, E. (2016). The complete and updated "rotifer polyculture method" for rearing first feeding zebrafish. J. Vis. Exp., e53629. https://doi.org/10.3791/53629.
80. Nagabhushana, A., and Mishra, R.K. (2016). Finding clues to the riddle of sex determination in zebrafish. J. Biosci. *41*, 145–155. https://doi.org/10.1007/s12038-016-9593-1.
81. Trapnell, C., Roberts, A., Goff, L., Pertea, G., Kim, D., Kelley, D.R., Pimentel, H., Salzberg, S.L., Rinn, J.L., and Pachter, L. (2012). Differential gene and transcript expression analysis of RNA-seq experiments with TopHat and Cufflinks. Nat. Protoc. *7*, 562–578. https://doi.org/10.1038/nprot.2012.016.
82. Thisse, C., and Thisse, B. (2008). High-resolution in situ hybridization to whole-mount zebrafish embryos. Nat. Protoc. *3*, 59–69. https://doi.org/10.1038/nprot.2007.514.
83. McCarthy, D.J., Campbell, K.R., Lun, A.T.L., and Wills, Q.F. (2017). Scater: pre-processing, quality control, normalization and visualization of single-cell RNA-seq data in R. Bioinformatics *33*, 1179–1186. https://doi.org/10.1093/bioinformatics/btw777.
84. McGinnis, C.S., Murrow, L.M., and Gartner, Z.J. (2019). DoubletFinder: doublet detection in single-cell RNA sequencing data using artificial nearest neighbors. Cell Syst. *8*, 329–337.e4. https://doi.org/10.1016/j.cels.2019.03.003.
85. Trapnell, C., Cacchiarelli, D., Grimsby, J., Pokharel, P., Li, S., Morse, M., Lennon, N.J., Livak, K.J., Mikkelsen, T.S., and Rinn, J.L. (2014). The dynamics and regulators of cell fate decisions are revealed by pseudotemporal ordering of single cells. Nat. Biotechnol. *32*, 381–386. https://doi.org/10.1038/nbt.2859.
86. Becht, E., McInnes, L., Healy, J., Dutertre, C.A., Kwok, I.W.H., Ng, L.G., Ginhoux, F., and Newell, E.W. (2018). Dimensionality reduction for visualizing single-cell data using UMAP. Nat. Biotechnol. *37*, 38–44. https://doi.org/10.1038/nbt.4314.
87. Haghverdi, L., Lun, A.T.L., Morgan, M.D., and Marioni, J.C. (2018). Batch effects in single-cell RNA-sequencing data are corrected by matching mutual nearest neighbors. Nat. Biotechnol. *36*, 421–427. https://doi.org/10.1038/nbt.4091.
88. Blondel, V.D., Guillaume, J.L., Lambiotte, R., and Lefebvre, E. (2008). Fast unfolding of communities in large networks. J. Stat. Mech. *2008*, P10008. https://doi.org/10.1088/1742-5468/2008/10/P10008.
89. Wolf, F.A., Hamey, F.K., Plass, M., Solana, J., Dahlin, J.S., Göttgens, B., Rajewsky, N., Simon, L., and Theis, F.J. (2019). PAGA: graph abstraction reconciles clustering with trajectory inference through a topology preserving map of single cells. Genome Biol. *20*, 59. https://doi.org/10.1186/s13059-019-1663-x.
90. Traag, V.A., Waltman, L., and van Eck, N.J. (2019). From Louvain to Leiden: guaranteeing well-connected communities. Sci. Rep. *9*, 5233. https://doi.org/10.1038/s41598-019-41695-z.
91. Moran, P.A. (1950). Notes on continuous stochastic phenomena. Biometrika *37*, 17–23. https://doi.org/10.2307/2332142.
92. Cao, J., Spielmann, M., Qiu, X., Huang, X., Ibrahim, D.M., Hill, A.J., Zhang, F., Mundlos, S., Christiansen, L., Steemers, F.J., et al. (2019). The single-cell transcriptional landscape of mammalian organogenesis. Nature *566*, 496–502. https://doi.org/10.1038/s41586-019-0969-x.
93. Alexa, A., and Rahnenfuhrer, J. (2020). topGO: Enrichment Analysis for Gene Ontology.
94. Sayols, S. (2020). Rrvgo: A Bioconductor Package to Reduce and Visualize Gene Ontology Terms.
95. Martin, M. (2011). Cutadapt removes adapter sequences from high-throughput sequencing reads. EMBnet. j. *17*, 10. https://doi.org/10.14806/ej.17.1.200.
96. Bonfield, J.K., Marshall, J., Danecek, P., Li, H., Ohan, V., Whitwham, A., Keane, T., and Davies, R.M. (2021). HTSlib: C library for reading/writing high-throughput sequencing data. GigaScience *10*. https://doi.org/10.1093/gigascience/giab007.
97. Daily, J. (2016). Parasail: SIMD C library for global, semi-global, and local pairwise sequence alignments. BMC Bioinf. *17*, 81. https://doi.org/10.1186/s12859-016-0930-z.
98. Needleman, S.B., and Wunsch, C.D. (1970). A general method applicable to the search for similarities in the amino acid sequence of two proteins. J. Mol. Biol. *48*, 443–453. https://doi.org/10.1016/0022-2836(70)90057-4.

STAR★METHODS

KEY RESOURCES TABLE

REAGENT or RESOURCE	SOURCE	IDENTIFIER
Antibodies		
PKCδ (D10E2) Rabbit mAb	Cell Signaling Technology	Cat# 9616S; RRID:AB_10949973
Phospho-PKCδ (Thr505) Rabbit Polyclonal Antibody	Cell Signaling Technology	Cat# 9374S; RRID:AB_2168837
Phospho-p44/42 MAPK (Erk1/2) (Thr202/Tyr204) (E10) Mouse mAb	Cell Signaling Technology	Cat# 9106S; RRID:AB_331768
p44/42 MAPK (Erk1/2) (137F5) Rabbit mAb	Cell Signaling Technology	Cat# 4695S; RRID:AB_390779
Phospho-Paxillin (Tyr118) Polyclonal Antibody	ThermoFisher Scientific	Cat# 44-722G; RRID:AB_2533733
Fli1 Rabbit Polyclonal Antibody	ThermoFisher Scientific	Cat# PA5-13440; RRID:AB_2106098
Gfp Tag Mouse Monoclonal Antibody (GF28R)	ThermoFisher Scientific	Cat# MA5-15256; RRID:AB_10979281
Goat anti-mouse AF-488	ThermoFisher Scientific	Cat# A32723; RRID:AB_2633275
Donkey anti-rabbit AF-594	ThermoFisher Scientific	Cat# A-21207; RRID:AB_141637
Biological samples		
Human Umbilical Vein Endothelial Cells, HUVEC Pooled	ThermoFisher Scientific	Cat# C01510C
Chemicals, peptides, and recombinant proteins		
EnGen® Spy Cas9 NLS	New England Biolabs	Cat# m0646
Recombinant Human IL-8/CXCL8 Protein	R&D Systems	Cat# 208-IL-010
HA-100 dihydrochloride	Santa Cruz Biotechnology	Cat# sc-203072
dactolisib	Selleck Chemicals	Cat# S1009
ibrutinib	Selleck Chemicals	Cat# S2680
ly294002	Selleck Chemicals	Cat# S1005
mk2206	Selleck Chemicals	Cat# S1078
sorafenib	Millipore Sigma	Cat# SML2653
AEB071	Cayman Chemical	Cat# 16726
AZD6244	Cayman Chemical	Cat# 11599
Phorbol 12-myristate 13-acetate (TPA)	Cayman Chemical	Cat# 10008014
1,2-didecanoyl-sn-glycerol (DDG)	Millipore Sigma	Cat# 800810P
Critical commercial assays		
Chromium™ Single Cell 3′ GEM, Library & Gel Bead Kit v3	10X Genomics	Cat# 1000092
LIVE/DEAD™ Viability/Cytotoxicity Kit, for mammalian cells	ThermoFisher Scientific	Cat# L3224
Taqman™ Gene Expression Assay (FAM), S (250 reactions/250 μL), assay ID: Hs00174103_m1	ThermoFisher Scientific	Cat# 4331182
Taqman™ Gene Expression Assay (FAM), S (250 reactions/250 μL), assay ID: Hs03003631_g1	ThermoFisher Scientific	Cat# 4331182
SMART-Seq v4 Ultra Low Input RNA Kit	Clontech	Cat# 634888
Zymo-Seq RiboFree Total RNA Library Kit	Zymo Research	Cat#R3000
ATAC-seq Kit	Active Motif	Cat# 53150
Pierce™ Crosslink Magnetic IP/Co-IP Kit	ThermoFisher Scientific	Cat# 88805
Chromium™ Single Cell ATAC Library & Gel Bead Kit	10X Genomics	Cat# 1000111
Deposited data		
Processed source data for analysis scripts	This paper	Mendeley Data: https://doi.org/10.17632/6s7vy929dc.1
FASTQs and cell-barcode matrices for scRNA-seq and scATAC-seq experiments	This paper	GEO: GSE191029

(*Continued on next page*)

Continued

REAGENT or RESOURCE	SOURCE	IDENTIFIER
GRCh38 Reference Sequence	Genome Reference Consortium	https://useast.ensembl.org/Homo_sapiens/Info/Index
GRCz11 Reference Sequence	Genome Reference Consortium	https://useast.ensembl.org/Danio_rerio/Info/Index
Zfin GRCz11 Gene Model	The Zebrafish Information Network	https://zfin.org/downloads
Experimental models: cell lines		
E4-HUVEC	This paper	N/A
Lenti-X™ 293T cell Line	Takara Bio	Cat# 632180
Experimental models: organisms/strains		
Zebrafish: *casper*	White et al.[76]	N/A
Zebrafish: GESTALT	McKenna et al.[29]	N/A
Zebrafish: *kdrl:EGFP: Tg(kdrl:EGFP)*	Beis et al.[21]	ZDB-ALT-050916-14
Zebrafish: *Runx1:EGFP: Tg(Mmu.Runx1:EGFP)*	Tamplin et al.[27]	ZDB-ALT-150512-1
Zebrafish: *lyve1b:dsRed*: Tg(-5.2lyve1b:dsRed)nz101	Okuda et al.[22]	ZDB-ALT-120723-3
Zebrafish: *prkcda(−/−)*	This paper	N/A
Zebrafish: *Runx1:cxcl8-2A-mCherry*:	This paper	N/A
Zebrafish: *sele:prkcda-2A-mCherry*:	This paper	N/A
Oligonucleotides		
Primer: raj_GP6: GAGGACTACACCATCGTGGAG	Raj et al.[77]	N/A
Primer: partial_read_1: GTGACTGGAGTTCAGACGTG TGCTCTTCCGATCTNNNNNNNNNNTCGAGCTCAAGC TTCGGAC	This paper	N/A
Primer: mod_GP12: CTACACGACGCTCTTCCGATCT	Modified from Raj et al.[77]	N/A
Primer: GESTALT F: ACACTCTTTCCCTACACGACG CTCTTCCGATCTTCGAGCTCAAGCTTCGG	Modified from McKenna et al.[29]	N/A
Primer: GESTALT R: GACTGGAGTTCA GACGTGTGCTCTTCCGATCTCTGCCATTTGTCT CGAGGTC	Modified from McKenna et al.[29]	N/A
Primer: prkcda_probe_F: CACCTCACTATCCTC GCTGG	This paper	N/A
Primer: prkcda_probe_R: TAATACGACTCACT ATAGGCTCATGGCTAGTTTGGTGG	This paper	N/A
HsPRKCD shRNA targeting sequence: CTTCG GAGGGAAATTGTAAAT	This paper	N/A
Recombinant DNA		
Plasmid: sele792-prkcda-2a-mcherry-395	This paper	N/A
Plasmid: sele792-mcs-2a-mcherry-395	This paper	N/A
Plasmid: pLV [Exp]-EGFP: T2A: Puro-hPGK> E4ORF1	This paper	N/A
Plasmid: prkcda-intron-1-enhancer-clover394	This paper	N/A
Plasmid: pLV[shRNA]-mCherry/Neo-U6>hPRKCD	This paper	N/A
Software and algorithms		
Project analysis scripts	This paper	https://github.com/blaserlab/pkc_cxcl8
Data processing scripts	This paper	Mendeley Data: https://doi.org/10.17632/6s7vy929dc.1
Analysis function library	This paper	https://github.com/blaserlab/blaseRtools
Supporting data for analysis functions	This paper	https://github.com/blaserlab/blaseRdata
Encode RNA seq pipeline	ENCODE Consortium	https://www.encodeproject.org/pipelines/ENCPL002LPE/
Encode ATAC seq pipeline	ENCODE Consortium	https://www.encodeproject.org/pipelines/ENCPL787FUN/

(*Continued on next page*)

Continued		
REAGENT or RESOURCE	SOURCE	IDENTIFIER
10X CellRanger v4.0	10X Genomics	https://support.10xgenomics.com/
10X CellRanger-ATAC v1.2	10X Genomics	https://support.10xgenomics.com/
ImageJ	Schneider et al.[78]	https://ImageJ.nih.gov/ij/
BZ-X700 Viewer Ver. 1.31	Keyence Corp	N/A
BZ-X700 Analyzer Ver. 1.31 BZ-H3AE	Keyence Corp	N/A
Other		
OctoMACs Dead Cell Removal Kit	Miltenyi Biotec	Cat#130-090-101
BZ-X710 Fluorescence Microscope	Keyence Corp	N/A
Nikon Ti Custom Microscope with Yokogawa Spinning Disk	Boston Microscopes and suppliers	N/A
Nikon A1R Live Cell Imaging System	Nikon	N/A
S9i stereomicroscope with integrated camera	Leica	N/A
VSV-G Lenti-X Packaging single shots	Takara Bio	Cat#631275

RESOURCE AVAILABILITY

Lead contact

Further information and requests for resources and reagents should be directed to and will be fulfilled by the lead contact, Bradley W. Blaser (bradley.blaser@osumc.edu).

Materials availability

Plasmids and zebrafish lines generated in this study are available upon request and subsequent completion of Uniform Biological Material Transfer Agreement.

Data and code availability

- The sequencing data generated during this study is available at GEO: GSE191029. Processed data are available as an R package via Mendeley Data: https://doi.org/10.17632/6s7vy929dc.1.
- Analysis code is publicly available at https://github.com/blaserlab/pkc_cxcl8. Raw data processing scripts and additional documentation are available within the R data package.
- Any additional information required to reanalyze the data reported in this paper is available from the lead contact upon request.

EXPERIMENTAL MODEL AND SUBJECT DETAILS

Zebrafish

The zebrafish, *Danio rerio*, was used for all studies. GESTALT zebrafish were a kind gift of A. Schier.[29] *Casper, kdrl:EGFP, Runx1:EGFP,* and *lyve1b:dsRed* zebrafish were previously reported.[76] All zebrafish were group housed in recirculating aquatic systems with automated control of temperature (28.5C), pH (7.4) and conductivity (1000 μS) under a 14h:10h light:dark cycle. Animals were fed live rotifers beginning at approximately 5 dpf[79] and commercial pelleted diets beginning at approximately 9 dpf (Gemma 75, Gemma 300, Skretting, Oregon, USA). Experiments were performed at the developmental stages indicated in the main text (72–96 hpf for embryos and larvae; 3 mpf and later for adults). Zebrafish sex determination occurs between 25 and 50 days post-fertilization so embryo/larvae experiments were performed on hermaphroditic animals.[80] Adult zebrafish experiments were performed on unselected populations of male and female animals. The M:F ratio was approximately 1:1. The OSUCCC Aquatic Facility is AAALAC-accredited and all experiments were performed under IACUC protocol 2018A00000012.

Cell lines and primary cultures

Pooled primary HUVEC cells from male and female donors were purchased from Thermo Fisher Scientific (C01510C), passaged twice and cryopreserved. Early-passage cells were used for all *in vitro* experiments (2–4 passages total). HUVEC and E4-HUVEC cells were cultured in M200 medium (ThermoFisher Scientific M200500) supplemented with 2% FBS, Hydrocortisone 1 μg/mL, human EGF 10 ng/mL, b-FGF 3ngmL and Heparin 10 μg/mL (LSGS kit, ThermoFisher Scientific). Cells were serum-starved in M200 alone for 8h prior to treatment with rhCXCL8 (RND Systems). 293T cells were cultured in high-glucose Dulbecco's Modified Eagles Medium supplemented with 10% fetal bovine serum, 4 mM L-glutamine, 1mM sodium pyruvate and penicillin/streptomycin. Cells were cultured in a humidified 5% $C0_2$ atmosphere at 37C.

METHOD DETAILS

FACS

Zebrafish embryos were euthanized by tricaine overdose, minced with a razor blade in PBS, and digested in collagenase with agitation (Liberase, Roche). Endothelial cells were isolated after two rounds of cell sorting. In the first round, kdrl:EGFP(+) cells were enriched from total live cells. Enriched endothelial cells were resorted into kdrl:EGFP(+); lyve1b:dsRed(+) and kdrl:EGFP(+); lyve1b:dsRed(−) fractions. For kidney marrow FACS, adult zebrafish were euthanized by ice water immersion, kidney marrow was dissected and triturated ice-cold PBS. Erythrocytes were lysed with NH_4Cl. For intracellular phosphoprotein staining, cells were fixed in PFA for 10 min, dehydrated in methanol, and washed before antibody staining in the presence of 0.5% BSA and 0.02% sodium azide. Sorting was performed on a BD FACSAria instrument and analysis was performed on a BD LSRII instrument.

Microscopy

For live zebrafish embryo imaging, animals were anesthetized in tricaine (MS-222, Sigma) and then mounted in 1 mL of 1.2% LMP agarose in E3 embryo medium containing 40 μL of tricaine solution. Fluorescence microscopy was performed using a BZ-X710 (KEYENCE Corp of America, Itasca, IL) digital microscope and maximum intensity projections generated using Keyence BZ-X Analyzer software and ImageJ.[78] For some experiments, images were obtained on a Nikon inverted Ti microscope using a Yokogawa spinning disc confocal and Andor iXon ×3 EMC cameras or a Nikon A1R live cell imaging microscope. Timelapse images were recorded at 15–20 min intervals and assembled into image stacks using ImageJ. For gross imaging of kidney marrow transplant recipients, anesthetized zebrafish were imaged using a Zeiss Discovery Dissecting Stereoscope using Axiovision v4.6. Fluorescence intensity in red and green channels was measured in the area of the kidney marrow and in an adjacent background area using ImageJ.[51] Green:Red ratio was calculated as: $\frac{G_{kidney} - G_{background}}{R_{kidney} - R_{background}}$.

Quantitative image analysis

For static imaging experiments, HSPCs within the bounds of the CHT (dorsal boundary: ventral aspect of the caudal artery; ventral boundary: dorsal aspect of the caudal vein; rostral boundary: termination of the yolk sac extension, caudal boundary: apex of the angle formed by the caudal artery and vein) were identified and manually counted using the multi-point tool in ImageJ. In order to quantify CHT residency time in time lapse experiments, individual HSPCs were identified and manually tracked through image stacks, noting the total number of frames each HSPC continuously remained in the CHT. To determine cuddling time, each timelapse frame in which an HSPC was in close proximity to the same endothelial cells from the preceding timelapse frame was marked as "cuddled". Percent cuddling time was calculated for each HSPC as:

$$\frac{cuddled\ timelapse\ frames}{total\ timelapse\ frames} \times 100$$

All quantitative image analysis was performed in a blinded fashion or with confirmation by a second observer.

Transgenesis and GESTALT barcoding

For transgenesis experiments, 20 pg of expression plasmid DNA was injected with 20 pg Tol2 mRNA in a volume of 1 nL into zebrafish embryos at the single-cell stage. For barcoding experiments, GESTALT sgRNAs 1–10 were synthesized at Horizon Discovery according to published sequences.[29] 20 pg of equimolar pooled GESTALT sgRNAs and 0.3 nL EnGen Spy Cas9 (20 μM) were added per nanoliter injected.

Single cell RNA sequencing

Raw cell suspensions from zebrafish kidney marrow were generated as for FACS analysis. For zebrafish larval scRNA-seq, animals were anesthetized with tricaine and euthanized on ice. Deyolking was performed in a solution of 55 mM NaCl, 1.8 mM KCl, and 1.25 mM $NaHCO_3$ until complete by visual inspection. After washing, larvae were dissociated in TrypLE Express with pipetting. Kidney marrow or larval cell suspensions were then gently triturated in FACSmax Cell Dissociation Solution (Genlantis, CA, USA) and passed through a 40 μm cell strainer. Cell suspensions were transferred to DNA lo-bind tubes on ice. Cells were filtered twice more with 40 μm flowmi filters. Red blood cells were lysed with NH_4Cl and cell suspensions underwent bead-based dead cell depletion using the Dead Cell Depletion kit with MS Columns (Miltenyi Biotec, Germany). Flow-through containing live cells was centrifuged at 500 g for 5 min and cells were resuspended in PBS with 0.04% BSA. Cell suspensions were counted using the Invitrogen LIVE/DEAD Viability/Cytotoxicity Kit using a Keyence BZ-X710 fluorescence microscope. Cell suspensions were loaded into the 10X chip, cDNA was synthesized and amplified, and sequencing libraries were prepared according to the 10X Genomics Chromium Next GEM Single Cell 3′ Reagent Kit v3.1 RevD protocol. Final gene expression libraries were quantified using Qubit, an Agilent DNA High-Sensitivity Bio-analyzer, and KAPA qPCR. Gene expression libraries were pooled and sequenced using the NovaSeq6000 SP PE 150bp kit.

Bulk GESTALT barcode sequencing

Peripheral blood was collected from anesthetized zebrafish by retro-orbital bleeding using a Hamilton syringe. Blood was added to 50 μL blood buffer (250 mg Heparin, 1 mL FBS, 49 mL of H2O) and DNA was extracted with the Zymo Quick DNA Miniprep Kit. 5 μL (approximately 1 μg) genomic DNA was used in a 50 μL PCR reaction using GESTALT F and R primers.[29] The PCR products were cleaned up using the Agencourt AMPure XP Purification Kit with 90 μL beads to bind the DNA and 42 μL of Elution Buffer. PCR product was visualized on a 1% agarose gel and 25 μL of a 20 ng/μL concentration was sent for Amplicon EZ sequencing (Genewiz). GESTALT barcode sequencing data was analyzed using SABER.[30]

Single cell GESTALT sequencing

GESTALT barcodes were amplified from 10X-cell barcoded cDNA using a semi-nested PCR approach adapted from a published protocol.[77] The first round of PCR amplification was performed in a 50 μL reaction with NEB Q5 mastermix using between 9.5 ng and 16.5 ng barcoded cDNA and 1.25 μL each of primers raj_GP6 and partial_read_1, each at 10 μM. Thermal cycling was one cycle of 98°C × 30 s (initial denaturation), fifteen cycles of 98°C × 10 s, 61°C × 25 s, 72°C × 30 s with finale extension of 72°C × 2 min. The reaction products were purified using 30 μL AMPure beads (0.6X ratio, Beckman Coulter) and eluted in 20 μL. The second round of amplification was performed in 50 μL with Q5 mastermix using 8 μL of the product from step 1, and 1.25 μL each of primers mod_GP12 and partial_read_1, each at 10 μM. Thermal cycling was one cycle of 98°C × 30 s (initial denaturation), 8 cycles of 98°C × 10 s, 60°C × 25 s, and 72°C × 30 s with a final extension of 72°C × 2 min. The reaction was cleaned up with 30 μL AMPure beads and eluted in 30 μL. This product was used as the input for the sample index PCR (step 5.4) of the 10X genomics Next GEM VDJ reagent kit v1.1 protocol. Single-cell GESTALT libraries were sequenced using a Miseq 300 cycle kit with a 28 x 301 configuration.

Single cell ATAC sequencing

Cells were prepared as described for scRNA-seq and cryopreserved. Nuclei were isolated from freshly thawed cells using the 10X Single Cell ATAC Sequencing Demonstrated Protocol for PBMCs, RevD. Nuclei were loaded onto the 10X Single Cell ATAC Chip E using version 1 Gel Bead and Library reagents. Libraries were prepared according to the manufacturer's protocol. ScATAC libraries were sequenced at Genewiz using a 2 x 150 configuration.

Bulk RNA sequencing

RNA sequencing libraries were made from zebrafish endothelial subsets sorted from 3 independent clutches using the SMART-Seq v4 Ultra Low Input RNA Kit (Clontech). E4 HUVEC RNA sequencing libraries were made using the Zymo-Seq RiboFree Total RNA Library kit. Libraries were sequenced in a paired-end fashion and data were pre-processed using the ENCODE paired-end/stranded long RNA pipeline for HUVECs (https://www.encodeproject.org/pipelines/ENCPL002LPE/) or TopHat/Cufflinks for zebrafish endothelial cells.[81] Differential gene expression was calculated in R using DESeq2 (HUVEC data) or Cuffdiff (zebrafish endothelial cells). For the Cuffdiff analysis, p values had a default lower bound of 10^{-5}.

Bulk ATAC sequencing

E4-HUVEC cells were trypsinized, nuclei isolated, and libraries prepared using the Active Motif ATAC Seq Kit. Libraries were sequenced at the Nationwide Children's Institute for Genomic Medicine using a 2 x 150 configuration. Data were processed using the ENCODE replicated ATAC seq pipeline with N = 3 biological replicates. Sequences were aligned to the GRCh38 reference sequence. Pooled bigwig track data and MACS2 peaks are shown. Data were visualized using blaseRtools functions (https://github.com/blaserlab) with gene model data from the UCSC hg38 assembly.

Embryo drug treatments

Maximum tolerated doses of HA-100, dactolisib, ibrutinib, ly294002, mk2206 and sorafenib were determined in preliminary dose-finding experiments. The MTD was defined as the maximum concentration where excess mortality and morphologic defects relative to untreated controls were not observed.

Kidney marrow treatments

Kidney marrow was harvested from adult *ubi:EGFP* and *ubi:mCherry* zebrafish[51] and RBC lysis was performed using NH_4Cl. *Ubi:EGFP* marrow was treated at room temperature with DDG or TPA for 4 h. In experiments using inhibitors, cells were pretreated for 60 min before adding TPA.

Kidney marrow transplantation

Casper recipient zebrafish were conditioned with 35 Gy gamma irradiation over 2 doses on D-1 and D0. *Ubi:EGFP* (40,000 cells) and *ubi:mCherry* (80,000) cells were injected into the retro-orbital plexus in anesthetized recipients. After recovery, fish were immediately placed on-flow. Transplant related mortality (recipient death in the first week) was typically less than 10%.

Lentivirus

Lentiviral construct pLV [Exp]-EGFP: T2A: Puro-hPGK>E4ORF1 was synthesized (Vector Builder, USA) and transfected into Lenti-X 293T cells using VSV-G Lenti-X Packaging single shots (Takara Bio, USA). Lentivirus-containing supernatant was harvested and purified using the Lenti-X Maxi Purification Kit. HUVEC cells were transduced in complete M200 medium with polybrene (5 μg/mL) using serial dilutions of purified viral particles. Transient expression of lentiviral constructs was observed using fluorescence microscopy. After 48 h, cell culture medium was exchanged and stably transfected cells were selected using 0.5 μg/mL puromycin. For gene knockdown experiments, commercially prepared lentivirus targeting human PRKCD or scramble control was purchased from Vectorbuilder (Chicago, USA). E4-HUVEC cells were transduced according to the manufacturer's instructions. Transduced cells were visualized by mCherry expression and selected in G418.

Immunoprecipitation and immunoblotting

HUVEC and E4-HUVEC cultures were harvested, washed with PBS, and lysed using Novex NP40 Cell Lysis Buffer (Invitrogen) and vortex mixing. Lysates were cleared by centrifugation at 10,000g for 10 min at 4°. Supernatants were stored in aliquots at −80C. Protein concentration was determined using the Pierce BCA Protein assay kit (Thermo Fisher Scientific). Protein lysates (20 μg) were loaded on iBolt 4–12% Bis-Tris gels (Invitrogen) and transferred to nitrocellulose membranes. Membranes were blocked in TBST with 5% BSA and then incubated with primary and HRP-conjugated secondary antibodies according to the manufacturers' recommendations. Detection was with SuperSignal West Pico Plus Chemiluminescent Substrate. Blots were imaged using an iBright imaging system (Thermo Fisher Scientific). Immunoprecipitation experiments were performed using the Pierce Crosslink Magnetic IP/Co-IP kit and anti-phospho PKC-δ.

Whole-mount in situ hybridization

Antisense RNA probe for *prkcda* was generated by PCR amplification of cDNA using prkcda_probe_F and prkcda_probe_R to generate a 400 bp product. *In vitro* transcription was performed using the Maxiscript T7 transcription kit (Thermo Fisher AM1314). DIG-labeled probe was generated using the Roche DIG RNA labeling kit (Sigma-Aldrich 11175025910) and resuspended in Hyb+ at a concentration of 50 ng/μL of RNA probe. Embryos were fixed at 72 hpf in 4% formaldehyde overnight and then stored in 100% methanol prior to performing *in situ* hybridization using standard techniques.[82] Embryos were stored in methanol prior to imaging using a Leica Microsystems S9i Stereomicroscope and camera at 5× magnification using Leica Application Suite EZ software (Wetzlar, Germany).

Immunofluorescence

Zebrafish embryos were euthanized and fixed in 4% paraformaldehyde at 4°C overnight, washed with PBS, and incubated with 30% sucrose in PBS until sinking to the bottom of the tube. 7-μm sections were sliced using a cryostat. Free-floating embryo sections were permeabilized in PBS containing 100 μM digitonin for 10 min and incubated with 1% BSA in PBST (PBS with 0.1% Tween 20) for 30 min. Primary antibody incubations were performed with anti-Fli1 (1:50) and anti-GFP/mClover (1:1000) in 1% BSA in PBST at 4°C overnight. After three PBS washes, embryos sections were incubated with following conjugated secondary antibodies: donkey anti-rabbit (AF-594, 1:500) and goat anti-mouse (AF-488, 1:500) for 1 h at room temperature. After three additional PBS washes, the stained embryo sections were mounted using mounting medium on microscope slides. Images were captured using Keyence BZ-X Analyzer software.

QUANTIFICATION AND STATISTICAL ANALYSIS

ScRNA-seq data preprocessing and quality control

10X scRNA-seq libraries were sequenced using a 151bp Read 1, 8 bp Index 1, 151 bp Read 2 configuration on an Illumina Novaseq instrument (Nationwide Children's Hospital Institute for Genomic Medicine). FASTQs were generated and filtered cell-barcode matrices generated using CellRanger 4.0 (10X Genomics). A minimum of 15,000 sequencing reads per cell were obtained. Alignment was performed to the GRCz11 reference. Low quality cells were identified using scater as those either with a percent of reads mapped to mitochondrial genes more than 2 median absolute deviations (MADs) greater than the median or a number of expressed genes less than 2 MADs below the median for each sample.[83] Doubletfinder was used to remove high-confidence doublets with a predicted doublet rate of 4%.[84]

Dimensionality reduction

Dimensionality reduction was performed in Monocle3 using principal components analysis (PCA) and uniform manifold approximation and projection (UMAP).[85,86] The top 100 principal components were used for UMAP dimensionality reduction. Sample alignment was performed using batchelor and UMAP coordinates were recalculated if significant batch effects were noted.[87]

Cell clustering

Depending on the level of resolution necessary, cell clustering was performed using the partition-based graph abstraction, Leiden and/or Louvain clustering algorithms as implemented in Monocle3 using default parameters.[88–90]

Dataset reanalysis

Gene expression profiles from mouse single cell data were used to aid identification of zebrafish cell clusters.[38,39] To map expression of published murine gene sets onto zebrafish scRNA-seq data, 1:1Mouse:Zebrafish orthologs were identified using the latest data available at https://zfin.org/downloads/mouse_orthos.txt.

Gene expression, gene module analysis, and aggregated gene scores

Size factors were calculated for each cell as the number of UMI counts in that cell divided by the geometric mean of UMI counts for all cells in the dataset. Expression values for single genes were calculated as size factor-normalized UMI counts and log-transformed for plotting. Variable genes were identified in each single cell data set by spatial autocorrelation using Moran's I test.[91] Gene modules were identified using UMAP dimensionality reduction and Louvain clustering on variable genes as implemented in Monocle3.[92] Aggregate gene expression scores from gene modules and published gene lists were calculated by taking the sum of size-factor normalized UMI counts within each gene group, scaling this value across gene groups and taking the mean of the scaled aggregate value across groups of cells.

Pseudotime analysis

Reversed graph embedding was used to calculate pseudotime coordinates for cellular partitions. Cellular trajectories were anchored by inspection of canonical gene expression.

GO-term analysis

GO term enrichment for gene lists indicated in Results was determined using topGO by mapping to the org.Dr.eg.db annotation in Bioconductor (https://doi.org/10.18129/B9.bioc.org.Dr.eg.db) and testing for significant associations with the "classicFisher" test.[93] GO term redundancy was reduced based on semantic similarity using rrvgo and enrichment was visualized using custom scripts.[94]

Single cell GESTALT barcode analysis

Adapter and poly-A trimming was performed with cutadapt.[95] Custom aligner software was written in the D programming language to identify the best matching GESTALT lineage barcode for each read pair. This software utilizes the dhtslib, HTSlib, dparasail, and parasail software libraries.[96,97] The aligner takes in FASTQ files paired reads containing the 10X single cell barcode and UMI (Read 1) and the GESTALT lineage barcode (Read 2). The aligner also takes as input whitelist files of known GESTALT lineage barcodes from bulk peripheral blood sequencing and known 10X single cell barcodes from the scRNA-seq data. For each 10X-GESTALT barcode read pair, a semi-global Needleman-Wunsch alignment algorithm was used to align the GESTALT lineage barcode read to all whitelisted GESTALT sequences using a match score of 3, a mismatch penalty of 4, a gap open penalty of 7, and a gap extension penalty of 4.[98] The alignment with the highest semi-global alignment score was chosen as the predicted GESTALT lineage barcode for that read. Similarly, the 10X barcode read was aligned against all whitelisted 10X cell barcodes with a match score of 2, a mismatch penalty of 2, a gap open penalty of 10, and a gap extension penalty of 5. The alignment with the highest semi-global alignment score was chosen as the predicted 10X barcode. Resulting alignments were then filtered to include those that had a similarity score of at least 0.95 for quality control.

Single cell ATAC-seq analysis

ScATAC data were pre-processed using 10X CellRanger-ATAC v1.2 using a custom zebrafish reference. A Seurat object was generated using the filtered peak-barcode matrix and fragment files produced by CellRanger-ATAC. To identify links between co-accessible peaks, the Seurat object was converted to a Cicero object using functions from SeuratWrappers. Links were generated in Cicero and transferred to the Seurat object. UMAP coordinates and cell clusters (Leiden method) were generated using the published Cicero workflow. Cell cluster identities were established by label transfer from scRNA-seq data obtained from the same pools of fish. Briefly, the Seurat GeneActivity function was used to compute counts per cell in the scATAC data within gene bodies and promoters. Gene activity scores were used as a surrogate for expression in the Seurat label transfer algorithm. The resulting individual cell type predictions were grouped according to scATAC Leiden cluster and a consensus label was assigned. ScATAC-seq data were visualized using blaseRtools functions.

General statistical analysis

Summary statistics and hypothesis testing as described in the text was performed using R v4.2. Unless otherwise indicated, data are presented as mean ± S.E.M. $P < 0.05$ was considered statistically significant.

PLOS ONE

RESEARCH ARTICLE

In vivo monitoring of leukemia-niche interactions in a zebrafish xenograft model

Anja Arner[1], Andreas Ettinger[2], Bradley Wayne Blaser[3], Bettina Schmid[4], Irmela Jeremias[1,5], Nadia Rostam[1,6], Vera Binder-Blaser[1]*

1 Department of Pediatric Hematology/Oncology, Dr. von Hauner Children's Hospital, Ludwig Maximilians University (LMU), Munich, Germany, **2** Institute of Epigenetics and Stem Cells, Helmholtz Centre Munich, German Research Center for Environmental Health, Munich, Germany, **3** Division of Hematology, The Ohio State University Comprehensive Cancer Center, Columbus, Ohio, United States of America, **4** German Center for Neurodegenerative Diseases (DZNE), Munich, Germany, **5** Research Unit Apoptosis in Hematopoietic Stem Cells, Helmholtz Centre Munich, German Research Center for Environmental Health, Munich, Germany, **6** Department of Biology, University of Sulaimani, Sulaymaniyah, Iraq

* vera.binder-blaser@med.uni-muenchen.de

OPEN ACCESS

Citation: Arner A, Ettinger A, Blaser BW, Schmid B, Jeremias I, Rostam N, et al. (2024) *In vivo* monitoring of leukemia-niche interactions in a zebrafish xenograft model. PLoS ONE 19(8): e0309415. https://doi.org/10.1371/journal.pone.0309415

Editor: Persio Dello Sbarba, Universita degli Studi di Firenze, ITALY

Received: April 7, 2024

Accepted: August 13, 2024

Published: August 30, 2024

Peer Review History: PLOS recognizes the benefits of transparency in the peer review process; therefore, we enable the publication of all of the content of peer review and author responses alongside final, published articles. The editorial history of this article is available here: https://doi.org/10.1371/journal.pone.0309415

Data Availability Statement: All relevant data are within the manuscript and its Supporting Information files.

Abstract

Acute lymphoblastic leukemia (ALL) is the most common type of malignancy in children. ALL prognosis after initial diagnosis is generally good; however, patients suffering from relapse have a poor outcome. The tumor microenvironment is recognized as an important contributor to relapse, yet the cell-cell interactions involved are complex and difficult to study in traditional experimental models. In the present study, we established an innovative larval zebrafish xenotransplantation model, that allows the analysis of leukemic cells (LCs) within an orthotopic niche using time-lapse microscopic and flow cytometric approaches. LCs homed, engrafted and proliferated within the hematopoietic niche at the time of transplant, the caudal hematopoietic tissue (CHT). A specific dissemination pattern of LCs within the CHT was recorded, as they extravasated over time and formed clusters close to the dorsal aorta. Interactions of LCs with macrophages and endothelial cells could be quantitatively characterized. This zebrafish model will allow the quantitative analysis of LCs in a functional and complex microenvironment, to study mechanisms of niche mediated leukemogenesis, leukemia maintenance and relapse development.

Introduction

Acute lymphoblastic leukemia (ALL) is the most common malignancy during childhood, with B-cell precursor (BCP)-ALL as the most common type of pediatric leukemia [1]. Prognosis after initial diagnosis is good (10 year survival rates ≥90%), due to the immense progress in diagnostics and treatment over the last four decades [2]. However, for patients suffering from refractory disease or relapse, outcome is still poor (5-year survival rates 50–60%). Current risk classification protocols for ALL exclusively consider cell intrinsic features like cytogenetics and molecular genetics of the leukemic cell [3,4]. Therefore, considering features of the surrounding tissue—the niche—might help to improve treatment options in refractory disease and

Funding: V.B-B received funds from the German Jose Carreras Foundation and the Bettina-Bräu Stiftung. The funders did not play any role in the study design, data collection and analysis, decision to publish, or preparation of the manuscript.

Competing interests: The authors have declared that no competing interests exist.

prevent relapse development. In the field of stem cell research, the term 'niche' describes the place of residence of stem cells where they can fulfill their desired function. Hence, the niche is (i) the anatomic region where stem cells reside and (ii) a distinct locale where specific signals are available to enable stem cell functions, such as self-renewal and differentiation. These specific signals can be provided by the extracellular matrix, cellular components, and secreted molecules which in turn help define stem cell fate [5–7]. With the development of the cancer stem cell concept in leukemia, which describes a distinct subpopulation of LCs possessing features of stem cells such as self-renewal [8,9], the question arose if specialized niches are equally important to maintain the leukemia, as they are for healthy tissue. In case the niche is decisive for leukemia development or maintenance, its components are very attractive therapeutic targets to eliminate malignant cells [5].

There is growing evidence that in addition to cell-intrinsic changes, the niche plays a pivotal role in leukemogenesis, leukemia maintenance and ultimately in relapse development [10]. However, while more and more is known about the signals that drive the interplay of LCs and the microenvironment [11], further detailed studies are needed to comprehensively understand the niches' functions.

Models to study the complex interplay of several cell types within a functional surrounding are scarce. In 2005, the first xenotransplantation of human cancer cells into zebrafish was performed [12]. Subsequently, further studies of different tumor entities were performed [13,14] and the process of xenotransplantation was optimized. Meanwhile, routine transplantation workflows were successfully applied by many groups and this allowed the efficient injection of several hundred embryos within only a few hours (h). Larval xenografts were an appreciated model that were successfully used to study diverse processes, such as tumor metastasis [15,16] and angiogenesis [13,14,17]. The feasibility to monitor fluorescently labeled cells in the living organism in real time over an extended period of time, due to the embryos' optical transparency [18], makes this model highly interesting. Furthermore, numerous studies emphasize the potential of the larval zebrafish as a preclinical model to test drugs [19–23].

The hematopoietic niches in zebrafish are well characterized and it could be shown that hematopoiesis takes place in different waves and different locations throughout development, similar to mammals [24,25]. After emerging from the ventral dorsal aorta (VDA), hematopoietic stem and progenitor cells (HSPCs) travel to the primary site of embryonic hematopoiesis, the caudal hematopoietic tissue (CHT). Analogous to the mammalian fetal liver, the CHT is a vascular plexus in the ventral region of the tail between the caudal artery and cardinal vein [26]. From approximately 48 to 96 hours post fertilization (hpf) HSPCs exit circulation by transmigrating through the vascular endothelium and settle on the abluminal face of the vasculature. Here, local signals, including KIT ligand b, Oncostatin M, thrombopoietin, colony stimulating factor 3a, Chemokine (C-C Motif) Ligand 25b (Ccl25b), Chemokine (C-X-C Motif) Ligand 8b (Cxcl8b), and Chemokine (C-X-C Motif) Ligand 12a (Cxcl12a), regulate their trafficking and expansion [6,7,27]. Vascular endothelial cells remodel to form a pocket around resident HSPCs, and somite-derived stromal cells anchor HSPCs during CHT occupancy [28]. Initially, HSPCs populate more dorsal perivascular spaces in the CHT as sparse, individual cells. Over the course of about 2 days HSPCs expand and migrate more ventrally as the vasculature of the CHT becomes less complex. By 4 to 5 days post fertilization (dpf) clusters of HSPCs occupy a more ventral region of the CHT concentrated along the cardinal vein, and the number of HSPCs approximately doubles [29]. Primitive neutrophils regulate HSPC egress through secretion of Matrix Metallopeptidase 9 (Mmp9), which cleaves locally produced Cxcl12a and beginning at 4 dpf, HSPCs begin to seed the adult niche, the kidney, where the HSPCs reside, self-renew and differentiate to produce blood for the lifetime of the animal [27].

Since zebrafish exhibit orthologues for >82% of human disease related genes [30], and there is high conservation of genes and molecular signaling pathways that are involved in hematopoiesis between zebrafish and mammals [31,32], they are an attractive and powerful model organism to study diseases of the hematopoietic system. Still, no study described the analysis of LCs within the CHT and the assessment of interactions with surrounding niche components.

Here, we describe an orthotopic larval zebrafish xenotransplantation model to study leukemia in a complex microenvironment. In our system, LCs homed to the expected niche site, engrafted and proliferated. Furthermore, a distinct localization pattern was observed and close and persisting interactions of LCs with macrophages were monitored, along with low rates of attraction of zebrafish macrophages to the CHT and only very few phagocytosis events. By adding the temporal dimension, which allows assessing dynamic changes in different cell populations in realtime, we propose a new tool to study leukemia in a functional environment. This allows to discover niche mediated effects on malignant processes such as leukemia development, maintenance and relapse.

Materials and methods

Ethical statement

Written approval of the representatives was given for all the primary materials used in this study. The study was performed in accordance with the institutional ethical review board (written approval of the 'Ethikkommission der Medizinischen Fakultät der LMU München' with the numbers 19–495, 068–08 and 222–10) and with the Helsinki Declaration.

All animal trials were performed in accordance with the official committee on animal experimentation. According to German law (Tierschutz-Versuchstierverordnung–TierSch-VersV—§14), no specific approved animal protocol was necessary for the present study. Zebrafish larvae did not exceed an age of 5 days post fertilization and therefore, they do not take up nutrition by themselves.

Cell preparation

The B-cell precursor acute lymphoblastic leukemia cell line NALM-6 was cultured in RPMI medium (Gibco, San Diego, CA, USA) supplemented with 10% FBS (Gibco, San Diego, CA, USA), without antibiotics or additional glutamine. PDX cells were freshly isolated from spleens of transplanted NOD.Cg-Prkds^{scid}Il2^{rgtm1Wjl}/SzJ (NSG) mice. For short-term *in vitro* culture, cells were cultured in StemSpan™ SFEM Medium (STEMCELL Technologies, Vancouver, Canada).

For cell proliferation analysis, cells were stained with 5 μM CFSE (Invitrogen™, Waltham, MA, USA) and resuspended in the respective medium for overnight cultivation. The next day, cells were transplanted. A small fraction of cells was kept *in vitro* for analysis.

Zebrafish xenotransplantation

Fluorescently labeled LCs were injected using pre-pulled borosilicate glass capillaries (1B120F-4, World Precision Instruments, Sarasota County, FL, USA) using a microinjector (FemtoJet 4i, Eppendorf, Hamburg, Germany) under a stereomicroscope (Stemi 2000-C, Zeiss, Oberkochen, Germany). Two dpf embryos of the Tg(kdrl:mCherry), Tg(mpeg-1:mCherry-F), AB wt or Casper line were anesthetized with 750 μM Tricain (Sigma-Aldrich, St. Louis, MO, USA) and approximately 200–500 cells were injected into the duct of Cuvier. Injected embryos were transferred to E3 medium and kept at 36˚C.

Flow cytometric analysis

At indicated time points post transplantation, larvae were euthanized and cut with a sharp scalpel in two parts right after the yolk sac extension. Tails were collected, pooled as indicated, resuspended in DPBS containing 50 μg/mL Liberase™ TM Research Grade (Sigma-Aldrich, St. Louis, MO, USA) and digested for 20–30 min at 37˚C. The suspension was filtered through a 30 μm mesh, washed once with DPBS and analyzed using a BD LSR Fortessa X20. *In vitro* cultivated cells were directly subjected to flow cytometric analysis.

Repetitive *in vivo* imaging

Larvae were anesthetized (750 μM Tricain), placed on an agarose plate (0.5% agarose in E3-medium) and oriented laterally. Larvae were covered with sufficient E3-medium to keep them moist. For each larva, a bright field and fluorescent image was acquired with a fluorescent stereomicroscope (SteREO Discovery.V8, Zeiss, Oberkochen, Germany) using the Axiovision software (8x magnification), that the whole CHT was visible. After completion, larvae were transferred to fresh E3-medium and further maintained.

To monitor engraftment of LCs after transplantation, the corrected total CHT fluorescence (CTCF), which determines the level of fluorescence within the CHT, was calculated from fluorescence microscopy images as follows: The brightfield image was used to draw a region of interest (ROI) of the CHT area. This ROI was applied to the fluorescent image. Using the 'Measure' function of ImageJ, the *area* of the ROI and the *mean fluorescent intensity* (MFI) were determined. For each larva, the integrated density was calculated. As a background level, the mean integrated density of ten untransplanted larvae was used. Ultimately, the CTCF was calculated for each individual transplanted larva. The following formulas were used:

$$\text{Integrated Density } [\text{RFU}*\mu m^2] = \text{Mean Inensity CHT } [\text{RFU}]* \text{ CHT Area } [\mu m^2]$$

$$\begin{aligned}&\text{CTCF } [\text{RFU}*\mu m^2]\\ &= (\text{Integrated Density }_{\text{Transplanted}} - \text{ Integrated Density }_{\text{Untransplanted}}) \ [\text{RFU}*\mu m^2]\end{aligned}$$

High resolution *in vivo* time lapse imaging

At indicated time points post injection, zebrafish xenografts were anesthetized and screened according to the presence of LCs within the CHT using a fluorescent stereomicroscope (SteREO Discovery.V8, Zeiss, Oberkochen, Germany). Successfully transplanted xenografts were selected randomly and embedded in a glass bottom dish (4 Chamber, 35 mm, #1.5, Cellvis, Mountain View, CA, USA) using pre-heated (50˚C) 1.5% low melting agarose (MetaPhor™ Agarose, Lonza, Basel, Switzerland) in E3-medium (750 μM Tricain).

Embryos were observed with an Andor Dragonfly 500 spinning disc confocal system attached to a Nikon Ti2 microscope and equipped with an Andor iXon 888 life electron multiplying charge-coupled device (EMCCD) camera (Nikon ECLIPSE Ti2; Andor Dragonfly 500; iXon Life 888) within a breeding chamber pre-heated to 36˚C. Temperature was maintained with a full-enclosure incubator equipped with a thermocouple to monitor temperature close to the specimen (Okolab, Italy). The CHT of individual larvae were imaged with a 20x CFI Plan Apochromat NA 0.75 air objective (Nikon, Japan) and 16-bit time lapse movies were generated. The ImageJ software was used to z-project the acquired multidimensional images by using maximal intensity projection. For visualization purpose, contrast enhancement was performed to get 0.1–0.3% saturated pixels. Three-dimensional (3D) surface renderings were performed using Imaris software. For specific renderings, surfaces were visualized with transparency as indicated in the figure legend.

Results

Acute lymphoblastic leukemic cells (ALL-LCs) home to the CHT after transplantation

Xenotransplantation of ALL-LCs into zebrafish was performed at 48 hpf (hours post fertilization), by injecting 200–500 cells into the common cardinal vein (CCV) [33]. Transplanted larvae were raised at 36˚C, as this temperature allows larvae to develop normally and human cells to survive and proliferate [34]. The CHT, which is the proper hematopoietic niche at this stage of development, was monitored for three subsequent days using microscopic and flow cytometric methods, to study LCs in an orthotopic manner (Fig 1A).

Transgenic NALM-6- eGFP cells, which is a BCP-ALL relapse cell line, were transplanted. Larvae were anesthetized and the caudal parts were imaged using a fluorescence stereomicroscope to monitor LCs at one and three days post injection (dpi). The eGFP signal of NALM-6 cells was detected in transplanted larvae (Fig 1B), which was absent in untransplanted larvae (S1A Fig). NALM-6 cells homed to the CHT, where they resided during the three days of follow up time (Fig 1B).

ALL cells engrafted and proliferated

The images of the transplanted larvae in Fig 1B showed an increase of the fluorescent signal within the marked niche area of the representative larva within two days. This could indicate that more LCs homed to the niche over time, but possibly also that cells proliferated. To better characterize LC engraftment, this process was analyzed in more detail. LCs within the CHT area were quantified over time in order to monitor colonization of the niche. Using non-invasive *in-vivo* microscopy allowed the analysis of the same animal at different time points. For ten transplanted larvae, the leukemic burden within the niche was determined by calculating the corrected total CHT fluorescence (CTCF) at one and three dpi. On average, the CTCF significantly increased by 68% within 48 hours (Fig 1C).

A flow cytometric approach was established to quantify LCs of transplanted larvae. To assess sensitivity of the assay, different numbers of NALM-6 cells were transplanted. For 50 larvae, the CTCF was calculated at one dpi. Larvae were divided into groups of ten (group A-E), according to the CTCF, prior to analyzing 10 larvae pooled as one sample, using flow cytometry (Fig 1D). Group A included larvae with the highest CTCFs (~3 x10^9 RFU*μm^2), while for group E larvae with the lowest CTCFs were pooled (~5 x10^7 RFU*μm^2) (Fig 1E). Representative dot plots of the flow cytometric analysis showed higher numbers of NALM-6 cells in group A than in group C (Fig 1F). As expected, for untransplanted larvae, no eGFP positive events were detected (S1B Fig). Furthermore, the correlation of imaging and flow cytometry for all five groups showed that both methods correlated linearly, as an increased fluorescent signal of the imaging analysis resulted in an increased number of detected cells as determined by flow cytometry (Fig 1G). Hence, both assays could equally be used to monitor engraftment of LCs at different time points.

To directly demonstrate LC proliferation *in-vivo*, a CFSE dilution assay was performed using the NALM-6 cell line and primary cells from two ALL patients (ALL-PDX: ALL-199 and ALL-265) (S1 Table). ALL-PDX cells expressing a fluorescent protein were generated by lentiviral transduction and serial passaging in NOD.Cg-Prkds^{scid}Il2^{rgtm1Wjl}/SzJ (NSG) mice [35]. Here, fluorescent protein expressing LCs (mCherry+ NALM-6; mTagBFP+ PDX cells) were labeled with the fluorescent proliferation sensitive dye CFSE, which covalently binds to proteins of the cells. Upon cell divisions, cells with halved CFSE signal can be detected using flow cytometry. Groups of transplanted larvae were sacrificed at one, two and three dpi and LCs

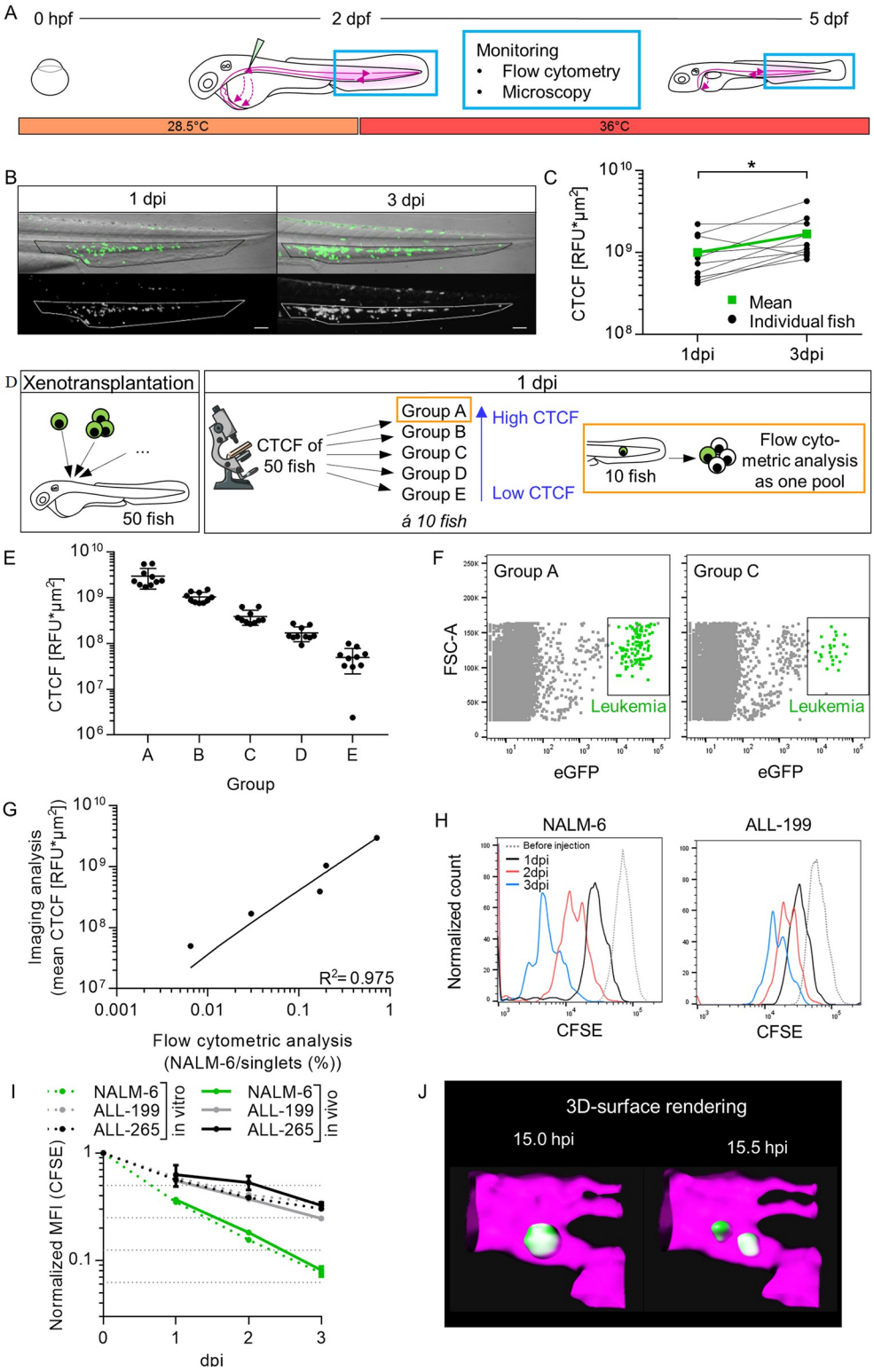

Fig 1. Establishment of zebrafish larval xenograft of human ALL cell line and PDX cells. (A) Schematic illustration of the workflow to monitor LCs within an orthotopic niche: Fertilized eggs were bred at 28.5˚C. At 2 dpf fluorescently labeled LCs got injected via the common cardinal vein. Subsequently, larvae were bred at 36˚C. In the following days, the CHT of larvae were analyzed using flow cytometry and microscopy. **(B)** Representative fluorescent (lower panel) and brightfield (merge, upper panel) images of the caudal part of a transplanted larva (NALM-6), at 1 and 3 dpi. The

outline of the niche area is highlighted and was used to assess the corrected total CHT fluorescence (CTCF) for transplanted larvae. **(C)** Measurement of the CTCF of 10 larvae at 1 and 3 dpi. Mean CTCF is indicated in green (n = 10, Wilcoxon matched-pairs signed rank test, * $p \leq 0.05$). **(D)** Experimental setup: Larvae were transplanted with NALM-6 cells (eGFP+). At 1 dpi CTCF was calculated and larvae were analyzed in groups of 10 according to the values obtained. Larvae of each group were pooled and measured as one sample using flow cytometry. **(E)** Grouping of the 50 analyzed larvae at 1 dpi with corresponding CTCF. Scatter-plot displays the calculated CTCF value per larva and mean value ± SEM per group. **(F)** Dot plot of the flow cytometry measurement of two representative transplanted samples (group A and C). Grey dots show cells in singlets gate; green dots show NALM-6 cells. For detailed gating see S2A and S2B Fig. **(G)** Correlation of the flow cytometric analysis and imaging analysis. One dot represents one group (for imaging analysis, mean value of the 10 larvae (E) is depicted, for flow cytometric analysis, the result of the pooled sample is depicted). Correlation curve and R^2 was calculated with linear regression. **(H)** Representative histograms of the CFSE signal of different transplanted LCs at daily measurements of 10 pooled larvae are depicted. **(I)** Quantification of the normalized MFI of the CFSE signal over time (*in vivo* samples: n = 3 (NALM-6: Mean value of three independent experiments performed in duplicates; ALL-199 & ALL-265: Values of one experiment performed in triplicates), mean value ± SEM; *in vitro* samples: NALM-6: n = 3 values of three independent experiments; ALL-199 & ALL-265: n = 1 value of one measurement in one experiment). **(J)** 3D- surface rendering of a NALM-6 cell undergoing cell division.

https://doi.org/10.1371/journal.pone.0309415.g001

were identified using the fluorescent marker and the CFSE intensity of the cells was analyzed (for gating see S1C Fig). The histogram of NALM-6 and ALL-199 cells in Fig 1H showed the CFSE signal of all transplanted LCs at each timepoint. Importantly, defined populations with halved CFSE-signal appeared over time, representing cells that underwent cell division (Figs 1H and S1D). Quantifying the MFI of three different transplanted leukemia samples over time showed that NALM-6 cells proliferated faster than the two analyzed PDX cells (Fig 1I). ALL-199 and ALL-265 showed similar proliferation rates. Comparing the MFI of LCs *in vivo* and *in vitro* showed similar cell division kinetics. Interestingly, ALL-199 showed slightly increased proliferation under *in vivo* conditions when compared to *in vitro* conditions (Fig 1I). On average, xenografted PDX cells divided twice within three days (Fig 1I); however, histograms show that some cells underwent up to three cell divisions (Fig 1H). For NALM-6 cells, the number of average cell divisions was four (Fig 1H), while the maximum within three days, was five divisions (Fig 1I).

In addition, *in vivo* time lapse shots of confocal microscopy clearly confirmed a cell division of a NALM-6 cell within the vasculature of a zebrafish at 15.5 hours post injection (hpi). After cell division, the two daughter cells remained at the site of division (S1E Fig). 3D surface rendering confirmed the presence of only one cell at the beginning and excluded one cell being behind the other (Fig 1J).

Taken together, these data demonstrate the successful xenotransplantation of human LC lines and PDX cells into larval zebrafish with homing to the physiological niche and cell division.

LCs and macrophages interacted for an extended period of time without phagocytosis

To further characterize LC interactions with the microenvironment, LCs and two different niche cell types were analyzed by time-lapse fluorescence microscopy. In a first step, the relative frequencies and distribution patterns of macrophages within the niche were examined for transplanted and untransplanted larvae. NALM-6 cells (eGFP+) were transplanted into Tg (mpeg1: mCherry-F) zebrafish larvae. At one dpi, the tail of transplanted larvae and untransplanted siblings were imaged using confocal microscopy. Macrophages were found throughout the tail but were mainly localized in the CHT. This was similar for transplanted and untransplanted larva (Fig 2A).

Time-lapse confocal microscopy was conducted for up to 10 hours to monitor interactions of LCs and macrophages over time. *Tg(mpeg1: mCherry-F)* larvae were transplanted with

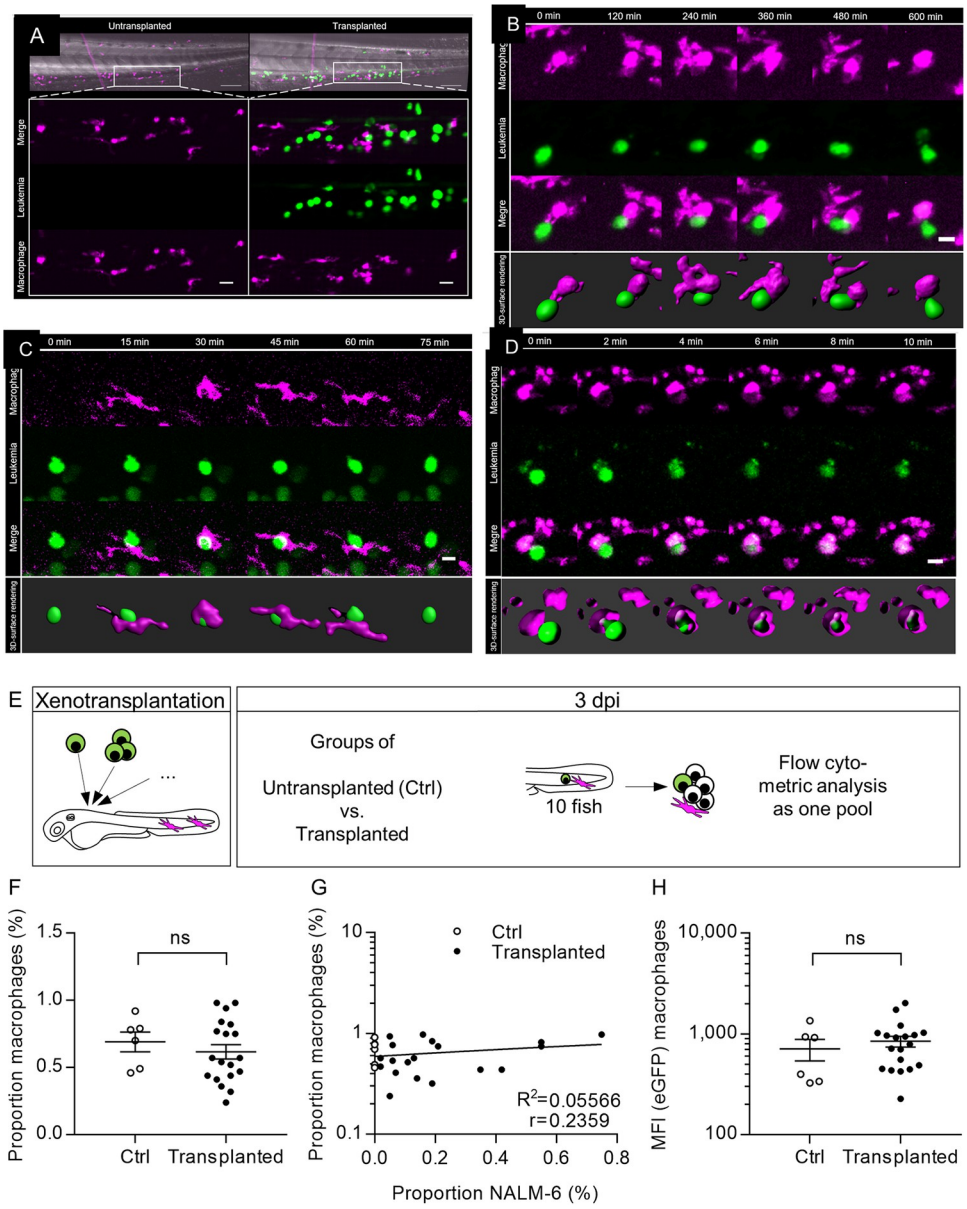

Fig 2. Extended interaction between LCs and zebrafish macrophages. (A) On the top, representative overview images of the caudal parts of an untransplanted (left) and a transplanted larva (right) at 1 dpi are depicted. Scale bar: 100 μm. Upper panels of the zoomed sections depict merged images of eGFP+ NALM-6 cells (green, middle row) and mpeg1:mCherry-F+ macrophages (magenta, lower row). Scale bar: 20 μm. **(B, C, D)** Six still frames of representative time lapse movies. Selected frames of the movies are depicted. Images show one macrophage mpeg1:mCherry-F+ (magenta, upper row) and LC (green, middle row) over time. Lower row shows the merged images. Scale bar: 10 μm. Separate panel below shows 3D-surface renderings. **(B)** Time lapse movie of a fish transplanted with NALM-6 cells (eGFP) starting at 31 hpi with a frame interval of 20 min. **(C)** Time lapse movie of a fish transplanted with NALM-6 cells (eGFP+) starting at 35 hpi with a frame interval of 5 min. **(D)** Time lapse movie of a fish transplanted with primary LCs (CFSE) starting at 23 hpi with a frame interval of 2 min, showing phagocytosis event. **(E)** Experimental setup: Tg(mpeg1:mCherry-F) larvae were transplanted with NALM-6 cells (eGFP+). At 3 dpi untransplanted (Ctrl) and transplanted larvae were grouped into groups of 10 and measured as one sample using flow cytometry **(F)** Quantification of the percentage of macrophages within singlets was assessed using flow cytometry. Each dot of the scatter-plot represents a group of ten larvae measured as one sample in three independent experiments. For gating details see S2 Fig **(G)** Dot plot of the correlation of the percentage of macrophages and NALM-6 cells of all samples analyzed in (F). Correlation curve was calculated using linear-regression (r = 0.2359, R2 = 0.056). **(H)** Quantification of the eGFP MFI of all detected macrophages using flow cytometry. Each point of the scatter-plot represents the MFI of all macrophages within the sample. **(F, H)** Mean value ± SEM is depicted. (untransplanted: n = 6; transplanted: n = 19). (unpaired t-test with Welch's correction, ns not significant).

https://doi.org/10.1371/journal.pone.0309415.g002

NALM-6 cells (eGFP+). At indicated time points post transplantation, larvae were anesthetized, embedded and imaged. In Fig 2B, one representative interaction was documented, which lasted for more than 10 hours. At the start of the interaction (0 min) it was visible that the macrophage forms two pseudopodial extensions that reach towards a LC. At 240 min and 360 min, it is visible how the macrophage embraced the LC during the interaction. 3D-surface renderings support the observations (Fig 2B). In Fig 2C, a shorter lasting interaction is depicted. The LC was stationary during the interaction while the macrophage arrived rapidly and embraced the LC within 15 min. However, after 45 min the contact ended and the macrophage moved away from the LC.

As close interactions of LCs and macrophages were observed and macrophages occasionally embraced LCs, we asked whether zebrafish macrophages can phagocytize human LCs or not, due to inter-species incompatibilities. Time lapse movies of transplanted larvae were manually reviewed looking for green fluorescent material of a LC within the purple signal of macrophages which we assumed to be a phagocytosis event. In Fig 2D, one representative phagocytosis event of a LC by a macrophage is depicted in real-time. Two minutes after contact, the macrophage began to embrace the LC. Six minutes after close contact, the LC was completely phagocytized by the macrophage. In the 3D renderings of Fig 2D, surfaces of macrophages were depicted with high transparency to demonstrate enclosure of the LC within the macrophage (Fig 2D). Taken together, this demonstrated that LC elimination via macrophage phagocytosis is possible in general in our xenotransplant-setting.

No enhanced recruitment of macrophages after xenotransplantation

After observing intensive contact between LCs and macrophages, we asked whether more macrophages were recruited to the CHT of transplanted larvae when compared to untransplanted control siblings. To investigate this, Tg(mpeg1: mCherry-F) larvae were transplanted with NALM-6 cells (eGFP+). Groups of ten larvae, either untransplanted (control (Ctrl)) or transplanted, were sacrificed at three dpi and the tails were analyzed by flow cytometry (Fig 2E). Proportions of macrophages among all singlets within the CHT were analyzed and compared between transplanted and control (Ctrl) larvae. The number of macrophages in larvae transplanted with LCs was similar to Ctrl larvae (Fig 2F). There was no correlation between leukemic burden and the number of macrophages identified in transplanted embryos (Fig 2G). In a next step, the MFI of all macrophages in the respective sample was calculated as a measure of phagocytosis activity. In case a macrophage engulfed a NALM-6 cell, the cells' fluorescence can be detected as demonstrated using confocal microscopy (Fig 2B and 2C). Here, no increased eGFP signal was detected for the macrophages of transplanted larvae when compared to Ctrl siblings (Fig 2H).

Taken together, macrophages were in contact with LCs as extended interactions were observed. In addition, zebrafish macrophages pursued their host-defense function as they phagocytized some malignant LCs.

LCs left the vasculature and formed clusters

Endothelial cells interact with normal and malignant blood cells and they are a prominent cell type within the CHT. This tissue can generally be considered as a very well perfused sinusoidal vascular plexus delimited by the caudal artery (CA) and vein (CV) [27]. On consecutive days after transplantation of NALM-6 cells (eGFP+), Tg(kdrl:mCherry) larvae were anesthetized and the CHT was imaged and analyzed using confocal microscopy. At one dpi, LCs were evenly distributed throughout the niche (Fig 3A). At two dpi distinct LC clusters emerged that were located extravasculary within the CHT, ventral of the CA. After transplantation, these

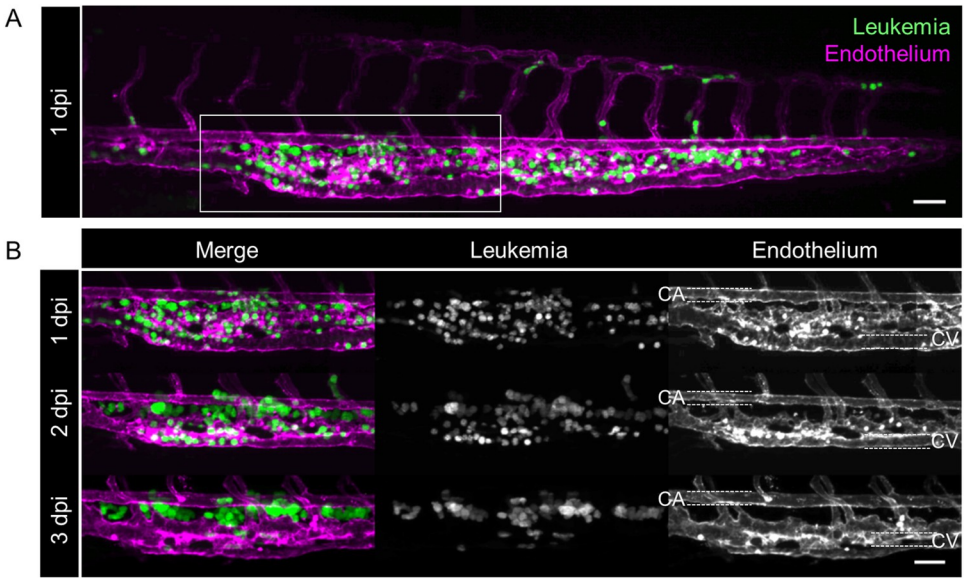

Fig 3. Interaction between LCs and zebrafish endothelial cells. Confocal microscopy of one representative transplanted Tg(kdrl:mCherry) larva over the course of three days is depicted. **(A)** Complete caudal part of the larva at 1 dpi. Marked area indicates field of view in (B). Scale bar: 50 μm. **(B)** Section of the CHT at three consecutive days. Left panel shows merged images of NALM-6 (green, middle panel) and the endothelium (kdrl:mCherry) (magenta, right panel). CV: Caudal vein (outlined with white dashed lines), CA: Caudal artery (outlined with white dashed lines). Scale bar: 50 μm.

https://doi.org/10.1371/journal.pone.0309415.g003

pockets were colonized with many LCs that formed clusters. At three dpi, LCs were almost exclusively found extraluminal (Fig 3B). This observation demonstrated that LCs were able to extravasate the endothelium. Extravasation is a complex process, since it requires signaling between extravasating cells and the endothelium [36]. Strikingly, this specific behavior of LCs was not exclusively observed for NALM-6 cells (Fig 3), as ALL-199 and ALL-265 and some primary samples showed the same specific behavior (S3 Fig). This suggests a functional interaction between human leukemic cells and zebrafish endothelial cells.

Discussion

The role of the microenvironment during BCP-ALL development, maintenance and relapse onset is not well understood. However, recent studies suggest a pivotal role of the leukemic niche in these processes [10,11]. Still, appropriate models that enable the analysis of LCs in an orthotopic niche are lacking and most studies investigate LCs independent from their surrounding tissue. Commonly, the analysis of LCs in the context of a functional microenvironment is performed with *in vitro* co-culture experiments where LCs are cultured in the presence of typically only one other cell type [37,38]. Mostly, the addition of expensive cytokines and growth factors is necessary to ensure cell viability and to mimic the niche to some extent [39]. *In vivo* mouse models enable analysis of LCs in the proper niche, but they are very costly and tedious and only a small number of animals can be analyzed per experiment [40]. Therefore, zebrafish is an emerging animal model in cancer research: (i) Studies show an adequate conservation of the zebrafish hematopoietic niche to study human LCs in a reasonable complex microenvironment, resembling human bone marrow [31,32], (ii) a large number of animals can be analyzed for statistically relevant numbers per experiment, and (iii) zebrafish are optically clear during development which enables *in vivo* imaging [32].

Here, we describe a model to study leukemia-niche interactions *in vivo* using a larval zebrafish xenograft model of pediatric BCP-ALL. We used cell lines and PDX cells and showed engraftment of LCs within the CHT and distinct interactions with niche macrophages and endothelial cells.

Larval xenotransplantation models of cell lines and primary cells of different tumor entities were published in the past [13,14], including leukemias [19–21]. Current gold standard for the developmental stage for xenotransplantation is 48 hpf [33]. The growing number of studies published showed that the transplantation procedure and subsequent rearing temperature differed greatly, depending on the research question. Human cancer cell injections directly into the yolk sac were widely used for pre-clinical drug testing [20,21] and the analysis of the metastatic phenotype of solid tumors [41], while systemic injections into the blood circulation were mainly used to study cell dissemination [42] and metastatic features [15]. In the present study, LCs were transplanted into the blood via the duct of Cuvier and allowed to disseminate throughout the whole body by blood circulation. In order to monitor LC homing and engraftment within the orthotopic niche, dissemination of the transplanted LCs was evaluated using *in vivo* imaging, demonstrating homing of LCs to the hematopoietic niche, the CHT area.

Given the differential body temperatures of humans and fish of 37˚C and 28.5˚C, respectively, it is an ongoing debate how to compromise best between the temperatures to not harm fish development but to support cancer cell proliferation and engraftment. Up to a developmental stage of 48 hpf, rearing at the physiologic temperature of fish is very important for optimal development. Rearing of the embryos at 36˚C after 48 hpf showed only minor mortality rates or malformations of the larvae when compared to rearing starting earlier at 36˚C [43]. Subsequent to the transplantation, increasing the rearing temperature to 36˚C enhanced proliferation and survival of human cells greatly, when compared to 34˚C [34], which was widely used in other studies [16,19], while transcriptional differences remained minor [43]. Adequate development of the larvae upon transplantation was essential when analyzing niche components of the fish; however, engraftment of LCs was considered equally important for the intended model. In conclusion, for the present project, embryos were bred at 28.5˚C until 48 hpf [34]. Subsequent to the xenotransplantation of LCs, larvae were kept at 36˚C. In our experiments, no severe developmental abnormalities were observed and most of the larvae developed normally. This is in line with the results of Cabezas-Sainz et al. [34].

In our described orthotopic model, we observed LCs homing and engraftment in the CHT within three days of follow up, with the tumor burden increasing over time as monitored with serial *in vivo* imaging. Notably, not exclusively LCs are documented to home to the CHT. Sacco *et al.* transplanted multiple myeloma cells into the blood circulation of larvae and showed that the myeloma cells resided in the CHT area shortly after transplantation, while cells of a cervix carcinoma did not [42]. Interestingly, a breast cancer cell line, known to build bone marrow metastasis, also homed to the CHT area [42,44]. In addition, primary cells of a breast cancer bone marrow metastasis engrafted within the CHT area [44], supporting the idea of an appropriate conservation of zebrafish niche components to resemble a bone marrow like environment, recognized by human cancer cells.

When analyzing LCs after systemic transplantation, monitoring of the tumor burden at a single time point is not sufficient to clearly demonstrate whether LCs underwent cell divisions or if they homed more efficiently to the CHT over time. As demonstrated using *in vivo* time lapse imaging, our results clearly demonstrate cell divisions of human LCs within the zebrafish. Furthermore, the analysis with a proliferation sensitive dye using flow cytometry showed that individual cells underwent up to five cell divisions within only three days. This result is comparable to the data of Vargas-Patron *et al.*, who demonstrated up to four cell divisions of

glioblastoma cells within three days using a similar approach [45]. Notably, to our knowledge no other study demonstrated cell divisions within larval xenografts of LCs in such detail.

Yet, larval xenografts were mainly used to study drug response [20,21,46] or metastatic properties of solid tumors [15,16,41,44] and the model was seldom used to analyze interactions with surrounding tissues. In order to assess the suitability of the model to identify characteristics of the microenvironment that are important in processes such as tumor development, maintenance and relapse onset, we investigated if and how LCs were in contact with certain niche cells. Larval zebrafish are especially good recipients for xenotransplanted cells as they did not develop adaptive immunity yet [47]. Still, the analysis of cellular parts of the innate immune system is feasible, as macrophages are already present as early as 24 hpf [48]. To date, only very few studies exist that analyzed the interplay of macrophages and BCP-ALL. Thus, we assessed the feasibility to use larval zebrafish as a model to study macrophages in more detail.

Macrophages belong to cellular elements of the innate immune system and are highly interesting niche cells to study as they are known to play diverse roles in malignant diseases. Different activation states of macrophages are described: an immune-stimulating and therefore anti-tumor (M1) and an immune-suppressive and therefore pro-tumor (M2) state [49]. In zebrafish embryos, macrophages are present as early as 24 hpf [48] and can be easily monitored in transgenic larvae expressing the fluorescent protein mCherry specifically in macrophages (Tg (mpeg1:mCherry-F)). Using *in vivo* imaging of macrophage-transgenic reporter larvae, we were able to monitor macrophage behavior of zebrafish larvae after xenotransplantation of human leukemic cells. While fulfilling their host defending function, they patrol throughout the fish. Interestingly, some macrophages slowed down and were very stationary during the observed contact with LCs. We were able to document dynamic, close and persisting cellular interactions between LCs and macrophages, which lasted up to 10 hours. Especially 3D renderings emphasized the close contact of the two cells. At the onset of the contact, macrophages changed their shape and developed protrusions to reach the LC. Later, the LC was fully embraced by the macrophage before they released each other and moved on. Contrary to these observations, we saw rapid phagocytosis events of macrophages eliminating transplanted LCs. This demonstrated that macrophages showed a very diverse behavior towards transplanted LCs, as they were temporarily closely interacting with LCs while it was shown that they clearly were able to eliminate LCs. During these periods of close contact, macrophages and LCs could possibly communicate extensively, resulting in processes, such as niche remodeling and leukemia progression. For instance, Roh-Johnson *et al*. were able to demonstrate in melanoma zebrafish xenografts that during such close contacts macrophages transferred cytoplasm to the melanoma cell, which then led to enhanced melanoma dissemination [50]. In contrast, Asokan *et al*. documented a prolonged interaction of an immune cell with a breast cancer cell, which finally got phagocytized [51], demonstrating the versatile polarization potential of macrophages. In another recent publication, Póvoa *et al*. identified that a colorectal cancer cell population (progressors) was able to block macrophage-mediated tumor clearance of another colorectal cancer cell population (regressors) in a co-transplantation approach. Using individual recipients for both populations, the regressive population could not engraft, demonstrating the progressors' potential to modulate macrophages towards a pro-tumoral polarization [52].

Despite the observation of intensive contact between LCs and macrophages, no enhanced infiltration or even recruitment of macrophages to the caudal part of the larva could be observed at three dpi, when analyzing relative cell numbers in a flow cytometric approach. In addition, no extensive phagocytosis of the fluorescently labeled LCs was detected when analyzing the inclusion of LCs' fluorescence within macrophages. Still, sporadic phagocytosis events were observed and demonstrated the inter-species ability of phagocytes to eliminate human cells. In contrast to our observation of mild phagocytosis activity, Asokan *et al*. detected

significantly more macrophages co-localizing with breast cancer cells, as a measurement of phagocytosis activity, after a comparable period of time after transplantation as we used for our experiments [51]. This indicates differential behavior of macrophages within different tumor microenvironments.

Our data suggests a leukemia-supporting polarization of the macrophages, as a result of the close and persisting interactions, rather than an anti-tumor phenotype, with extensive phagocytosis and active macrophage recruitment to the niche. To our knowledge, this is the first study visualizing and analyzing the interaction of innate immune cells and LCs in a zebrafish model and demonstrates the potential of the model to study their interplay in more detail.

In a next step, the localization pattern of LCs within the CHT area over time was analyzed. The larval zebrafish model enables repetitive imaging of individual larvae at different days. Here, we were able to monitor an increase in LC burden over time. With regards to the localization of LCs, it became apparent that at one dpi, LCs were rather uniformly spread within the vasculature of the niche, while starting at two dpi, LCs tended to build clusters within physiologically emerging extraluminal pockets. At three dpi, LCs were almost exclusively localized within these extravasal pockets around the main artery. As we observed this dissemination pattern of LC localization for a number of different LCs, the extravasation and cluster formation seemed to be a specific process rather than a random behavior. Extravasation is a complex process and requires functional signaling between extravasating LCs and the endothelium [36], demonstrating a functional signaling between human LCs and the zebrafish endothelium in the present model. Subsequent to LC homing to the CHT, LCs were surrounded by a dense vessel bed, enabling signaling and thereby reprogramming of this niche component. For HSPCs, Tamplin *et al*. showed that the remodeling of endothelial cells around HSPCs, which they called "endothelial cuddling", led to HSPC proliferation [28]. A similar important function of the endothelium might be conceivable for LCs. The accumulation of cancer cells within extraluminal pockets was also described by Marcatali *et al*. when they were transplanting breast cancer cells. They observed these cells within these pockets for two more days, up to five dpi [44]. Interestingly, ventral of the main artery, at around three to five dpf, a vessel of the lymphoid system was emerging [53]. This is exactly the time span in which we observed the specific distribution pattern towards the pockets. Lymphatic organs are known to be infiltrated with tumor cells [54], so there is a possibility that the pockets are associated to lymphatic tissue. This hypothesis could be proven with a suitable reporter fish line. Notably, these extraluminal pockets are not colonized by healthy HSPCs. While HSPCs are also evenly distributed throughout the CHT at three dpf, they shift towards the caudal vein at four dpf, before relocation to the kidney marrow [29]. Therefore, it could also be speculated that oxygen tension or expression of different cytokine receptor types between leukemic cells and endogenous HSPCs could be responsible for these diverging migration patterns within the hematopoietic niche.

Conclusions

Taken together, the generated larval xenograft model is suitable to study leukemia in a complex environment. In line with studies of other tumor entities [44,51,52], LCs showed close and persisting interactions with macrophages and a specific dissemination pattern within the vasculature, suggesting a functional interplay with the microenvironment. Thus, this model is useful to study effects of the leukemia microenvironment and will help to better understand its role in processes such as leukemia development, maintenance and relapse in the future.

Supporting information

S1 Fig. EGFP and CFSE intensities of NALM-6 and PDX cells. (A) Representative fluorescent (lower panel) and brightfield (merge, upper panel) images of the caudal part of an untransplanted larva at 1 and 3 dpi. The outline of the niche area is highlighted and was used to assess the CTCF of the larvae. **(B)** Dot plot of the flow cytometry measurement of an untransplanted sample. Grey dots show cells in singlets gate; green dots show NALM-6 cells. For detailed gating see S2A and S2B Fig. **(C)** Gating strategy for single cell suspension of transplanted larvae: 'Lymphocyte' gate was established using FSC-A/SSC-A of a pure leukemia sample (not shown). This gate was applied on the target sample and processed further. 'Singlets' were gated using FSC-H/FSC-W. mCherry positive 'Leukemia' cells (here NALM-6) were selected by gating on mCherry positive events using mCherry/FSC-A. These cells were used to analyze CFSE intensities and distribution patterns. **(D)** Representative histograms of the CFSE signal of PDX-265 at daily measurements of 10 pooled larvae. **(E)** Six frames of a time lapse video between 14 and 16.5 hpi with a frame interval of 30 min are depicted. Upper row shows the merged image of eGFP+ NALM-6 cells (green, middle row) and kdrl:mCherry endothelial cells (magenta, lower row). These images illustrate a NALM-6 cell located in a vessel for an extended period of time. Between 15 and 15.5 hpi the NALM-6 cell divided. CA: Caudal artery (outlined with white dashed lines). Scale bar: 10 μm.
(TIF)

S2 Fig. Detailed gating strategy for FCAS analysis of leukemic cells after xenotransplantation. (A) 'Cells' were selected using FSC-A/SSC-A. 'Singlets' were gated using FSC-H/FSC-W. mCherry positive 'macrophages' were selected by gating on mCherry positive events using mCherry/FSC-A. 'Leukemia cells' were detected by applying the 'lymphocytes gate that was drawn using a leukemia cell sample (see (B)) on the singlets gate (FSC-A/SSC-A). Next, events that were positive for the fluorescent marker (here: eGFP) were considered as leukemia cells by eGFP/FSC-A. **(B)** Exemplary gates of the pure LC sample. **(C)** Exemplary plots of untransplanted larvae sample.
(TIF)

S3 Fig. Imaging of PDX leukemic cells after transplantation. Confocal microscopy of the caudal parts of either one representative Tg(kdrl:mCherry) larva, transplanted with PDX-ALL-199 cells (top) or PDX-ALL-265 cells over the course of three days is depicted. Left panel shows merged images of LCs (green, middle panel) and the endothelium (kdrl:mCherry) (red, right panel). CV: Caudal vein (outlined with white dashed lines), CA: Caudal artery (outlined with white dashed lines). Scale bar 50 μm.
(TIF)

S1 Table. Clinical data of patients with BCP-ALL.
(TIF)

Acknowledgments

We thank Bettina Schmid and her team (German Center for Neurodegenerative Diseases (DZNE, Munich, Germany) for excellent animal care services. Christina Zeller for providing the eGFP lentivirus, Anna-Katharina Wirth for providing ALL-199 and ALL-265.

Author Contributions

Conceptualization: Anja Arner, Bradley Wayne Blaser, Vera Binder-Blaser.

Data curation: Anja Arner, Andreas Ettinger.

Formal analysis: Anja Arner, Andreas Ettinger, Bradley Wayne Blaser.

Funding acquisition: Vera Binder-Blaser.

Investigation: Anja Arner.

Methodology: Anja Arner, Vera Binder-Blaser.

Project administration: Bettina Schmid, Vera Binder-Blaser.

Resources: Bettina Schmid, Irmela Jeremias, Vera Binder-Blaser.

Software: Vera Binder-Blaser.

Supervision: Bettina Schmid, Irmela Jeremias, Vera Binder-Blaser.

Validation: Anja Arner, Bradley Wayne Blaser, Vera Binder-Blaser.

Visualization: Anja Arner.

Writing – original draft: Anja Arner, Vera Binder-Blaser.

Writing – review & editing: Anja Arner, Andreas Ettinger, Bradley Wayne Blaser, Bettina Schmid, Irmela Jeremias, Nadia Rostam, Vera Binder-Blaser.

References

1. Erdmann F KP, Grabow D, Spix C. German Childhood Cancer Registry—Annual Report 2019 (1980–2018). Institute of Medical Biostatistics, Epidemiology and Informatics (IMBEI) at the University Medical Center of the Johannes Gutenberg University Mainz. 2020.
2. Inaba H, Pui CH. Advances in the Diagnosis and Treatment of Pediatric Acute Lymphoblastic Leukemia. J Clin Med. 2021; 10(9). Epub 2021/05/06. https://doi.org/10.3390/jcm10091926 PMID: 33946897; PubMed Central PMCID: PMC8124693.
3. Vrooman LM, Blonquist TM, Harris MH, Stevenson KE, Place AE, Hunt SK, et al. Refining risk classification in childhood B acute lymphoblastic leukemia: results of DFCI ALL Consortium Protocol 05–001. Blood Advances. 2018; 2(12):1449–58. https://doi.org/10.1182/bloodadvances.2018016584 PMID: 29941458
4. Teachey DT, Pui CH. Comparative features and outcomes between paediatric T-cell and B-cell acute lymphoblastic leukaemia. Lancet Oncol. 2019; 20(3):e142–e54. Epub 2019/03/08. https://doi.org/10.1016/S1470-2045(19)30031-2 PMID: 30842058.
5. Scadden DT. The stem-cell niche as an entity of action. Nature. 2006; 441(7097):1075–9. Epub 2006/07/01. https://doi.org/10.1038/nature04957 PMID: 16810242.
6. Binder V, Li W, Faisal M, Oyman K, Calkins DL, Shaffer J, et al. Microenvironmental control of hematopoietic stem cell fate via CXCL8 and protein kinase C. Cell Rep. 2023; 42(5):112528. Epub 2023/05/20. https://doi.org/10.1016/j.celrep.2023.112528 PMID: 37209097.
7. Blaser BW, Moore JL, Hagedorn EJ, Li B, Riquelme R, Lichtig A, et al. CXCR1 remodels the vascular niche to promote hematopoietic stem and progenitor cell engraftment. The Journal of experimental medicine. 2017; 214(4):1011–27. https://doi.org/10.1084/jem.20161616 PMID: 28351983; PubMed Central PMCID: PMC5379982.
8. Lapidot T, Sirard C, Vormoor J, Murdoch B, Hoang T, Caceres-Cortes J, et al. A cell initiating human acute myeloid leukaemia after transplantation into SCID mice. Nature. 1994; 367(6464):645–8. Epub 1994/02/17. https://doi.org/10.1038/367645a0 PMID: 7509044.
9. Wang X, Huang S, Chen JL. Understanding of leukemic stem cells and their clinical implications. Mol Cancer. 2017; 16(1):2. Epub 2017/02/01. https://doi.org/10.1186/s12943-016-0574-7 PMID: 28137304; PubMed Central PMCID: PMC5282926.
10. Méndez-Ferrer S, Bonnet D, Steensma DP, Hasserjian RP, Ghobrial IM, Gribben JG, et al. Bone marrow niches in haematological malignancies. Nat Rev Cancer. 2020; 20(5):285–98. Epub 2020/03/01. https://doi.org/10.1038/s41568-020-0245-2 PMID: 32112045.
11. Bajaj J, Konuma T, Lytle NK, Kwon HY, Ablack JN, Cantor JM, et al. CD98-Mediated Adhesive Signaling Enables the Establishment and Propagation of Acute Myelogenous Leukemia. Cancer Cell. 2016;

30(5):792–805. Epub 2016/12/03. https://doi.org/10.1016/j.ccell.2016.10.003 PMID: 27908736; PubMed Central PMCID: PMC5137811.

12. Lee LM, Seftor EA, Bonde G, Cornell RA, Hendrix MJ. The fate of human malignant melanoma cells transplanted into zebrafish embryos: assessment of migration and cell division in the absence of tumor formation. Dev Dyn. 2005; 233(4):1560–70. Epub 2005/06/22. https://doi.org/10.1002/dvdy.20471 PMID: 15968639.

13. Haldi M, Ton C, Seng WL, McGrath P. Human melanoma cells transplanted into zebrafish proliferate, migrate, produce melanin, form masses and stimulate angiogenesis in zebrafish. Angiogenesis. 2006; 9(3):139–51. https://doi.org/10.1007/s10456-006-9040-2 PMID: 17051341.

14. Nicoli S, Ribatti D, Cotelli F, Presta M. Mammalian tumor xenografts induce neovascularization in zebrafish embryos. Cancer research. 2007; 67(7):2927–31. Epub 2007/04/06. https://doi.org/10.1158/0008-5472.CAN-06-4268 PMID: 17409396.

15. Drabsch Y, He S, Zhang L, Snaar-Jagalska BE, ten Dijke P. Transforming growth factor-β signalling controls human breast cancer metastasis in a zebrafish xenograft model. Breast Cancer Res. 2013; 15 (6):R106. Epub 2013/11/08. https://doi.org/10.1186/bcr3573 PMID: 24196484; PubMed Central PMCID: PMC3978640.

16. He S, Lamers GE, Beenakker JW, Cui C, Ghotra VP, Danen EH, et al. Neutrophil-mediated experimental metastasis is enhanced by VEGFR inhibition in a zebrafish xenograft model. J Pathol. 2012; 227 (4):431–45. Epub 2012/03/01. https://doi.org/10.1002/path.4013 PMID: 22374800; PubMed Central PMCID: PMC3504093.

17. Zhao C, Wang X, Zhao Y, Li Z, Lin S, Wei Y, et al. A novel xenograft model in zebrafish for high-resolution investigating dynamics of neovascularization in tumors. PloS one. 2011; 6(7):e21768. Epub 2011/07/19. https://doi.org/10.1371/journal.pone.0021768 PMID: 21765912; PubMed Central PMCID: PMC3135597.

18. White RM, Sessa A, Burke C, Bowman T, LeBlanc J, Ceol C, et al. Transparent adult zebrafish as a tool for in vivo transplantation analysis. Cell stem cell. 2008; 2(2):183–9. https://doi.org/10.1016/j.stem.2007.11.002 PMID: 18371439; PubMed Central PMCID: PMC2292119.

19. Pruvot B, Jacquel A, Droin N, Auberger P, Bouscary D, Tamburini J, et al. Leukemic cell xenograft in zebrafish embryo for investigating drug efficacy. Haematologica. 2011; 96(4):612–6. https://doi.org/10.3324/haematol.2010.031401 PMID: 21228037; PubMed Central PMCID: PMC3069240.

20. Bentley VL, Veinotte CJ, Corkery DP, Pinder JB, LeBlanc MA, Bedard K, et al. Focused chemical genomics using zebrafish xenotransplantation as a pre-clinical therapeutic platform for T-cell acute lymphoblastic leukemia. Haematologica. 2015; 100(1):70–6. https://doi.org/10.3324/haematol.2014.110742 PMID: 25281505; PubMed Central PMCID: PMC4281315.

21. Corkery DP, Dellaire G, Berman JN. Leukaemia xenotransplantation in zebrafish—chemotherapy response assay in vivo. British journal of haematology. 2011; 153(6):786–9. https://doi.org/10.1111/j.1365-2141.2011.08661.x PMID: 21517816.

22. Fior R, Póvoa V, Mendes RV, Carvalho T, Gomes A, Figueiredo N, et al. Single-cell functional and chemosensitive profiling of combinatorial colorectal therapy in zebrafish xenografts. Proc Natl Acad Sci U S A. 2017; 114(39):E8234–e43. Epub 2017/08/25. https://doi.org/10.1073/pnas.1618389114 PMID: 28835536; PubMed Central PMCID: PMC5625889.

23. Jung DW, Oh ES, Park SH, Chang YT, Kim CH, Choi SY, et al. A novel zebrafish human tumor xenograft model validated for anti-cancer drug screening. Mol Biosyst. 2012; 8(7):1930–9. Epub 2012/05/10. https://doi.org/10.1039/c2mb05501e PMID: 22569777.

24. Davidson AJ, Zon LI. The 'definitive' (and 'primitive') guide to zebrafish hematopoiesis. Oncogene. 2004; 23(43):7233–46. https://doi.org/10.1038/sj.onc.1207943 PMID: 15378083.

25. de Jong JL, Zon LI. Use of the zebrafish system to study primitive and definitive hematopoiesis. Annual review of genetics. 2005; 39:481–501. https://doi.org/10.1146/annurev.genet.39.073003.095931 PMID: 16285869.

26. Murayama E, Kissa K, Zapata A, Mordelet E, Briolat V, Lin HF, et al. Tracing hematopoietic precursor migration to successive hematopoietic organs during zebrafish development. Immunity. 2006; 25 (6):963–75. Epub 2006/12/13. https://doi.org/10.1016/j.immuni.2006.10.015 PMID: 17157041.

27. Wattrus SJ, Zon LI. Stem cell safe harbor: the hematopoietic stem cell niche in zebrafish. Blood Adv. 2018; 2(21):3063–9. Epub 2018/11/15. https://doi.org/10.1182/bloodadvances.2018021725 PMID: 30425071; PubMed Central PMCID: PMC6234371 Therapeutics, CAMP4 Therapeutics, and Scholar Rock. S.J.W. declares no competing financial interests.

28. Tamplin OJ, Durand EM, Carr LA, Childs SJ, Hagedorn EJ, Li P, et al. Hematopoietic stem cell arrival triggers dynamic remodeling of the perivascular niche. Cell. 2015; 160(1–2):241–52. https://doi.org/10.1016/j.cell.2014.12.032 PMID: 25594182; PubMed Central PMCID: PMC4346256.

29. Xue Y, Lv J, Zhang C, Wang L, Ma D, Liu F. The Vascular Niche Regulates Hematopoietic Stem and Progenitor Cell Lodgment and Expansion via klf6a-ccl25b. Developmental cell. 2017; 42(4):349–62 e4. Epub 2017/08/15. https://doi.org/10.1016/j.devcel.2017.07.012 PMID: 28803829.

30. Howe K, Clark MD, Torroja CF, Torrance J, Berthelot C, Muffato M, et al. The zebrafish reference genome sequence and its relationship to the human genome. Nature. 2013; 496(7446):498–503. https://doi.org/10.1038/nature12111 PMID: 23594743; PubMed Central PMCID: PMC3703927.

31. Chen AT, Zon LI. Zebrafish blood stem cells. J Cell Biochem. 2009; 108(1):35–42. Epub 2009/07/01. https://doi.org/10.1002/jcb.22251 PMID: 19565566.

32. Jing L, Zon LI. Zebrafish as a model for normal and malignant hematopoiesis. Dis Model Mech. 2011; 4 (4):433–8. https://doi.org/10.1242/dmm.006791 PMID: 21708900; PubMed Central PMCID: PMC3124047.

33. Konantz M, Balci TB, Hartwig UF, Dellaire G, André MC, Berman JN, et al. Zebrafish xenografts as a tool for in vivo studies on human cancer. Ann N Y Acad Sci. 2012; 1266:124–37. Epub 2012/08/21. https://doi.org/10.1111/j.1749-6632.2012.06575.x PMID: 22901264.

34. Cabezas-Sainz P, Guerra-Varela J, Carreira MJ, Mariscal J, Roel M, Rubiolo JA, et al. Improving zebrafish embryo xenotransplantation conditions by increasing incubation temperature and establishing a proliferation index with ZFtool. BMC cancer. 2018; 18(1):3. Epub 2018/01/03. https://doi.org/10.1186/s12885-017-3919-8 PMID: 29291719; PubMed Central PMCID: PMC5748948.

35. Vick B, Rothenberg M, Sandhöfer N, Carlet M, Finkenzeller C, Krupka C, et al. An advanced preclinical mouse model for acute myeloid leukemia using patients' cells of various genetic subgroups and in vivo bioluminescence imaging. PloS one. 2015; 10(3):e0120925. Epub 2015/03/21. https://doi.org/10.1371/journal.pone.0120925 PMID: 25793878; PubMed Central PMCID: PMC4368518.

36. Wettschureck N, Strilic B, Offermanns S. Passing the Vascular Barrier: Endothelial Signaling Processes Controlling Extravasation. Physiol Rev. 2019; 99(3):1467–525. Epub 2019/05/30. https://doi.org/10.1152/physrev.00037.2018 PMID: 31140373.

37. Pezeshkian B, Donnelly C, Tamburo K, Geddes T, Madlambayan GJ. Leukemia Mediated Endothelial Cell Activation Modulates Leukemia Cell Susceptibility to Chemotherapy through a Positive Feedback Loop Mechanism. PloS one. 2013; 8(4):e60823. https://doi.org/10.1371/journal.pone.0060823 PMID: 23560111; PubMed Central PMCID: PMC3613371.

38. Lee YC, Chiou TJ, Tzeng WF, Chu ST. Macrophage inflammatory protein-3alpha influences growth of K562 leukemia cells in co-culture with anticancer drug-pretreated HS-5 stromal cells. Toxicology. 2008; 249(2–3):116–22. Epub 2008/06/10. https://doi.org/10.1016/j.tox.2008.04.017 PMID: 18538911.

39. Bruserud Ø, Glenjen N, Ryningen A, Ulvestad E. In vitro culture of human acute lymphoblastic leukemia (ALL) cells in serum-free media; a comparison of native ALL blasts, ALL cell lines and virus-transformed B cell lines. Leuk Res. 2003; 27(5):455–64. Epub 2003/03/07. https://doi.org/10.1016/s0145-2126(02)00227-8 PMID: 12620297.

40. Duarte D, Amarteifio S, Ang H, Kong IY, Ruivo N, Pruessner G, et al. Defining the in vivo characteristics of acute myeloid leukemia cells behavior by intravital imaging. Immunol Cell Biol. 2019; 97(2):229–35. Epub 2018/11/14. https://doi.org/10.1111/imcb.12216 PMID: 30422351; PubMed Central PMCID: PMC6446728.

41. Marques IJ, Weiss FU, Vlecken DH, Nitsche C, Bakkers J, Lagendijk AK, et al. Metastatic behaviour of primary human tumours in a zebrafish xenotransplantation model. BMC cancer. 2009; 9:128. Epub 2009/04/30. https://doi.org/10.1186/1471-2407-9-128 PMID: 19400945; PubMed Central PMCID: PMC2697170.

42. Sacco A, Roccaro AM, Ma D, Shi J, Mishima Y, Moschetta M, et al. Cancer Cell Dissemination and Homing to the Bone Marrow in a Zebrafish Model. Cancer research. 2016; 76(2):463–71. https://doi.org/10.1158/0008-5472.CAN-15-1926 PMID: 26744527.

43. Cabezas-Sainz P, Coppel C, Pensado-López A, Fernandez P, Muinelo-Romay L, López-López R, et al. Morphological Abnormalities and Gene Expression Changes Caused by High Incubation Temperatures in Zebrafish Xenografts with Human Cancer Cells. Genes (Basel). 2021; 12(1). Epub 2021/01/23. https://doi.org/10.3390/genes12010113 PMID: 33477746; PubMed Central PMCID: PMC7832305.

44. Mercatali L, La Manna F, Groenewoud A, Casadei R, Recine F, Miserocchi G, et al. Development of a Patient-Derived Xenograft (PDX) of Breast Cancer Bone Metastasis in a Zebrafish Model. Int J Mol Sci. 2016; 17(8). Epub 2016/08/25. https://doi.org/10.3390/ijms17081375 PMID: 27556456; PubMed Central PMCID: PMC5000770.

45. Vargas-Patron LA, Agudelo-Dueñas N, Madrid-Wolff J, Venegas JA, González JM, Forero-Shelton M, et al. Xenotransplantation of Human glioblastoma in Zebrafish larvae: in vivo imaging and proliferation assessment. Biol Open. 2019; 8(5). Epub 2019/05/16. https://doi.org/10.1242/bio.043257 PMID: 31085547; PubMed Central PMCID: PMC6550087.

46. Deveau AP, Bentley VL, Berman JN. Using zebrafish models of leukemia to streamline drug screening and discovery. Exp Hematol. 2017; 45:1–9. Epub 2016/10/31. https://doi.org/10.1016/j.exphem.2016.09.012 PMID: 27720937.

47. Lam SH, Chua HL, Gong Z, Lam TJ, Sin YM. Development and maturation of the immune system in zebrafish, Danio rerio: a gene expression profiling, in situ hybridization and immunological study. Dev Comp Immunol. 2004; 28(1):9–28. https://doi.org/10.1016/s0145-305x(03)00103-4 PMID: 12962979.

48. Herbomel P, Thisse B, Thisse C. Ontogeny and behaviour of early macrophages in the zebrafish embryo. Development. 1999; 126(17):3735–45. Epub 1999/08/06. https://doi.org/10.1242/dev.126.17.3735 PMID: 10433904.

49. Qian BZ, Pollard JW. Macrophage diversity enhances tumor progression and metastasis. Cell. 2010; 141(1):39–51. https://doi.org/10.1016/j.cell.2010.03.014 PMID: 20371344; PubMed Central PMCID: PMC4994190.

50. Roh-Johnson M, Shah AN, Stonick JA, Poudel KR, Kargl J, Yang GH, et al. Macrophage-Dependent Cytoplasmic Transfer during Melanoma Invasion In Vivo. Developmental cell. 2017; 43(5):549–62.e6. Epub 2017/12/06. https://doi.org/10.1016/j.devcel.2017.11.003 PMID: 29207258; PubMed Central PMCID: PMC5728704.

51. Asokan N, Daetwyler S, Bernas SN, Schmied C, Vogler S, Lambert K, et al. Long-term in vivo imaging reveals tumor-specific dissemination and captures host tumor interaction in zebrafish xenografts. Sci Rep. 2020; 10(1):13254. Epub 2020/08/09. https://doi.org/10.1038/s41598-020-69956-2 PMID: 32764590; PubMed Central PMCID: PMC7411039.

52. Póvoa V, Rebelo de Almeida C, Maia-Gil M, Sobral D, Domingues M, Martinez-Lopez M, et al. Innate immune evasion revealed in a colorectal zebrafish xenograft model. Nature communications. 2021; 12(1):1156. Epub 2021/02/21. https://doi.org/10.1038/s41467-021-21421-y PMID: 33608544; PubMed Central PMCID: PMC7895829.

53. Yaniv K, Isogai S, Castranova D, Dye L, Hitomi J, Weinstein BM. Live imaging of lymphatic development in the zebrafish. Nat Med. 2006; 12(6):711–6. Epub 2006/05/30. https://doi.org/10.1038/nm1427 PMID: 16732279.

54. Futami M, Corey SJ. Chapter 328—Signaling Targets in Lymphoid Leukemias. In: Bradshaw RA, Dennis EA, editors. Handbook of Cell Signaling (Second Edition). San Diego: Academic Press; 2010. p. 2831–5.